IMPERIAL

Imperial College of Science, Technology and Medicine

Department of Chemical Engineering

Enhanced Olefin and Aromatic Production in a Coupled Bio-Oil Hydroprocessing and Alkane Dehydrogenation System

Abdullah Hassan Baubaid

May 12, 2024

Submitted in part fulfillment of the requirements for the degree of Doctor of Philosophy in Chemical Engineering of Imperial College London and the Diploma of Imperial College London.

Abdullah Hassan Baubaid

in partial fulfillment of the requirements for the degree of

Doctorate

in Chemical Engineering

at the Imperial College of London,

Defended in July 2024.

Supervisor:	Dr. Marcos Millan,	Imperial College London
Examination committee:		
Internal examiner	Prof. Klaus Hellgardt,	Imperial College London
External examiner	Dr. Marcelo Domine,	Instituto de Tecnologia Quimica, CSIC, Spain

Abstract

Biomass-derived oil (bio-oil) is regarded as a key hydrocarbon source capable of diminishing reliance on fossil fuels for chemicals. However, to prepare bio-oil for value-added chemical production, it must be upgraded by removing heteroatoms, mainly oxygen, through hydrodeoxygenation hydrodeoxygenation (HDO). Catalytic HDO of guaiacol, a bio-oil model compound, using in-situ produced hydrogen by alkane (ethane) dehydrogenation (DeH) is investigated to evaluate the use of an alternative to expensive molecular hydrogen (produced ex-situ). Coupling simultaneous ethane DeH with bio-oil upgrading could be a potentially attractive process in terms of the economic outlook by co-producing ethylene, a high-value-added chemical, alongside aromatics and phenols. In this work, these tandem reactions are investigated using different configurations of hydroprocessing and/or alkane DeH catalytic systems and thermodynamic favourable operating conditions for HDO of guaiacol and ethane DeH to achieve valuable products. Alkane DeH demonstrated its potential as a hydrogen source by leading to an improvement in HDO product distribution with the production of species with no or lower oxygen content, benzene and phenol, besides the production of ethylene. However, the extent of HDO declines with time due to catalyst deactivation caused by oxygenated hydrocarbon condensate, which limits ethane from reaching active sites for hydrogen formation. Yet, ethylene was co-produced in experiments that showed a better extent of HDO measured by O-to-aromatic ratio in comparison with the use of an excess of externally supplied hydrogen. The findings underscore the importance of ensuring stable hydrogen formation through DeH and maintaining selective HDO active sites within the catalyst bed to enhance the DeH-HDO coupling process's efficacy. From an economic perspective, the coupling demonstrates significant potential in replacing hydrogen with on-purpose alkane DeH, as evidenced by experimental results. A set of reaction and process requirements are established, based on the experimental results and literature findings, to further enhance the coupling's feasibility.

Declaration of Originality

I certify that all the work contained in this thesis is my own and all else is appropriately referenced.

Abdullah Hassan Baubaid
London, May 2024

Copyright Declaration

The copyright of this thesis rests with the author. Unless otherwise indicated, its contents are licensed under a Creative Commons Attribution-Non Commercial 4.0 International Licence (CC BY-NC). Under this licence, you may copy and redistribute the material in any medium or format. You may also create and distribute modified versions of the work. This is on the condition that: you credit the author and do not use it, or any derivative works, for a commercial purpose. When reusing or sharing this work, ensure you make the licence terms clear to others by naming the licence and linking to the licence text. Where a work has been adapted, you should indicate that the work has been changed and describe those changes. Please seek permission from the copyright holder for uses of this work that are not included in this licence or permitted under UK Copyright Law

ACKNOWLEDGMENTS

I am profoundly thankful to everyone who has contributed to the completion of this thesis, a journey marked by various experiences and obstacles. Without the consistent support and guidance of many individuals, this accomplishment would have been unattainable. Their encouragement, expertise, and empathy have been invaluable throughout the past four years.

I am deeply indebted to my supervisor, Dr. Marcos Millan, who entrusted me with the opportunity to explore a complex research topic and provided unwavering support, encouragement, and trust. Over the last four years, Marcos has generously dedicated his time, offered guidance, and shared his knowledge. His patience and flexibility in exploring different avenues have created an excellent research environment, and I am honoured to have completed my PhD thesis under his supervision. I also want to thank Prof. Jason Hallett for being my thesis's assessor, as well as Dr. Marcelo Domine and Prof. Klaus Hellgardt for accepting the invitation to examine this work.

Additionally, I extend my gratitude to all current and former members of the fuel conversion group for fostering a collaborative and supportive environment conducive to sharing knowledge and experiences. Special thanks to Dr. Kagiso Bikane, Dr. Xiangyi Long, and Jaxian Luo for their assistance during daily laboratory activities. I am also thankful for the generous support provided by the college's electrical and mechanical workshops, led by Chin Lang and Tony Meredith, respectively. Furthermore, I acknowledge the invaluable assistance from the college's analytical lab, which facilitated training and access to various essential instruments.

I express my appreciation to the Saudi Basic Industries Corporation (SABIC) for enabling me to pursue further education at Imperial College London and for providing the necessary assistance to support my academic endeavours in the United Kingdom. Many individuals have contributed to my journey, from the initial application to the scholarship program to monitoring my PhD progress. Special thanks to Dr. Sari Al-Sayegh, Dr. JR Johnson, Mr. Ahmad Al-Blowi, and Alice for their invaluable support.

Finally, I convey my heartfelt appreciation for the unwavering encouragement from my parents, siblings, and spouse. I am especially grateful to my beloved daughter, Alyaa, whose presence has brought immense joy to my life as I near the completion of my PhD. My family and friends' constant motivation and faith of have been fundamental to my achievements. I am deeply grateful to all the teachers who have played a significant role in shaping my academic journey, from my earliest years of education to the completion of my thesis, their guidance and mentorship have been instrumental in my growth and success.

Abdullah Hassan Baubaid London, January 2024

"If the soul is impartial in receiving information, it devotes to that information the share of critical investigation the information deserves, and its truth or untruth thus becomes clear. However, if the soul is infected with partisanship for a particular opinion or sect, it accepts without a moment's hesitation the information that is agreeable to it. Prejudice and partisanship obscure the critical faculty and preclude critical investigation. The results is that falsehoods are accepted and transmitted"

The Muqaddimah of Ibn Khaldun

Abbreviations: Experimental

BET	Brunauer-Emmett-Teller
DDM	direct demethoxylation
DeH	dehydrogenation
DeH-HDO	dehydrogenation-assisted hydrodeoxygenation
DeHA	dehydroaromatisation
DeHD	dehydration
DFT	density functional theory
DME	demethylation
DOAr	double oxygen per aromatic ring
EDS	dispersive x-ray spectroscopy
EOR	end of run
FCC	fluid catalytic cracking
FID	flame ionisation detector
FT	Fischer-Tropsch
GC	Gas chromatography
GDP	gross domestic product
HDC	hydrocracking
HDO	hydrodeoxygenation
HDR	hydrogenolysis
HOHC	heavy oxygenated hydrocarbon compounds
HYD	hydrogenation
LPG	liquefied petroleum gas
MOR	middle of run
MS	mass spectroscopy
MTH	methylation
NGL	natural gas liquefied
NODeH	non-oxidative dehydrogenation
O:A	oxygen per aromatic ring
ODeH	oxidative dehydrogenation
OTC	oil-to-chemicals
PAH	polycyclic aromatic
PID	proportional–integral–derivative
RWGS	reverse water gas-shift
SC	steam cracking
SEM	scanning electron microscopy
SOAr	single oxygen per aromatic ring
SOR	start of run
SR	steam reforming
TCD	thermal conductivity detector
TGA	thermogravimetric analysis
TOS	time-on-stream
XRD	X-Ray diffraction
XRF	x-ray fluorescence

Abbreviations: Chemicals

ANS	Anisole
BTX	benzene-toluene-xylenes
CAT	catechol
CRSL	cresol
GUA	guaiacol
PHL	phenol
TOL	toluene

Abbreviations: Economic potential

APEA	aspen process economic analyser
BFD	block flow diagram
CapEx	capital expenditure
EP	economic potential
GHG	green house gas
kta	kilo-tonnes per annum
LCA	life cycle assessment
NPV	net present value
OpEx	operational expenditure
PFD	process flow diagram
TEA	techno-economic assessment
tpd	tons per day
TRL	technological readiness level

Contents

Abstract **ii**

1 Introduction **1**

1.1 Research objective 6

1.2 Thesis structure 7

2 Literature Review **8**

2.1 Biomass valorisation to fuels and chemicals 8

2.1.1 Biorefinery v.s. crude refinery 10

2.1.2 Biomass-based stream as energy source 11

2.1.3 Biomass-based building-block chemicals 13

2.2 Lignin valorisation to bio-oil 16

2.2.1 Lignin nature, types and processing 16

2.2.2 Lignin to bio-oil 17

2.2.3 Bio-oil characterisation 20

2.2.4 Bio-oil upgrading processes 21

2.3 Bio-oil upgrading via hydrodeoxygenation (HDO) 23

2.3.1 Conventional HDO 25

2.3.2 Atmospheric pressure HDO for continuous flow systems 28

2.3.3 Hydrogen production routes 31

2.4 H-donor for bio-oil hydrodeoxygenation 32

2.4.1 H-donor approach for upgrading low-value hydrocarbon streams 33

2.4.2 Bio-oil HDO via in-situ H_2 generated through carbon rejection 35

2.4.3 Alcohols as hydrogen source for bio-oil HDO 36

2.4.4 Supercritical water as hydrogen source for HDO 38

2.4.5 Heavy hydrocarbons as hydrogen source from bio-oil HDO 39

2.4.6 Light hydrocarbons as hydrogen source from bio-oil HDO 41

2.5 Catalytic system for coupled reactions (dehydrogenation-assisted hydrodeoxygenation (DeH-HDO)) . . . 43
2.5.1 Unsupported Mo-based catalysts . . . 44
2.5.2 Supported NiMo-based catalysts . . . 46

3 Methodology **52**
3.1 Experimental Methodology . . . 52
3.1.1 Experimental approach . . . 52
3.1.2 Experimental procedure . . . 53
3.1.3 Materials . . . 55
3.2 Experimental testing rig . . . 55
3.2.1 Experimental testing rig description . . . 55
3.2.2 Feeding section . . . 55
3.3 Reactor modelling . . . 58
3.3.1 Involved physics in COMSOL model . . . 60
3.3.2 Model observations . . . 62
3.4 Mass balance and product analysis . . . 66
3.4.1 Gaseous product: GC-TCD . . . 67
3.4.2 Liquid product: GC-FID . . . 67
3.4.3 Solid deposition: thermogravimetric analysis (TGA) . . . 69
3.4.4 Data Reliability and Repeatability . . . 70
3.5 Solid catalyst characterisation techniques . . . 70
3.5.1 X-ray diffraction (XRD) . . . 70
3.5.2 X-ray fluorescence (XRF) . . . 70
3.5.3 Brunauer-Emmett-Teller (BET) . . . 70
3.5.4 Scanning Electron Microscopy – Energy Dispersion X-Ray (SEM-EDS) . 70
3.6 Operating conditions . . . 71

4 The Potential of HDO of Bio-oil Derivatives via In-situ Hydrogen Generation **73**
4.1 Introduction . . . 73
4.1.1 Chapter structure . . . 74
4.1.2 Understanding the coupling potential . . . 75
4.2 Catalyst preparation and characterisation . . . 78
4.3 Conventional HDO at elevated pressures using NiMo/γ-Al_2O_3 (NiMoAl) . . . 80

4.4 Ethane dehydrogenation (DeH) . . . 83
4.4.1 Thermal ethane DeH . . . 83
4.4.2 Catalytic ethane DeH using NiMo/γ-Al_2O_3 catalysts . . . 84
4.5 The effect of "in-situ" hydrogen generation on HDO . . . 87
4.5.1 Thermal coupling of DeH-HDO . . . 87
4.5.2 Catalytic coupling of DeH-HDO using P-NiMo/γAl_2O_3 . . . 88
4.6 Eliminating the effects of Ni and acidic support using unsupported MoO_3 . . . 94
4.7 DeH-HDO based on alkane DeH catalyst Cr_2O_3/Al_2O_3 . . . 96
4.7.1 Catalytic ethane DeH . . . 96
4.7.2 Catalyst characterisation . . . 96
4.7.3 Catalytic ethane DeH . . . 97
4.7.4 Catalytic DeH-HDO on alkane DeH catalyst . . . 98
4.7.5 Optimising the processing parameters to maximise BTX yield . . . 99
4.8 Conclusions . . . 101

5 Optimising DeH-HDO with Synergistic Dual Catalyst System 103

5.1 Introduction . . . 103
5.1.1 Background . . . 104
5.1.2 The utilisation of dual catalytic system for DeH-HDO . . . 104
5.1.3 The potential role of dual active sites for DeH-HDO . . . 105
5.1.4 Chapter structure . . . 107
5.2 MoO_3-Cr catalytic system . . . 107
5.2.1 The effect of replacing molecular hydrogen to ethane DeH . . . 108
5.2.2 Particle size effects . . . 111
5.2.3 Space velocity effect . . . 111
5.2.4 Molar ratio effect . . . 112
5.3 DeH-HDO in PNiMo-Cr catalytic system . . . 114
5.3.1 Thermal and HDO catalytic effects . . . 114
5.3.2 DeH-HDO improvement via reducing partial pressure? . . . 116
5.4 Coke formation investigation under scanning electron microscopy (SEM) . . . 119
5.4.1 Coke formation on Cr_2O_3/Al_2O_3 . . . 119
5.4.2 Coke formation on catalytic system: 1:1 weight ratio P-NiMoAl_2O_3 and Cr_2O_3/Al_2O_3 . . . 121
5.5 Discussion on the production of BTX and its limitations . . . 124

5.6 Proposed reaction pathway for DeH-HDO . . . 126
5.7 Experimental results from an industrial perspective . . . 127
5.8 Conclusions . . . 130

6 Tailored Catalyst Synthesis for Enhanced DeH-HDO Coupling 132
6.1 Introduction . . . 132
6.1.1 Chapter structure . . . 133
6.1.2 Why zeolite for DeH-HDO? . . . 133
6.2 Alumina support . . . 135
6.2.1 Catalyst synthesis and bed preparation . . . 135
6.2.2 Ethane DeH on Cr and Mo in Al_2O_3 supported catalysts . . . 136
6.2.3 Reactivity test performance: Guaiacol and ethane DeH-HDO on Cr and Mo in Al_2O_3 supported catalysts . . . 139
6.3 Zeolite support . . . 146
6.3.1 Catalyst synthesis . . . 146
6.3.2 Catalyst preparation and characterisation . . . 146
6.3.3 Cr and Mo in zeolite supported catalysts for ethane DeH . . . 148
6.3.4 Cr and Mo in zeolite supported catalysts for ethane and guaiacol DeH-HDO . . . 150
6.4 Conclusions . . . 153

7 Techno-Economic Feasibility for Integrating Alkane DeH with Bio-Oil HDO Processes 154
7.1 Introduction . . . 154
7.1.1 Chapter structure . . . 154
7.1.2 The industrial implication of coupling DeH-HDO . . . 155
7.2 Techno-economic (TEA) based on experimental findings . . . 156
7.2.1 Economic Potential . . . 156
7.3 DeH-HDO process synthesis for TEA . . . 159
7.3.1 Process boundary limits . . . 159
7.3.2 HDO conversion section . . . 161
7.3.3 HDO liquid separation section . . . 161
7.3.4 Economic evaluation . . . 162
7.3.5 Monte-Carlo and economic sensitivity analysis . . . 164

7.3.6 Sensitivity analysis: Improved ethane DeH 166
7.3.7 DeH-HDO Integration to the chemical Industry 168
7.4 DeH-HDO implementation in HDO-FCC process integration 176
7.4.1 The economic potential of replacing HDO by DeH-HDO in HDO-FCC integration 176
7.4.2 Economic incentive of integrating DeH-HDO to FCC 180
7.5 Conclusion: HDO Industrial scalability and process integration 184

8 Conclusions **188**

9 Future Prospects **191**
9.1 Processing parameters 191
9.2 Catalytic system 193
9.3 Reactor configuration 193
9.4 Process integration 194

A Experimental **222**

B Analytical Instrument **227**

C Process development and techno-economic supplementary information **235**

List of Figures

1.1 Power capacity allocation by source 2
1.2 Bio-energy source allocation for net zero emission scenario 2
1.3 Market share for plastics by feedstock source in 2019 and 2030 forecast . . 3
1.4 Current and five-year projections of global capacity for bio-plastics 3
1.5 Possible crude oil and biomass integrated chemical value chain 4
1.6 Proposed integration of bio-oil hydrodeoxygenation with ethane steam cracking 5

2.1 Lignocellulosic biomass conversion routes to bio-fuels and chemicals . . . 9
2.2 Conventional and biomass refinery integration 11
2.3 Simplified biomass routes to bio-based energy, fuels and chemicals 12
2.4 Representative lignin structure 16
2.5 Chemical structure of the building block of lignin: monolignols 17
2.6 H/C and O/C of different types of petroleum and bio-oil feeds 19
2.7 Summarised Bio-oil upgrading technologies: advantages and catalyst types 21
2.8 Number of published articles on HDO and alkane DeH 24
2.9 Development in HDO of bio-derived oil and associated challenges 25
2.10 Proposed pathways for guaiacol HDO and hydrogenation 26
2.11 Proposed mechanisms for atmospheric HDO of guaiacol in continuous flow reactors 28
2.12 Temperature and pressure range for refinery processes 30
2.13 Hydrogen production map from different sources,processes and energy sources 32
2.14 External hydrogen sources for HDO as molecular hydrogen alternatives . . 33
2.15 Comparison of HHC upgrading technologies in term of HHC conversion, severity and CapEx requirement (the scale in the figure represents HHC conversion 36
2.16 Proposed mechanism of guaiacol HDO via in-situ hydrogen produced from isopropanol pyrolysis 37

2.17 Proposed mechanism for in-situ HDO using alkane DeH as hydrogen source 40
2.18 Schematic representation of hydrogen transfer from hexane DeH for cresol HDO 42
2.19 Desired changes of H/C and O/C in catalytic upgrading of lignin to benzene 44
2.20 Reported hypothesis in using bifunctional active sites for HDO 47

3.1 Designed experimental framework for investigated catalytic systems 53
3.2 Stages of a DeH-HDO experiment run 54
3.3 In-house built hydroprocessing rig to evaluate atmospheric hydrodeoxygenation of guaiacol using molecular hydrogen or in-situ generated hydrogen . 56
3.4 Modified gas feed-line system to accommodate two mass flow control (MFC) for safety, calibration and mixed feed experiments. 57
3.5 Temperature profile for ethane DeH experiment at different locations at NiMo/Al_2O_3 catalytic bed 59
3.6 Temperature profile for DeH-HDO experiment at different locations at NiMo/Al_2O_3 catalytic bed 60
3.7 Schematic of reactor modelling depicting electrical potential distribution in voltage 61
3.8 The temperature profile at various locations within the NiMo/Al_2O_3 catalytic bed, as generated by COMSOL. 64
3.9 Reaction product extracts collection, preparation and quantification techniques 66

4.1 A schematic of the combined reaction of in-situ HDO via alkane DeH of ethane 74
4.2 Thermodynamic analysis of ethane DeH, and phenol hydrogenation and hydrogenolysis at different operating temperatures and pressures using Aspen Plus® 76
4.3 The effects of operating DeH-HDO in a single reactor bed using first order reaction for each reaction independently using COMSOL Multiphysics . . . 77
4.4 Outlet temperature of coupled DeH-HDO in a single catalytic bed using at different phenol/ethane molar ratio calculated by COMSOL Multiphysics . 77
4.5 XRD for investigated catalysts in this chapter: MoO_3, NiMo/Al_2O_3 (NiMoAl), Cr/Al_2O_3 (CrAl) and P-NiMo/Al_2O_3 (PNiMoAl) 78
4.6 High pressure (up to 25 bar) guaiacol HDO using NiMo/γ-Al_2O_3 82

4.7 Atmospheric pressure ethane DeH in a SiC bed at different temperatures . 83
4.8 Temperature programmed ethane DeH at atmospheric pressure using NiMo/Al_2O_3 in a SiC bed 84
4.9 Atmospheric ethane DeH using NiMo-based catalysts 86
4.10 Atmospheric ethane DeH using NiMo/Al_2O_3 at different temperatures . . . 86
4.11 Atmospheric pressure thermal coupling of DeH-HDO in a SiC bed 87
4.12 Atmospheric pressure in-situ hydrogen generated and ex-situ HDO P-NiMo/γ -Al_2O_3 catalyst and thermal deoxygenation 88
4.13 Atmospheric HDO of guaiacol via in-situ hydrogen generation from ethane DeH using P-NiMo/Al_2O_3 90
4.14 Proposed reaction network for guaiacol HDO using hydrogen produced from ethane DeH 91
4.15 HDO of guaiacol via in-situ hydrogen generation from ethane DeH using P-NiMo/Al_2O_3 at atmospheric pressure, 550 °C 92
4.16 Composition of gas product stream of DeH-HDO integration for guaiacol and ethane on P-NiMo/γ -Al_2O_3 catalyst at 550 °C, an atmospheric pressure . . 93
4.17 Catalytic atmospheric HDO of guaiacol using MoO_3 95
4.18 Atmospheric HDO of guaiacol via in-situ hydrogen generation from ethane DeH using MoO_3 96
4.19 Catalytic ethane DeH of ethane using Cr_2O_3/Al_2O_3 at different space velocity and activation procedure 97
4.20 Atmospheric HDO of phenol via ethane as hydrogen source using Cr_2O_3/Al_2O_3 100

5.1 Targeted synergistic effects of mixing HDO and alkane DeH catalysts in a single catalytic bed 106
5.2 Atmospheric pressure HDO of guaiacol using MoO_3-Cr 110
5.3 Ethylene-to-ethane ratio of DeH and DeH-HDO using MoO_3-Cr at atmospheric pressure 112
5.4 Atmospheric HDO of guaiacol via in-situ hydrogen generation from ethane DeH at 600 °C 115
5.5 Atmospheric HDO of guaiacol using ethane DeH as a hydrogen donor reaction at 600 °C 116
5.6 Gas product of atmospheric HDO of guaiacol using ethane DeH as a hydrogen donor reaction using PNiMo-Cr catalytic system 118

5.7 Atmospheric pressure HDO of guaiacol via in-situ hydrogen generation from ethane DeH using catalytic system of 1:1 weight ratio of P-NiMo/Al_2O_3 and C_2O_3/Al_2O_3 119
5.8 SEM Images of spent catalyst Cr_2O_3/Al_2O_3 for atmospheric pressure ethane DeH 120
5.9 SEM Images of spent catalysts of Cr_2O_3/Al_2O_3 DeH-HDO under atmospheric pressure using ethane and guaiacol 121
5.10 SEM Images of spent catalyst of atmospheric DeH-HDO using 1:1 weight ratio P-NiMo/Al_2O_3 and Cr_2O_3/Al_2O_3 catalytic system 123
5.11 Atmospheric pressure HDO of guaiacol via ex-situ using MoO_3-Cr catalytic system at 600 °C 125
5.12 Proposed reaction network for guaiacol HDO using hydrogen produced from ethane DeH 127
5.13 Integration of catalytic systems to improve BTX formation based on experimental results 128

6.1 Particle size effects on atmospheric ethane DeH using Cr-based catalysts . 136
6.2 X-Ray diffraction (XRD) patterns for investigated catalysts 139
6.3 Ethylene formation with the presence and absence of guaiacol for atmospheric HDO via ethane DeH as a hydrogen donor reaction at different synthesised alumina supported catalysts 140
6.4 Ethylene formation from atmospheric HDO of guaiacol via ethane DeH as a hydrogen donor reaction using different synthesised alumina supported catalysts 141
6.5 Liquid fraction of atmospheric HDO of guaiacol via ethane DeH as a hydrogen donor reaction using different synthesised alumina supported catalysts 143
6.6 The progress of heavy oxygenated hydrocarbon compounds (HOHC) and benzene-toluene-xylenes (BTX) formation for atmospheric DeH-HDO using Cr-Mo/Al_2O_3 145
6.7 Nitrogen physisorption isotherms for ZSM-5 catalysts with Cr and Mo active sites 147
6.8 Ethane DeH using Mo and Cr zeolite catalysts 148
6.9 Ethane DeH using Mo and Cr zeolite catalysts 150
6.10 DeH-HDO using Mo and Cr zeolite catalysts 151

6.11 Hydrogen transfer in DeH-HDO using Mo and Cr zeolite catalysts 152

7.1 Economic potential for using alkane DeH for HDO of bio-oil at different feedstock and product prices. 158
7.2 The product distribution in the economic potential of DeH-HDO approach 159
7.3 Block flow diagram (BFD) of conventional HDO using external (ex-situ) hydrogen source defined as HDO 160
7.4 BFD of HDO using ethane DeH (in-situ) as hydrogen source defined as DeH-HDO 160
7.5 Proposed separation sequence based on experimental findings [205] 163
7.6 Monte Carlo analysis for DeH-HDO's net present value (NPV) for 20 years with 30% tax and 5% discount rate 165
7.7 NPV sensitivity analysis based on feedstock,product and utilities value variation by stander deviation 166
7.8 Block Flow Diagram (BFD) of conventional HDO 169
7.9 Simplified process flow diagram (PFD) of the integration of DeH-HDO with steam cracking. 171
7.10 Saved energy from steam cracking (cracker) by integrating DeH-HDO 175
7.11 Block flow diagram of biomass processing to chemicals. 178
7.12 Investigating required alkane DeH conversion and selectivity to perform Vispute et al. HDO-FCC integration at range of ethane-to-aromatic ratio . . . 178
7.13 Probability of hydrogen availability via alkane DeH performance at different aromatic content in bio-oil as well as ethane-to-aromatic ratio (R) 180
7.14 Product distribution from the integration of in-situ hydrogenation via H-donor reactions 184

9.1 Conceptual membrane reactor for DeH-HDO 195
9.2 BFD of lignocellulosic biomass (non-food biomass) maximum utilisation for bio-based building block chemical production for the chemical industry. . 196

A.1 Picture of hydrocracker setup for parts inside the cabinet 222
A.2 Hydrocracker reaction zone 223
A.3 Gas flow sparger positioned inside the reactor below the catalyst bed 223
A.4 Hydrocracker control box and LabVIEW interface 224

B.1 Picture of used Gas chromatography (GC) with a TCD detector for gas analysis 228
B.2 An example of GC-TCD chromatogram 229
B.3 Picture of used GC with a FID detector for liquid analysis 230
B.4 An example of GC-FID chromatogram 230
B.5 Picture of used GC with MS and FID detectors for liquid compound identification 231
B.6 An example of TGA results 231
B.7 Picture of used for spent catalyst analysis 232
B.8 Picture of used Brunauer-Emmett-Teller (BET) for catalyst surface analysis 232
B.9 Picture of used x-ray fluorescence (XRF) for catalyst composition analysis . 233
B.10 Gas analysis of thermally decomposed coke deposition on catalyst's surface 233
B.11 Weight loss during catalyst calcination for zeolite-supported catalysts . . . 234

C.1 Aspen developed flowsheet for DeH-HDO based on experimental findings . 236
C.2 PFD for HDO separation section (Adopted from [205]) 236
C.3 Continued PFD for HDO separation section (Adopted from [205]) 237
C.4 Aspen developed flowsheet for improved DeH-HDO with improved process performance based on published findings for HDO 239
C.5 Aspen developed flowsheet for improved DeH-HDO with improved process performance based on published findings for HDO 240
C.6 Aspen developed flowsheet for improved DeH-HDO with improved process performance based on published findings for HDO 242

List of Tables

2.1 Composition of lignocellulosic biomass derivatives based on their origin . . 9
2.2 Oil conversion cost for different applications 13
2.3 Conversion of biomass intermediates from upgrading processes into value-added chemicals 15
2.4 Element composition of oils originated from different sources 20
2.5 Selected literature findings for atmospheric HDO in continuous flow reactor 30
2.6 Bond dissociation energy (BDE) of oxygenated functional groups 43
2.7 Published works on catalytic HDO at atmospheric pressure. 50
2.8 Published works on catalytic HDO at atmospheric pressure. 51

3.1 The impact of power supply and response on temperature distribution for 30-min run after achieving a steady state in a reaction zone containing $NiMo/Al_2O_3$ 63
3.2 The impact of SiC addition on temperature distribution for 30-min run after achieving a steady state in a reaction zone containing $NiMo/Al_2O_3$ 65
3.3 List of varied parameters for HDO and DeH experiments 72

4.1 Physicochemical properties of investigated catalysts in Chapter 4 79
4.2 Guaiacol HDO under elevated pressures with H_2/GUA molar ratio of 5.0 a using $NiMo/\gamma$-Al_2O_3 for TOS of 120 min 80
4.3 Elemental analysis of catalysts used in this chapter using XRF 85
4.4 Overall atmospheric pressure HDO performance at using P-$NiMo/\gamma$ -Al_2O_3 93
4.5 Overall atmospheric pressure HDO performance using MoO_3 95
4.6 Atmospheric pressure HDO of guaiacol using hydrogen or ethane in a Cr_2O_3/Al_2O_3 catalytic bed 99

5.1 Guaiacol conversion and liquid product selectivity of DeH-HDO using catalytic system of 1:1 weight ratio of MoO_3 and Cr_2O_3/Al_2O_3 108
5.2 Atmospheric DeH-HDO of guaiacol and ethane at different catalytic systems 114

5.3 The effectiveness of operating alkane DeH at reduced ethane partial pressure for a catalytic system of 1:1 weight ratio of P-NiMo/Al_2O_3 and Cr_2O_3/Al_2O_3 in nitrogen environment . . . 117
5.4 EDS Elemental composition on a DeH-HDO spent catalyst using Cr_2O_3/Al_2O_3 . . . 122
5.5 Quantification of coke and condensate deposition of DeH-HDO on P-NiMo/Al_2O_3 and Cr_2O_3/Al_2O_3 catalytic system . . . 124
5.6 BTX, double aromatic (Heavy) products in term of selectivity and coke production at different catalytic systems . . . 126
5.7 Mass balance for integration of catalytic systems for BTX and HDO improvement based on experimental findings . . . 129

6.1 Elemental analysis of catalysts used in this chapter using XRF . . . 136
6.2 Atmospheric ethane DeH results for alumina-supported catalysts for Cr and Mo active sites . . . 138
6.3 Physicochemical properties of synthesised alumina supported Cr and Mo catalysts . . . 138
6.4 Atmospheric DeH-HDO results for alumina-supported catalysts with Mo and Cr active sites . . . 142
6.5 Elemental analysis of all the catalysts used in this work using XRF. . . . 147
6.6 Physicochemical properties of synthesised zeolite supported Cr and Mo catalysts . . . 148
6.7 Atmospheric pressure DeH-HDO coupling using zeolite-supported Cr and Mo oxides . . . 152

7.1 Material balance of guaiacol processing via conventional HDO and DeH-HDO based on experimental findings. Scaled-up to a guaiacol processing capacity of 99.1 ton·hr^{-1} . . . 157
7.2 Chemical prices used for economic potential (EP) calculation based on historical data. . . . 157
7.3 Used conversion of developed reaction network based on experimental findings. . . . 162
7.4 Net production mass balance from the Aspen flowsheet for the production of 200 kilo-tonnes per annum (kta) phenol. . . . 163
7.5 Total capital investment breakdown. . . . 164

7.6 Monte-Carlo statistical analysis for a thousand-simulation run for DeH-HDO improvement via boosting alkane DeH performance. 167
7.7 Production rate based on DeH-HDO process using Aspen Plus flowsheet . . 172
7.8 Global market capacity for DeH-HDO product streams as of 2022. 173
7.9 DeH-HDO with ethane steam cracking integration flowsheet summary and economic evaluation at different ethane cut from steam cracking feed using the experimental results in Table 7.1. 173
7.10 DeH-HDO with ethane steam cracking integration flowsheet summary and economic evaluation at different ethane cut from steam cracking feed using the experimental results in Table 7.1. 174
7.11 DeH-HDO economic evaluation at different ethane cut from steam cracking feed using the experimental results in Table 7.1. 175
7.12 Alkane conversion reactions for the production of hydrogen, alkenes and aromatics, and parameters requirement to achieve sufficient hydrogen for DeH-HDO integration with fluid catalytic cracking (FCC). 181
7.13 Aspen Plus process results for the integration of DeH-HDO with FCC of processing 3,300 tons per day (tpd) 183
7.14 Summary of current advantages and disadvantages for the process integration, as well as future potential and technical challenges. 187

A.1 Properties of all chemicals observed in gas phase at standard operating condition 224
A.2 Properties of the main non-aromatic chemicals and solvent observed in liquid phase at standard operating condition 224
A.3 Properties of the main chemicals observed in liquid phase at standard operating condition 225
A.4 Parameters used for defining the catalytic bed parameters in COMSOL . . 226

B.1 TCD calibration mixtures used in this work to develop TCD calibration curves for target gases. 228
B.2 TCD calibration factors used to quantify the gas composition. 228
B.3 TCD calibration factors used to quantify the gas composition. 229

C.1 Main nit operation list of DeH-HDO integrated with steam cracking (SC) . . 238
C.2 Main unit operation list of DeH-HDO integrated with FCC 241

Chapter 1

Introduction

Global demand for both fuel and chemicals is on the rise, driven primarily by factors such as population growth and the emergence of new markets [1]. This growing demand generates a necessity for increased production capacities, particularly in the chemical industry. Hence, immediate investments for additional capacities are imperative, particularly with an estimated three-fold increase in chemical demand growth compared to fuels [1]–[3]. For instance, in 2016, propylene and gasoline have compounded annual growth rate of 6.0% and 2.0%, respectively [2]. Furthermore, this demand is projected to exceed gross domestic product (GDP) growth [1], [3]. The challenge lies in the fact that only a small portion, approximately 14%, of crude oil is currently allocated for chemical production [3]. To address this challenge, various research and development initiatives have been launched in the field of oil-to-chemical oil-to-chemicals (OTC) programs. These programs aim to maximise the yield of chemical products from each barrel of oil, with a target of reaching 40-60% crude to chemical conversion [4]. This is even higher for some companies, for example Aramco aims to reach a conversion of 70-80%, where one of the OTC projects is estimated for 70% conversion [4]. While the transportation industry is rapidly transitioning towards electrification and alternative fuel sources as shown in Figure 1.1, the chemical industry remains reliant on hydrocarbons derived from fossil fuels to meet the global demand.

In response to increasing global regulations and commitments to address climate change, there has been a significant push to develop suitable alternatives to fossil fuels, including for the chemical industry. One notable renewable hydrocarbon source is biomass, which has garnered attention for its potential. Biomass can be converted into fuel and has seen successful commercial applications, including aviation fuels. Moreover, biomass valorization presents substantial opportunities as feedstock for chemical production due to its richness of natural hydrocarbons that can reduce the reliance on fossil-fuel-based hydrocarbons. For instance, commercially, first-generation biomass, edible biomass, is

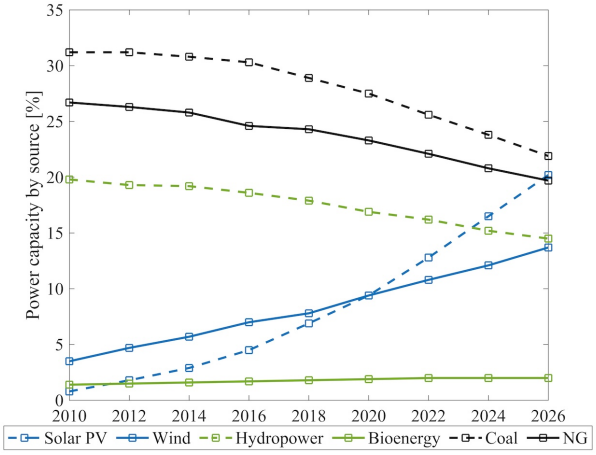


Figure 1.1: Power capacity allocation by source (Adapted from IEA [5])

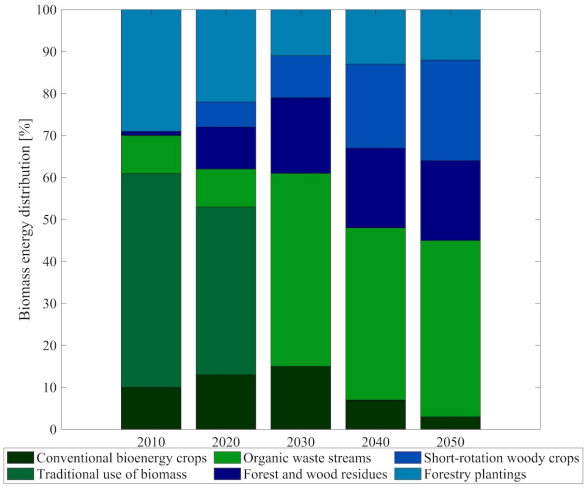


Figure 1.2: Bio-energy source allocation for net zero emission scenario (Adapted from IEA [6])

converted to alcohols and biodiesel. However, first-generation biomass has endured considerable resistance and regulation as it has social and environmental impacts. Therefore, second-generation biomass, derived from non-food sources, woody and agricultural residues, and industrial and municipal wastes, has received increased attention. The importance of second-generation biomass is reflected on the effort to increase its allocation for net zero scenarios as estimated by the International Energy Agency (IEA) in Figure 1.2.

In particular, extracted lignin from lignocellulosic biomass (woody residue) has gained substantial interest due to its high aromatic structure. With adequate extraction and pyrolysis processes, lignin is converted to a pyrolysis oil that can be transformed into a wide range of products. Thus, there has been a growing focus on exploring biomass-to-chemical processes, which can be seen as an analogous approach to the oil-to-chemicals concept.

The thermal treatment of lignin through rapid pyrolysis generates an oil composed of a mixture of mostly oxygenated species. The presence of oxygen hinders its potential, both as source of fuel and chemicals, as the pyrolysis oil requires complex extraction to lead to a pure chemical cut. In a way analogous to crude oil hydroprocessing, bio-oil is subjected to upgrading treatments to remove impurities, mainly oxygen functionalities. HDO is a critical reaction that can convert low-value biomass streams into sustainable source for energy and chemicals. In response to the increasing demand for chemicals, HDO has been utilised to convert bio-oil into valuable building block chemicals, including alcohols, alkanes, and aromatics [7]–[9]. These products serve as precursors for a diverse array of applications,

including plastics production. This approach aims to address the anticipated five-fold increase in the production of biomass-derived plastics by 2030, as projected by KPMG [10]. The projection from KPMG aligns with the forecast by European Bio-Plastics (EUBP), which anticipates a four-fold increase in global capabilities bio-plastics by 2028 compared to 2022 [11], as illustrated in Figures 1.3 and 1.4. This growth increase can be realised through the integration of biomass derivatives into the chemical value chain, as depicted in Figure 1.5.

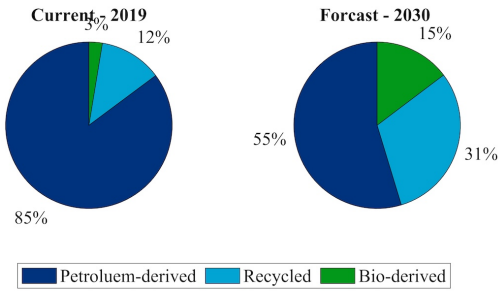


Figure 1.3: Market share for plastics by feedstock source in 2019 and 2030 forecast (adapted from KPMG [10])

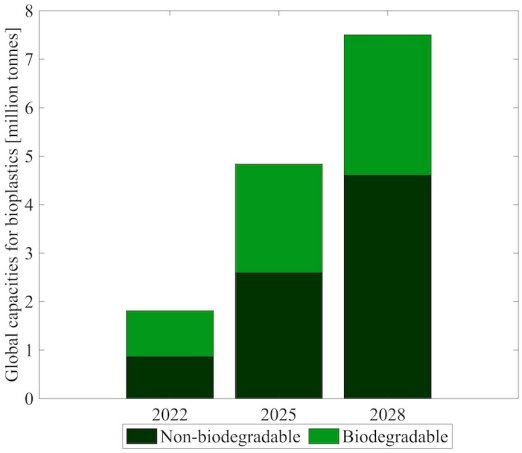


Figure 1.4: Current and five-year projections of global capacity for bio-plastics, classified as biodegradable and non-biodegradable (adapted from EUBP [11])

Conventional HDO uses expensive molecular hydrogen to upgrade low-value bio-based streams, which may hinder the potential biorefinery's economy. Furthermore, steam reforming the main process for hydrogen production has a negative environmental impact caused by the intensity of fossil-fuel-based energy requirements. As a result, researchers have investigated the possibility of upgrading biomass and conventional crude oil streams through alternative hydrogen sources. Published works have included hydrogen-rich organic solvents such as alcohols [12], [13]. Furthermore, the investigation includes solvents operating at near- and supercritical temperatures [14]–[16].

This PhD proposes integrating an alternative hydrogen source into HDO to create economic incentives. By incorporating an on-purpose hydrogen-generating reaction, the aim is to enrich the outlet stream with lignin-derived BTX through HDO, alongside alkenes from alkane dehydrogenation (DeH). Moreover, it enables rapid integration of biomass into the chemical value chain, as depicted in Figure 1.5. To understand the reaction coupling potential, this PhD investigates guaiacol HDO via in-situ hydrogen generation from ethane DeH to ethylene.

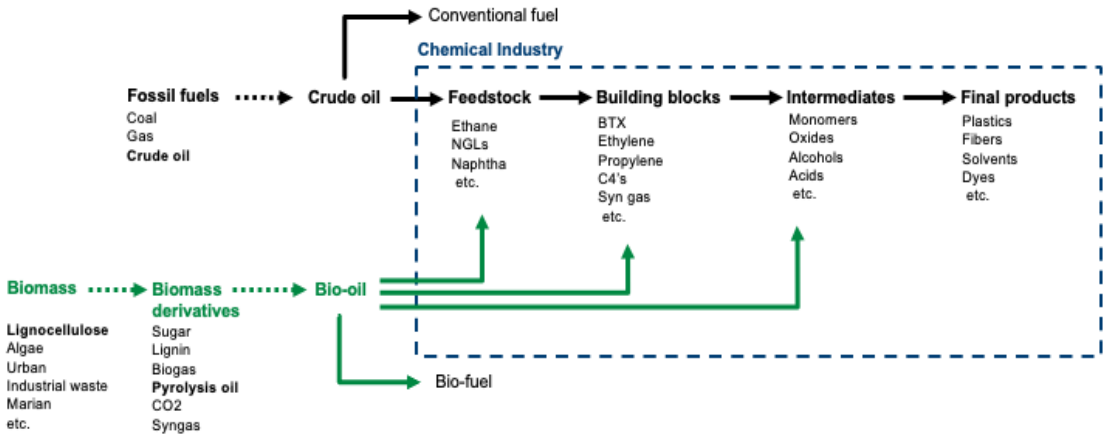


Figure 1.5: Integrated chemical chain from crude oil and biomass as carbon sources for the chemical industry [17], [18]

Coupling two reactions in a single catalytic bed has the potential to improve overall production by having mutually positive impacts on each other. Theoretically, the continuous removal of hydrogen produced by alkane DeH via "in-situ" HDO would improve alkene (ethylene) production by shifting the equilibrium conversion of Reaction 1 to the right. Enhancements in catalytic alkane DeH via hydrogen removal, using membrane reactors, or consumption by another reaction are reported in the literature [19]–[21]. Moreover, the in-situ generated hydrogen is expected to have higher reactivity in atomic form absorbed on the catalytic surface than stable molecular hydrogen. This leads to an improvement in the degree of HDO presented by Reaction 2. Furthermore, the coupling may compensate for the endothermic nature of alkane dehydrogenation by the overall exothermic nature of HDO.

$$\mathrm{m\ C_nH_{2n+2} \leftrightarrow m\ H_2 + m\ C_nH_{2n}} \tag{R1}$$

$$\mathrm{C_XH_YO_mC_xH_y + m\ H_2 \rightarrow C_XH_{(Y+m)} + O_mH_{(m+y)}C_x} \tag{R2}$$

Integrating biorefineries with crude oil refineries or petrochemical production plants can greatly improve efficiency and economic sustainability [22]. One approach is to couple reactions for efficient material exchange and improved heat management. From a reaction coupling perspective, H-transfer and direct contact of endothermic-exothermic reactions are addressed. This benefit can be scaled to the process level. An illustrative example of assisted-integration by DeH-HDO coupling is combining biorefineries with olefin (alkene)

plants, as depicted in Figure 1.6. Processing a fraction of the alkene plants feed, alkanes, as H-donor for bio-oil HDO, where the DeH-HDO product gas stream can be processed in existing alkene plants. Furthermore, the generation of biogas, primarily bio-methane from HDO bio-oil, offers an additional energy source for use in energy-intensive alkene plants, thereby facilitating further integration. Utilising biogas in steam crackers within alkene plants can reduce the external energy required per product, consequently lowering carbon emissions. Additionally, biomass materials such as lignin and pyrolysis oil can yield a bio-based alkane mixture, potentially increasing alkene production within the DeH-HDO process.

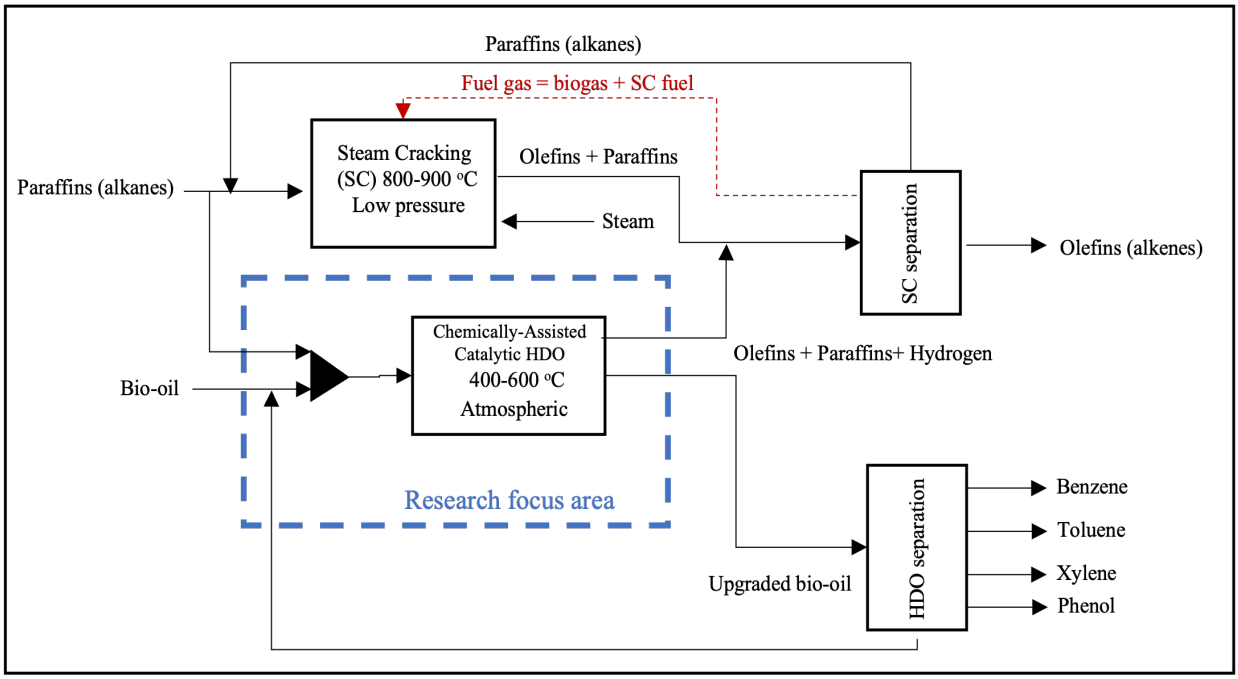


Figure 1.6: Proposed integration of bio-oil hydrodeoxygenation with ethane steam cracking

While standalone DeH-HDO coupling may encounter challenges in economic feasibility, mainly for handling an alkane/alkene mixture due to capital-intensive cryogenic distillation or the utilisation of valuable mixture as an energy source. Thus, integration with existing plants may enhance the economic viability of both processes. Overall, the integration of DeH-HDO presents a promising pathway for advancing efficiency and sustainability in the biorefinery and petrochemical sectors.

While these incentives offer promising opportunities for the petrochemical industry, particularly in alignment with emission reduction initiatives such as electrification, they are not without challenges. A key challenge in the proposed coupling is the differing thermodynamic preferences regarding pressure and temperature conditions. Conventional HDO

of bio-oil aromatic-based model compounds are improved under high hydrogen pressure (above 40 bar) and relatively low temperatures (200-300 °C) [23]. Conversely, alkane DeH requires higher temperatures and operates under atmospheric partial pressure. However, there is a growing interest in exploring atmospheric-pressure HDO as a more intensified approach to mitigate undesirable excessive hydrogenation of the aromatic ring [21], [24]–[27].

Another significant challenge lies in the differing activation mechanisms and active sites required for the coupled reactions. Additionally, bio-oil HDO typically operates with low residence time, while alkane DeH is a rapid reaction conducted continuously. Hence, developing a single, efficient catalytic system is crucial for the success of the coupling. Nevertheless, recent literature has demonstrated several advancements in bio-oil HDO operating within a flow system with catalytic systems reported to have a potential for alkane DeH. These recent strides provide a promising foundation for the proposed reaction coupling.

In conclusion, the proposed coupled reaction system in this PhD thesis, which involves simultaneously transferring hydrogen from catalytic alkane dehydrogenation to hydrodeoxygenation of pyrolysis oil in a single catalytic bed, is based on the following hypotheses:

- Hypothesis 1: Consistent consumption of hydrogen produced from alkane dehydrogenation could enhance the conversion of alkanes using Cr-based catalysts.
- Hypothesis 2: "In-situ" hydrogenation has the potential for greater hydrogen reactivity compared to externally-supplied molecular hydrogen on MoO_3 active sites.
- Hypothesis 3: The integration of catalytic alkane dehydrogenation and hydrodeoxygenation of biomass in a single catalytic bed enhances the economic viability and accelerates their commercialisation.

1.1 Research objective

This study explores the viability and feasibility of substituting molecular hydrogen with in-situ dehydrogenation of H-donor for the HDO of bio-oil. The H-donor in this work is on-purpose ethane DeH reaction, which aims to produce valuable ethylene and enhanced bio-oil. Thus, in order to comprehend the viability, feasibility, and combined impacts of both reactions, several research questions are established:

- Is "in-situ" ethane DeH a suitable H-donor for bio-oil upgrading compared to molecular hydrogen?
- Does HDO upgrading improve ethane DeH to produce relatively more ethylene?
- Does the overall integration of both reactions have economic feasibility and technical viability?
- What is the target operating window for the integration to positively impact the existing ethane and BTX plants?

1.2 Thesis structure

The stated hypotheses and the concept's potential are derived from the literature studies presented in Chapter 2. To validate these hypotheses, Chapter 3 defines a methodology that elucidates and rationalises the experimental approaches employed in the subsequent chapters. The research questions emerge to evaluate the DeH-HDO coupling hypotheses stated in this chapter. In order to address these questions, there are four chapters detailing the results. Chapter 4 serves as a proof of concept by experimentally validating the hypotheses in a single catalytic bed; studying the use of commercial catalysts that are commonly employed in hydroprocessing and alkane DeH. Furthermore, the study focuses on guaiacol HDO using molecular hydrogen and ethane, along with the examination of various operating conditions. In Chapter 5, the catalytic bed is improved through the development of a mixed catalytic system that comprises of catalysts studied in Chapter 4. The catalytic system consists of HDO and alkane DeH catalysts within a unified catalytic bed. Chapter 6 focuses on advancing the improvement with the development of bifunctional catalysts. The bifunctional catalysts contain active sites that facilitate both DeH and HDO reactions, and are located in close vicinity to enhance hydrogen transfer. Chapter 7 explores the techno-economic evaluation of combining DeH-HDO based on experimental findings and its possible incorporation into current processes. As this concept is still in its early stages of technological development, Chapter 9 summarises future work proposals stemming from this PhD, spanning from material selection to process development.

Chapter 2

Literature Review

This chapter highlights key knowledge and recent advancements in the hydroprocessing of biomass-derived renewable feedstocks. In order to establish a comprehensive foundation for this thesis, this chapter commences in Section 2.1 by defining biomass-produced hydrocarbons and demonstrating their potential as a feedstock for the chemical industry. Subsequently, it briefly summarises extensively studied processes for biomass conversion, highlighting their current state and constraints in Section 2.2. As this thesis focuses explicitly on catalytic HDO as the core technology, the present progress regarding catalytic systems and operating conditions is explored in Section 2.3. In addition, this chapter moves on from the conventional HDO process and focuses on novel approaches that underline the current advancements in operating at low pressure using low- or value-added hydrogen sources in Section 2.4. Moreover, this section explores the prospect of utilising alkanes DeH as a source of hydrogen. The chapter finishes by discussing the catalytic system used for HDO and other comparable catalytic systems described for alkane DeH in Section 2.5. This demonstrates the possibilities of incorporating both processes into a single catalytic system.

2.1 Biomass valorisation to fuels and chemicals

Biomass has emerged as a promising renewable energy and hydrocarbon source, offering a potential solution to mitigate reliance on fossil fuels. Currently, biomass is commercially employed as a fuel source via the production of first-generation biofuels derived from food crops, such as sugar and starch. However, the reliance on these crops and competition with food production for their utilisation pose sustainability issues, prompting the exploration of alternative sources like lignocellulosic biomass (2^{nd} generation) and algae (3^{rd} generation) for sustainable biofuel development [28].

Lignocellulosic biomass has garnered increased interest due to its derivation from eco-

nomically less valuable sources, including agricultural wastes, hardwoods, municipal solid refuse, and energy crops [29]. Therefore, due to its anticipated affordability and reduced dependency on edible resources, lignocellulosic biomass will emerge as the foremost source of biomass [30]. Furthermore, lignocellulosic biomass holds potential for the production of valuable bio-based chemicals in addition to biofuels derived from its rich-aromatic content.

Table 2.1: Composition of lignocellulosic biomass derivatives based on their origin [29]

Lignocellulosic biomass	Cellulose (%)	Hemicellulose (%)	Lignin (%)	others (%)
Agricultural residues	38	32	17	13
Hardwoods	50	23	22	5.0
Municipal solid waste	45	9.0	10	36
Energy crops	45	30	15	10

Cellulose and hemicellulose, the primary constituents of lignocellulosic biomass, play a significant role in bio-fuel production through polysaccharide fermentation [31], [32]. Table 2.1 outlines the composition of lignocellulosic biomass based on its origin. Additionally, the rich-aromatic structure of lignin presents opportunities for the synthesis of a range of bio-based chemicals, primarily phenols and BTX as showing in Figure 2.1 [31]–[33].

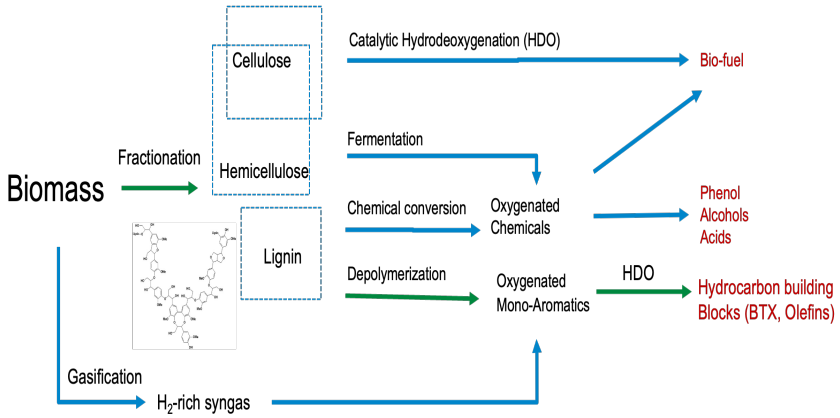


Figure 2.1: Lignocellulosic biomass conversion routes to bio-fuels and chemicals (Adapted from [32])

Realising the potential of lignocellulosic biomass requires comprehensive separation and conversion processes integrated into various biorefinery configurations [30]. These processes are designed based on factors such as the type of feedstock, targeted products, and involved processes. While biorefineries are predominantly categorised by the feedstock they utilise, the focus in biomass valorisation often centres on fuels derived from advanced, second-generation biomass, particularly lignocellulosic biomass. Despite the promising potential, the complexity of separating its components remains a challenge, requiring up-

grading routes to maximise high-value stream yield while minimising low-value streams.

2.1.1 Biorefinery v.s. crude refinery

The term "biorefinery" refers to the process of converting bio-based natural resources into high-value fuels and chemicals, mirroring the analogous transformation of crude oil into a range of fuels and chemicals within a conventional refinery. The development of biorefineries serves to complement conventional refineries, addressing market demands while advancing sustainable alternatives to fossil fuel-derived crude. Analogous to crude oil refineries, the primary aim of biorefineries is to convert heavy bio-based hydrocarbon streams into high-value hydrocarbon streams that are convertible as fuel sources or intermediate chemical streams. Despite the similarities in the primary aim of both refineries, their processing mechanisms differ depending on the nature of the feed. Despite the differences in the processing mechanisms of both refineries, hydroprocessing is a common treatment step that involves adjusting the hydrogen-to-carbon ratio to produce smaller, high-value chemicals and removing impurities [34]–[36]. The primary impurity in bio-based hydrocarbons is the excessive presence of oxygen, which impedes its potential as a fuel source [37].

However, in certain applications, the presence of oxygen can be beneficial, as it can shorten the conversion process to produce high-value oxygenated hydrocarbons such as phenol. In the conventional petrochemical value chain, phenol is typically produced through a multi-step conversion process involving expensive building block chemicals, namely propylene and benzene, with the inclusion of oxygen in what is known as the cumene route (Hock process) [38]. It is worth noting that propylene and benzene are primarily produced through the energy-intensive steam cracking of naphtha, while oxygen is separated through another energy-intensive process known as air separation. Nevertheless, phenol can also be extracted from pyrolysis oil produced via the rapid pyrolysis of lignocellulosic biomass, thereby transforming a low-value stream into a high-value intermediate for the chemical industry. However, the production of aromatics, particularly benzene, from a biorefinery poses a significant challenge and involves multiple processes that are still under development.

Another issue in biorefinery is the presence of oxygenated hydrocarbon compounds, which require multiple processes, unlike fossil fuel routes. Direct fractionation might not be feasible for producing high-value chemical streams. Therefore, various configurations have been explored in the literature to combine the benefits of both refineries. One approach is the

mixing of streams from both refineries for further co-processing, mainly for fuel production [39], [40]. Figure 2.2 illustrates several processes for integrating bio and crude refineries to produce building block chemicals, liquefied petroleum gas (LPG) and olefins, and important fuel streams such as jet fuel and gasoline [22]. Yet, these co-processings are based on the current limited full biomass conversion.

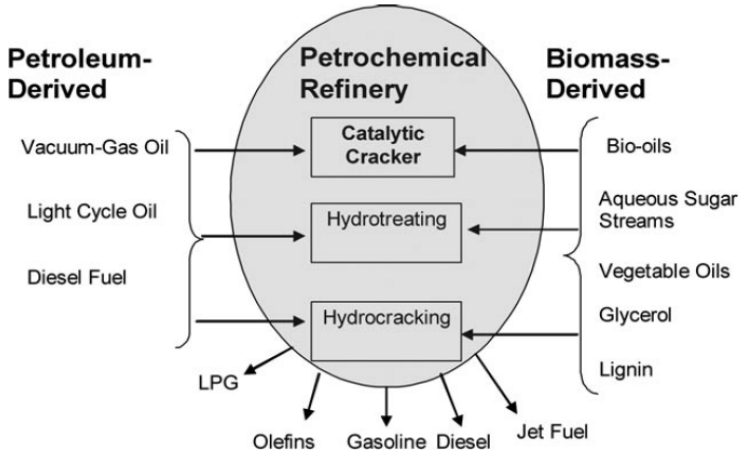


Figure 2.2: Conventional and biomass refinery integration (Adopted from [22])

Another approach involves the intentional full conversion of bio-based streams into hydrocarbons for integration into the chemical industry. The produced stream can be combined with corresponding fossil-derived streams, such as benzene with bio-benzene, for use in the chemicals industry. Despite some building block chemicals being used for producing pre-existing chemicals, the second approach offers flexibility for different applications. The preference for one integration over the other, including other factors, may depend on the targeted process's boundary limits. In conclusion, while crude refining is a well-developed process with understood limitations associated with environmental aspects, biorefining offers a potential solution, despite its underdeveloped processes. Therefore, the focus nowadays shifts to biorefinery products.

2.1.2 Biomass-based stream as energy source

Bio-based energy, referred to as bioenergy, plays a significant role among renewable energy sources, alongside solar, wind, and hydro energy, offering a promising avenue to reduce reliance on fossil-fuel-based energy. Figure 2.3 illustrates various pathways for biomass utilisation, originating from both food and non-food sources, ultimately leading to the production of biofuels and electricity. The added value of biofuels as a renewable energy source lies in their potential to address challenges related to decarbonising sectors such as heavy transportation and aviation [41]. The energy efficiency (η_{energy}) in converting biomass feed-

stock to bio-fuel can be calculated by Equation 1.

Where the variables $\eta_{biofuel}$, η_{feed}, and $\eta_{process}$ symbolise the energy content associated with the biofuel product, feedstock, and energy consumption during the production process [34]. Thus, epitomising the efficiency of biomass-to-fuel conversion relies on managing both the volume and quality of the produced output. In addition energy efficiency emerges as a critical factor in the selection of an appropriate conversion process.

$$\eta_{energy} = \frac{\eta_{biofuel}}{\eta_{feed} - \eta_{process}} \qquad \text{(Equation 1)}$$

Furthermore, there has been notable progress in the development of biofuels, with advancements now extending to include algae as a third-generation biomass, aimed at meeting the growing global energy demand and reducing dependence on fossil fuel-based energy sources. However, while biomass conversion to biofuels represents significant progress, it does not entirely eliminate the dependence on fossil fuel-derived hydrocarbons as a source of chemicals. Consequently, there is growing interest in direct biomass conversion into chemicals, such as lignin to chemicals and bio-ethanol conversion to a wide range of building block chemicals, holding promise for the chemical industry.

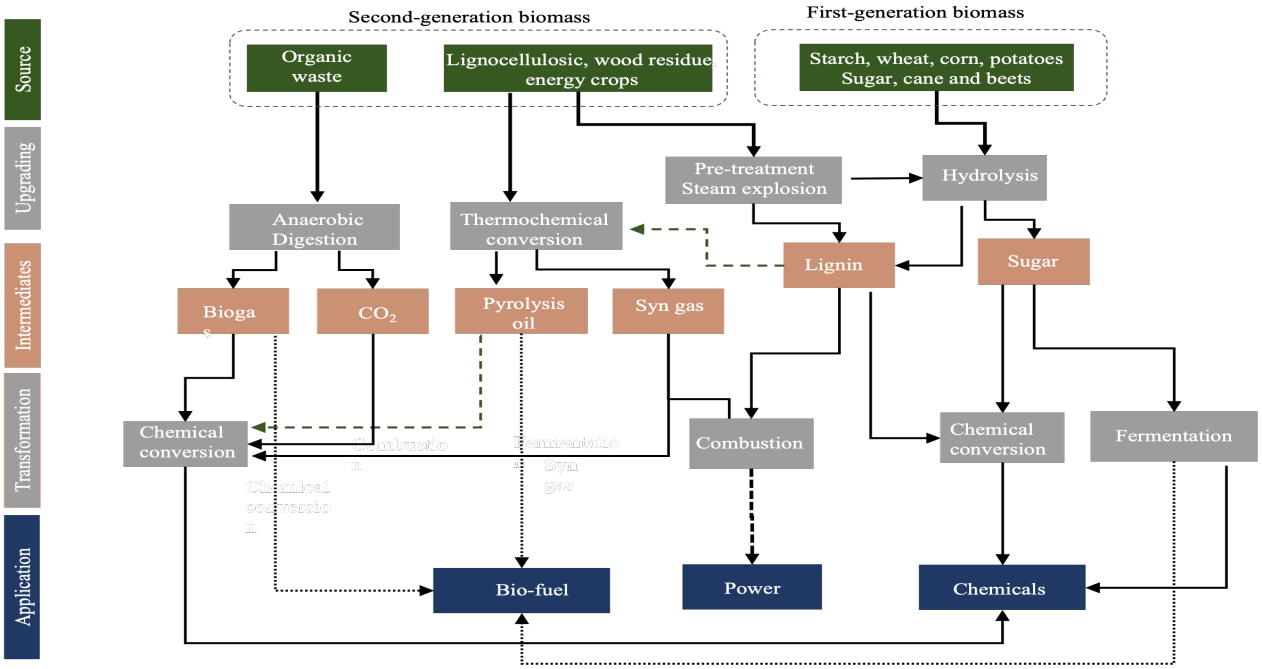


Figure 2.3: Simplified biomass routes to bio-based energy, fuels and chemicals (adapted from [33], [42])

The global capacity of bio-ethanol is estimated at 80,800 kta, with limited production of bio-

based ethylene, the main building block for the chemical industry, at 200 kta [33]. Despite this, there are well-known approaches for converting ethanol to ethylene via dehydration to balance bio-based fuels and chemical outputs [33]. Furthermore, biomass conversion to biofuels is well understood, leading to a relatively small gap in the cost of production in comparison to petroleum oil, as demonstrated in Table 2.2 [30]. On the other hand, the cost gap in chemical production highlights the importance of increasing the focus on biomass conversion to chemicals.

Table 2.2: Oil conversion cost for different applications [30]

	Fossil fuel-based feed (€·GJ^{-1})	Biomass-based feed (€·GJ^{-1})
Heat	3.0	4.0
Power	6.0	22
Transportation fuel	8.0	10
Average bulk chemicals	30	75

Heat and power are based on coal, fuel and chemicals are based on oil.

Therefore, some of the biofuels may be redirected to chemical conversion processes due to the higher market growth for end-chemicals, such as polymers with 8.8% in comparison with alcohols with 4.4% [43]. Additionally, direct conversion of biomass to chemicals, such BTX, represents another avenue for leveraging bio-based resources in the chemical industry.

2.1.3 Biomass-based building-block chemicals

Chemical conversion of extracted streams from biorefineries serves as an integration zone between both biorefinery and crude refinery, as these processes are either already in commercial use or currently under investigation. Table 2.3 demonstrates several valuable streams from biorefinery that are known or are targeted by the petrochemical industry for utilisation for commodity chemicals. For instance, the petrochemical industry has implemented CO_2 conversion initiatives to reduce the need to store excessive amounts of CO_2. The primary pathways for CO_2 utilisation are hydrogenation to methanol, direct urea synthesis, and dry reforming since they produce important intermediate chemicals. Rafiee et al. review possible pathways for CO_2 utilisation [44]. Hence, the integration of biorefineries with methanol and urea synthesis processes or dry reforming is regarded as a crucial move towards achieving a sustainable shift to bio-based hydrocarbons. Other valuable streams such as syngas, biogas, lignin, and pyrolysis oil can be re-directed from combustion for energy purposes to further chemical conversion processing to improve the overall economic value and meet rising chemical demands.

Biogas is another significant gas derived from biomass, which can be produced through thermochemical conversion or anaerobic digestion, as illustrated in Figure 2.3. While biogas is often utilised as a reliable source of electricity and heat via combustion, its value can be significantly enhanced by extracting biomethane and following conventional methane valorization pathways for chemical production. The primary route involves converting biomethane into syngas through steam reforming [45], directly integrating biogas into the traditional petrochemical value chain. For instance, syngas can be fed into well-established commercial processes for the production of key intermediates such as hydrogen, methanol, and ammonia, as shown in Table 2.3, which are essential commodities in the chemical industry.

Another valued platform for bio-based chemicals is sugar, which can be obtained from both first- and second-generation biomass primarily through hydrolysis and acid-catalysed steam explosion, yielding glucose and xylose, as shown in Figure 2.3. Beyond traditional sugar fermentation into alcohols (e.g., ethanol), these sugars can be further processed into various valuable chemicals. For example, dehydration can convert them into critical compounds such as lactic acid, succinic acid, furfural, and levulinic acid, all serving as critical intermediates in producing bioplastics, solvents, and fuels [46], [47]. In addition, chemical conversion methods such as oxidation, reduction, and esterification further expand the range of bio-based chemicals that can be synthesised from sugars, offering diverse applications in green chemistry [48]. Glucose, in particular, has attracted attention as a potential renewable alternative to benzene for bio-phenol production, providing a sustainable pathway to replace fossil-based phenol. The production of bio-phenol from glucose strengthens the economic viability of sugar-based platforms. It supports the shift toward more sustainable chemical processes, making sugar an essential intermediate in the bio-refinery value chain.

Table 2.3: Conversion of biomass intermediates from upgrading processes into value-added chemicals as illustrated in Figure 2.3

Platform	Process	Product	Technological	Incentive
CO_2	Hydrogenation [49] Dry reforming (+ biogas) Direct synthesis (+ammonia) [51] Co polymerisation (+epoxides) [52]	Methanol Hydrogen Urea Polycarbonate microalgea	commercialised [50] underdevelopment commercialised underdevelopment underdevelopment	Reducing CO_2 emission by using CO_2 as an oxidant or feedstock for the generation of commodity of specialised chemicals
Syngas	Hydrogen extraction Methanol synthesis Ammonia synthesis	H_2 Methanol Ammonia	commercialised commercialised commercialised	Produce green hydrogen that can be utilised in further upgrading
Biogas	Dry/steam reforming [45]	syngas	DR: underdevelopment SR: commercialised	Direct integration to petrochemical processes
Sugar	Acid hydrolysis [53] concentrated, diluted, solid acids	Glucose xylose	Underdevelopment limited by capital investment	Complete utilisation of lignocellulosic biomass
Lignin	Direct fast pyrolysis	Phenols, BTX	underdevelopment	Avoid intermediate processing to generate valuable BTX
Pyrolysis oil	Catalytic hydrodeoxygenation	Phenols, BTX	underdevelopment	Production of building block chemical for various applications

Commercially, lignocellulose conversion undergoes various processes, such as steam explosion and enzymatic hydrolysis, primarily to produce bio-ethanol [54]. However, these methods have not fully exploited the potential of lignocellulosic biomass. In 2004, the US Department of Energy identified several high-potential carbohydrates that could be derived from cellulose and hemicellulose on a large scale [55]. Nevertheless, the economic value of lignocellulose remains unrealised without comprehensive exploration of lignin conversion [56], which constitutes a large fraction of lignocellulosic biomass. Although lignin is currently utilised in commercial processes for fuel generation, such as steam and electricity production, its utilisation is not maximised [54]. This focus on fuel underutilised the rich lignin structure, as fuels could be replaced by less valuable streams. Therefore, the value pyramid of the chemical industry and biorefineries emphasises the necessity of complete conversion of lignocellulosic biomass fractions, particularly with a shift from fuel to chemical production [54]. To achieve that, one approach is to investigate the lignin fraction for chemical production.

2.2 Lignin valorisation to bio-oil

2.2.1 Lignin nature, types and processing

Lignin is an abundant natural polymer found in biomass, serving as a significant renewable carbon source. It is primarily composed of aromatic and cyclic hydrocarbons, which are associated with various oxygenated functional groups such as carboxyl, carbonyl, hydroxyl, and methoxy. Its amorphous structure consists of a complex network of oxygenated aromatics that varies depending on its source. Figure 2.4 shows a representative lignin structure.

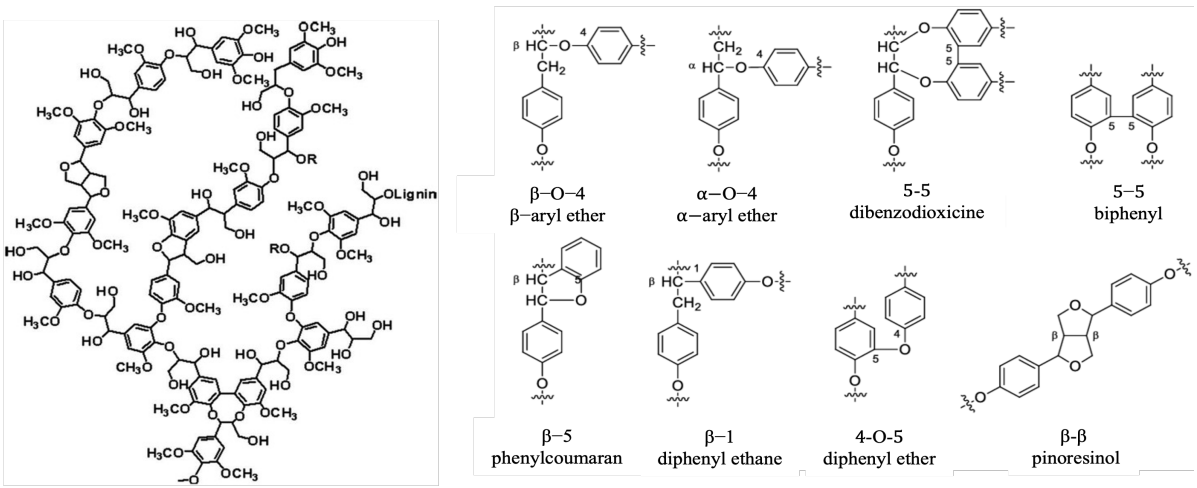


Figure 2.4: Representative lignin structure (left) and various types of linkages (right). Adapted from [57], [58]

The primary building blocks of lignin are methoxylated phenyl propanols known as monolignols: sinapyl, coniferyl, and p-coumaric alcohols, as illustrated in Figure 2.5 [59], [60]. These monolignols are linked by two main types of bonds: ether linkages and condensed linkages [59], [60]. Ether linkages, particularly β-O-4 bonds, are the most occurring and can be relatively easily broken during lignin depolymerization, making them significant for biomass conversion technologies. Ether linkages include diphenyl ether, β-aryl ether, and α-aryl ether, as shown in Figure 2.4. In contrast, condensed linkages, such as C-C bonds, are more resistant to cleavage. They contribute to lignin's structural stability while posing challenges for chemical processing. Understanding the distribution and nature of these linkages is crucial for developing effective lignin upgrading strategies.

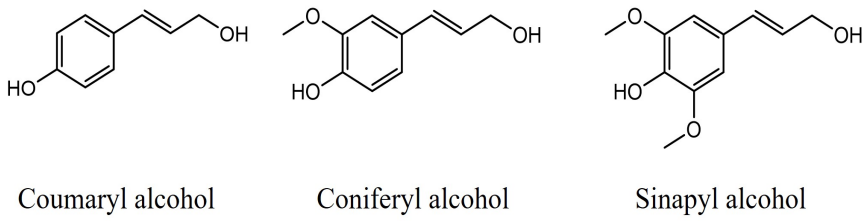


Figure 2.5: Chemical structure of the building block of lignin: monolignols [60]

Overall, lignin's rich carbon structure characterizes it as a highly promising renewable hydrocarbon stream (HHC). Its potential for upgrading stems from its presence in low-value processing and waste streams from agricultural by-products, forestry residues, and crop waste [60]. Consequently, lignin upgrading presents significant opportunities for the chemical industry, providing a sustainable feedstock through the biorefinery approach.

2.2.2 Lignin to bio-oil

To address the presence of oxygen in lignin, initial treatment involves depolymerisation into smaller heteroatom-containing compounds via processes such as pyrolysis or liquefaction, resulting in the formation of bio-oils. This depolymerisation process yields a mixture of smaller hydrocarbons, known as bio-oil, through cleavage of both carbon-oxygen (C-O) and carbon-carbon (C-C) bonds, leading to the formation of oxygen-containing compounds, commonly referred to as lignin derivatives. However, the presence of oxygen in these compounds limits their suitability for fuel applications due to their instability and propensity for polymerisation. Consequently, HDO emerges as a critical step [37], [61].

To address this challenge, lignin conversion to bio-oil primarily occurs via two main processes: pyrolysis and liquefaction, each with distinct mechanisms for breaking down the

complex lignin structure, with a preference for producing single aromatic compounds. Pyrolysis is a thermal process conducted in the absence of oxygen, using high temperatures of up to 600 °C under low or atmospheric pressures to break the lignin linkages [62]–[64]. The residence time plays a critical role in determining product distribution; longer residence times (as in slow pyrolysis) lead to excessive gas and coke formation [62], [64]. Consequently, fast pyrolysis is favoured for lignin conversion due to its higher bio-oil yield and fewer by-products. Recent advancements have also explored catalytic fast pyrolysis, where lignin depolymerization and bio-oil upgrading are integrated into a single step using zeolite-based catalysts [62], [65]. Despite these developments, fast pyrolysis remains the leading process for lignin-to-bio-oil conversion.

Liquefaction, another primary process for lignin conversion, involves breaking down lignin in a liquid medium at elevated pressures and temperatures ranging from 200 °C to 350 °C [63], [66]. Hydrothermal liquefaction (HTL) utilises water as both a solvent and a reactant, enabling lignin depolymerization without the need for biomass drying. HTL operates under subcritical and supercritical water conditions to achieve optimal depolymerization efficiency [66]. Alternatively, solvothermal liquefaction employs organic solvents such as alcohol, acetone, ethylene glycol, and alcohol-water mixtures [63]. While both HTL and solvothermal processes occur in liquid media, HTL holds a notable advantage due to water's role, which eliminates the need for solvent recovery and biomass drying. Furthermore, HTL-derived bio-oil contains fewer oxygenates, reducing the level of upgrading required in downstream fuel and chemical production processes [67]. Advances in both HTL and solvothermal techniques have incorporated catalytic systems to improve bio-oil yield [63]. Additionally, efforts to develop continuous HTL processes are underway to make the technology more viable for industrial implementation [67].

In contrast, gasification is a high-temperature (up to 1000°C) process carried out in the presence of oxygen [63]. Unlike pyrolysis and liquefaction, gasification does not produce bio-oil but rather syngas, a mixture of hydrogen, carbon monoxide, and other gases. Syngas can be further processed to create valuable chemicals and fuels.

While the processes of pyrolysis and liquefaction are essential for converting lignin into bio-oil, the subsequent upgrading of these derivatives is equally critical for fuel and chemical production. The removal of oxygen is crucial for upgrading renewable lignin derivatives,

making the O/C molar ratio a key indicator of the upgrading process's effectiveness. The previously mentioned processes aim to break down the complex lignin network, which may involve a slight reduction in the O/C ratio. As illustrated in Figure 2.6, while pyrolysis oil may exhibit a lower O/C ratio, it still requires further upgrading to match crude oil quality. Consequently, the bio-oil produced from lignin depolymerization necessitates additional processing to eliminate oxygen from the lignin derivatives. Typically, these derivatives consist of single aromatic or cyclic hydrocarbons with branched oxygenated functional groups. Various oxygenated lignin derivatives resulting from depolymerization processes have been documented in the literature [37], [61].

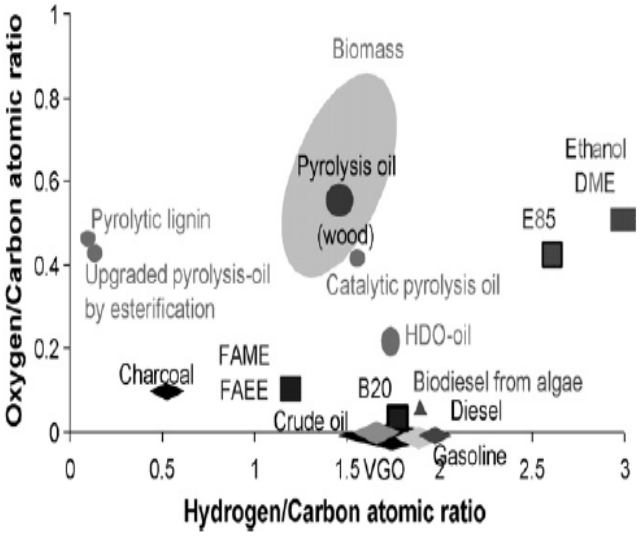


Figure 2.6: H/C and O/C of different types of petroleum and bio-oil feeds (Adopted from [68])

To investigate the HDO of lignin derivatives on a fundamental level, researchers utilise model compounds that mimic the functional groups present in these derivatives. Guaiacol is among the extensively studied model compounds for HDO, owing to its composition of two distinct functional groups (hydroxy and methoxy) attached to an aromatic ring [69]–[71]. Ultimately, the role of HDO within the bio-oil mixture is to reduce the H/C ratio, analogous to petroleum-derived heavy hydrocarbons. However, HDO aims to achieve an O/C ratio of near zero to yield high-quality fuels and chemicals, as depicted in Figure 2.6. The figure illustrates the significant reduction in the O/C ratio required for HDO oil compared to pyrolysis oil. Notably, the specific target O/C ratio varies based on the types of fuels and chemicals being produced.

2.2.3 Bio-oil characterisation

Bio-oils, like petroleum crude oil, require upgrading to eliminate impurities and enhance the H/C ratio. While sulphur removal is crucial for petroleum crude oil due to its high content, biomass-based oil has a low sulphur content, as indicated in Table 2.4. The main challenge in processing bio-oil lies in its higher oxygen content, limiting its use as a fuel source due to a reduced heating value of 16-19 $MJ \cdot kg^{-1}$ compared to 40 $MJ \cdot kg^{-1}$ for petroleum-based oils [72], [73]. Liquefied bio-oil, however, exhibits a wider heating value range of 25-46 $MJ \cdot kg^{-1}$ depending on biomass source and hydrothermal process conditions [74].

Table 2.4: Element composition of oils originated from different sources [37]

Element		Conventional crude	Coal-derived naphtha	Oil shale crude	Bio-oils (Liquefaction)	Bio-oils (Pyrolysis)
Carbon	[wt%]	85.2	85.2	85.9	74.8	45.3
Hydrogen	[wt%]	12.8	9.6	11.0	8.0	7.5
Sulphur	[wt%]	1.8	0.1	0.5	<0.1	<0.1
Nitrogen	[wt%]	0.1	0.5	1.4	<0.1	<0.1
Oxygen	[wt%]	0.1	4.7	1.2	16.6	46.9
H/C	[mol/mol]	1.8	1.4	1.5	1.3	2.0
O/C[1]	[mol/mol]	$8.8 \cdot 10^{-4}$	0.048	0.01	0.19	0.91

[1] O/C values were calculated based on the given data

Furthermore, bio-oil faces challenges with high moisture content, which is inversely correlated with its heating value [72], yet serves as an agent to reduce viscosity. Another drawback is the low pH (high acidity) and high viscosity [75] as fuel properties. The acidity is attributed to the substantial presence of carboxylic acids in bio-oil [73]. Processing low-acidity streams carries the risk of corrosivity, necessitating specific construction measures for safe operation [72], [73]. Viscosity, a factor hindering the processability of bio-oil akin to petroleum-based crude, exhibits significant variation in the case of bio-oil [72], [73].

The complexity of bio-oil arises from diverse biomass sources, compositional variations, and conversion methods, making a universal characterisation challenging. Despite this complexity, upgrading bio-oil is essential for its utilisation as energy or as a hydrocarbon source. To simplify measuring the degree of bio-oil upgrading, the O/C ratio is heavily considered, as depicted in Figure 2.6, enhancing the heating value. For transforming bio-oils into chemicals, the H/C ratio assesses the upgrading process based on the target—high H/C for alkane production or low H/C for BTX, both desirable routes. Caution is needed to avoid excessive aromatic ring saturation, which may diminish the value of the chemical stream.

2.2.4 Bio-oil upgrading processes

The upgrading of bio-oil employs processes adapted from those used in petroleum-based oil refining. These processes fall into two categories: physical and conversion mechanisms, all aimed at enhancing the physicochemical properties of bio-oil [34], [75]. Physical technologies include solvent addition, emulsification, esterification, and chemical extraction, while conversion technologies involve hydrotreatment, hydrocracking, and steam reforming [34], [75]. Hydroprocessing, a key conversion technology, improves bio-oil quality, while steam reforming focuses on hydrogen production. The choice of technology depends on the intended application of the bio-oil, spanning clean hydrogen production, power generation, biofuel production, or chemical synthesis. Figure 2.7 provides an overview of primary technologies and their key features for upgrading fast pyrolysis bio-oil. Selection of an approach depends on feed characteristics and desired product stream. Esterification, emulsion, and solvent addition enhance product stream quality for biofuels, but can also serve as intermediate steps to enhance processability for final conversion to bio-based chemicals [34]. Oxygen removal through hydroprocessing and catalytic cracking is crucial for the final step in upgrading to bio-based chemicals. Therefore, the thermochemical approach is critical in the upgrading process. Subsequent sections will discuss recent advancements in bio-oil utilisation.

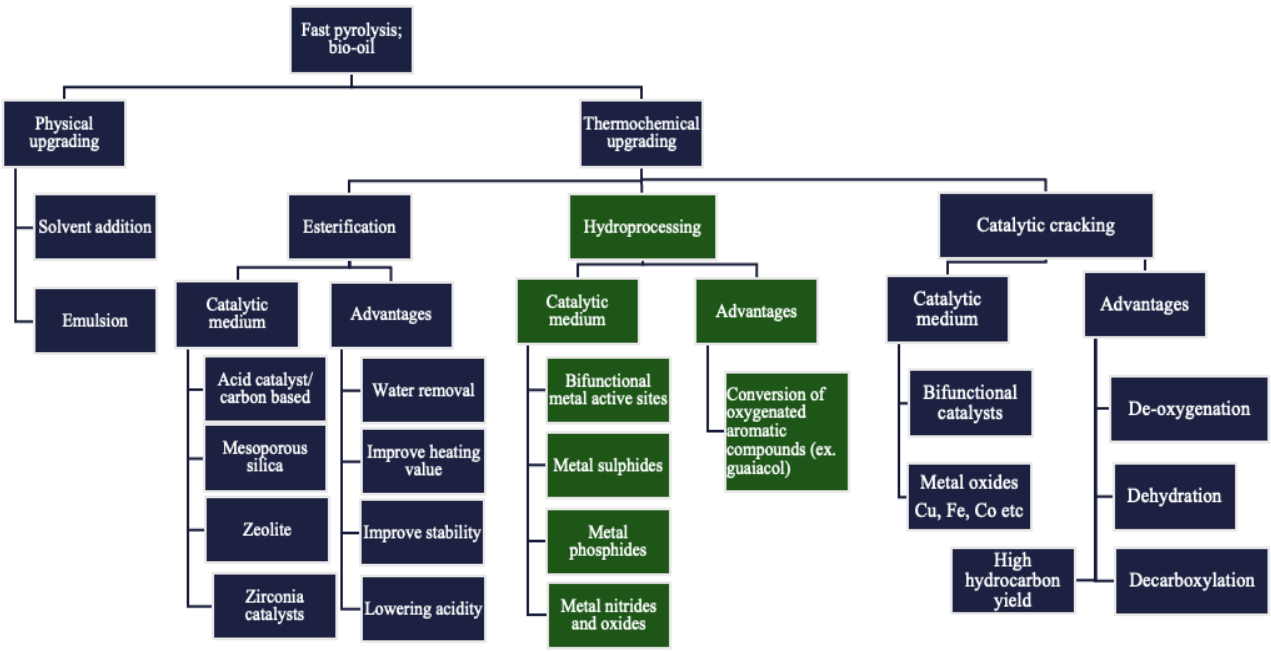


Figure 2.7: Bio-oil upgrading technologies: advantages and catalyst types as summarised by Mostafazadeh et al. (Adapted from [34])

2.2.4.1 Physical technologies: solvent addition

Upgrading bio-oil using solvent addition targets improving the processability of bio-oil as fuel. Solvent (alcohol) addition has a direct impact on bio-oil by reducing its viscosity and corrosiveness and improving fuel quality and stability (heating value). These physical changes are caused by the nature of alcohols, which have a relatively higher heating value than bio-oils [75], [76]. Normally, methanol, ethanol, and butanol are employed. Several studies have explored the potential of employing a combination of solvents to enhance the overall quality of bio-oil for fuel applications. Since quality improvement is driven by the physical properties of the mixture, some studies have examined the use of physical processes, such as ultrasonic, to ensure the homogeneity of the solvent and optimise interaction. This approach could be reactive with the addition of catalysts to convert undesirable carboxylic acid functional groups using alcohol into esters. Acidic, base, and ion-exchange catalysts were investigated for esterification. In addition, cresol, which is an aromatic-based alcohol, is employed as a reactive solvent for esterification, along with other similar compounds.

2.2.4.2 Conversion technology to gas: biomass steam reforming

Catalytic steam reforming (SR) is particularly well-studied due to its role in producing hydrogen and synthesis gas. Although this process yields the desired products efficiently, it has not yet reached commercial implementation despite the high demand for hydrogen. The main challenge lies in its instability due to rapid coke formation. Various catalytic systems have been explored to address this issue, aiming to break C-C bonds and prevent coke formation. The complexity of the SR process arises from the diverse chemical components present, making the development of a suitable catalytic system a challenging task [77], [78]. Efforts to mitigate carbon deposition on the catalyst have included investigating the SR of biomass in fixed-bed and fluidized-bed reactors. However, neither configuration has reached the required level of technological readiness for implementation. Alternative configurations, such as aqueous phase reforming (APR) and two-step biomass reforming, have emerged to enhance the process outcomes [78].

APR has shown promise in reducing coke formation by lowering the operating temperature and increasing the operating pressure, typically around 250 °C and 20-60 bar, respectively [78], [79]. Moreover, APR can produce alkanes, which can be advantageous depending on the catalytic activity. Instead of targeting C-C cleavage, efforts should focus on C-O

cleavage. However, APR is limited to biomass with an O-to-C ratio of 1, primarily due to the lower temperature requirements resulting from reduced thermodynamic demands for C-C cleavage in oxygenated compounds compared to non-oxygenated hydrocarbons [79]. Another approach to biomass SR involves using two reformers. This concept utilises the low-temperature properties of biomass in the first reformer to generate methane, followed by conventional methane steam reforming to produce hydrogen [79]. However, biomass steam reforming is constrained by the catalytic system, as highlighted by Setiabudi et al., who provided a roadmap for catalyst development [77].

2.3 Bio-oil upgrading via hydrodeoxygenation (HDO)

Thermochemical conversion methods are favoured for chemical production, although the choice of approach significantly impacts the value of the resulting product stream. While steam reforming (SR) effectively produces valuable compounds from bio-based sources, it also releases carbon in the form of CO_2. To improve chemical conversion, it is essential to conserve carbon to achieve a hydrocarbon-rich stream. Two leading technologies are recognised for this purpose: catalytic cracking and HDO, depicted in Figure 2.7 [34], [75], [80], [81]. Catalytic cracking has demonstrated potential for deoxygenation, but it results in carbon loss in the form of CO_2, as illustrated in Reaction 3 [80]. This emission hinders the attractiveness of catalytic cracking. The 34% carbon loss can be mitigated by HDO, as shown in Reaction 4 [80]. An overall reaction is proposed by Fogassy et al., in Reaction 5, for HDO coupling with FCC for biomass and crude oil mixture [68]. The proposed reaction demonstrates the cracking effects by molecular re-distribution, which indicates hydrogen and/or carbon loss for oxygen removal.

$$C_1H_{1.33}O_{0.43} + 0.26\ O_2 \rightarrow 0.66\ C_{1.2} + 0.34\ CO_2 + 0.27\ H_2O \tag{R3}$$

$$C_1H_{1.33}O_{0.43} + 0.77\ H_2 \rightarrow CH_2 + 0.43\ H_2O \tag{R4}$$

$$C_xH_yO_z \rightarrow aC_{x-b-d-e}H_{y-2c}O_{z-2b-c-d} + dCO + bCO_2 + cH_2O + eC \tag{R5}$$

HDO is a widely studied upgrading processes for biomass conversion to biofuels and chemical production using hydrogen to remove oxygen forming water. In particular, catalytic HDO

is widely investigated for conversion of lignin-derived bio-oil, mainly phenolic compounds, to saturated and unsaturated hydrocarbons [41]. Significant progress in scientific research has been observed for HDO of lignocellulosic biomass. Figure 2.8 shows the evolving developments in this field over the past decade, indicating minimal activity before 2010. Limited activity before 2010 can be attributed to the primary focus on first-generation biofuels derived from food-based biomass. The commercialisation of biomass-to-biofuel processes raised concerns regarding their impact on food resources. As a result, there was a shift toward the use of lignocellulosic biomass for biofuels and bio-products, given that these resources are derived from non-food biomass.

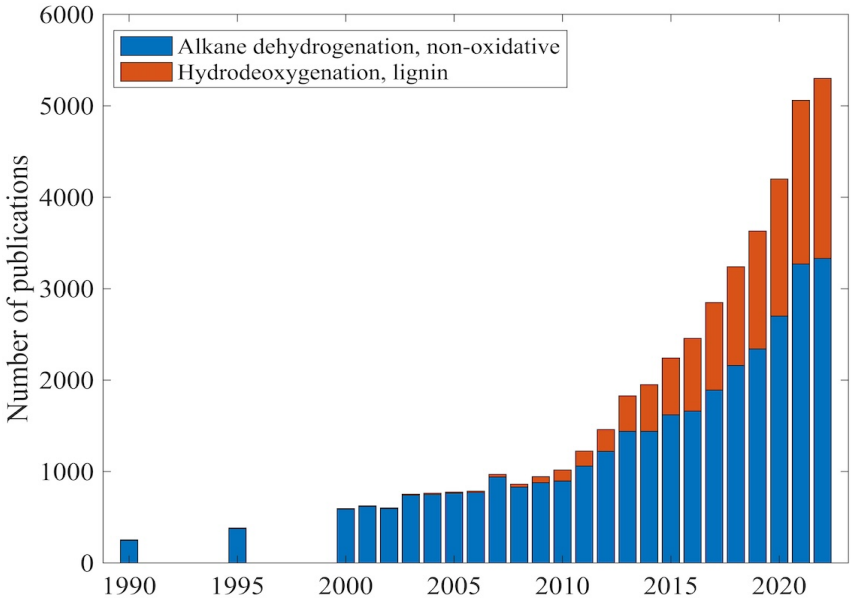


Figure 2.8: Number of published article on HDO and alkane DeH using google scholar search engine. HDO keywords: HDO, lignin; DeH keywords: alkane DeH, non-oxidative

The development of bio-oil HDO centres around finding adequate operating conditions for processability and catalytic systems to improve the degree of HDO. Figure 2.9 summarises the progress of bio-oil HDO observed in the literature, each stage with its limitations to finally reach the proposed DeH-HDO. The H-donor reaction, alkane DeH has been receiving extensive attention to replace state-of-the-art steam cracking to produce building-block chemicals for the chemical industry, in particular alkenes and/or aromatics, depending on the cracking feedstock. The accounted publications in Figures 2.8 consider only non-oxidative alkane DeH, which is the focus mechanism in DeH-HDO. In general, the scientific efforts in alkane DeH are centred around finding a suitable catalytic system and reaction configuration, as well as the consideration of oxidants that can overcome the endothermicity of the reaction [82]–[84]. It is worth mentioning that catalytic DeH has been commercialised

for propane but not ethane due to the demanding thermodynamic requirements of ethane DeH as well as its competitiveness with well-studied and commercialised steam cracking [82], [83]. Therefore, utilising ethane as an H-donor for bio-oil HDO requires an adequate operating condition and catalytic system.

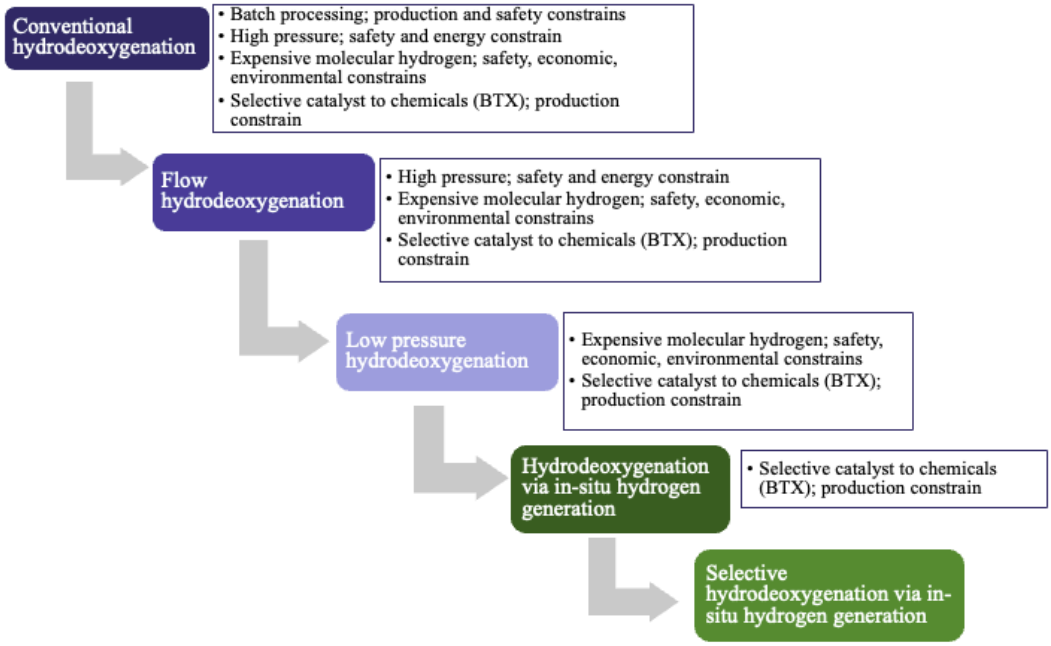


Figure 2.9: Development in HDO of bio-derived oil and associated challenges

In the following sections, selected published studies are highlighted to determine the progress of HDO and the most favourable operational parameters for the coupling of both reactions. Furthermore, the review aims to identify suitable catalytic systems that facilitate hydrogen transfer, resulting in the spontaneous production of alkenes and targeted aromatics. This is achieved by exploring hydrogen donors as alternatives to molecular hydrogen. Due to the limited studies on H-donor for bio-oil feed, its application in the context of upgrading petroleum-based feedstocks is included to realise the possibility of incorporating this approach into bio-based feedstock processing. Finally, this chapter discusses various catalytic systems that show promise in combining both HDO and hydrogen transfer reactions.

2.3.1 Conventional HDO

Conventional HDO processes involve the use of hydrogen to enhance the quality of oxygenated hydrocarbon compounds by eliminating oxygen functional groups. Lignin, for instance, possesses a carbon-to-oxygen ratio higher than 2:1, necessitating prolonged processing times to achieve significant or complete removal oxygenates. Consequently, HDO reactions are often conducted within batch reactors. Batch-mode not only facilitates the necessary extended residence times but also accommodates the utilization of catalytic sys-

tems, thereby demanding a comprehensive understanding of reaction kinetics, particularly in laboratory-scale operations. This understanding is required due to the complexity of biomass-based feed HDO due to distinct structures; several mechanisms are primarily observed: dehydration, hydrocracking, hydrogenolysis, decarboxylation, and hydrogenation [61].

The complexity of heteroatom removal in hydroprocessing is especially pronounced for oxygen, relative to sulfur and nitrogen, due to the strength of the $C_{aromatic}$-O bond [37]. This makes oxygen removal from lignin-derived derivatives, which are rich in aromatics, more challenging. For bio-oil mixtures, the degree of HDO is measured by the O/C molar ratio of dried products, predicting the amount of residual oxygen in the product streams. To better understand the extent of HDO and its underlying mechanisms, model compounds, such as guaiacol, are extensively studied. Guaiacol HDO focuses on removing methoxy and hydroxy functional groups to produce benzene or saturated aromatic rings. Figure 2.10 illustrates a proposed mechanism for HDO of guaiacol.

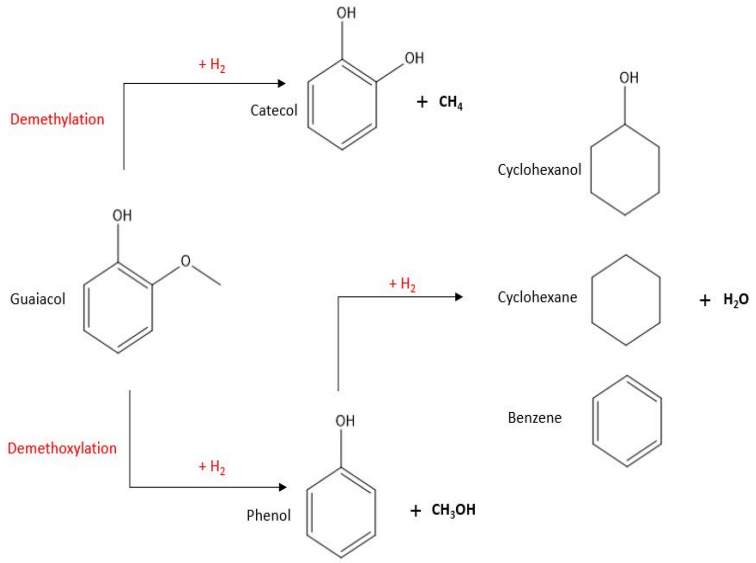


Figure 2.10: Proposed pathways for guaiacol HDO and hydrogenation as summarised by [61]

Producing benzene, a high-value chemical, from bio-oil is especially desirable, as it reduces hydrogen consumption associated with aromatic hydrogenation. However, in the absence of a selective catalyst, HDO often requires the saturation of aromatic rings to facilitate the removal of methoxy and hydroxy groups, due to bond dissociation energy differences. For instance, the dissociation energy of the –OH bond in phenol is 468 kJ·mol^{-1}, compared to 385 kJ·mol^{-1} in cyclohexanol [37]. Therefore, the selection of catalyst materials is crucial

for driving the reaction toward the desired products.

Conventionally, the upgrading process typically unfolds under elevated hydrogen pressures ranging from 100 to 200 bar and temperatures between 300 and 400 °C. The use of these operating conditions to facilitate hydrogenation of the guaiacol aromatic ring reduces the difficulty of removing the hydroxy functional group, while the methoxy group is relatively easier either via HDO to form another hydroxy group or its complete removal. The correlation given Equation 2 where m is H_2 moles estimate the required pressure for complete conversion of phenol and benzofuran to be roughly 125 and >200 bar, respectively [37].

$$Log(Kp) = log(\frac{P_{reactant}}{(P_{product}}) - mlog(P_{H2}) \quad \text{(Equation 2)}$$

However, beyond thermodynamics, HDO is known to be a catalytic process, even operating at high pressure to obtain the required selectivity. Saidi et al. reviewed the catalytic upgrading of lignin-derived bio-oils using a wide range of operating conditions, catalytic mediums, and reactor configurations [61]. In addition, Saidi et al. summarised the reported HDO mechanisms of distinct model compounds using different types of active sites and supports [61], which in addition to the operating conditions markedly affect the product distribution.

Literature studied different active sites for HDO including noble and transition metals, sulphide, phosphide, nitride, and carbide metals supported on zirconia, alumina, and silica [61]. Gutierrez et al. studied the catalytic HDO of guaiacol on noble catalysts supported on zirconia and compared it to the conventional sulphide $CoMo/Al_2O_3$ in a batch system [71]. The study investigates both thermal and catalytic roles in guaiacol conversion and product distribution using a pure hydrogen supply at 8 MPa for 5 hours of operation. At a low operating temperature of 100 °C, guaiacol conversion was significantly affected by the catalyst employed, from 5.6% conversion for a non-catalytic experiment to roughly 98% conversion for $Rh\text{-}Pt/ZrO_2$ and Rh/ZrO_2 [71]. In terms of product distribution, hydrogenation was profound because it thermodynamically favours low temperatures. Cyclohexanol was dominant in the non-catalytic experiment. For the catalytic system, the dominance of cyclohexanol and 1-methyl-1,2-cyclohexanediol varied. Cyclohexanol dominated product distribution for the low conversion catalysts, whereas 1-methyl-1,2-cyclohexanediol dominated for high conversion catalysts. At the high-temperature experiments, 300 °C, both

the conventional sulphide catalyst and noble metal catalysts resulted in near-completion conversion, producing benzene as the dominant product [71]. However, Gutierrez et al. reported that the use of a sulphide catalyst contaminates the product by losing some of its content into the product stream, as well as causing higher carbon deposition in comparison to Rh-Pt/ZrO_2 and Rh/ZrO_2 [71].

2.3.2 Atmospheric pressure HDO for continuous flow systems

In recent years, an increasing number of studies have considered operating HDO at atmospheric pressure to eliminate all the concerns associated with operating hydrogen at elevated pressure [24], [85]–[92]. This technological breakthrough in HDO processing has revealed previously unknown reaction pathways that restrict the hydrogenation mechanism of aromatic rings. Although the process of hydrogenating the aromatic rings to eliminate $C_{aromatic}$-OH requires a significant amount of energy, numerous catalytic systems have been able to effectively produce BTX without any intermediary steps involving ring saturation. However, ring saturation may result from further hydrogenation resulting in cyclohexane, as reported by Olcese et al. using Co-based catalysts [32]. Atmospheric pressure HDO adds an advantage for DeH-HDO coupling since alkane DeH requires low-pressure operation.

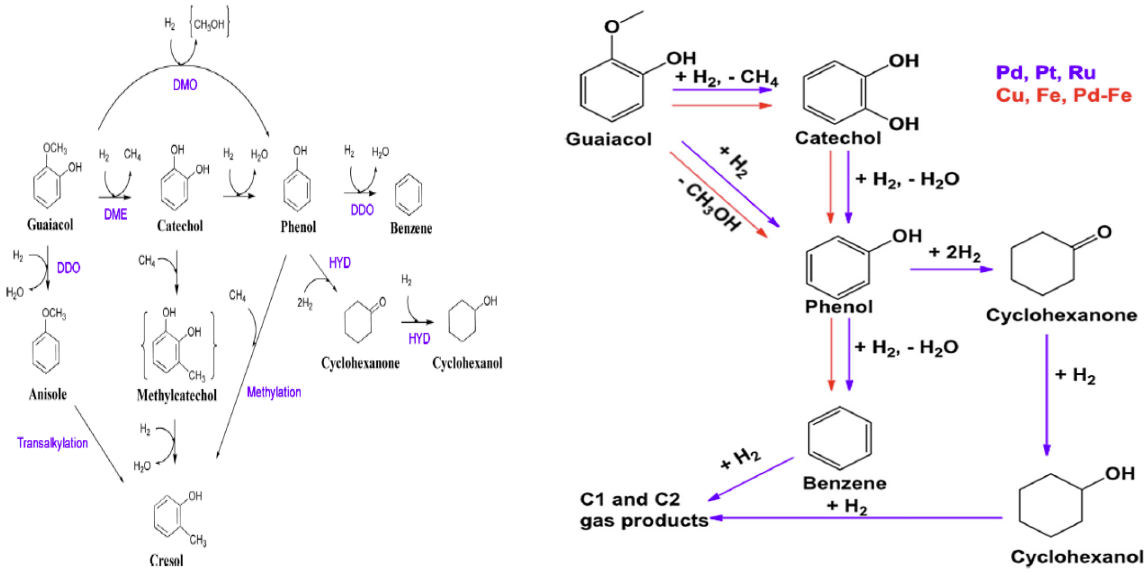


Figure 2.11: Proposed mechanisms for atmospheric HDO of guaiacol in continuous flow reactors [Right] reported by Sun et al. using metal active sites on carbon (Adopted from [93]), [Left] reported by Wu et al. using Ni_2P supported catalysts (Adopted from [87])

Using Ni_2P on various supports including alumina, zirconia, and silica, atmospheric pressure resulted in almost no ring saturation, where benzene selectivity reached 72% depending on the residence time [87]. Furthermore, Wu et al. investigated Ni-based catalysts

supported on zeolite [94] at atmospheric pressure. The proposed mechanism did not show any signs of ring saturation. Instead, methylation took place after the HDO. Another study conducted by He et al. confirmed that no ring saturation was observed using Ni-Mo on silica for HDO of phenol, anisole, and guaiacol [90]. In addition, He et al. reported several literature findings for atmospheric pressure HDO [90], which agrees with listed published works summarised by Pourzolfaghar et al. [95].

In addition to Ni-based catalysts, Mo-based catalysts have also demonstrated a high conversion rate of oxygenated aromatic compounds into benzene, without or with minimal ring saturation [24], [92], [96]. In addition, Ni-Mo was investigated in titanium oxide support, showing that combing both active sites yielded higher guaiacol conversion at atmospheric pressure, which is attributed to the improved dispersion of Ni promoted by the addition of Mo [86]. Replacing Mo with V reduced the selectivity towards phenol and m-cresol yielding more cyclohexane, which was potentially caused by a higher surface area, more acidic active sites, or mesostructure [86].

The dual active site system (Ni-Mo) was further investigated on a range of catalyst supports, including alumina and zirconia supports. However, titanium oxide oxide demonstrated a higher degree of HDO [86]. Furthermore, Ag/TiO_2 was investigated on atmospheric pressure at different temperatures [85]. Phenol was selectivity converted to benzene by more than 89% at 140 °C, where the selectivity increased with temperature to 99.3% at 320 °C.

Olcese et al. investigated gas-phase HDO of guaiacol in a continuous flow system at low pressures for BTX production [32]. Unconventionally, this study used a relatively inexpensive metal, Fe, supported on silica, varying the operating pressure and temperature within the 0-0.9 bar and 350-450 °C, respectively. A guaiacol conversion of 74% was achieved with a BTX yield of 38%, which is a promising result considering guaiacol HDO at low operating pressures is favourable if using alkane DeH as a hydrogen source [32]. This study agrees with thermodynamic observations for hydrogenation, which is suppressed at a high temperature and a low pressure operation, as indicated in Figure 2.12, and typically carried out at high pressure.

The reported literature findings highlighted the importance of the catalyst role as well as the operating conditions in enhancing HDO outcomes, which measure the success of lignin

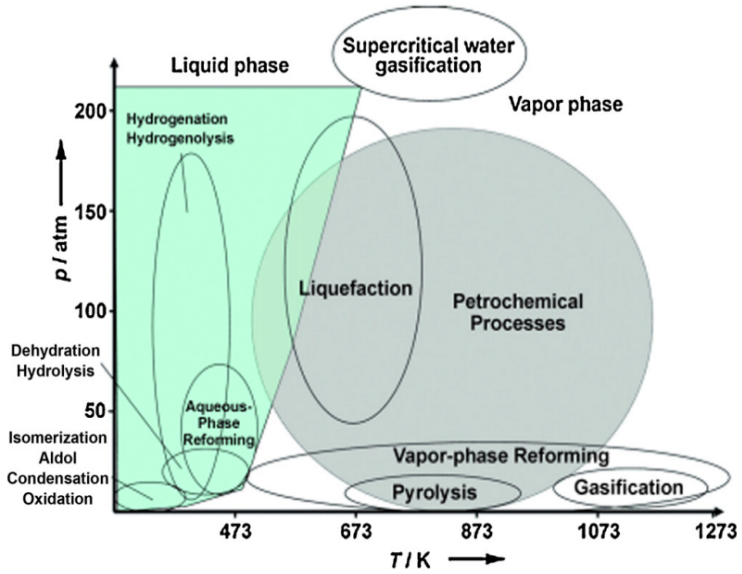


Figure 2.12: Temperature and pressure range for refinery processes (Adopted from [97])

conversion to high-value chemicals. Table 2.5 presents further literature findings regarding the conversion of bio-oil model compounds in a continuous flow reactor at atmospheric pressure.

Table 2.5: Selected literature findings for atmospheric HDO in continuous flow reactor

Catalyst	Temperature °C	Feed	Conversion %	BTX selectivity %	ring saturation %	ref
MoO_3	400	Anisole	65.0	98.6	-	[96]
Mo_2C	280	Phenols	95.0	92.0	7.00	[92]
Ni-Mo//SiO_2	410	Guaiacol	99.8	97.5	-	[90]
1% Pt/SiO_2	400	Anisole	100	70.0	N/A	[25]
1% Pt/HBeta	400	Anisole	100	89.4	N/A	[25]
Pd/ZrO_2	300	Phenol	12.6	29.9	68.7	[98]
Pd/Al_2O_3	300	Phenol	7.50	11.4	86.2	[99]
Pd/TiO_2	300	Phenol	7.00	66.8	33.2	[99]
5Ru/C[1]	250	Guaiacol	92.0	12.0	5.00	[93]
2Pd10Fe/C	450	Guaiacol	95.0	75.0	N/A	[93]

[1] The results are approximated from figures.

The collected research outcomes, except those associated with Pd-based catalysts, consistently indicate a notable degree of selectivity towards BTX. These observations highlight the potential of atmospheric HDO as a technological advancement in transforming bio-oil into value-added chemicals, particularly when employing catalytic systems that restrict ring saturation. However, the continued reliance on expensive molecular hydrogen poses a persistent challenge in enhancing the value of low-cost bio-based streams through hydroprocessing.

2.3.3 Hydrogen production routes

Tremendous research efforts were invested in developing a cost-effective and environmentally friendly hydrogen generation system. A system that consists of feedstock, technology schemes, and an energy source. In nature, hydrogen is the most abundant component, but it does not appear in large quantities or high purity in its molecular form [100]. Therefore, hydrogen has to be extracted or produced from rich hydrogen sources, mainly organic compounds. Fossil fuel is the conventional source for hydrogen production due to the relative ease of extracting hydrogen from hydrocarbon streams as well as the amount of available hydrogen. For instance, coal, gasoline, and natural gas contain 4%,12% and 25% of hydrogen on a weight basis, respectively [100]. Alternatives to fossil fuels, such as water and biomass, have been heavily studied. However, nowadays, fossil fuels still account for 96% of hydrogen production, while 4% comes from water [100], [101]. Despite water and biomass being cheap feedstocks and environmentally friendly sources, they lack cost-effective hydrogen extraction technology [102], [103]. From a technological perspective, hydrogen production technologies are based on thermochemical, gasification, and pyrolysis routes. Figure 2.13 is a hydrogen production map from different feeds: biomass, fossil fuels, and water. To evaluate the attractiveness and feasibility of a single route using a single feed type, economic and environmental aspects have to be taken into account when considering the superior technology for hydrogen production.

Conventionally, state-of-the-art hydrogen technology is steam reforming of natural gas, which produces syngas with a 3:1 molar ratio of H_2-to-CO. Primarily, syngas is used for ethanol, methanol, ammonia, and hydrogen production. To promote H_2 production from syngas, steam reforming is followed by a water-gas shift reaction to improve the hydrogen yield, followed by an expensive separation unit. Although methane reforming is a conventional technology, hydrogen is still considered a costly commodity chemical, priced in the range of $1000-$1800 per metric tonne for the period 2000-2014 [104]. Consequently, the integration of hydrogen production and catalytic hydroprocessing, HDO in particular, has to be optimised. An approach to reduce the economic and environmental concerns regarding hydrogen utilisation, an alternative sustainable hydrogen source beyond molecular hydrogen has to be considered.

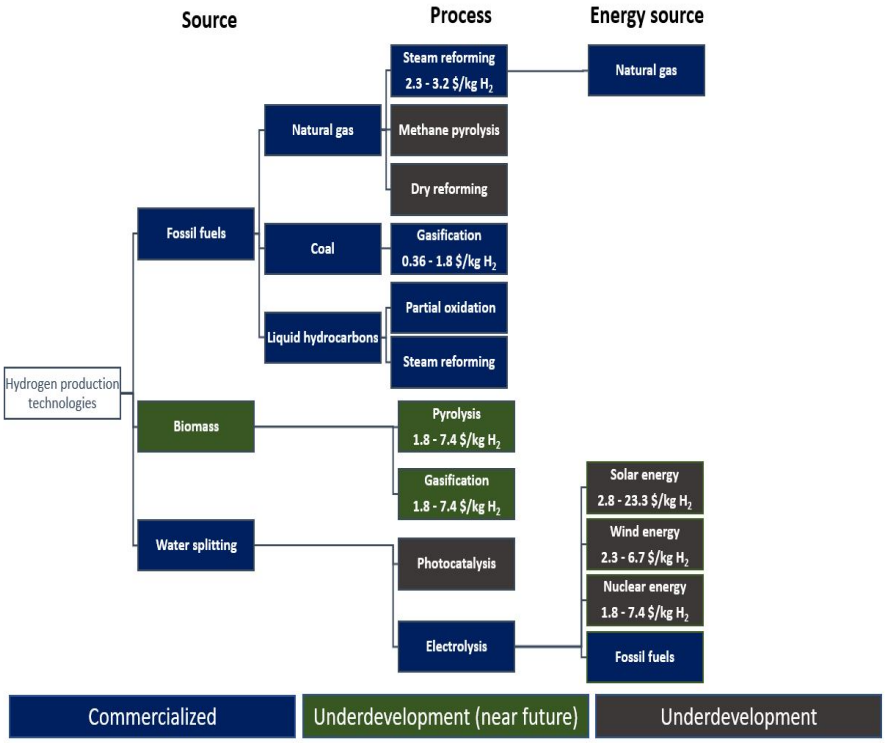


Figure 2.13: Hydrogen production map from different sources,processes and energy sources adopted and summarised from [100], [101], [103]

2.4 H-donor for bio-oil hydrodeoxygenation

As described in the former sections, hydrogen is a costly molecule that holds significant potential for use in various industries for the purpose of generating environmentally friendly energy. Therefore, looking for alternative hydrogen sources is essential, especially in upgrading low-value streams where the use of molecular hydrogen may negatively impact its economic feasibility. Consequently, researchers have developed the concept of a hydrogen donor (H-donor) as a substitute for molecular hydrogen. Researchers initially explored this concept in hydroprocessing petroleum-based heavy hydrocarbons to remove existing impurities, including S, N, and O. Recently, researchers have applied the same approach to upgrading bio-oils, mainly in HDO, due to the high oxygen content. Two different forms of H-donor exist: (1) as a solvent, where the oxygenated hydrocarbon is diluted in an aqueous phase facilitating H-transfer, or (2) in-situ hydrogen generation from an external reactant. Figure 2.14 summarises the reported types of H-donors for bio-oil in the literature. The below subsections present examples of reported promising findings.

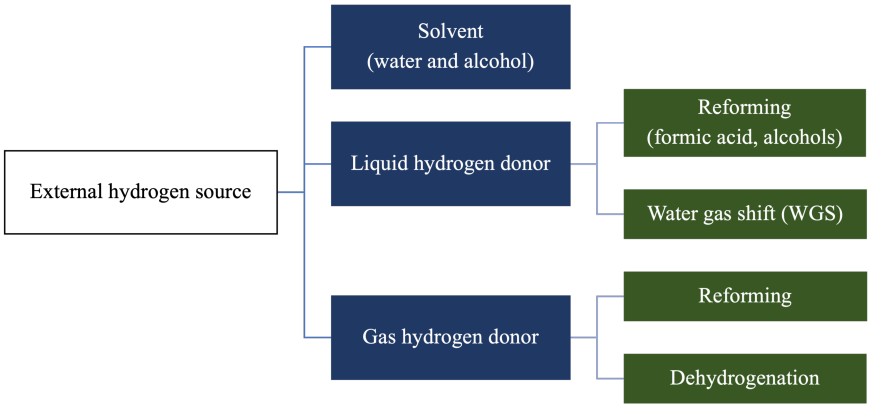


Figure 2.14: External hydrogen sources for HDO as molecular hydrogen alternatives

2.4.1 H-donor approach for upgrading low-value hydrocarbon streams

Before considering its application for bio-based feed upgrading, recent literature advocates for the utilisation of an H-donor to enhance catalytic hydroprocessing of petroleum-based feeds, thus eliminating the need for externally supplied hydrogen [105]–[110]. The H-donor facilitates the generation of hydrogen, which in turn facilitates the partial or complete upgrading of heavy hydrocarbons (HHCs) within a single reactive zone. H-donors can be generated either through the use of an H-donor solvent [105], [110] or through DeH reactions within a catalytic medium [106]–[109]. Among the investigated solvents, tetralin and decalin have received the most attention for their role as H-donors in the catalytic upgrading of petroleum-based oils [110], [111]. Conversely, methane serves as an H-donor via DeH reactions, owing to the abundance of natural gas sources associated with petroleum processing [105]–[109]. The application of a H-donor mechanism, also referred to as "in-situ" upgrading, to thermal processes presents several advantages for petroleum feed processing. "In-situ" upgrading improves feed viscosity and hydrotreats the feed, consequently enhancing feed conversion and product quality by increasing the hydrogen-to-carbon ratio (H/C) and inhibiting coke formation. In catalytic systems, Aleman et al. have classified hydrogen transfer between a H-donor and a H-acceptor into two approaches [105].

- Hydrogen is generated at the reaction medium (catalyst) in atomic form by H-donor dehydrogenation

- Hydrogen is generated by H-donor in the form of an H_2 molecule which exists in the gas phase and acts as pure hydrogen to the reaction

2.4.1.1 Solvent as H-donor

The catalytic hydroprocessing of heavy oil and vacuum residue (VR) has been explored using tetralin and decalin solvents as alternatives to molecular hydrogen in MoS_2 and $NiMo/Al_2O_3$ catalysts, respectively [110], [111]. At operating conditions of 400 °C and 100 bar, the thermal cracking of VR demonstrated enhanced performance when employing an H-donor compared to a nitrogen environment [111]. The degree of improvement was assessed by measuring coke formation, which followed a specific order: naphthalene (NPTH) < 1-methyl naphthalene (1-MN) < decalin < tetralin. Additionally, the presence of MoS_2 further mitigated coke formation in a hydrogen environment (7.2%); however, this reduction was more pronounced when hydrogen was replaced by naphthalene and tetralin, resulting in reductions of 2.9% and 1.2%, respectively [111]. These reductions in coke formation were attributed to the efficient transfer of hydrogen, indicating the effectiveness of H-donors.

This observation aligns with the findings of Hart et al., who investigated heavy oil upgrading, as measured by viscosity, density, and coke formation using hydrogen, tetralin, and decalin at 425 °C and 15 bar [110]. Compared to a nitrogen environment as a baseline, upgrading was found to be enhanced in terms of density in the order of H_2 < tetralin < decalin, while in terms of suppressing coke formation, the order was tetralin < H_2 < decalin [110]. These improvements were attributed to the enhanced solubility provided by the H-donors, where H_2 showed limited solubility due to the low operating pressure. The superiority of decline over naphthalene and tetralin can be explained due to the saturated rings, which have the capability of higher hydrogen transfer. However, solubility is also important to facilitate the H-transfer before active hydrogen does not convert to molecular hydrogen. Therefore, hydroprocessing, in particular HDO, operates at high operating pressure to improve the contact between H_2 and the feeds.

2.4.1.2 Methane activation as H-donor

The H-donor mechanism remains unclear; however, since H-donors are used to replace the use of expensive hydrogen, the hydrogen transfer mechanism has to be fast to eliminate free radical formation to avoid chain propagation [105]. Therefore, hydrogen donors have to be capable of releasing hydrogen from the catalytic surface at the reaction temperature and pressure applied [105]. Guo et al. claim methane activation was achieved in a relatively

mild reaction environment, which led to partial upgrading of bitumen [106]. The reaction occurred in a batch reactor assisted by an Ag-Zn/ZSM-5 catalyst at a temperature and pressure of 380 °C and 50 bar, respectively [106]. As a sign of upgrading HHCs, the methane environment has significantly reduced the feed viscosity of 848 080 cP at ambient temperature to 1276, 414, and 280 cP in the catalytic inert, methane, and hydrogen environments, respectively [106]. In addition, Ovalles et al. claim the use of methane as a hydrogen source to upgrade extra-heavy crude oil in a batch reaction using an iron-dispersed catalyst [108]. At a temperature of 410 °C, a pressure of 110 bar, and a one-hour residence time, the methane environment has reduced the feed viscosity by two orders of magnitude. A pure hydrogen environment resulted in a slight improvement in product distribution and a slight reduction in feed conversion [108].

2.4.2 Bio-oil HDO via in-situ H_2 generated through carbon rejection

Heavy hydrocarbon (HHC) and oxygenated heavy hydrocarbon compound upgrading technologies are mainly based on two approaches: hydrogen addition and carbon rejection. The two approaches target increasing the H/C ratio at a molecular level, which means that HHCs are cracked and hydrogenated into small hydrocarbons. Figure 2.15 depicts various technologies categorised by their upgrading approach. 81% of residue upgrading occurs in carbon rejection technologies, while 15% are based on hydrogen addition [36]. In the context of petroleum-based heavy hydrocarbons. In literature, both approaches were studied in the presence or absence of a catalytic medium. In the hydrogen addition approach, hydrogen is added to increase the H/C ratio, as in hydrocracking technology [36]. In the carbon rejection approach, carbon is redistributed to form molecules with low H/C or coke and molecules with increased H/C [36]. Coke and low-H/C formation products require further processing or a reduction in carbon efficiency for the entire process. Furthermore, coke buildup on the catalyst surface causes the catalyst pores to plug up and prompts deactivation [112]. As a result, the deactivation of the catalyst has a detrimental impact on the conversion and quality improvement of HHC.

Another approach for HDO or deoxygenation of bio-oil derivatives is the use of in-situ H_2 generated from the bio-oil itself via different mechanisms. This approach is similar to the petroleum-based approach, where atomic hydrogen re-distribution occurs for upgrading purposes. A reported mechanism by Fisk et al. shows that H_2 can be produced from bio-

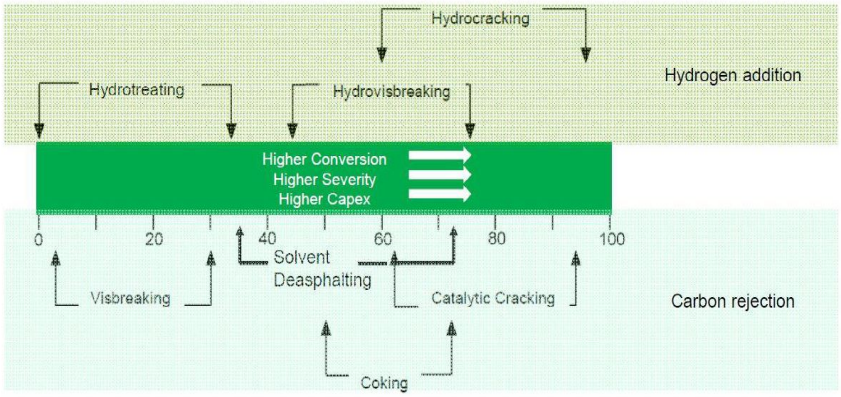


Figure 2.15: Comparison of HHC upgrading technologies in term of HHC conversion, severity and CapEx requirement (the scale in the figure represents HHC conversion [4]

oil via partial reforming of the feed (carbon rejection approach), while the other portion of the feed undergoes HDO, forming benzene [113]. This mechanism was created using Pt-based catalysts with different supports, which resulted in a significant drop in O/C. The highest drop in O/C using alumina-based catalysts resulted in a high yield of solids. In contrast, catalysts based on zirconia exhibited a 67% decrease in the ratio of oxygen to carbon while also showing a notable decrease in the creation of solid materials. The bio-oil in-situ H_2 generation and consumption approach has trade-offs between O/C reduction and solid formation since carbon rejection comes in the form of CO_2 or carbon deposition.

2.4.3 Alcohols as hydrogen source for bio-oil HDO

Alcohols are the most investigated H-donors to replace molecular hydrogen as a solvent or reactant. An interesting factor in selecting alcohol as H-donor is that it can be produced from biomass, which leads to the production of green chemicals. Another advantage is that some alcohols, such as glycerol, can be reformed at low temperature, below 300 degree C which is close to HDO temperature [114], [115].

Fan et al. studied the use of isopropanol as an H-donor for the HDO of guaiacol and real bio-oil in a continuous-flow reactor. The catalytic HDO was carried out at pressure and temperature of 20 bar and 350 °C, respectively, in HZSM-5-based catalysts. The modified Ni/HZSM-5 catalyst exhibited the highest level of activity, resulting in a 97.7% degree of HDO and a 34.4% selectivity towards BTX. The diagram in Figure 2.16 highlights the proposed reaction mechanism. This mechanism illustrates how not only free hydrogen radicals react with oxygenated hydrocarbons, but also propylene might be involved to increase the transalkylation mechanism. While transalkylation may enhance H/C of the mixture, it concurrently diminishes the selectivity towards specific compounds, hence limiting its potential

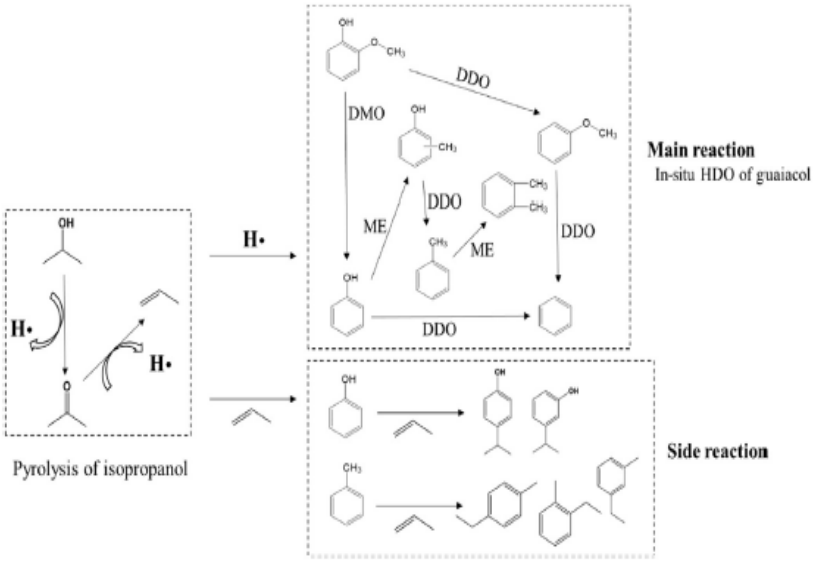


Figure 2.16: Proposed mechanism of guaiacol HDO via in-situ hydrogen produced from isopropanol pyrolysis (Adopted from [116])

for the production of specific green chemicals. Fan et al. further demonstrated that catalyst functionality has a key impact in determining the reaction pathways [116].

Methanol and ethanol reforming were also investigated as in-situ hydrogen generation for phenol HDO [13]. In that study, in-situ hydrogen was compared with molecular hydrogen using a Raney Ni and Pd-based catalyst. The conversion of molecular hydrogen is higher compared to the conversion of ethanol and methanol through aqueous reforming in both catalysts. This was attributed to the restricted amount of hydrogen that is adsorbed on the surface of the catalyst. Another factor contributing to the poor conversion is the dispersed distribution of adsorbed hydrogen and phenol. Yfanti et al. reported a similar finding when they used methanol reforming as the source of hydrogen for glycerol HDO [117]. Glycerol presence inhibits methanol reforming activity in comparison to non-glycerol experiment, as it exhibits higher adsorption on the active sites. Hence, the design of active sites is a crucial method for integrating reactions inside a single reactor zone.

In addition, a few studies explored the integration of in-situ hydrogen derived from alcohol reforming in the aqueous HDO of a different alcohol solvent [117], [118]. Zhang et al. investigated the process of HDO by using in-situ hydrogen produced from glycerol reforming in a supercritical ethanol environment [118]. When using a Ru/C catalyst, in-situ hydrogen exhibited superior performance compared to molecular hydrogen in terms of the degree of deoxygenation and heating value, specifically up to a temperature of 300 °C. Molecular hydrogen exhibited superior performance at elevated temperatures (320-350 °C). Further, a

crude bio-oil was examined for ex-situ and in-situ hydrogenation, leading to a higher yield of aromatic compounds in the in-situ experiment.

Despite alcohol promise as a hydrogen source, the addition of extra oxygen to the reaction system could complicate the accurate assessment of de-oxygenation and HDO. This is because the oxygenated functional groups may react with active bio-oil derivatives. Further research is necessary to fully understand and improve the utilization of in-situ hydrogen obtained from alcohol reforming. Due to the recent development of this domain, numerous studies may be attractive, ranging from material development to process design.

2.4.4 Supercritical water as hydrogen source for HDO

Similar to the previous H-donor upgrading approaches, supercritical water has been considered for petroleum based feed as hydrogen source or reaction medium [15], [16], [119]. Despite the observed improvements in the upgrading process via the production of lighter hydrocarbons and the removal of heteroatoms, the reaction mechanism is not completely understood [16]. In the case of biomass-based feed, recently, Vutolkina et al. conducted a study on the HDO of guaiacol using in-situ hydrogen produced via the water-gas shift (WGS) reaction. The study was conducted in a batch reactor for 6–8 hours, employing Ni-Mo sulphide catalysts, with a CO pressure of 50 bar and a reaction temperature range of 320–380 °C [120]. The primary outcomes of this study indicate that the reaction rate and operating temperature play a crucial role in determining the extent of HDO. Low temperature and short reaction time lead to a decreased WGS reaction rate, leading to decreased hydrogen availability for HDO and causing the condensation of phenols with other aromatics. The condensation was overcome by enhancing the desorption of aromatic compounds from the catalyst surface by increasing the temperature, leading to higher hydrogen formation and consequently an improved degree of HDO.

Furthermore, Miao et al. carried out a study to demonstrate the effectiveness of producing valuable hydrocarbons (paraffins) from fatty acids via hydrogen produced from the WGH reaction [121]. Similar to Vutonlkina's study, the operating temperature lays in the range of 320–340 °C in batch mode for up to 6 hours. The employed catalytic system is Ni-supported on zirconia. Extending the reaction time has been shown to result in a complete transformation of fatty acids into liquid and gaseous paraffins, as well as non-condensable gases. The reaction temperature is also an important parameter to achieve a complete conversion.

However, excessive increases in temperature may lead to the reduction of liquid paraffin to methane due to cracking mechanisms.

Jin et al. proposed employing a batch reactor to hydrodeoxygenate guaiacol in a water medium using multifunctional catalysts [122]. The catalysts are designed for producing hydrogen by water activation and facilitating HDO under high pressures. The catalytic system employed in thiar study comprises of Ni and NiMo-based catalysts, which are supported on ceria and carbon. This study concluded that despite the relatively low guaiacol conversion up to 20%, the concept has a potential to replace expensive molecular hydrogen. Regarding the catalytic system, the utilisation of a carbon support has resulted in a significant increase in conversion rates due to its ability to enhance the dispersion of active sites of Ni and ceria. Ni is identified as the site that facilitates de-oxygenation, while ceria is responsible for activating water.

Beyond the reactive involvement, water in supercritical conditions has demonstrated its potential for upgrading bio-oil, enhancing the reactivity and selectivity of NiCo active sites supported on carbon nanofibers (CNFs) [14]. Roman et al. have emphasised the decrease in sulphur (S) and oxygen-to-carbon (O/C) ratios on a weight basis, as well as the increase in hydrogen-to-carbon (H/C) ratios using elemental analysis, consistent with previous studies [14]. The deoxygenation occurs via decarboxylation and decarbonylation. Consequently, the catalytically treated liquid has resulted in improved heating values. Temperature has a declining impact on the ability of CNFs to undergo deoxygenation, as indicated by the H/C, O/C, and heating values, despite the increase in liquid and gas yields at the cost of solids.

2.4.5 Heavy hydrocarbons as hydrogen source from bio-oil HDO

An alternative approach for “in-situ” hydrogen generation for HDO involves blending petroleum-based catalytic cracking feed with lignin-derived fast pyrolysis products [85], [123], [124]. This approach aims to crack petroleum-heavy hydrocarbon feed and hydrodeoxygenate bio-oil feeds to improve blend properties. It holds significant promise for integrating the biorefinery stream with petroleum-based refineries and downstream processing for the production of fuels and chemicals. This integration involves the utilisation of zeolite-based fluid catalytic cracking catalysts. Various investigations have highlighted hydrogen transfer for HDO while underscoring rapid deactivation due to coke accumulation [85], [123], [124]. In

the context of this thesis, these studies explore the use of alkanes as hydrogen sources [85], [124]. Graca et al. proposed a mechanism for integrating heavy alkanes with HDO of guaiacol via hydrogen transfer, as illustrated in Figure 2.17.

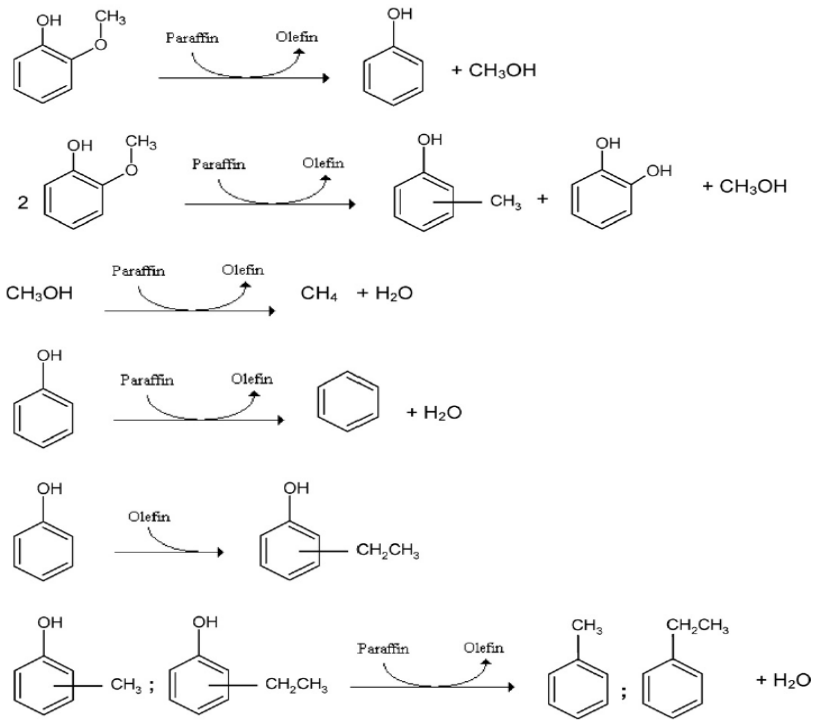


Figure 2.17: Proposed mechanism for in-situ hydrogen generation HDO via large alkane DeH as hydrogen source (Adopted from [124])

Heuchel et al. examined the catalytic co-processing of n-decane and 2-ethylphenol mixtures using a range of zeolites at 480 °C in a continuous flow reactor [85]. A significant finding was that the bio-oil model compound led to substantial coke formation on the spent catalyst, resulting in a rapid conversion decline. The degree of coke formation and deactivation varied depending on the porosity of the zeolites studied. While there was no improvement in conversion compared to studies using only n-decane, the inclusion of 2-ethylphenol led to enhanced aromatic selectivity, indicating effective deoxygenation through hydrogen transfer. Particularly, zeolites with larger pores exhibited higher aromatic selectivities, attributed to their superior hydrogen transfer capability. Gueudre et al. investigated the co-processing of catalytic cracking and HDO of a vacuum gas oil (VGO) and wood-based pyrolysis oil mixture on commercial FCC zeolite catalysts, with and without the addition of USY zeolite [123]. Their findings align with those of Heuchel et al., suggesting that using bio-oil resulted in increased carbon deposition. Furthermore, the increase in carbon deposition was not solely attributed to the presence of additional bio-coke but also to an increase in petroleum-based coke with bio-oil addition, attributed to various chemical routes of coke formation during co-processing.

Moreover, Graca et al. observed that when maintaining constant conversion of gasoline-guaiacol mixtures in both HZSM-5 and HZSM-5 with equilibrium FCC catalysts, there was an increase in coke formation compared to tests without guaiacol [124]. Processing the petroleum-based model compound n-heptane with guaiacol at 450 °C revealed a clear and detrimental impact of guaiacol on n-heptane conversion. This phenomenon was consistent for both HY and HZSM-5 zeolites, with the latter exhibiting a more significant and rapid decrease. The rapid deactivation were attributed to zeolite pore blockage, externally caused by limitations in guaiacol penetration due to differences in molecule and pore sizes. This observation was validated through pore size measurements on fresh and spent catalysts. The rationale for in-situ hydrogen generation and transfer stemmed from phenols in the gasoline mixture.

The aforementioned studies have examined the integration of alkanes with bio-oil derivatives, which aligns with the objective of this thesis, despite variations in the co-processing mechanisms. These studies employed cracking or dehydroaromatization processes to produce hydrogen using zeolite catalysts. Thus, research gaps still arise in the utilisation of simultaneous alkane DeH and HDO approaches. A possible approach to investigate is the utilisation of an alternative catalytic support that does not hinder guaiacol diffusion to active sites through fast deactivation. Furthermore, the examination of lighter hydrocarbons as a potential source of hydrogen is appealing given the high value of the olefins that would be produced.

2.4.6 Light hydrocarbons as hydrogen source from bio-oil HDO

The preceding discussion has investigated the potential of hydrogen transfer between petroleum-based heavy hydrocarbons and bio-based feeds for oxygen removal. As previously highlighted, several studies have explored using methane as H-donor for upgrading petroleum-based hydrocarbons [105]–[108], and this approach has also been considered for bio-based feeds. He et al. investigated the direct upgrading of sawdust using methane in a continuous flow reactor under atmospheric pressure [109]. The study focused on HZSM-5-based catalysts loaded with various metal species, with zinc (Zn) demonstrating best H/C and O/C performance. The performance of zinc loading was evaluated and compared with non-catalytic conditions and with ex-situ hydrogen. The findings suggested that catalytic in-situ hydrogen production from methane yields superior H/C and O/C ratios compared to non-

catalytic HDO, and even outperforms catalytic HDO with molecular hydrogen produced "ex-situ." Notably, HZSM-5 exhibited a 10% higher O/C ratio under in-situ conditions compared to Zn/HZSM-5, albeit with a 20% lower H/C ratio. Nevertheless, the utilisation of the loaded HZSM-5 was deemed preferable due to its higher oil output.

Despite the promising potential of methane as an H-donor owing to its abundance, even from biomass processing as biogas, its side product carbon may adversely affect catalyst performance. Consequently, Wang et al. investigated the use of hexane DeH as an H-donor for cresol HDO [21]. Among the catalysts studied, the Pt-WOx catalyst exhibited superior activity in the coupled reaction, surpassing the equilibrium conversion of hexane DeH by nearly threefold (2.8%) at 400 °C and 36 bar pressure. Figure 2.18 illustrates the hydrogen transfer mechanism as reported by Wang et al. [21]. The study concluded that the coupled reaction is primarily governed by hexane DeH rather than being influenced by cresol concentration. Notably, there was no rapid deactivation observed in the coupled system, even at atmospheric pressure. This absence of rapid deactivation was explained by a microkinetic model employing propane as a hydrogen source that suggests the lower conversion at high pressures correlates with the reduced formation of coke precursors.

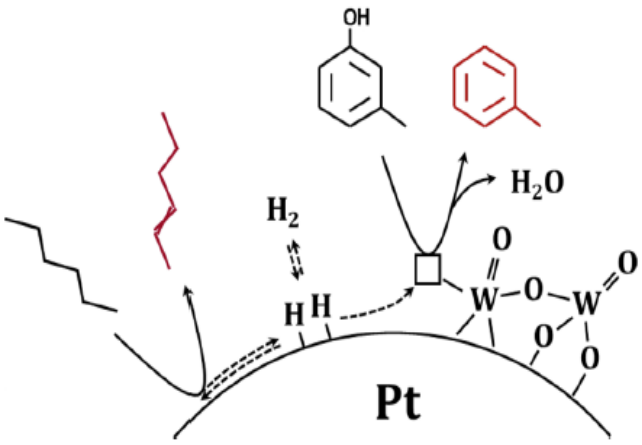


Figure 2.18: Schematic representation of hydrogen transfer from hexane DeH for cresol HDO (Adopted from [21])

The previous sections exhibited the possibility of replacing molecular hydrogen via in-situ hydrogen generation through various reactions. Some works indicated that "in-situ" generation leads to a greater extent of HDO than ex-situ due to the adsorbed hydrogen at the catalytic surface. Regarding the enhancement of H-donor conversion using HDO, it was observed that the catalytic conditions played a crucial role in achieving a conversion rate that surpassed the equilibrium conversion. Theoretically, the ideal H-donor is the one that

produces valuable byproducts beside hydrogen to improve the product stream value. This can only be accomplished via an on-purpose DeH reaction, as shown by Wang et al [21]. Nevertheless, the existing literature lacks sufficient study on the in-situ approach for bio-oil HDO, resulting in a gap in knowledge that can be addressed in this PhD. In order to fully unlock the synergistic effects of coupling two reactions, the operating conditions and catalytic system must be designed for the targeted objectives. Henceforth, the subsequent sections will focus on investigating possible catalytic systems for the coupled reaction in this study.

2.5 Catalytic system for coupled reactions (DeH-HDO)

Both the bio-oil (represented in this thesis by guaiacol as a model compound) HDO and alkane (ethane in this work) DeH reactions necessitate catalysts to drive the conversion towards the desired products. Thermodynamics, as depicted in Table 2.6, tends to favour the cracking of ethane to methane rather than the formation of ethylene due to the lower energy requirement for C-C cleavage. Similarly, for guaiacol, the thermal energy required for dissociating the hydroxy group is higher without saturating the aromatic ring, as indicated by the $C_{aromatic}$-OH and R-OH energies. Therefore, to couple these reactions, a suitable catalytic system is essential, so that their output is kinetically-controlled.

Table 2.6: Bond dissociation energy (BDE) of oxygenated functional groups [125], [126]

Functional groups	BDE (kJ·mol^{-1})	Functional groups	BDE (kJ·mol^{-1})
H—H	436	R—OH	385
H—O	429	R—OR	338
CH_3—CH_3	368	$C_{aromatic}$-OR	422
CH_3CH_2—H	410	$C_{aromatic}$-OH	468
		R=O	758

The objective of the catalytic system is to dehydrogenate ethane to ethylene and ideally reduce the O/C ratio of HDO product to zero, as illustrated in Figure 2.19. However, the differentiation in processing bio-oil in HDO to fuels or chemicals is determined by the target H/C ratio. Since BTX is the target for guaiacol HDO, a H/C ratio near 1.0 is the objective. Figure 2.19 primarily showcases noble metals in comparison with non-precious CoMo catalytic systems, indicating that Mo-based catalysts hold promise for HDO. Furthermore, Tables 2.7 and 2.8 provide a compilation of literature findings on leading catalysts for HDO at atmospheric pressure, targeted pressure for alkane DeH.

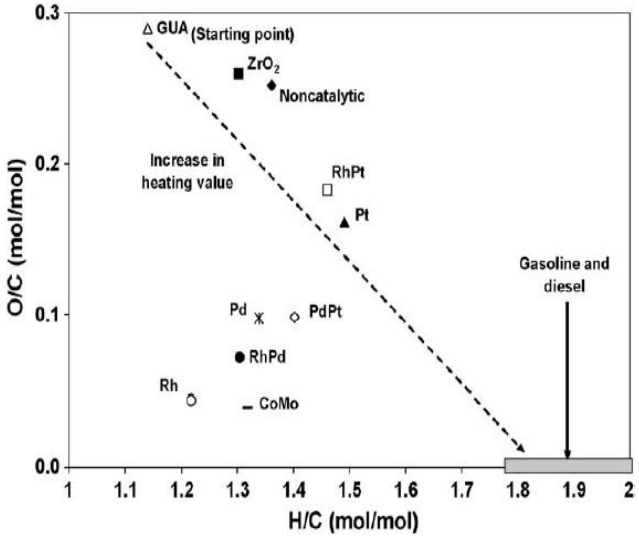


Figure 2.19: Desired changes of H/C and O/C in catalytic upgrading of lignin to benzene, reproduced from (Adopted from [32])

2.5.1 Unsupported Mo-based catalysts

Several studies have highlighted the effectiveness of unsupported molybdenum catalysts as active sites for the direct conversion of biomass to bio-oil via fast pyrolysis (FP) or for upgrading the resulting bio-oil into valuable aromatics [24], [91], [92], [96], [127]. These investigations typically operate in continuous fixed-bed reactors under near-atmospheric pressure conditions, which aligns with the objectives of this study.

To assess the potential of MoO_3, Prasomsri et al. investigated the HDO products of various model compounds, representative of those found in bio-oil, possessing distinct oxygenated functional groups [91], [96]. A key finding was the selectivity of MoO_3 towards targeted value-added chemicals. While thermodynamics suggest that guaiacol HDO favours demethylation over demethoxylation due to bond dissociation energy, Prasomsri et al. observed a preference for demethoxylation of guaiacol to phenol rather than demethylation, resulting in catechol formation [91]. Additionally, the study reported that guaiacol conversion could be completed rapidly by increasing the temperature to 400 °C, with higher selectivity towards benzene [91].

In another study, Prasomsri et al. expanded their investigation to include non-aromatic bio-oil-derived oxygenates such as acetone, hexanone, cyclohexanone, and furan, confirming MoO_3 ability to selectively convert model compounds into desired value-added chemicals, such as alkenes in the case of acetone and unsaturated aromatics for investigated oxy-

genated aromatics [96].

Moreover, Zhou et al. explored the effects of upgrading acetone, guaiacol, and real biomass vapour at atmospheric pressure and elevated temperatures [24]. At 400 °C, oxygenated compounds (guaiacol and acetone) were almost completely converted, primarily into benzene in the liquid product from guaiacol and a propane/propylene mixture from HDO of acetone. Similar to findings by Prasomsri et al., Zhou et al. observed no saturated aromatics or catechol and relatively low phenol levels, suggesting MoO_3 selectivity towards guaiacol HDO favouring demethylation and demethoxylation [24]. The high reactivity of the catalytic bed in Zhou et al. can be attributed to the high catalyst load, 1.6-1.7 g_{cat} for 1.0 g of oxygenated hydrocarbon per hour. Additionally, an increase in temperature was observed to enhance reactivity but towards a cracking mechanism, leading to less organic liquid formation [24].

While these studies provide positive indications that atmospheric pressure hydrogen has the potential to upgrade bio-oil, the investigated temperature range falls short of the targeted temperature for alkane DeH. Thus, significantly reducing the catalyst loading might help to limit cracking while maintaining unsaturated aromatics. The deactivation of MoO_3 catalyst was attributed to carbon formation, catalyst reduction to an inactive state, and water poisoning. Another study expanded the search of unsupported Mo-based catalysts to include MoP and MoS_2. Although conducted at high pressure (4.4 MPa) in a stirred batch reactor, it provides insight into MoO_3 performance compared to other unsupported Mo-based catalysts. MoS_2 was observed to be more selective towards unsaturated aromatics (toluene) starting from cresol, with 70-80% selectivity to toluene and the remaining as hydrogenated products [127]. In the case of MoO_3 and MoO_2, both exhibited similar selectivity performances of 60-70%, contradicting the previously reported hypothesis that catalyst deactivation is caused by reduction [127]. Furthermore, it was stated that the saturation (hydrogenation) of cresol aromatic ring was limited with the oxides and sulphide forms, which is preferred for the current study. The selectivity of molybdenum oxides in comparison with phosphide was confirmed by Boullosa-Eiras et al. with a TiO_2 support at 25 bar [128].

Another molybdenum form (Mo_2C) was studied by Chen et al. for HDO of a phenolic mixture of anisole, guaiacol, dimethoxybenzene (DMB), and cresol at atmospheric pressure [92]. This study also observed that saturation of the aromatic ring is limited, with over 80% se-

lectivity towards BTX. The cleavage of aromatic-methoxy and aromatic-hydroxy require 376 kJ mol^{-1} and 456 kJ mol^{-1}, respectively. Chen et al. claim that limited saturation of the aromatic ring results from successive hydrogenation, even at high hydrogen-to-oxygenated aromatic feed ratios [92]. Thus, selective HDO via direct hydrogenolysis of the hydroxy group in the case of phenolic compounds instead of hydrogenation-hydrolysis mechanism makes MoO_3 at low pressure an attractive choice in the present study. Furthermore, MoO_3 was investigated for HDO of non-aromatic oxygenated hydrocarbons such as ketones (acetone) and aldehydes (acrolein) to include most bio-oil oxygenated derivatives for generating aromatics and alkanes [24], [129], [130].

In summary, MoO_3 has demonstrated its selectivity towards HDO in the direct (single-step) lignin pyrolysis and in-situ processes. Increasing catalyst loading and temperature lead to greater HDO by reducing oxygen presence [95]. Multiple contributions have observed the selective HDO pathway in small surface-unsupported Mo-based catalysts, particularly molybdenum oxides, at atmospheric pressure. Thus, the simplicity of the molybdenum oxide system is an attractive approach to understanding the role of active sites in HDO and/or alkane DeH.

2.5.2 Supported NiMo-based catalysts

2.5.2.1 Guaiacol HDO

The preceding sections of this review have investigated various upgrading approaches for petroleum and biomass feeds, employing different configurations employing molecular hydrogen or H-donors. Among the well-researched catalysts are NiMo-based catalysts, particularly in continuous flow HDO, as shown in Table 2.8. The previous section has illustrated the potential of unsupported MoO_3, yet incorporating Ni is aimed at enhancing the functionalities to evaluate HDO processes. These functionalities are crucial in assessing the proposed DeH-HDO approach.

Ni active sites have been extensively investigated for their role in HDO processes, as evidenced by Tables 2.7 and 2.8. Ni-active sites are known to facilitate hydrogenolysis via C-O cleavage. Additionally, Ni serves as a hydrogenating metal [131]. However, to facilitate C-O cleavage (deoxygenation), an oxygen vacancy mechanism is considered an effective strategy using MoO_x [126]. The enhancement with Mo is attributed to the strength of Mo-O bonds, with Mo-O and Ni-O bond energies being 607 and 366 kJ·mol^{-1}, respectively [131]. Con-

sequently, the strength of Mo-O bonds eases the dissociation of C-O, as hypothesised in Figure 2.20, where hydrogenation occurs at Ni active sites, activating H-H bonds. Thus, oxygen vacancies in MoOx promote the deoxygenation mechanism by creating Mo-O [126]. This hypothesis finds support in a study utilising Ni-Mo on titanium oxide catalysts, which demonstrated improved HDO of guaiacol through the synergistic effect of both active sites at atmospheric pressure with molecular hydrogen [86].

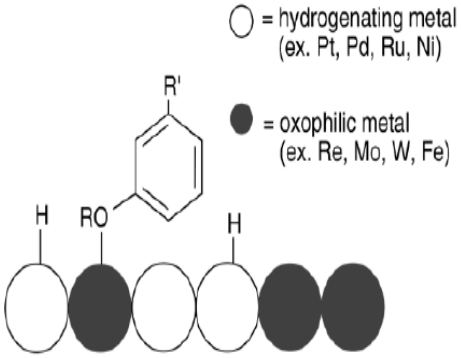


Figure 2.20: Reported hypothesis in using bifunctional active sites (ex. Ni-Mo) for HDO (Adopted from [131])

Furthermore, Vutolkina et al. investigated the influence of Ni on the extent of HDO with Mo in an effort to develop bifunctional catalysts for upgrading guaiacol using water as an H-donor [120]. Despite the involvement of an H-donor, Ni is active in the water gas shift reaction (WGS) and hydrogenation. The study revealed that certain Ni loadings (Ni:3Mo) led to reduced O/C ratios and increased H/C ratios, indicative of improved HDO [120]. This observation suggests distinct mechanisms at each active site, wherein the loading must be improved based on the rate of each process, as an unbalanced ratio may hinder the synergy between the two active sites.

In WGS applications, unsupported NiMo was dispersed in water. However, for non-aqueous processing, support may be crucial to disperse active sites optimally and achieve an ideal surface area. Furthermore, the acidity of the support has been reported to enhance interaction with hydrogenation active sites and is considered a DeH promoter, further assessing Mo active sites [131]. Therefore, NiMo on alumina support has been extensively studied for complex processes such as the upgrading oxygenated heavy hydrocarbon streams.

2.5.2.2 Alkane DeH

As previously illustrated in Figure 2.8, alkane DeH is heavily investigated and regarded as the emerging process to replace energy-intensive steam cracking (SC) for alkene production.

Since it is a catalytic conversion-based process, the research efforts are mainly devoted to finding a suitable catalyst. Yet, several configurations of alkane DeH have been commercialised for C3 and C4 with Cr and Pt-based catalysts [83], [132], [133]. Therefore, Cr and Pt are recognised as the leading active sites, with V, Mo, and Ga identified as promising but underdeveloped alternatives [83].

In particular, several studies and reviews have considered Mo-based catalysts for alkane DeH [83], [132], [134], [135]. Heracleous el at. studied oxidative and non-oxidative DeH of ethane using MoO_3/Al_2O_3. The study reported that thermal DeH in the absence of oxygen at 600 °C resulted in 2% conversion, while the catalytic system conversion is 15% [134]. The lowest studied reaction temperature was 500 °C, which resulted in a 5.5% conversion. Heracleous et al. claimed that despite the presence of oxygen in some runs, ethane pyrolysis to ethylene is the main mechanism for the DeH reaction [134].

Furthermore, despite being well-known for hydrotreating applications, supported Ni-Mo catalysts have also been investigated for alkane DeH in both oxidative and non-oxidative environments, particularly for propane [136]–[138]. Saihvashi and his colleagues investigated the use of Mo-Ni/Al_2O_3 for propane DeH [136]. Propane conversion, and propylene, methane and hydrogen productions were observed at the temperature of 500 °C in the non-oxidative dehydrogenation (NODeH) system. The presence of oxygen and the increased temperature enhance propane conversion [136]. Moreover, the study investigated the effects of pressure in the reaction performance with the presence of oxygen. The increase of pressure from 1.0 bar to 5.0 bar led to roughly 10% reduction of propane conversion (90% to 80%), which corresponded to 10% improvement in propylene selectivity [136]. oxidative dehydrogenation (ODeH) is thermodynamically favoured with the continuous removal of hydrogen by the presence of oxygen, which leads to increasing alkenes yield. It could be hypothesised that catalytic DeH is an interesting H-donor with the continuous removal of hydrogen by hydrocracking of HHCs, although their hydrogenation is less exothermic than that of oxygen.

In one study, high hydrogen formation was observed in the oxidative mechanism, while higher alkene (propylene) formation occurred in the non-oxidative mechanism [136]. Moreover, computational studies by Wang et al. identified alumina-supported Ni-Mo as a promising non-precious metallic catalyst that can outperform Pt-based catalysts for propane DeH,

a finding that was experimentally validated [137]. Pt-based catalysts exhibited higher, stable conversion rates of 10-20%, whereas Ni-Mo showed stable conversion rates of roughly 10%. However, Ni-Mo demonstrated 2-3 times higher conversion rates than Pt catalysts, resulting in higher propylene yields. As observed in our experimental findings, lower selectivity was attributed to the effects of Ni [137].

Wang et al. computationally investigated nearly 2000 bimetallic catalysts and identified NiMo supported on MgO as a promising candidate [138]. Experimentally, it was confirmed that NiMo/MgO synthesized via incipient wetness co-impregnation outperformed Pt-based catalysts for ethane DeH in terms of ethane conversion and ethylene selectivity. Despite differences in bimetallic composition and operating conditions, the experimental results in this study for alkane DeH are promising for combination with HDO processes [138].

Kinetically, ethane conversion on supported Ni-Mo catalysts is influenced by the bifunctional metal active sites as well as the acidic alumina support. Ni-based catalysts have been extensively considered for alkane conversion to replace leading alkane DeH Pt and Cr-based catalysts [139], [140] due to their high activation energy [141]. However, Ni active sites target the dissociation mechanism of C-C rather than C-H due to their relatively lower activation energy. Consequently, the presence of Ni leads to the formation of undesirable methane and accelerates coke formation, making it a highly regarded active site for ethane cracking to hydrogen and carbon [139], [140]. Nevertheless, NiMo on alumina shows potential as an excellent catalyst for DeH-HDO processes, given the distinct functionalities of the support and active sites.

Table 2.7: Published works on catalytic HDO at atmospheric pressure.

Group	Feed	Catalyst	Reactor type	Temp. °C	Observation	Citation
Chang et al.	GUA	Ni_2P varies	WHSV 0.67-5.34 h^{-1}	300	• Reactivity toward BTX SiO_2>ZrO_2>Al_2O_3 • Shorter residence time leads to higher conversion and selectivity to BTX	[87]
Rom´an-Leshkov et al.	GUA	MoO_3 no support	0.0029-0.035 mmol $gcat^{-1}$ h^{-1}	300-350	• Selective catalyst to de-methoxylation and high yiel of BTX • Guaiacol conversion notably increases with temperature	[91]
Li et al.	GUA	Fe/Ni HBeta	1.5-4.0 h^{-1}	250-400	• Ni presence increases trensmethylation, degree of HDO and selectivity to BTX • Guaiacol reach completion at 300 °C with no significant changes in selectivities with longer longer WHSV and higher temperature. Aromatics yield up to 20%.	[142]
Bando et al.	GUA	Ni_2P varies	5.0 s	420-450	• Limited BTX, guaiacol to cresol and phenol • Degree of HDO ASA>FCC>ZSM-5 acidity play role in product distribution.	[143]
Wang et al.	GUA	Ni HUSY		350	• Atmospheric pressure HDO only produce phenolic compounds and aromatic hydrocarbon which limit hydrogen consumption over Ni active sites.	[94]

Table 2.8: Published works on catalytic HDO at atmospheric pressure.

Group	Feed	Catalyst	Reactor type	Temp. °C	Observation	Citation
Slowing et al.	GUA	Pd/HS CeO_2	Batch (4h)	100	• The operating condition favours ring saturation with minimum HDO • Excess hydrogen with presence of water led to near complete conversion of guaiacol	[89]
Gates et al.	GUA	Pt Al_2O_3	20.0 $g_{gua}/(g_{cat}$ h)	300	• Metal active site facilities hydrogenolysis, hydrogenation and where alumina support caused transalkylation • Limited BTX, with 0.5 bar increase better HDO was observed	[144]
Mahinpey et al.	GUA	Ni-Mo TiO_2	0.5-2.0 H_2/GUA molar ratio	200-350	• Ni-Mo resulted on enhanced HDO than Ni and Mo only active site caused improved metal dispersion. • Higher temperature and hydrogen resulted on enhanced HDO, but no BTX.	[86]
Zhu et al.	GUA	Pt SiO_2 HBeta	0.25-1.75 h	350	• Metal site catalyse demtylation and acid site work on transalkylation and dehydroxylation. • The addition of water improves guaiacol conversion.	[145]
Wu et al.	GUA	Ni-Mo SiO_2	1.5 h^{-1} H_2/GUA molar= 5	400-420	• High selectivity toward BTX reaching 97.5% • Methyl radicals transformed into benzene due to access acidic sites • Catalyst regenerated 15 times at stable performance.	[90]

Chapter 3

Methodology

This chapter serves to establish the foundational framework for the thesis. It commences with Section 1.1, which articulates the principal research questions and outlines the structure of the subsequent chapters to address them. Subsequently, Section 3.1 addresses the experimental approach and procedure, emphasising the catalytic systems investigated and the rationale guiding their selection. A detailed description of the experimental setup employed for all experiments is provided in Section 3.2. Given the novelty of the DeH-HDO coupling using alkane and bio-oil, Section 3.6 is dedicated to explaining the selection and ranges of operating conditions used in this thesis. Finally, Section 3.4 covers product collection, treatment, and analysis, as well as performance calculation to address the research questions.

3.1 Experimental Methodology

3.1.1 Experimental approach

Experimental activity up to date focuses on understanding the potential of lignin-derived oxygenated aromatics HDO via hydrogen generated from alkane DeH. The integrated reactions necessitate catalytic activity to improve guaiacol and ethane conversion while maintaining targeted selectivity towards BTX. Thus, selecting the appropriate catalytic bed is crucial for studying the potential of integrated reactions. Since each reaction is well-documented in literature, well-known catalytic beds are considered in this project to demonstrate integration potential. Initially, a single catalytic bed is used for HDO with in-situ hydrogen generation and ex-situ produced hydrogen, as well as for alkane DeH, to establish a baseline. This approach is chosen due to the reaction temperature and pressure (500-600 °C and atmospheric pressure) being conducive to alkane DeH, and selective catalysts are employed to facilitate HDO towards high-value chemicals. Therefore, experimental activity is divided into:

- Conventional HDO of guaiacol at elevated pressures via Ni-Mo based catalyst
- Conventional HDO of guaiacol at atmospheric pressure via Mo-based catalysts
- Non-oxidative DeH of ethane for hydrogen generation
- HDO of guaiacol via in-situ alkane DeH

DeH-HDO of guaiacol (GUA) is investigated across various catalytic systems, operating temperatures, pressures, and liquid-to-gas feed ratios (FG/FL). The investigated catalytic systems, in Chapters 4 and 5 include Ni-Mo/Al_2O_3 catalysts, MoO3, and Cr/Al_2O_3, which have been extensively studied in literature for either or both reactions as described in Chapter 2. In summary, Cr-based catalysts are widely researched for non-oxidative alkane DeH and commercialised for C_3-C_4 DeH [133], [138], [140]. Bimetallic supported catalysts (Ni-Mo) have been extensively explored for HDO and hydroprocessing in general, and in limited works for alkane DeH separately [23], [136]. Additionally, both supported and unsupported MoO_3 have been investigated for each reaction [24], [37], [138], [140]. Utilising these well-studied catalysts is an essential step for evaluating the proposed DeH-HDO coupling. The rational of utilising these distinct catalysts to explore different functionalities for the novel DeH-HDO coupling. Figure 3.1 summarises the exploration structure for catalytic systems included in this work.

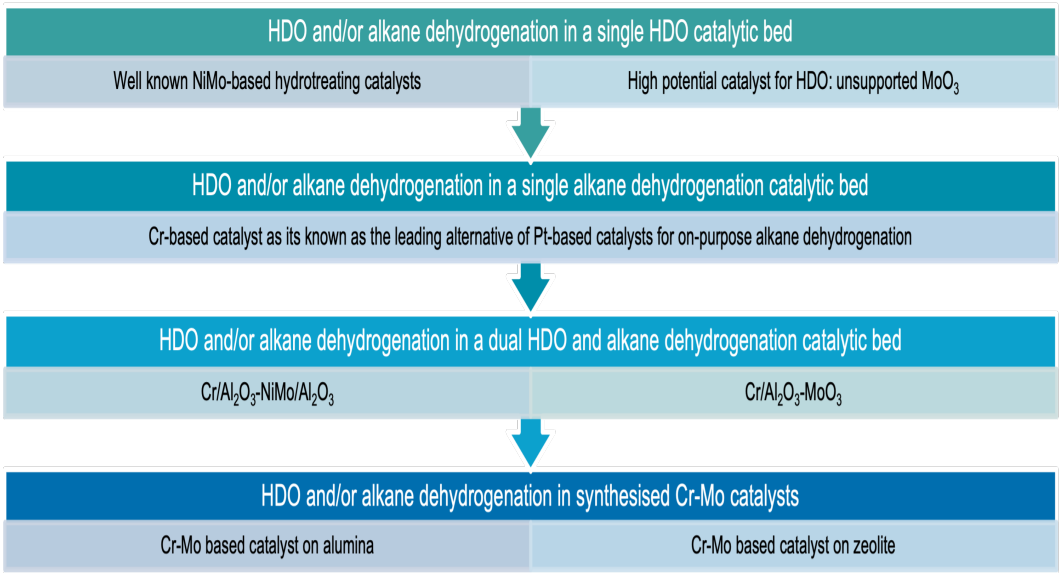


Figure 3.1: Designed experimental framework for investigated catalytic systems

3.1.2 Experimental procedure

Each experimental run consists of multiple stages to ensure the readiness of the catalytic bed at the appropriate temperature, catalyst activation, and proper collection and sampling

of the products, as illustrated in Figure 3.2. Initially, the catalytic bed undergoes a moisture removal stage, during which the reactor temperature increases to 200 °C at a rate of 25 °C·min^{-1}. This stage lasts for 60 min to ensure the elimination of water absorbed by the catalyst, with the water content potentially reaching up to 2% according to TGA assessments of newly prepared catalysts. While the moisture adsorption rate may vary depending on the material type, an average value of 2% is considered sufficient to evaporate within the allotted 60 min.

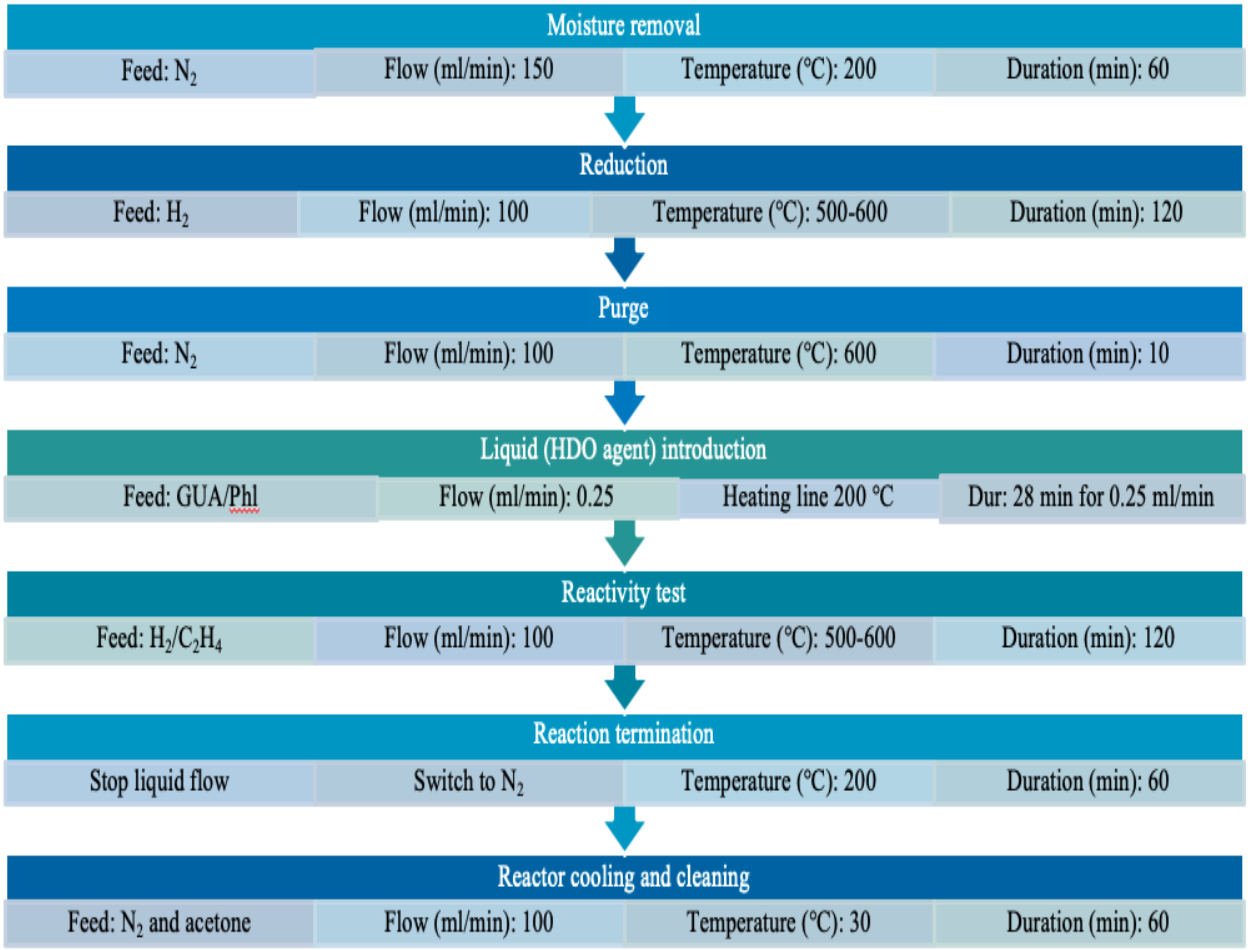


Figure 3.2: Stages of a DeH-HDO experiment run

The reduction stage is a critical process to activate the catalyst and eliminate the oxidation reaction caused by the metal oxide. This step is essential since a non-oxidative DeH process is conducted, aiming to eliminate the presence of oxygen content through HDO. Reduction occurs at the intended reaction temperature, although it is feasible to achieve reduction at low temperatures as 450 °C. Prior to initiating an experiment, a system purge is carried out using nitrogen gas (N_2) to completely eliminate all hydrogen from the system. This purge persists for 10 min, in addition to the required guaiacol hold-up period, i.e. the time required for guaiacol to reach the catalytic zone through the liquid feed line. Empirical measurements

determined the hold-up period to be 28 min, with a flow rate of 0.25 mL·min^{-1}. Upon guaiacol reaching the catalytic bed, the flow of ethane commences simultaneously with the initiation of the reaction.

Upon completion of the reaction test, the temperature is lowered to 200 °C, and the gas is switched to nitrogen. This stage aims to remove all liquid from the collection and sample apparatus. Controlling the temperature and gas switch is crucial to prevent additional reactions and control the boiling point of guaiacol and the average HDO product to prevent condensation. Following 60 min of N_2 flow, further cooling occurs in the reactor before it is opened and the spent catalyst retrieved.

3.1.3 Materials

This work utilised various materials including gases, solvents, reactants, and catalyst precursors. For liquid reactants, guaiacol and phenol were obtained from Sigma-Aldrich, with purities exceeding 99% for guaiacol (FG grade) and phenol (puriss grade), respectively. Gas reactants, hydrogen and ethane, were sourced from BOC (high purity grade) and Air Liquide (2.5 grade), respectively.

3.2 Experimental testing rig

3.2.1 Experimental testing rig description

The hydroprocessing studies were carried out in a hydrocracking setup that was created and built in-house by Dr. Marcos Millan's research group [146]. In the past, the system was utilised to conduct catalytic hydrocracking trials on model compounds and HHC (residues) derived from petroleum-based refineries, employing a hydrogen supply of exceptional purity. The rig has the ability to handle hydrocarbon feed under high pressures, up to 250 bar. A comprehensive description and rationale of the original design can be found in [146]. The initial rig design was altered to meet the specific needs of this project. The rig comprises three primary sections: (1) feeding (2) reaction zone, and (3) product separation and recovery, as depicted in Figure 3.3. The modifications were mostly made to the reaction and recovery sections.

3.2.2 Feeding section

The objective of this stage is to provide hydrogen or a hydrogen source in the form of a gas and a model compound of bio-oil in the form of a liquid to the reaction section. Figure 3.4

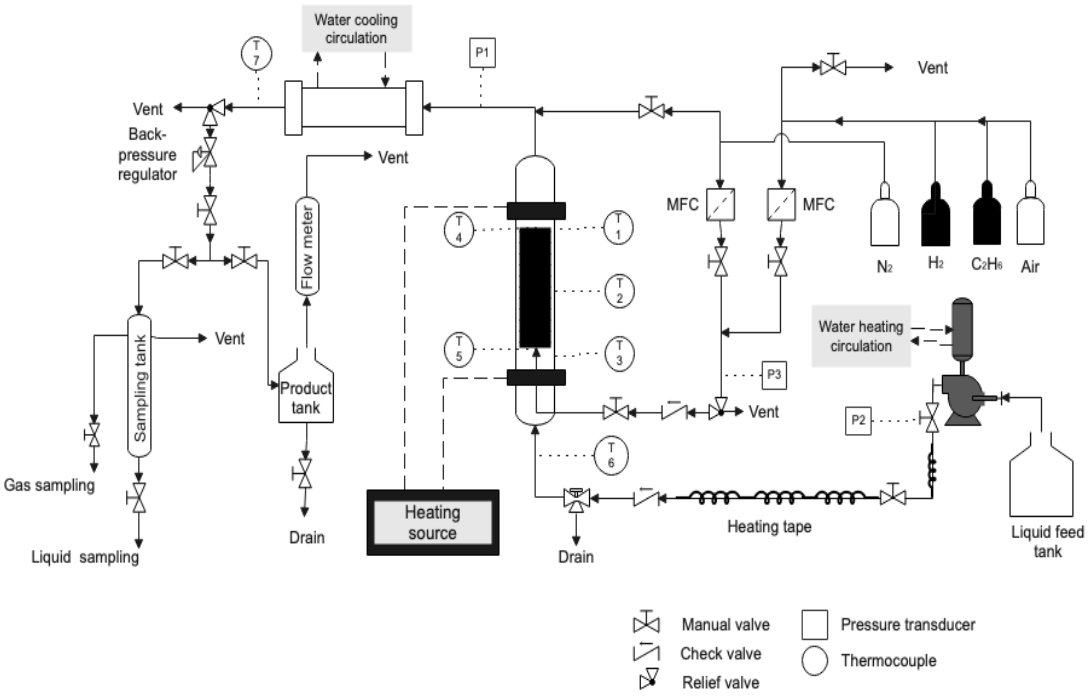


Figure 3.3: In-house built hydroprocessing rig to evaluate atmospheric HDO of guaiacol using molecular hydrogen or in-situ generated hydrogen

shows the gas feeding stage. The initial conditioning stage takes place outside the rig cabinet via gas feeding lines, while additional conditioning happening inside the cabinet through a gas process line. The gas feeding lines comprise a hydrogen source and intermediate lines, with each line being regulated by manual valves to route the gases into the setup via a mass flow controller (MFC) or a safety vent system. The hydrogen source often originates from a gas cylinder that has the ability to supply the feed at the necessary pressure. The hydrogen source cylinder is linked to the setup through a manifold system that incorporates emergency mechanisms to address back pressure or pressure breaches. Furthermore, a high-pressure conduit is provided to supply an inert gas, typically nitrogen, for the purposes of gas dilution, leak testing, gas purging, and rig cleaning. Two mass flow controllers were utilised to independently regulate the flow of each line. However, the combination of gases occurs in the case of dilution after the feeding lines and before reaching the reaction zone. The gas process line passes through a filter, manual valve, and check valve within the setup cabinet before entering the reaction zone.

The liquid feed line originates from a feed container and flows via a syringe pump and safety valves before reaching the reaction zone. The syringe pump is a TELEDYNE isco model 260D, equipped with a liquid tank capable of holding 266 mL. The tank is equipped with a cooling and heating jacket that is regulated by an external water circulation system

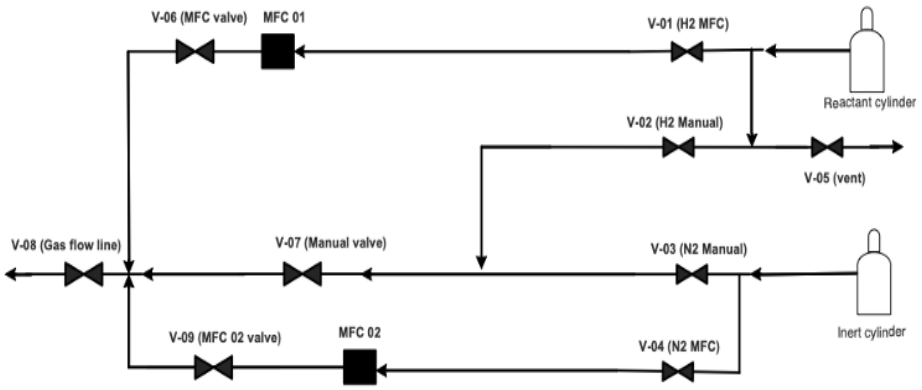


Figure 3.4: Modified gas feed-line system to accommodate two mass flow control (MFC) for safety, calibration and mixed feed experiments.

in order to maintain the liquid at the proper temperature and avoid solidification in the case of experiments with phenol. The pump flowrate range is 0.001-90 mL·min^{-1}, while maintaining a maximum pressure of 517 bar. The pump pushes the liquid to be treated through a pipeline that is fitted with a manual valve, drain valve, and check valve. To vaporise the HHCs, a heating wire is wrapped around the feeding line if the liquid needs to be heated up to 150 °C. The liquid feed line and gas process line are combined into a single input in the reaction zone.

3.2.2.1 Reaction section

The reaction section is designed for continuous up-flow fixed bed experiments. The reactor is made of a 60-cm Inconel tube that is connected to Joule heating electrodes, serving as a heat source. The selection of Inconel was made for processing at a high pressure of 250 bar [146]. The reactor has a distance of only 25 cm between the electrodes, which is considered the reaction zone. The catalyst bed is located at the centre of the reaction zone, ensuring that the temperature gradient along the bed is minimised. The reactor volume below the bed serves as a vaporising zone for the liquid feed as well as an initial mixing zone for the vaporised liquid and gas feeds. The volume above the bed serves as the initial cooling stage. Undoubtedly, the reaction zone is the pivotal phase in the setup, as it processes combustible reactants under elevated operating pressure and temperature. Hence, the reactor is equipped with thermocouples and pressure transducers to guarantee that the reaction is conducted at the intended temperature and pressure.

3.2.2.2 Product separation and recovery

Following the reaction zone, the product separation section aims to enable collection of both liquid and gas products for analysis. This section starts with a heat exchanger designed to lower the temperature of the product stream exiting the reaction section to below 50 °C. This cooling is achieved using a water circulation system with water fed at ambient temperature. The pressure within the setup is controlled by a back-pressure regulator located downstream from the condenser. Subsequently, the product can be directed either towards a sampling collection line or a vent line, which are both controlled by manual valves. The sampling line is further divided into distinct points for collecting liquid and gas. Similarly, the vent line is split into a vent line for gaseous products and a storage tank for liquid products. A flow metre is in place to monitor the flow of gases in the vent route. However, in order to measure gas flow accurately, it is necessary to close the gas sampling valve. Notably, the sampling collection section is situated outside the cabinet and cannot withstand high pressures. As a safety precaution, this stage is equipped with a thermocouple, pressure transducer, and pressure relief valve to ensure the safe execution of the sampling collection process.

3.2.2.3 Setup controllers

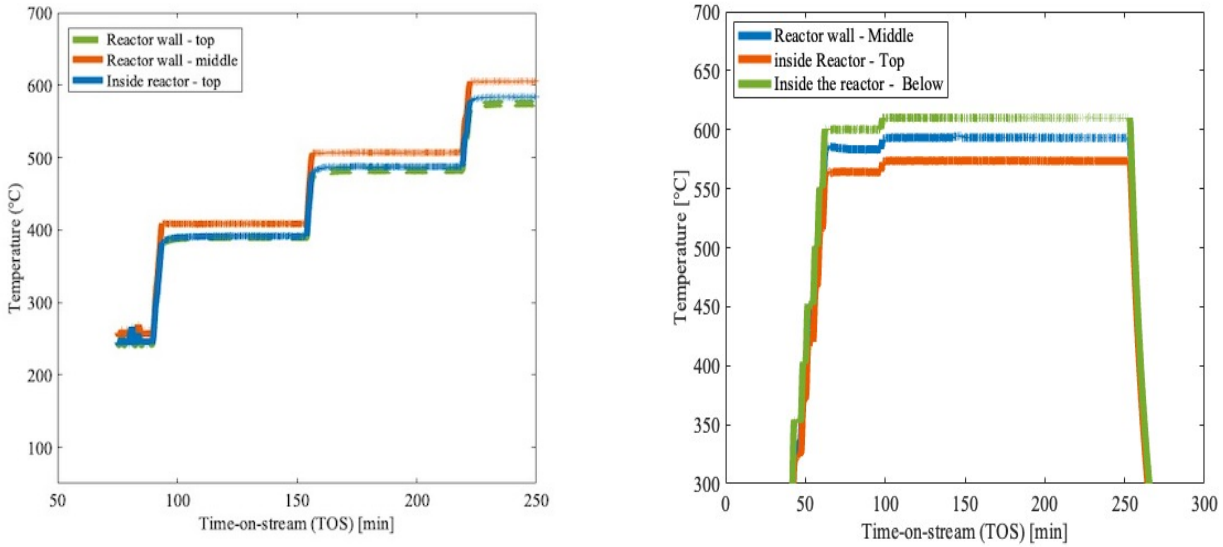
All the above-mentioned components are connected by a control panel and monitored via a LabView interface for safe and improved operation. The control panel displays pressure readings and a temperature reading inside the reactor, as well as inlet and outlet reactor temperatures. Furthermore, the syringe pump and Joule heating are powered by the control panel. For safe operation, an automated shutdown protocol is initiated if the reaction temperature exceeds the targeted temperature, which is indicated by a safety thermocouple. Therefore, the safety thermocouple location, which is positioned at the reactor wall, is critical. In addition, non-responsive LabView initiates the automated protocol to account for all hardware issues during the experiment. Manual shutdown is also designed by pressing the designated button on the control panel.

3.3 Reactor modelling

The experimental reactor was modelled using COMSOL Multiphysics to better understand the temperature profiles generated by Joule heating and possible reactions. This step was taken due to significant temperature fluctuations observed in the initial experiments, which made it difficult to maintain accurate temperature readings.

Experimentally, the reactor operates through Joule heating, powered by a Power Ten DC power supply (Model P62B-30100), where current flows between two electrodes. Initially, a single thermocouple above the catalytic bed was used, but due to overheating and unstable readings, additional thermocouples were added along the reactor wall. These thermocouples, positioned at the top, centre, and bottom of the catalytic bed, provided closer monitoring of temperature deviations. Two more thermocouples were placed at the top and bottom of the catalytic bed inside the reactor. A detailed schematic of the thermocouple positions is shown in Figure A.2.

During ethane dehydrogenation (DeH) experiments, these thermocouples revealed an axial temperature gradient, as shown in Figure 3.5. The figure shows temperature readings for experiments with and without SiC in Figure 3.5b and Figure 3.5a, respectively. Uniform temperature distribution was observed during the nitrogen ramp-up phase, but noticeable gradients appeared once ethane flow began, with reaction temperatures of 400, 500, and 600 °C. These gradients remained consistent, suggesting the reaction temperature was the main cause, with limited improvement from SiC.

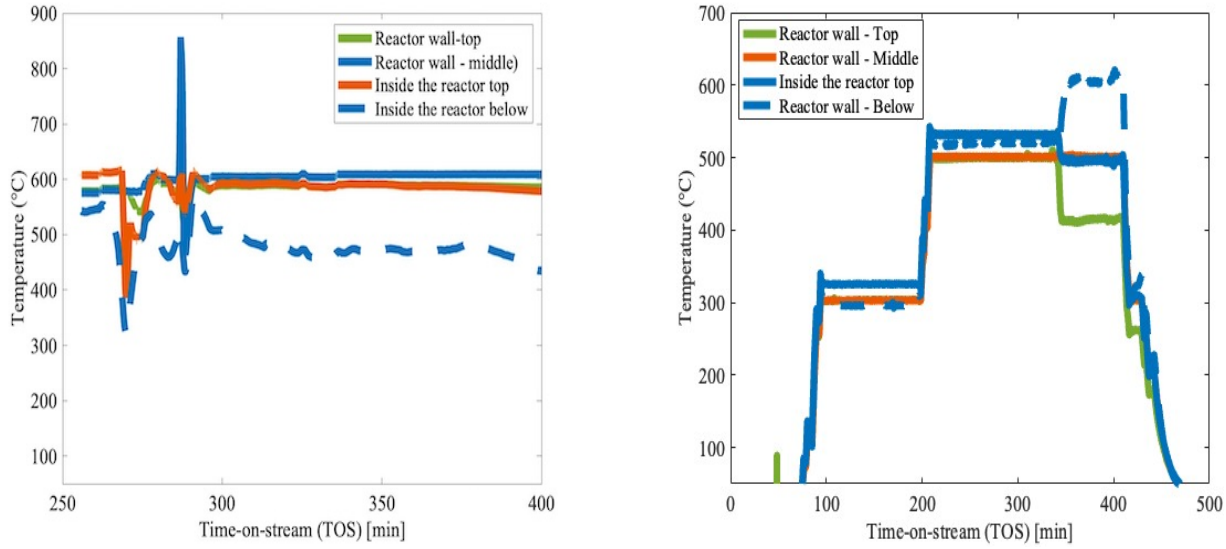


(a) Catalyst **(b)** Catalyst-SiC (1:1 weight ratio)

Figure 3.5: Temperature profile for ethane DeH experiment at different locations at $NiMo/Al_2O_3$ catalytic bed

In DeH-HDO experiments, the presence of the HDO reactant (guaiacol) further amplified the temperature gradient and instability upon reaching the catalyst bed, as shown in Figure 3.6. Temperature instability was observed without the use of SiC in Figure 3.6a. While adding SiC helped control the instability, significant temperature gradients and changes in the temperature profile still persisted as illustrated in Figure 3.6b. These gradients, combined

with temperature profile variations, posed challenges in reactor control, likely due to the endothermic and exothermic nature of the reactions and the heat generation mechanisms. Consequently, reactor modeling with COMSOL Multiphysics was used to refine operational protocols and improve temperature control.



(a) Catalyst **(b)** Catalyst-SiC (1:1 weight ratio)

Figure 3.6: Temperature profile for DeH-HDO experiment at different locations at $NiMo/Al_2O_3$ catalytic bed

3.3.1 Involved physics in COMSOL model

The model is governed by three fundamental physics: Joule heating, conduction and convection heat transfer within porous materials and fluids, and fluid dynamics. The physics are determined by a set of equations, which are solved numerically employing the finite element method. The primary aspect of the model is electric current, determined by Equation 1, which accounts for the introduction and flow of current.

$$J = \sigma(-\nabla V) + \frac{\partial D}{\partial t} + J_e \qquad \text{(Equation 1)}$$

Where σ is electric conductivity and V is the voltage potential. D is the measure of dielectric properties, assumed to be measured by the relative permittivity of the materials involved in the reaction domain. Figure 3.7 shows the voltage potential distribution along the reactor. The voltage potential demonstrates the flow of current from the lower electrode to the upper electrode, under the assumption of electrical conservation and insulation around the reactor.

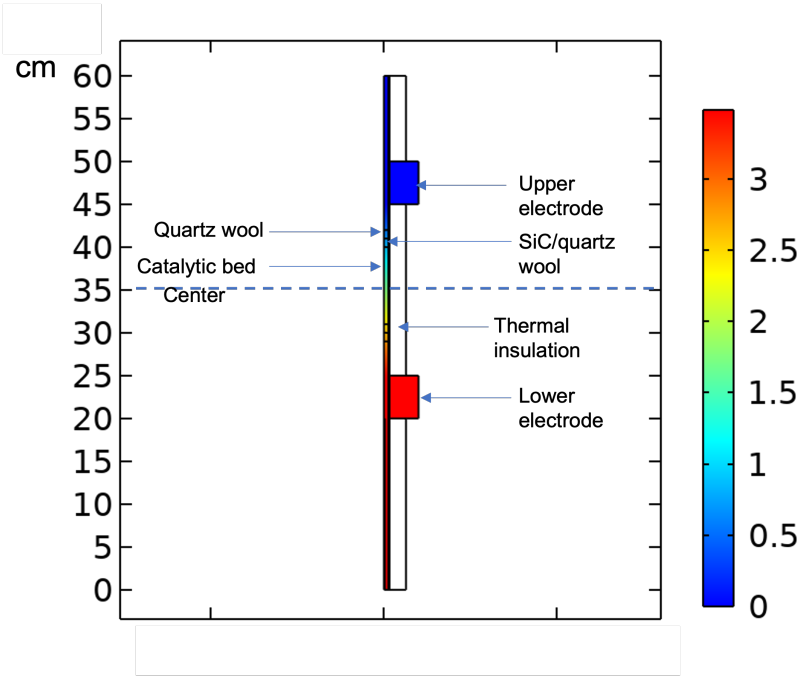


Figure 3.7: Schematic of reactor modelling depicting electrical potential distribution in voltage

The second physics is heat transfer within the fluid and porous medium, where the fluid represents the reactants and the porous medium represents the catalytic bed. These phenomena are governed by equations Equation 2, with Equation 3 and Equation 4 included to compute the heat capacity and thermal conductivity of the solid and fluid medium within the designated domains.

$$(\rho C_p)_{eff}\frac{\partial T}{\partial t} + \rho C_p u \cdot \nabla T = \nabla(\lambda_{eff}\nabla T) + Q \qquad \text{(Equation 2)}$$

$$(\rho C_p)_{eff} = (1-\tau_p)\rho_{air}Cp_{air} + \tau_p(x_1\rho_1 Cp_1 + x_2\rho_2 Cp_2) \qquad \text{(Equation 3)}$$

$$\lambda_{eff} = (1-\tau_p)\lambda_{air} + \tau_p(x_1\lambda_1 + x_2\lambda_2) \qquad \text{(Equation 4)}$$

Q represents the heat generated by the power supply, attributed to electrical resistivity, while 'u' symbolizes the flow rate. Under inert flow conditions, hydrogen serves as the fluid within a porous medium. This porous medium exhibits properties similar to $NiMo/Al_2O_3$, necessitating adjustments in density (ρ), specific heat capacity (Cp), thermal conductivity

(λ), and electrical conductivity (σ).

These physics are linked by establishing a linkage between governing equations. In the the case of electric flow and thermal transfer, 'Q' is the linked parameter. This heat source (Q) is integrated into the model as a charge density ranging from 1.0-5.0 $\times 10^{+6}$ A$\cdot m^{-3}$, correlating with the power supply from the generator.

To mimic the power supply and heating mechanism, a conditional equation is employed to deactivate electric heating once the desired temperature is reached at a specific location within the catalytic bed. This designated spot serves as the monitoring point for thermocouple measurements. Additionally, an emergency safety is implemented to the hydrocracker to avoid overshooting temperature, by terminating the power supply if the temperature in any thermocouple reaches 100 °C above the reaction temperature. Electric heating is reinstated once the temperature at this location decreases by 5-10 °C.

3.3.2 Model observations

Three key factors were explored to enhance temperature distribution and reactor control: adjustments to the power supply settings, refinement of control response, and enhancement of thermal conductivity within the reactor. These parameters collectively govern the heating rate, localise heating density, and heat transfer. Failure to enhance these aspects can lead to pronounced temperature non-uniformity over time. This complexity is further heightened when multiple reactions occur simultaneously, as reaction performance typically evolves over time. Consequently, heating parameters must be tailored accordingly to accommodate these dynamic reaction changes.

In this investigation, current flow improvement was achieved by adjusting both voltage and current to regulate the heating rate, with specific parameters of 1.0 V and 2.0 mA identified as ideal for this study. Non-improved power settings influence the temperature axial and radial gradients, which have direct effect to the reaction performance. In the model, this parameters are assigned as a charge density measured in 1.0-5.0 $\times 10^{+6}$ A$\cdot m^{-3}$. Therefore, the setting has to be studied for each investigated mixture (liquid and gas) and the feeding composition as the coupled reactions (DeH-HDO) has complex endothermic-exothermic reactions.

Moreover, the proportional–integral–derivative (PID) power supply response parameters are

controlled via LabView to manage the reaction temperature. A comprehensive description of the control mechanism is given in Sivena's PhD thesis [146]. The PID for the power supply is kept constant in this work at P=1000, I=0.0 and D=0.01. The importance of PID to ensure homogeneous temperature distribution while maintaining the designed reaction temperature. Inadequate PID selection leads to localised heating, and temperature overshoot caused by gain and damping control dynamic. In the model, PID is adjusted by the the temperature deviation range, where the supply switches on/off. Localise heating in influenced by the combining by all the parameters. PID has to ensure sufficient timing for heat transfer between reactor wall and temperature at the middle of the reactor - where temperature is measured.

Table 3.1: The impact of power supply and response on temperature distribution for 30-min run after achieving a steady state in a reaction zone containing NiMo/Al_2O_3

Case	Power[1] [Normalised]	Temp. deviation [°C]	Temp. distribution [°C]
A.1	1.0	5.0	28
A2	1.0	7.0	severe localised heating[2]
A.3	1.0	10	severe localised heating
A.4	1.0	15	55
B.1	0.5	10	33
B.2	1.1	10	38
B.3	0.9	10	40
B.4	1.5	10	35

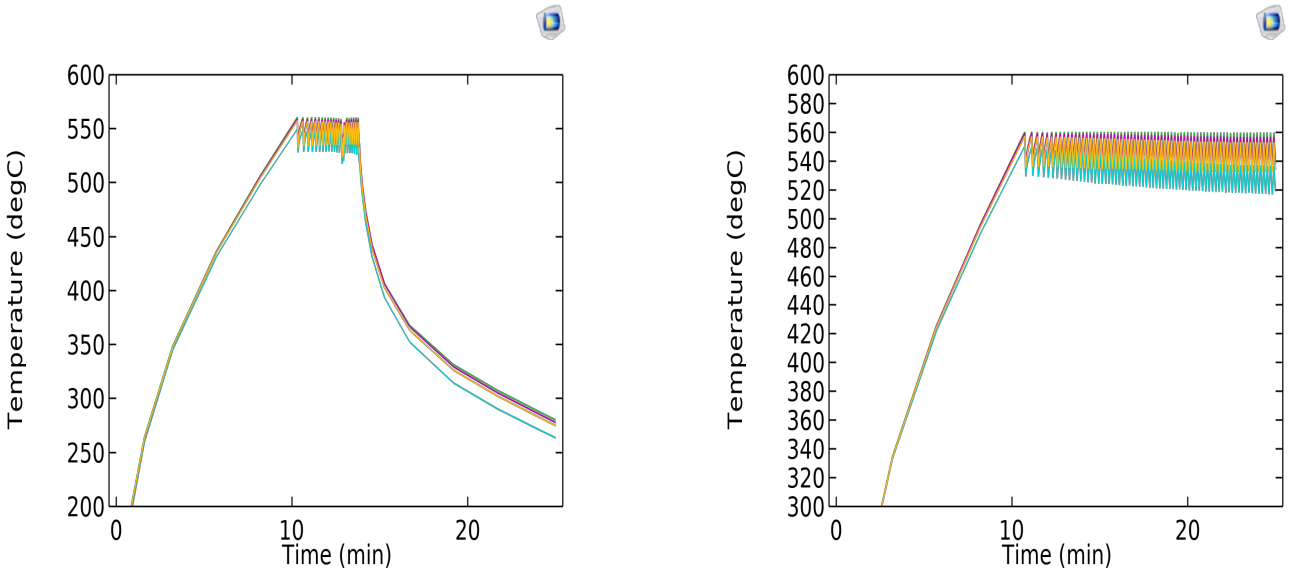
[1] Power is represented by charge density of 4.5 $\times 10^{+6}$ A$\cdot m^{-3}$ for a base-case, where normalisation it relative to the base-case.
[2] Severe localised heating denotes a scenario where the temperature at the wall surpasses the safe operating temperature.

In Table 3.1, the term "severe localised heating" denotes a scenario where the temperature at the wall surpasses 650 °C (the safety temperature), while the temperature inside the catalytic bed decreases due to slow heat transfer from the wall to the interior. An illustration of a severe localised heating scenario is provided in Figure 3.6a, where the temperature inside the reactor drops to 250 °C, despite the targeted temperature being 550 °C. In this case, the power supply continuously adds energy, resulting in localised heating in the reactor wall. Table 3.1 demonstrates that both temperature deviation and power supply influence each other, with no independent correlation for each parameter with temperature distribution. Therefore, tuning these parameters is crucial. Nonetheless, a temperature range of 5.0 °C is considered suitable for setting PID control.

To mitigate the risk of localised runaway reactions, enhancing thermal conductivity inside the reactor is identified as a critical parameter for improving temperature distribution. The

objective is to facilitate more efficient heat transfer from the reactor wall to the catalytic bed. When the controlled temperature is within the bed, localised heating can occur if the thermal conductivity lags behind the heating response, resulting in significant temperature gradients from the wall to the centre of the catalytic bed.

One strategy to improve thermal conductivity involves incorporating SiC into the porous medium of the catalyst bed. This modification aims to enhance the thermal conductivity of the catalytic medium. Specifically, the thermal conductivities for SiC and the catalyst are specified as 19.2 and 130 J·kg-K^{-1}, respectively. Detailed calculations for determining the properties of the catalytic medium are provided in Appendix A.3. Figures 3.8a and 3.8b operate under Case A.3 conditions but with two different catalytic bed compositions. The addition of SiC offers notable advantages in maintaining the catalytic bed temperature due to its high thermal conductivity.



(a) Catalyst

(b) Catalyst-SiC (1:1 weight ratio)

Figure 3.8: The temperature profile at various locations within the NiMo/Al_2O_3 catalytic bed, as generated by COMSOL.

The periodic oscillations in the reaction temperature, as shown in Figure 3.8, result from continuous adjustments made by the model's controller. This controller mimics the behaviour of the experimental PID system by activating or deactivating the heating element when the temperature deviates by 5.0 °C from the set point. This control mechanism was incorporated into the model to replicate the experimental behaviour, as improper PID tuning can adversely affect the temperature profile. The oscillatory pattern observed in the model closely mirrors that seen in the experimental temperature profiles, thereby enhancing the accuracy of the model's predictions.

The selection of the 1:1 catalyst-to-SiC ratio is based on an analysis of different SiC loadings, as shown in Table 3.2. At a temperature deviation of 10 °C, increasing the SiC loading significantly reduces the temperature variation across the catalytic bed, from a 40 °C spread at 7% SiC loading (C.5) to 30 °C at 50% loading (C.2). Notably, in a similar condition with no SiC (A.3), severe localised heating was observed. While no improvement in temperature distribution was seen at a 5.0 °C deviation, SiC remains crucial because even a slight increase in temperature deviation to 7.0 °C without SiC resulted in localised heating. In contrast, with 50% SiC, no localised heating occurred even with a temperature deviation of up to 10 °C.

Table 3.2: The impact of SiC addition on temperature distribution for 30-min run after achieving a steady state in a reaction zone containing $NiMo/Al_2O_3$

Cases	SiC loading	Power [Normalised]	Temp. deviation [°C]	Temp. distribution [°C]
C.1	50%	1.0	5.0	28
C.2	50%	1.0	10	30
C.3	25%	1.0	10	33
C.4	13%	1.0	10	severe localised heating
C.5	7%	1.0	10	40

[1] Power is represented by charge density of 4.5 $\times 10^{+6}$ A$\cdot m^{-3}$ for a base-case, where normalisation it relative to the base-case.
[2] Severe localised heating denotes a scenario where the temperature at the wall surpasses the safe operating temperature.

Experimentally, while Figure 3.5a depicts a seemingly smooth temperature profile for ethane DeH, it lacks precise insight into the actual reaction temperature. To address this limitation, a redesign of the reactor feed-line was implemented, enabling the installation of a thermocouple below the catalyst bed. This modification provides a more accurate indication of the reaction temperature, as shown in Figure 3.5b. Notably, the temperature within the reactor below the catalytic bed highlights the endothermic nature of the reaction, with temperatures surpassing those observed above the catalytic bed. In addition, Figure 3.6b shows DeH-HDO with SiC where the temperature profile is better controlled and stable. The change in temperature gradient profile is attributed to the addition of endothermic reaction which is expected to influence the outlet temperature corresponding to the degree of endothermicity.

Consequently, based on the reactor model, the experimental catalyst bed is physically mixed with SiC to mitigate the axial temperature gradient resulting from poor thermal conductivity. Additionally, as depicted in the figure, the coupled DeH-HDO temperature is influenced

by the integration of both exothermic and endothermic reactions. Thus, obtaining a temperature reading above the catalyst bed (the outlet temperature) is considered inappropriate. Consequently, an additional thermocouple is installed below the catalyst bed and designated as the primary indicator of reaction temperature.

3.4 Mass balance and product analysis

The performance of the DeH-HDO coupling is evaluated by quantifying gaseous and liquid products, as well as solid deposition. In HDO experiments involving the use of molecular hydrogen, all resulting compounds are derived from hydrodeoxygenation (HDO). However, during DeH-HDO experiments, ethane DeH contributes to gaseous products and carbon deposition, in addition to HDO. Nevertheless, liquid products are presumed to originate from HDO unless specified otherwise.

In ethane DeH experiments, it is assumed that the conversion of ethane to a liquid product such as benzene via dehydroaromatisation (DeHA) does not occur. This assumption is derived from the lack of any visible evidence of liquid product generation in ethane conversion experiments conducted in the absence of bio-oil feed. Therefore, due to the complexity of the coupled reaction system, a weight-based mass balance with over 75% recovery was considered acceptable, as some materials (such as water) could not be measured with the available methods. However, aromatic-based mass balances achieved over 95% recovery, assuming that the solids formed on the catalyst surface were primarily polyaromatics. An overview of the extracts obtained from the reaction result is provided in Figure 3.9, and it is further explained in the following sections.

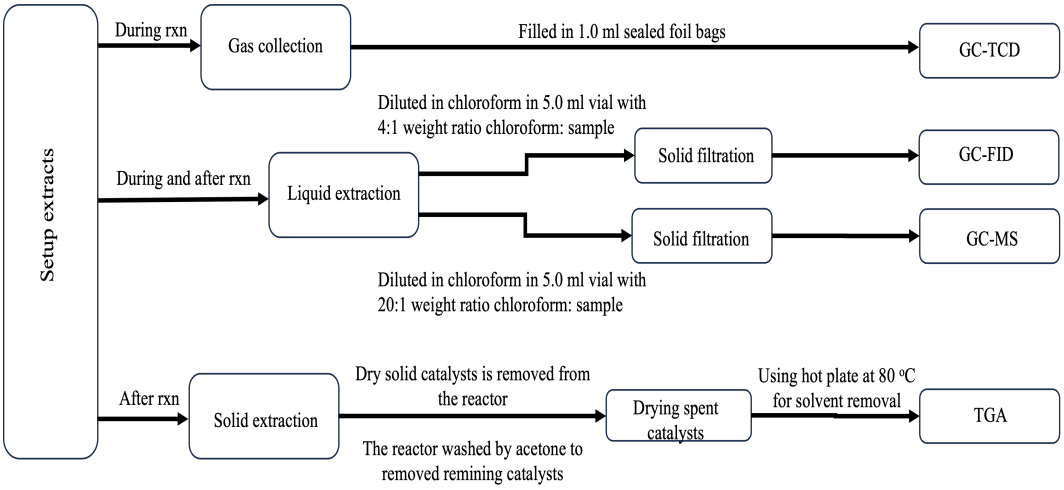


Figure 3.9: Reaction product extracts collection, preparation and quantification techniques

3.4.1 Gaseous product: GC-TCD

The gaseous product is collected in gas bags and analysed using a PerkinElmer Clarus 500 gas chromatograph (GC) with a thermal conductivity detector (TCD). A Carboxen TM 1010 PLOT capillary column supplied by SUPELCO is employed as it is capable of separating permanent gases, alkanes, and alkenes flowing with Ar as the carrier gas. TCD detector and injector temperatures are both set to 150 °C. Data obtained from TCD are analysed to quantify the feed and product concentrations. The concentrations are calculated based on calibration curves created for all of the available gases in the product. More information on the instrumentation and calibration curve can be found in Appendix B.1. Feed conversion is evaluated by Equation 5. Product selectivities are measured based on concentration ratios to the feed concentration.

$$X_j = \frac{F_{in,j} - [j]F_{out}}{F_{in,j}} \qquad \text{(Equation 5)}$$

$$S_{C_2H_4} = \frac{[C_2H_4]}{\sum[HC]_i} \qquad \text{(Equation 6)}$$

Where X_j refers to the feed conversion, which is hydrogen or ethane in this study. F_{in} and F_{out} refer to the inlet and outlet flow rates, respectively, measured in mL·min^{-1}. Ethylene selectivity is calculated based on Equation 6, where [HC] refers to the concentration of generated hydrocarbon molecules: methane, ethylene, propane, and propylene. In this work, the degree of DeH is also evaluated based on the ethylene-to-ethane ([C_2H_4][C_2H_6]$^{-1}$, C_2"/C_2) volumetric ratio in the product (yield). It is also used to capture possible ethane production from the liquid phase caused by the de-methylation mechanism. The ratio also avoids the complexity of quantifying ethane in conversion in the coupled DeH-HDO.

3.4.2 Liquid product: GC-FID

Liquid samples are continuously collected in 5 mL vials and analysed using a Clarus 500 gas chromatography system from PerkinElmer, equipped with a flame ionisation detector (FID) and an HT5 column from SGE. The column dimensions are 25 m in length, 0.32 mm in diameter, and 0.1 µm in thickness. To facilitate better detection and separation in the column, the liquid product is diluted in acetone. The oven and detector temperatures are

set to reach up to 300 °C and 250 °C, respectively. Analysis of the collected liquid samples is conducted to calculate the conversion (Equation 7) and selectivity (Equation 8), based on reactants and products in the outlet. Additional information on the instrumentation and calibration curves can be found in Appendix B.2. The liquid inlet in all experiments comprises 100% guaiacol, unless indicated.

$$X_{GUA} = (1 - [GUA]_{out}) \times 100 \quad \text{(Equation 7)}$$

$$S_i = \frac{[i]_{out}}{1 - [GUA]_{out}} \times 100 \quad \text{(Equation 8)}$$

Where X_{GUA} represents guaiacol conversion, and S_i denotes the selectivity of component i. [i] and $[GUA]_{out}$ represent the normalised concentrations of targeted components in the liquid product. Note, this conversion excludes the conversion to produced solids: heavy condensate and carbon deposition. This approach is used due to non-linear carbon formation during the run. In addition, there are two sources for solid formation, alkane DeH, and guaiacol HDO, which increase the difficulty to distinguish the carbon deposition source. Undesirable solid formation is measured independently, as discussed next.

To identify components present in liquid samples observed by FID, a Nexis GC-2030 SHIMADZU GC equipped with an MS detector is used. The samples are filtered and diluted in a 20:1 weight basis chloroform-to-sample ratio. The mass spectroscopy (MS) detector is operated with a mass range of 40 - 300 m/z. The peaks in the MS spectrum are identified using software provided by SHIMADZU containing built-in libraries. The GC is also equipped with a FID detector, where the peaks are matched and compared with the main GC-FID used in this work, as explained in Section 3.4.2. The GC method program can be found in Appendix B.3.

The degree of HDO is also measured in terms of oxygen per aromatic ring (O:A) ratio, indicating the number of oxygen atoms per aromatic ring present for each component in the product and adjusted based on the selectivity of each component. This is referred to as O:A in the product (on a selectivity basis), where the liquid O:A (on a yield basis) accounts for unreacted bio-oil model compound, mainly guaiacol.

$$OA_{product} = \sum S_i(F_i) \quad \text{(Equation 9)}$$

$$OA_{liquid} = \sum X_{GUA} S_i(F_i) + 2(1 - X_{GUA}) \quad \text{(Equation 10)}$$

Where F_i is the ratio for oxygen-per-aromatic in component i. For instance, guaiacol and phenol have F of 2.0, and 1.0, respectively. The peaks in the GC-FID are identified using a GC-MS. Information of used GC-MS is available in Appendix B.3.

3.4.3 Solid deposition: TGA

Following the experimental run, the catalytic bed is manually extracted from the reactor. Subsequently, a solvent washing process is conducted on the spent catalyst. The subsequent step involves placing the recovered spent catalyst in an oven set to 80 °C to facilitate the evaporation of any residual solvent. Once the solvent has evaporated, the collected and dried spent catalyst undergoes analysis using TGA. This analysis aims to quantify the deposition in terms of condensate formation, denoted by Equation 11, and the extent of coke formation, represented by Equation 12. Condensate deposition refers to solid deposition that is desorbed from the catalyst surface in an inert environment (nitrogen flow) up to 500 °C, whereas coke deposition is deposition that requires combustion under an air flow up to 800 °C.

$$\text{Condensate}(g/g_{cat}) = \frac{M_i - M_h}{M_c - W_{oxi}} \quad \text{(Equation 11)}$$

$$\text{Coke}(g/g_{cat}) = \frac{M_h - M_c}{M_c - W_{oxi}} \times 100 \quad \text{(Equation 12)}$$

Where M_i corresponds to the initial weight of the spent catalyst after the moisture removal step. M_h represents the weight of the spent catalyst after heating up to 500 °C in an inert environment, and M_c indicates the remaining weight of the spent catalyst after combustion using an air flow of 40 mL·min^{-1}. W_{oxi} represents the increase in catalyst weight due to oxidation measured by oxidising reduced catalysts in TGA. A detailed description of TGA

method and a sample of the obtained weight and temperature profile is available in Appendix B.4.

3.4.4 Data Reliability and Repeatability

In this thesis, data reliability was ensured through continuous and periodic calibration of analytical instruments using calibration standards for the TCD, FID, and TGA. Appendix B provides more details on the calibration procedures. To ensure repeatability, each experiment and analytical measurement was performed in duplicate. In cases where significant deviations occurred between measurements, a third run was conducted for validation. Consequently, all reported data represent the average of at least two measurement runs, ensuring reproducible outcomes.

3.5 Solid catalyst characterisation techniques

3.5.1 X-ray diffraction (XRD)

XRD analysis was conducted in PANalytical X'Pert Pro X-ray diffractometer equipped with Cu Kα radiation (λ = 1.5406 Å). The XRD is used to identify crystalline phases of metal oxides. The XRD was operated at voltage and current of 40 kV and 20 mA, respectively. The data collection set range of 5° to 90° with a step size of 0.033° and a scan speed of 2° min^{-1}.

3.5.2 X-ray fluorescence (XRF)

XRF analysis was conducted using to quantify metal and metal oxides of both catalyst support and active site using Epsilon 3 benchtop XRF spectrometers from PANalytical. The used XRF features a high resolution silicon drift detector. The XRF is equipped with metal-ceramic tube and used energy setting is 20 kV and 2 mA.

3.5.3 Brunauer-Emmett-Teller (BET)

Micromeritics TriStar 3000 surface area and porosity analyzer was used with nitrogen as adsorbent for the isotherm measurement to evaluate surface area and porosity characteristic. The TriStar software calculates pore size assuming uniform cylindrical pores using measured area and volume (4V/A).

3.5.4 Scanning Electron Microscopy – Energy Dispersion X-Ray (SEM-EDS)

A Zeiss Auriga SEM is used to visualise coke formation on spent catalyst samples. The SEM is fitted with an Oxford Instruments INCA dispersive x-ray spectroscopy (EDS) to conduct

chemical composition analysis to determine carbon formation on active sites. The range of used SEM resolution and magnification is 10-20 nm, x1000-250,000, respectively.

3.6 Operating conditions

The determination of process parameter ranges in the experimental activity is guided by considerations of the experimental rig limitations, principles of thermodynamics, and insights from literature reviews. Chapter 2 discusses that the temperature range of 250-350 °C is the most investigated for HDO due to hydrogenation mechanisms, whereas alkane DeH typically initiates at higher temperatures, around 450 °C. Accordingly, a temperature range of 500-600 °C is selected for the DeH-HDO coupling, where ex-situ HDO experiments conducted across temperatures ranging from 300 to 600 °C. The influence of pressure on the HDO reaction mechanism is significant, as it shifts from the hydrogenation of aromatic rings followed by hydrogenolysis of oxygenated functional groups to a direct hydrogenolysis process based on thermal equilibrium. Additionally, preliminary experiments have shown that temperatures exceeding 250 °C can lead to frequent condensation in the rig due to liquid condensation, attributed to the low melting points of guaiacol and phenol (26°C and 40 °C, respectively, at atmospheric pressure), which decrease further under elevated pressure. Any heating failure may lead to the accumulation of HDO feed, causing blockages in the rig. Catalyst loading plays a pivotal role in conversion kinetics, where insufficient loading can hinder conversion rates, while excessive loading may lead to the formation of undesired by-products. In the context of DeH-HDO, inadequate catalyst loading may impede the efficiency of the HDO process. Conversely, excessive catalyst loading, despite accelerating hydrogen production rates, can promote undesirable side reactions such as excessive DeH of alkanes to alkynes or facilitate the cracking mechanism. Moreover, ensuring homogeneous heat distribution throughout the catalytic bed is critical for ensuring data accuracy and reliability. Higher catalytic loading may compromise temperature measurement precision, particularly in systems like the hydrocracker rig, which employs Joule heating technology and may affect temperature distribution in reactors with high loading.

Flow rates of liquids and gases are expressed in terms of moles per hour to accommodate volume changes during phase transitions for liquids. The use of hours to denote time aligns with gas and liquid space velocities, quantified as the molar rate per catalyst weight on an hourly basis. Controllers were custom-built to regulate volumetric flow rates, ensuring

Table 3.3: List of varied parameters for HDO and DeH experiments

Operating parameters		Conventional HDO "ex-situ"	DeH-HDO "in-situ"
Liquid space velocity	$mol \cdot g_{cat}^{-1} \cdot h^{-1}$	0.05 - 1.00	0.05 - 1.00
Liquid flow rate	$mL \cdot min^{-1}$	0.25 - 2.0	0.10 - 2.0
Gas space velocity	$mol \cdot g_{cat}^{-1} \cdot h^{-1}$	0.10 - 2.7	0.05 - 0.5
Gas flow rate	$mL \cdot min^{-1}$	100 - 1000	50 - 200
Temperature	°C	350 - 600	500 - 600
Pressure	bar	1.0 - 25.0	0.5 - 1.0
Catalyst loading	g	1.0 - 3.0	1.0 - 5.0

consistency in both in-situ and ex-situ evaluations, with conversions to moles as necessary. In Table 3.3, the term "conventional" denotes ranges specified for hydrogen usage as a hydrogen source, while "in-situ" refers to the utilisation of alkane, specifically ethane, as a hydrogen source in this context.

Chapter 4

The Potential of HDO of Bio-oil Derivatives via In-situ Hydrogen Generation

4.1 Introduction

This chapter is dedicated to assessing the feasibility of coupling alkane DeH and bio-oil HDO within a single catalytic bed. Given the limited literature on this specific coupling, the chapter serves as a foundational exploration to understand its potential. The coupling focuses on the two reactions involving ethane and guaiacol as illustrated in Reactions 6 and 7. Guaiacol is selected as a representative model compound for lignin-derived mono-aromatics obtained from fast pyrolysis, notable for its two distinct oxygenated functional groups: methoxy and hydroxy [37]. Traditionally, HDO processes have operated at high pressures of molecular hydrogen to eliminate these oxygenated functional groups [95]. However, recent trends favour atmospheric pressure processing [24], [85], [92], [96], [142], [147], which aligns well with the requirements of DeH-HDO integration. This shift arises from the favourable equilibrium conversion at low pressures and high temperatures, making atmospheric pressure conducive to the DeH-HDO framework [82], [140].

$$C_2H_6 \leftrightarrow C_2H_4 + H_2 \qquad \Delta H = +136\,\mathrm{kJ{\cdot}mol^{-1}} \tag{R6}$$

$$C_7H_8O_2 + 3\,H_2 \rightarrow C_6H_6 + 2\,H_2O + CH_4 \qquad \Delta H = -206\,\mathrm{kJ{\cdot}mol^{-1}} \tag{R7}$$

The proposed coupling theoretically enhances both reactions by continuously removing hy-

drogen produced via alkane DeH through HDO. The consumption of hydrogen drives the equilibrium conversion towards increased hydrogen and ethylene formation. This mechanism emulates membrane reactors, where alkane DeH has exhibited potential due to hydrogen removal. Several published works have reported surpassing the equilibrium conversion of alkane DeH through hydrogen removal to the permeate side in membrane reactors [19], [20]. Moreover, this coupling aims to enhance HDO by generating reactive hydrogen from ethane (C_2H_5-H), which requires lower thermal dissociation compared to molecular hydrogen ($H-H$). Figure 4.1 illustrates the potential hydrogen transfer between the two reactions within a single catalyst.

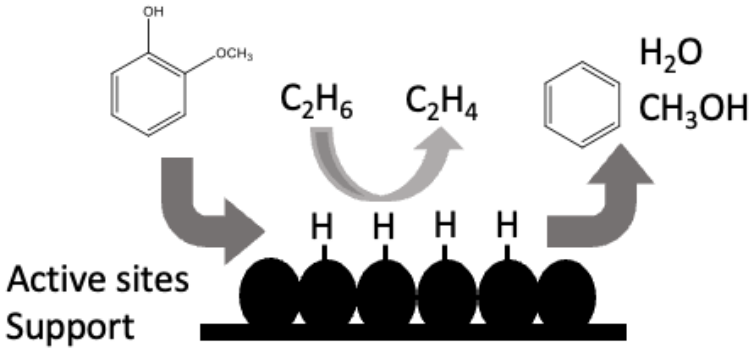


Figure 4.1: A schematic of the combined reaction of in-situ HDO via alkane DeH of ethane

In order to accomplish the coupling objective, four distinct catalysts are examined in this chapter: PNiMo/Al_2O_3 (PNiMoAl), NiMo/Al_2O_3 (NiMoAl), MoO_3 (MoO_3), and Cr/Al_2O_3 (CrAl). These catalysts are chosen based on their reported effectiveness, primarily for HDO, with the exception of CrAl, which serves as the catalyst for ethane DeH as discussed in Chapter 2.

4.1.1 Chapter structure

This chapter commences by understanding the potential advantages of studying this coupling in Section 4.1.2. Experimentally, to establish a baseline for utilising the catalysts in the hydrocracker configuration described in Section 3.2 for conventional HDO, an investigation into the HDO process under elevated pressures of up to 25 bar and a moderate temperature of 400 °C was carried out and is presented in Section 4.3. Section 4.2 demonstrates catalyst preparation and characterisation. Similarly, to establish a baseline for ethane DeH, the chapter explores thermal DeH to ascertain the minimum temperature required for the reaction and assess the catalyst performance in Section 4.4.

Subsequently, the chapter analyses the experimental outcomes concerning the tandem between HDO and DeH in both thermal and catalytic setups, utilising the previously mentioned catalysts: NiMo-based catalysts in Section 4.5.2, MoO_3 in Section 4.6, and CrAl in Section 4.7. The study compares externally supplied molecular hydrogen, referred to for short as "ex-situ" hydrogen, with hydrogen generated in ethane DeH, termed "in-situ" hydrogen, as the catalysts are examined. Given that this coupling represents a novel approach to creating an effective synergy between two reactions with distinct thermodynamic equilibrium behaviours as a function of temperature and pressure, a range of operating conditions are considered.

4.1.2 Understanding the coupling potential

4.1.2.1 Thermodynamic effects on the DeH-HDO coupling

The integration of alkane DeH with bio-oil HDO ("in-situ" HDO) poses challenges in terms of thermodynamics since each mechanism requires a different pressure and temperature range. Alkane DeH favours low pressure ($\leq$1 bar) and high temperature to maximise alkenes and hydrogen production, as shown in Figure 4.2. Generally, the longer the alkane chain, the lower the temperature requirement to reach acceptable DeH conversion. However, longer alkanes carry a higher possibility of alkane cracking producing undesirable alkanes and methane caused by by the lower energy dissociation energy for C-C for larger alkanes [125]. The cracking products are undesirable since they consume or limits hydrogen formation that is required for HDO. For example, using propane for alkane DeH as an H-donor might produce less hydrogen if propane undergoes cracking mechanisms. In summary, although ethane requires a higher temperature, it has a better H/C ratio, its side reaction is limited to ethane cracking into methane, and it is relatively easier to study for concept validation.

On the contrary, the process of HDO of oxygenated aromatics follows the hydrogenation of the aromatic ring prior to hydroxy group removal. This order is due to the dissociation energy of aromatic-OH requiring higher energy than cyclohexane-OH. Therefore, phenol-to-cyclohexanol hydrogenation favours low temperatures and high pressure from a thermodynamic perspective. Additionally, from a thermodynamic perspective, phenol, as the simplest oxygenated aromatic, requires 3 moles of hydrogen, which are limited by alkane DeH even at high temperatures and low pressure systems. Therefore, thermally, integrating both reactions is challenging in the absence of a catalyst. Ideally, the required catalyst or catalytic system must exhibit both activity and selectivity for the involved reactions. Initially, a cat-

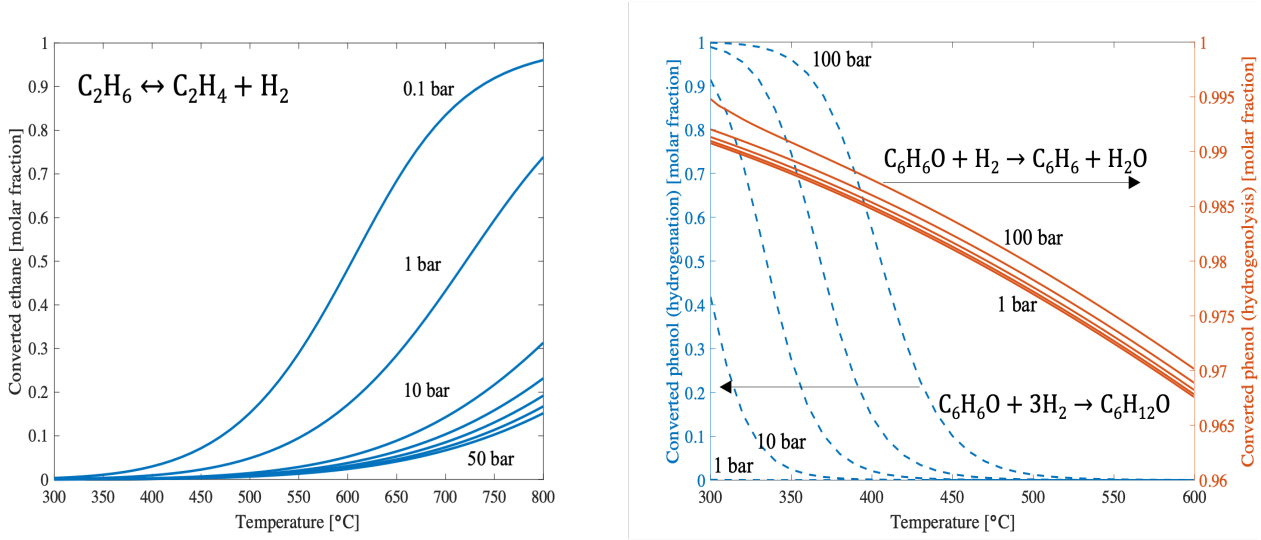


Figure 4.2: Thermodynamic analysis of ethane DeH, and phenol hydrogenation and hydrogenolysis at different operating temperatures and pressures using Peng-Robinson model in Aspen Plus®

alytic system that can selectively drive ethane conversion towards ethylene and hydrogen instead of methane formation by C-C bond cleavage. Theoretically, methane doesn't only affect the product value of ethane DeH but also consumes hydrogen, hence restricting HDO.

Furthermore, the required catalytic system must be active and selective for HDO by deriving the reaction to remove oxygenated functional groups directly to BTX and limiting hydrogenation-deoxygenation-dehydrogenation (indirect HDO). The indirect HDO consumes a larger amount of hydrogenation and adds another type of product: saturated aromatics. Thus, an adequate catalytic system is critical to selectively maximise ethylene and hydrogen from the alkane DeH and direct guaiacol to the deoxygenation of aromatic rings without causing ring saturation.

4.1.2.2 Beyond thermodynamic limitations

This section investigates the synergistic effects of alkane DeH and bio-oil HDO using a COMSOL Multiphysics model. The model uses ethane alkane DeH to ethylene and hydrogen and phenol HDO to benzene. Assuming independent kinetics based on published activation energy and reaction constants, the model aims to visualise the improvement in alkane conversion with continuous hydrogen consumption (Figure 4.3). Venkatesan et al. reported detailed kinetics parameters for HDO of oxygenated aromatics including phenol in a zeolite catalyst [148]. At 600 °C, the figure shows that a low phenol-to-ethane molar ratio limits phenol conversion to benzene, despite hydrogen presence. Operating in adiabatic mode at this temperature results in limiting ethane conversion to 24%.

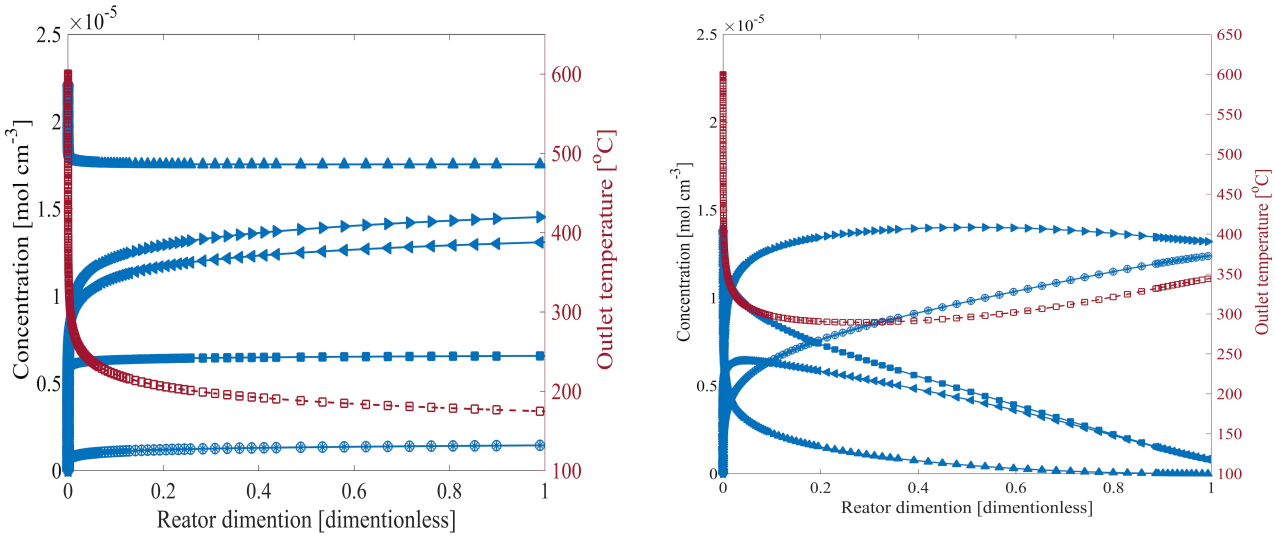


Figure 4.3: The effects of operating DeH-HDO in a single reactor bed using first order reaction for each reaction independently using COMSOL Multiphysics: ethane (▲), ethylene (►), hydrogen (◄), phenol (■), benzene (◯), water (★) and outlet temperature (□)

Increasing the phenol-to-ethane ratio to 1.0, while maintaining identical reaction kinetics leads to notable improvements in ethane and phenol conversions, along with a higher hydrogen consumption rate. Additionally, the higher phenol flow resulting in an increased degree of HDO leads to a significant enhancement in the net energy consumption across the reactor, as demonstrated by the outlet temperature in Figure 4.3. Furthermore, Figure 4.4 studies outlet reaction temperature with an increased phenol-to-ethane ratio. Hence, determining the experimental condition is necessary to maximise the synergistic effects. In summary, the integrated reactions exhibit synergistic effects that include thermal and material benefits shown by outlet reaction temperature and alkane conversion, respectively.

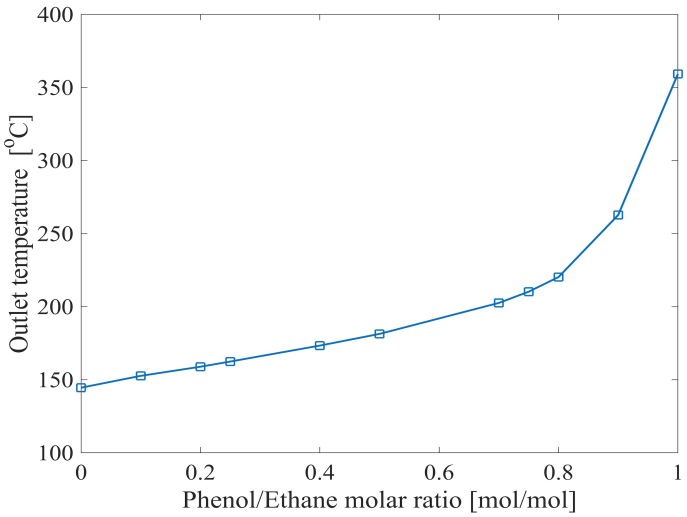


Figure 4.4: Outlet temperature of coupled DeH-HDO in a single catalytic bed using at different phenol/ethane molar ratio calculated by COMSOL Multiphysics

4.2 Catalyst preparation and characterisation

The catalytic bed is prepared with the aim of obtaining good reactivity from thermal and kinetic perspectives. For thermal axial uniformity, the catalytic bed consists of quartz wool layers sandwiching the catalyst bed to preserve a specific position where the joule heating temperature profile is flat. From a kinetics perspective, all catalysts were crushed and sieved to sustain a specific particle size range of 150-212 μm, unless indicated otherwise, to mitigate mass transfer limitations. Prior to the experiment, nitrogen and hydrogen were used to pre-treat and activate the catalyst, respectively. For moisture removal, nitrogen circulated through the catalytic bed at a rate of 8.2 mmol·min^{-1} and a temperature of 200 °C for one hour. The reactor was then heated at a rate of 20 °C min^{-1}. Next, the catalytic bed underwent two hours of in-situ hydrogen reduction at the reaction temperature to activate the catalyst and ensure that the oxide form of the metal oxide catalyst does not initiate an oxidation reaction.

This work considers the impact of phosphorus (P) on alkane DeH performance to gain insights into coke formation resulting from both reactions. Additionally, MoO_3 is examined due to its significant relevance to HDO. All catalysts undergo crushing and sieving to attain the desired particle size. The employment of high-loading metal catalysts (as shown in Table 4.3) broadens the range of active sites for HDO and mitigates the effect of support acidity, which could lead to increased coke formation. Moreover, this chapter investigates the utilisation of a CrAl catalyst for alkane DeH to elucidate its role in the coupled system.

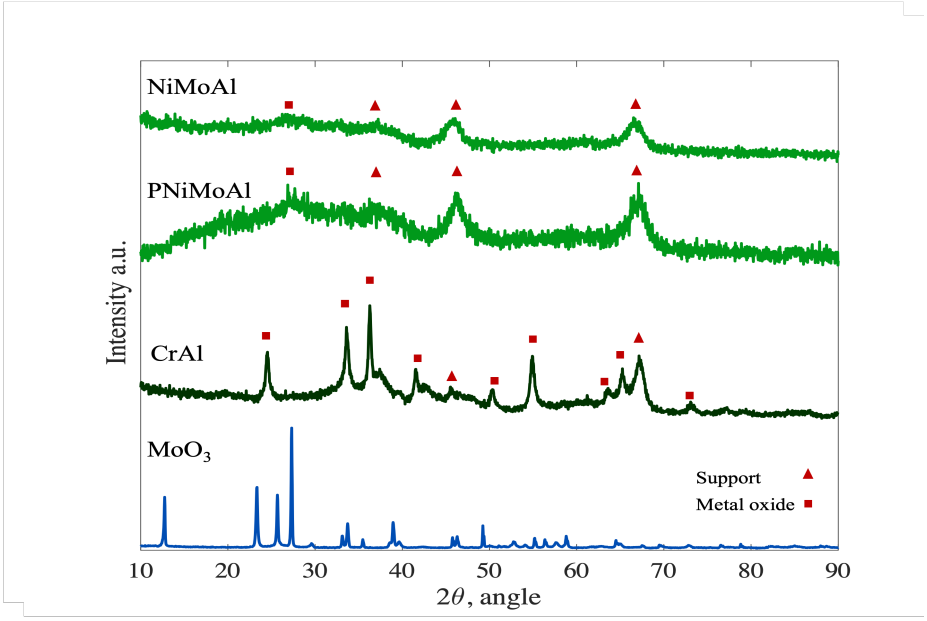


Figure 4.5: XRD for investigated catalysts in this chapter: MoO_3, NiMo/Al_2O_3 (NiMoAl), and Cr/Al_2O_3 (CrAl) and P-NiMo/Al_2O_3 (PNiMoAl).

The obtained XRD patterns for the investigated catalysts reveal the presence of active sites and the support material. For Ni-Mo supported on alumina, the XRD pattern indicates that the catalyst is amorphous, despite the high metal oxide loading, in contrast to MoO_3, where the crystalline structure is observed. The XRD analysis confirms that Ni-Mo is supported on γ-alumina, as evidenced by peaks at θ angles of 46°and 68°, which have also been observed in other studies [149]–[151].

Despite the amorphous nature of Ni-Mo catalyst, the molybdenum oxide phase is identified by a characteristic peak at 28°, as seen in MoO_3 and consistent with the XRD analysis conducted by Zhang et al. for Ni-Mo catalyst supported on alumina [150]. The interaction between Ni and Mo in the $NiMoO_4$ phase is evident from a single peak observed at 14.3°, although another peak around 29° could not be detected [151], [152]. Furthermore, NiO could not be detected due to its relatively low loading, which does not rule out the presence of NiO before reduction, as it predominantly converts to $NiMoO_4$ after reduction. XRD analysis of the bulk MoO_3 utilized in our study did not reveal any signs of oxide phases like MoO_2 or Mo_4O_{11} based on peaks provided by [147]. These specific phases are formed during the pre-reduction process employing hydrogen, and they are of paramount importance for HDO due to the significant role played by oxygen vacancies in the reaction [96], [147]. Zhang et al. concluded that oxygen vacancy is the active site for the hydrogenolysis of phenol to benzene [147]. Non-reduced MoO_3 has weak HDO compared to H_2-treated catalyst [147].

Table 4.1: Physicochemical properties of investigated catalysts in this chapter

		BET surface area ($m^2 \cdot g^{-1}$)	Average volume of pores ($m^3 \cdot g^{-1}$)	Average pore diameter (nm)
$PNiMo/Al_2O_3$	PNiMoAl	127.0	0.38	11.4
$NiMo/Al_2O_3$	NiMoAl	181.1	0.58	9.2
MoO_3	MoO_3	2.70	0.01	3.3
Cr/Al_2O_3	CrAl	53.5	0.22	14.9

According to the XRF measurements, the phosphorus modified NiMo has a higher concentration of metal oxide (active site) on a weight basis. This results in a lesser amount of acidic alumina support, as shown in Table 4.3. The increase of metal oxide loading leads to a decrease in the BET surface area and the average volume of pores for the PNiMo catalyst due to the existence of active sites on the highly porous alumina substrate. Consequently, the reactivity results of both catalysts are influenced by the presence of various, more active sites and a less acidic support, as well as the impact of phosphorus modification. Moreover,

this phenomenon is also seen in the case of the Cr catalyst. T.Xing et al. demonstrate that the decrease in surface area of Cr-alumina is directly proportional to the increase in Cr loading. This observation is consistent with the obtained value of 53.3 m^2 g^{-1} by BET for a chromium oxide content of 36.4%.

4.3 Conventional HDO at elevated pressures using NiMo/γ-Al_2O_3 (NiMoAl)

Experimental investigations in this work started by employing conventional HDO with molecular hydrogen at relatively moderate conditions, with temperatures held at 400 °C and pressures of 5, 9, and 25 bar. It is important to note that these pressure ranges were considered relatively low when compared to the conventional HDO processes discussed in the literature review chapter. These experiments utilised NiMoAl catalysts, a widely recognised choice for hydrotreatment applications. The selected temperature was situated at the higher end of the HDO temperature range, approaching the lower limit for alkane DeH. These initial experiments were designed to establish a reference point, assess the performance of the experimental setup, and make preliminary parameter choices. In this specific section, guaiacol was processed with an excess of hydrogen, maintaining a 5.0 hydrogen-to-guaiacol molar ratio (H:G). Table 4.2 indicates the performance of guaiacol HDO at targeted operating conditions.

Table 4.2: Guaiacol HDO at 400 °C at elevated pressures with H_2/GUA molar ratio of 5.0 and GHSV of hydrogen of 2.7 mol·g_{cat}^{-1}·h^{-1} using NiMo/γ-Al_2O_3 for TOS of 120-min.

Pressure bar	GUA conversion vol%	BTX selectivity vol%	Condensate g/g_{cat}	Coke deposition g/g_{cat}
5.0	8.7	1.87	0.476	0.495
9.0	9.5	19.3	0.375	0.437
9.0[1]	9.2	22.8	-	-
9.0[2]	6.2	0.21	-	-
25.0	12.1	10.5	0.270	0.079
25.0[2]	6.9	3.9	-	-

[1] Hydrogen GHSV= 1.35 mol·g_{cat}^{-1}·h^{-1}
[2] Hydrogen GHSV=0.8 mol·g_{cat}^{-1}·h^{-1}, H:G= 1.0

In general, experimental observations at a molar ratio of 5.0 for hydrogen to guaiacol (H:G) in the feed indicate BTX formation at the studied pressures, despite the relatively low conversion rates. Therefore, the effects of altering the molar flow and gas space velocity on guaiacol conversion and BTX formation were explored. In principle, the limited conversion can be attributed to operating pressures, as thermodynamics suggest that hydrogenation is

favoured at higher pressures and lower temperatures, while in this work experimental temperature is moderate for hydrogenolysis mechanisms. Regarding guaiacol conversion, the results clearly show an increasing trend as operating pressure rises. This increase in pressure results in reduced coke deposition as a consequence of enhanced hydrogen reactivity for HDO. Improved hydrogen reactivity implies that available reactive hydrogen effectively prevents the polymerisation of adsorbed phenolic compounds, thus reducing coke formation on the catalyst surface, which has been referred to as a "condensate pool" by Li et al. [142]. The condensate content, which refers to solid deposition on the catalyst that desorbed at high temperature in an inert environment measured as described in Section 3.4.3, also increases at lower pressures, but the variation in condensation at different pressures is within a 20% range and does not correlate with coke deposition. Yet, Xiong et al. proposed that condensate generated from oxygenated aromatic is generated at low and high temperature, but has low oxygen content [142].

This observation provides evidence that the catalytic system remains active and controls the conversion and selectivity, with guaiacol conversion primarily driven by the adsorption at the active sites. The condensate ratio indicates the rate at which oxygenates accumulate, ranging from 0.4 to 0.47 g per g of catalyst. Regarding BTX formation, a significant increase in BTX selectivity is observed when the pressure is increased from 5.0 to 9.0 bar, reaching a tenfold increase. At 9.0 bar, despite a GHSV of 1.35 $\text{mol}\cdot\text{g}_{cat}^{-1}\cdot\text{h}^{-1}$ and the same H:G ratio of 5.0, an 18% BTX selectivity was achieved, with no noticeable improvement in guaiacol conversion. This underscores the saturation of the catalyst bed with condensate, limiting further enhancements under these operating conditions. Another noteworthy observation at 9.0 bar, highlighting the significance of hydrogen, involves operating at a stoichiometric H:G ratio of 1.0. Despite the reduced GHSV, guaiacol conversion and BTX selectivity decreased. Interestingly, further increasing the pressure to 25.0 bar does not result in a higher BTX selectivity, despite the conversion increasing to 12.1%, as depicted in Table 4.2. This observation suggests that hydrogen plays a crucial role in preventing coke deposition. Similar to the operation at 9 bar, transitioning to a stoichiometric H:G ratio of 1.0 with a lower GHSV led to a decline in guaiacol HDO performance. The impact on guaiacol conversion and the formation of BTX over a 120-min period at varying pressures is illustrated in Figure 4.6.

At both 5 and 25 bar, guaiacol conversion experiences a 50% reduction due to catalytic

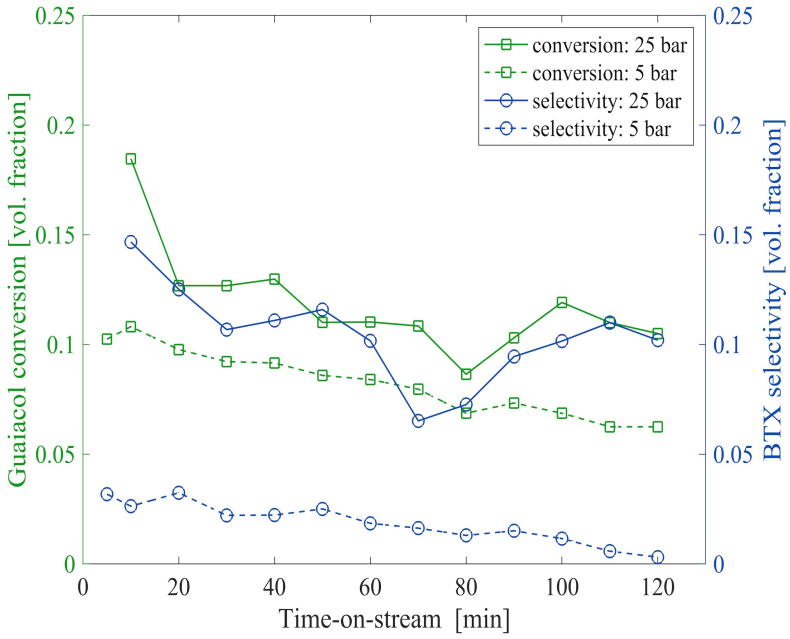


Figure 4.6: Guaiacol HDO at 400 °C at elevated pressures with hydrogen-to-guaiacol molar ratio (H:G) of 5.0 and 1.0 g of NiMo/γ-Al_2O_3 for TOS of 120-min.

deactivation. Although coke deposition is low at 25 bar, noticeable declines in guaiacol conversion and BTX selectivities are observed. Notably, no heavy hydrocarbons, such as naphthalene, were detected in the liquid product at 25 bar, unlike other pressure conditions, suggesting that condensation might obstruct active sites, given the nearly consistent condensate rate across all pressures, leading to deactivation. Another contributing factor is the excessive reduction of catalytic active sites, which eliminates oxygen vacancies for HDO. Oxygenated functional groups from guaiacol adsorb onto these vacancies and are subsequently reduced by the flowing hydrogen. However, excessive hydrogen flow can result in over-reduction, potentially altering the phase of Mo oxide from an active to a less active state. Zhang et al. reported a decrease in conversion from 68.5% in the reduced case to 63.6% for MoO_3, the primary active site in the investigated catalyst on a weight basis [147]. Over-reduction also led to a decline in BTX formation [147]. Deactivation due to sintering effects, especially for Ni active sites, is mitigated by the relatively low operating temperature of 400 °C, compared to reforming processes where sintering is a dominant deactivation mechanism. Furthermore, the use of a bimetallic NiMo system allows for enhanced HDO, as metal dispersion reduces the agglomeration of active sites, in contrast to single metal active sites [86]. Additionally, surface area analysis using BET did not reveal significant changes in the surface area of spent catalysts after regeneration using TGA.

4.4 Ethane dehydrogenation (DeH)

4.4.1 Thermal ethane DeH

The reported catalysts in this work were examined for non-oxidative ethane DeH with no HDO to build a baseline for DeH-HDO coupling. Since DeH of ethane as well as HDO of guaiacol may occur thermally and be affected by the reaction temperature, the catalysts are diluted in 1:1 weight ratio with SiC to maintain axial and radial homogeneous temperature distribution in the catalytic bed. Therefore, to distinguish the thermal and kinetic effects on ethane conversion, and ethylene selectivity to methane as higher hydrocarbons, SiC was thermally investigated as an inert bed material. Figure 4.7 illustrates ethane to ethylene yield on temperature-programmed alkane dehydrogenating using a SiC catalytic bed as a non-reactive system. Ethylene formation exponentially increased with increasing the temperature up to 700 °C. Increasing the temperature by 20 °C resulted in a two-fold increase in ethylene formation rate emphasising the importance of maintaining a uniform temperature axially and radially within the reactive zone. This highlights the importance of using SiC in the catalytic bed to improve the thermal conductivity. Particularly, given the complex coupling of HDO and DeH, where exothermic and endothermic reactions are involved.

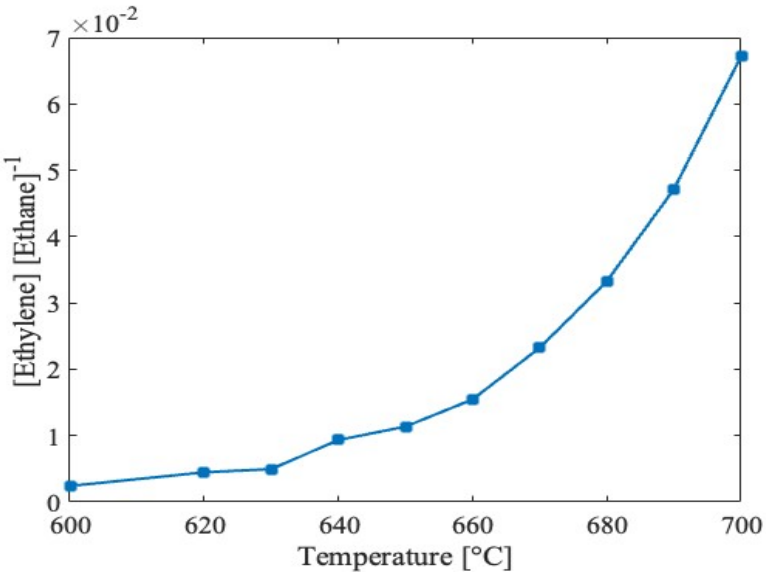


Figure 4.7: Atmospheric pressure ethane DeH in a SiC bed at different temperatures and ethane flow of 4.3 mmol·min^{-1}

The thermal non-oxidative conversion of ethane results in the formation of methane and carbon. With the increase in conversion, ethylene selectivity increased to 80vol%. In the thermal conversion of ethane, the selectivity of the reaction indicates the existence of dis-

sociation, C-C cleavage forming methane, and DeH, (C-H) forming ethylene, mechanisms. However, thermodynamically, ethane DeH is favoured at higher temperatures. In addition, the employed ethane flow rate at the operating temperature did not result in the formation of acetylene. The target temperature for this research is less than 600 °C, as appears in Figure 4.7, at two hours operation ethylene-to-ethane is below $2.5{\cdot}10^{-2}$. Therefore, thermal ethane conversion is assumed to be negligible. In addition, SiC is nonreactive, and catalytic pathway is the main factor in ethane DeH.

4.4.2 Catalytic ethane DeH using NiMo/γ-Al_2O_3 catalysts

The selectivity improves with time as Ni active site reaches deactivation, and Mo active site sustain ethylene production via DeH mechanism. The higher ethylene/ethane ratio after 100 min running time relative to SiC at 600 °C indicates the contribution of the catalytic activity towards ethylene formation. Due to the absence of oxidant, catalyst deactivation is inevitable, but can be lowered by operating at lower temperatures as appears in Figure 4.8. The role of Ni active site is also observed at the two NiMo variations, the one with less Ni active site have noticeable higher ethane conversion, and ethylene selectivity. Although higher Ni presence may increase H_2 formation at the beginning of the reaction, but accelerates the deactivation rate and losses carbon efficiency for producing valuable ethylene. Although the existence of Ni may hinder ethane DeH, yet, it has another role in HDO. Primarily, to eliminate aromatic branches that include oxygenated functional groups.

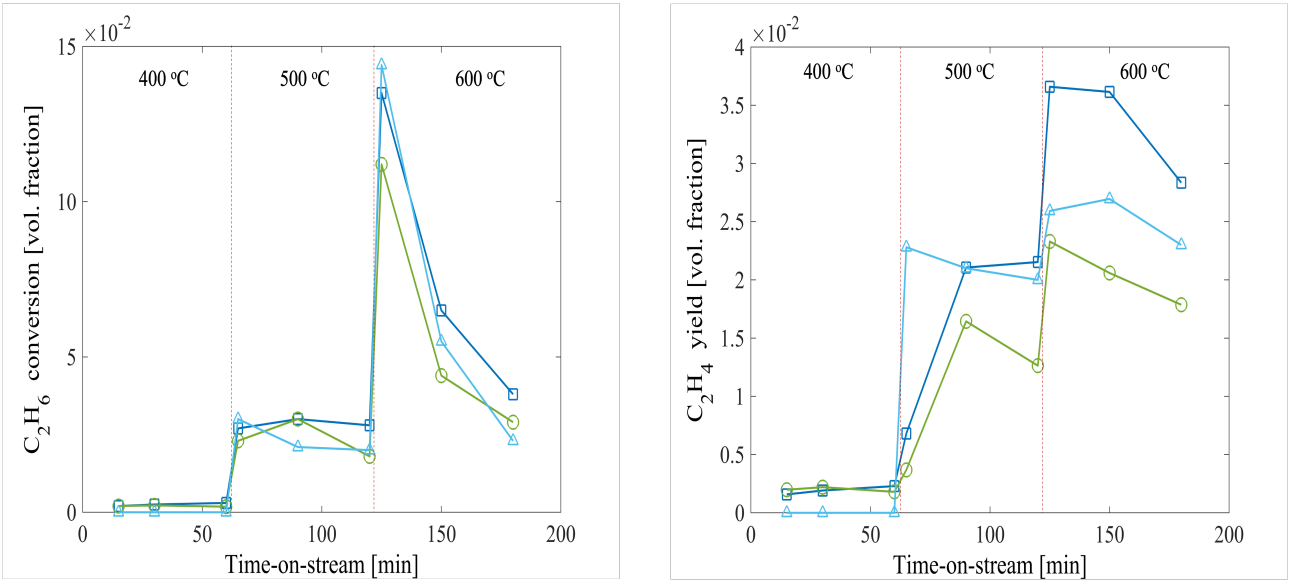


Figure 4.8: Temperature programmed ethane DeH at atmospheric pressure using 1.0 g of $NiMo/Al_2O_3$ in a SiC bed at: 0.27 $mol{\cdot}g_{cat}^{-1}{\cdot}h^{-1}$ (□), 0.20 $mol{\cdot}g_{cat}^{-1}{\cdot}h^{-1}$ (○) and 0.33 $mol{\cdot}g_{cat}^{-1}{\cdot}h^{-1}$ (△).

4.4.2.1 The effect of phosphorus doping on NiMo/Al_2O_3

Two variations of NiMo-based catalysts, PNiMoAl and NiMoAl, were studied. Both are well known in hydroprocessing applications, where P has reported its effectiveness in hydrotreating [9], [153], [154], and HDO in particular [154]. Additionally, the promotion of P is reported to reduce coke formation. The two variations have similar Mo-to-Ni ratios around 3-4, but different NiMo loadings on the support, as shown in Table 4.3. This ratio was found by Vutolkina et al. to be ideal for guaiacol HDO [120]. In addition, one variation is promoted by P (PNiMoAl).

Table 4.3: Elemental analysis of catalysts used in this chapter using XRF

Metal oxide composition (%)		Al (Al_2O_3)	Ni (NiO)	Mo (MoO_3)	P	Cr (Cr_2O_3)
PNiMo/Al_2O_3	(PNiMoAl)	54.0	9.20	33.6	3.20	-
NiMo/Al_2O_3	(NiMoAl)	68.0	7.00	25.0	-	-
Cr/Al_2O_3	(CrAl)	63.6	-	-	-	36.4
MoO_3	MoO_3	-	100	-	-	

Figure 4.9 illustrates higher ethylene selectivity for the doped catalyst (PNiMoAl) by 29%. However, a sharp decline was observed at 50 min during the 180-min reaction, where the undoped catalyst demonstrated highest performance at 600 °C. Beyond 50 min, both catalysts exhibited stable conversion and improving selectivity. The enhanced selectivity could be attributed to the deactivation of Ni active sites, leading to C-C dissociation. Although Ni active sites have been investigated for alkane conversion to replace the leading alkane DeH Pt and Cr-based catalysts [139], [140] due to their high activation energy [141], they primarily target the dissociation mechanism of C-C instead of C-H due to the relatively lower activation energy. Thus, the presence of Ni leads to the formation of undesirable methane and accelerates coke formation, making it a highly considered active site for ethane cracking to hydrogen and carbon [139], [140]. Yet, its presence is considered for HDO, where the literature survey emphasised the importance of Ni-based catalysts.

Since the coupling is designed to favour both reactions while operating in the thermodynamic regime (high temperature and low pressure) that favours ethane DeH, the catalyst must favour HDO, particularly for Mo-based catalysts. Therefore, the operating conditions must be improved to suit PNiMoAl as the base catalyst in this work.

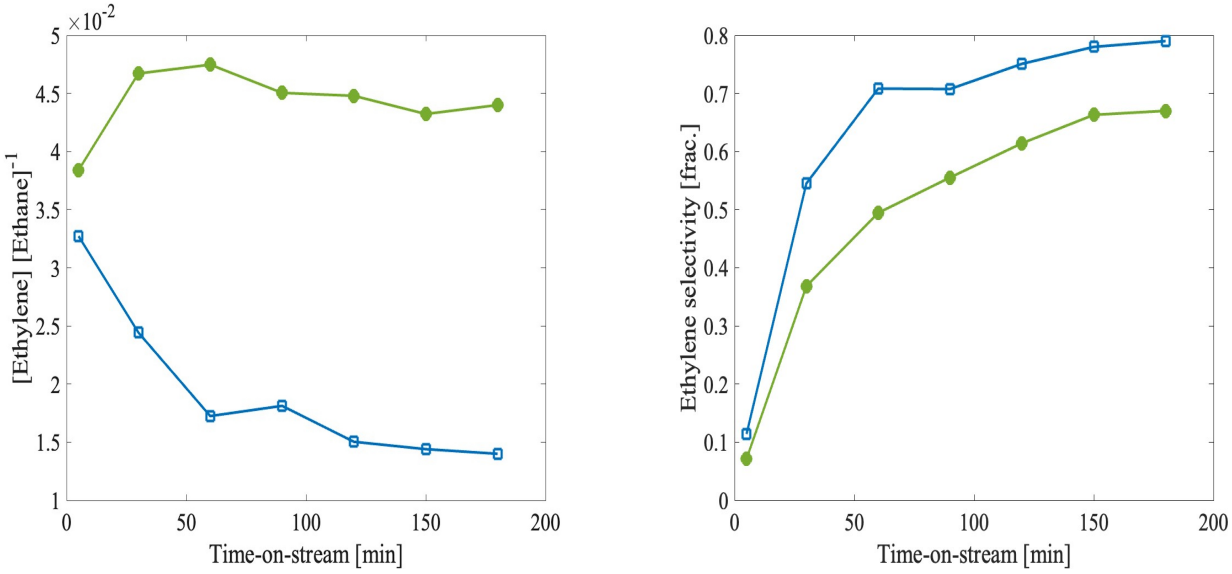


Figure 4.9: Atmospheric ethane DeH using 1.0 g of NiMo-based catalysts in a SiC bed at: 0.25 mol·g_{cat}^{-1}·h^{-1} and 600 °C: PNiMo (□), NiMo (•)

4.4.2.2 Temperature effects on P-doped NiMoAl

The impact of P-NiMo/Al_2O_3 on ethane DeH was assessed at 550 °C and 600 °C, as shown in Figure 4.10. Despite its limited performance in DeH at 600 °C compared to NiMoAl, P-doped NiMoAl was further studied due to its reported potential as a hydrotreating catalyst. Selecting a lower temperature aims to boost ethylene production by restricting the dissociation mechanism of C-C instead of C-H.

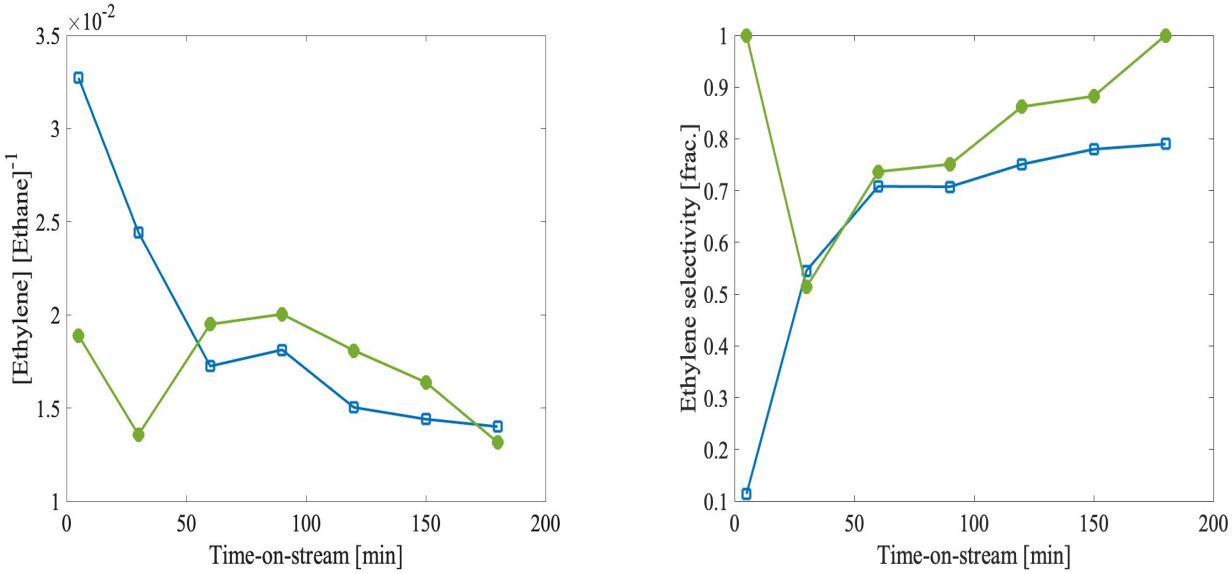


Figure 4.10: Atmospheric ethane DeH using 1.0 g of NiMo/Al_2O_3 in a SiC bed at: 0.25 mol·g_{cat}^{-1}·h^{-1} and temperatures of 550 °C (•) and 600 °C (□).

Figure 4.10 illustrates high conversion and low selectivity at 600 °C and low conversion and high ethylene selectivity at 550 °C. Operating at 600 °C tends to undergo a cracking mechanism, where ethylene selectivity is low at the beginning of the experiment. As the

reaction progresses, the conversion decreases due to the deactivation of the cracking active sites, leading to better DeH performance. However, the accelerated deactivation is at high temperature yields better overall performance at low temperature (550 °C). Therefore, in the subsequent sections, PNiMoAl is further investigated at 550 °C, which is preferred for HDO compared to 600 °C.

4.5 The effect of "in-situ" hydrogen generation on HDO

4.5.1 Thermal coupling of DeH-HDO

The potential of DeH-HDO in enhancing ethylene formation by introducing guaiacol into a non-reactive zone is evaluated. SiC is assumed to be non-reactive zone due to the limited conversion observed in Figure 4.7. Figure 4.11 illustrates a gradual increase in ethylene production with guaiacol addition, contrasting with limited ethylene formation in the absence of guaiacol. Both scenarios start with the same initial ethylene/ethane ratio at 10 minutes. Ethane conversion, depicted in Figure 4.11, steadily rises and stabilises at approximately 35%, surpassing the equilibrium conversion of 14% for ethane to ethylene at 600 °C, as shown in Figure 4.2.

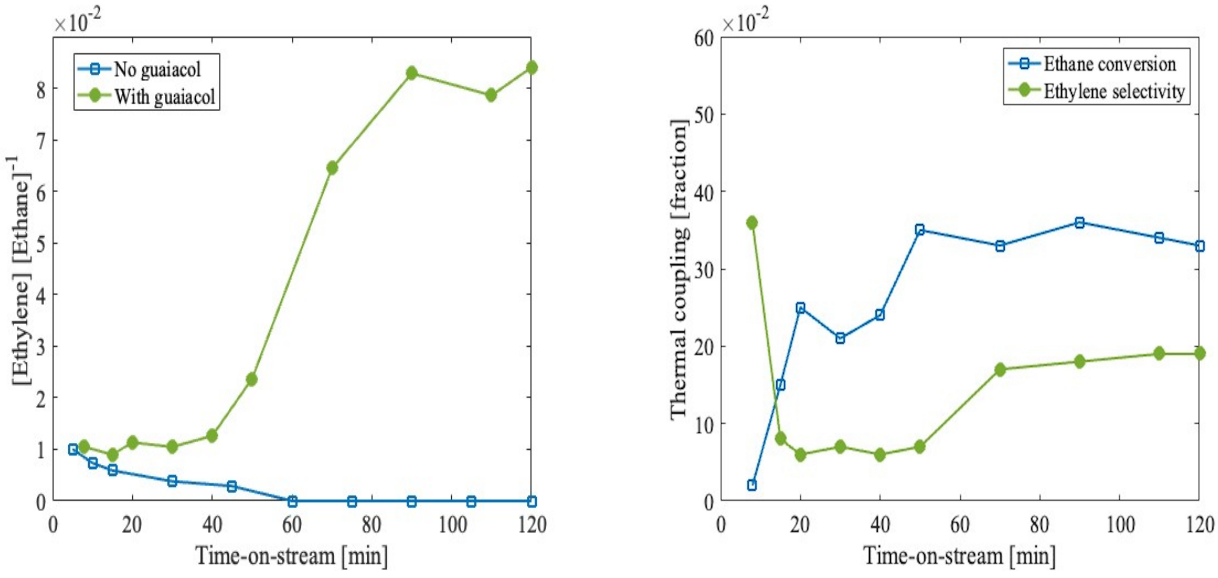


Figure 4.11: Atmospheric pressure thermal coupling of DeH-HDO by ethane DeH in a SiC bed at 600 °C and ethane flow of 4.3 mol·min^{-1} and GUA flow 2.2 mmol·min^{-1}

However, despite the improved ethylene/ethane ratio, ethylene selectivity from DeH-HDO decreases due to additional bio-methane formation from guaiacol HDO. The increase in ethylene formation after 40 minutes in Figure 4.11a can be attributed to guaiacol HDO's

role in hydrogen consumption. Over a 120-minute run, the average ethylene/ethane ratio increases seven-fold. The 27.2 mL/min methane generated with guaiacol introduction is likely biogas, considering that methane formation in the no-guaiacol run has less than 5% selectivity.

4.5.2 Catalytic coupling of DeH-HDO using P-NiMo/γAl_2O_3

To investigate the coupling between ethane DeH and HDO, this study employs a well-studied hydrotreating catalyst to visualise the viability of the concept in comparison to conventional hydrogen supply. The comparison was based on fixing the inlet volumetric flow of the gases, ethane or hydrogen, to 0.27 mol·g_{cat}^{-1}·h^{-1} (unless indicated otherwise). This in fact means more H_2 being available when supplied externally relative to generated hydrogen from the alkane DeH as ethane conversion is limited both by thermodynamics and kinetics. Furthermore, several parameters were investigated on in-situ to enhance HDO products and the ethylene/ethane ratio.

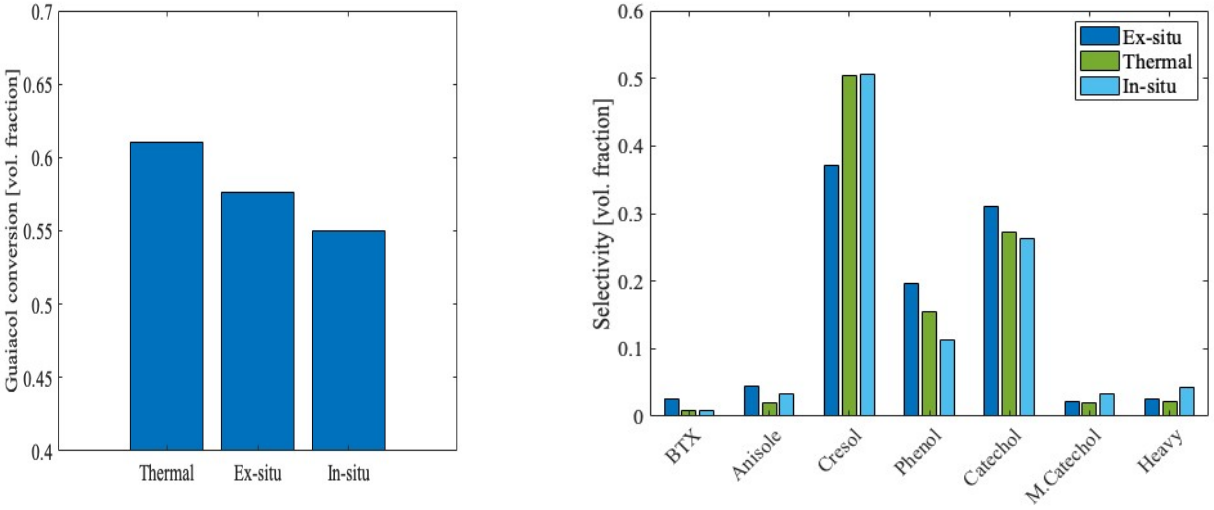


Figure 4.12: Atmospheric pressure in-situ hydrogen generated and ex-situ HDO using PNiMoAl catalyst, and thermal deoxygenation (using N_2) at 550 °C: gas flow 0.27 mol·g_{cat}^{-1}·h^{-1} and guaiacol flow 0.54 mol·g_{cat}^{-1}·h^{-1} for 120-minute run

In-situ HDO was compared to ex-situ using hydrogen flow and to thermal deoxygenation using N_2, as shown in Figure 4.12. In terms of guaiacol conversion, all three approaches: thermal deoxygenation, in-situ, and ex-situ showed comparable results, highlighting the significant influence of operating conditions such as gas and guaiacol flows, as well as reaction temperature. However, thermal deoxygenation achieved a 61.4% conversion, while ex-situ and in-situ reached 57.6% and 55.0%, respectively. The lower conversion in both in-situ and ex-situ is attributed to two reaction mechanisms, where H_2 and C_2H_6 consume energy during dissociation to generate reactive species at the catalyst surface. Addition-

ally, for in-situ, the operating temperature is considered relatively low for effective ethane dehydrogenation.

In terms of liquid selectivity, at the investigated condition, in-situ has demonstrated comparable results with the thermal deoxygenation approach. No different components were detected using the different gas source. BTX were more pronounced for ex-situ deoxygenation, owing to the excess molecular hydrogen. In-situ deoxygenation, on the other hand, has less BTX on average of TOS of 120 min, but produces more heavy hydrocarbons which indicates that although HDO occurs, the lack of hydrogen promotes the polymerisation of aromatic rings, forming naphthalene-like two-aromatic rings compounds. For the three deoxygenation approaches investigated, the formation of phenolic compounds (cresol and phenol) is comparable. However, the in-situ deoxygenation approach exhibits less catechol. This reduction in catechol formation is compensated by the slight increase in methyl catechol, which was promoted by methane radicals formed from alkane DeH. Overall, Table 4.4 confirmed that in-situ deoxygenation generates slightly higher O/aromatic ratio in terms of liquid yield than ex-situ deoxygenation. The use of N_2 produces similar O/aromatic ratio, but the collected liquid is low due to polymerisation which generated solidified products after condensation. The observed results from HDO products emphasises that hydrogen from alkane DeH plays a significant role in HDO and its limitations can hinder the product value.

4.5.2.1 Guaiacol/Ethane ratio

To determine the degree of HDO related to liquid-to-gas (GUA-to-ethane) ratio, the ethane flow rate was held constant while the guaiacol flow rates were varied between 0.054-0.54 $mol{\cdot}g_{cat}^{-1}{\cdot}h^{-1}$. At the investigated flow rates of GUA and ethane flow of 0.27 $mol{\cdot}g_{cat}^{-1}{\cdot}h^{-1}$, NiMoAl catalyst resulted on guaiacol conversion of 55-65%, as illustrated in Figure 4.13. Guaiacol conversion increased with less guaiacol flow, which can be due to reduced aromatic per catalytic active site. In terms of product selectivity, in-situ HDO products showed limited BTX formation, as a consequence of the limited hydrogen available for HDO. Similar to reported literature for continuous flow experiment at atmospheric pressure, aromatic ring saturation was not detected. Lack of hydrogenation of the aromatic ring is not merely caused by low hydrogen availability from ethane DeH since the literature has reported similar observations for ex-situ.

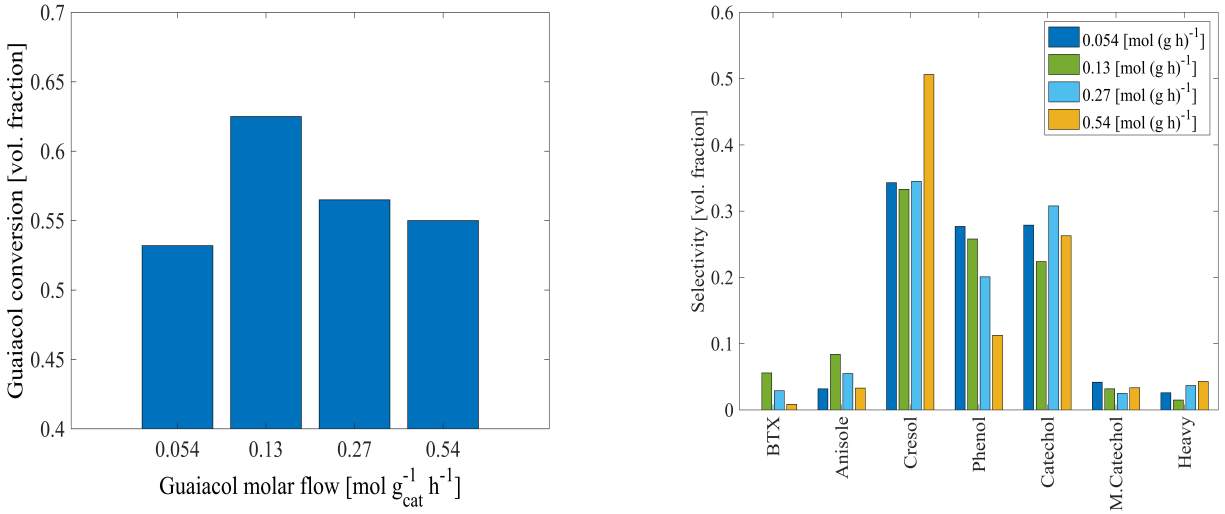


Figure 4.13: Atmospheric HDO of guaiacol via in-situ hydrogen generation from ethane DeH using P-NiMo/Al_2O_3 at 550 °C with constant ethane flow of 0.27 mol·g_{cat}^{-1}·h^{-1}

As shown in Figure 4.13 with decreasing GUA flow rate (decreasing liquid-to-gas ratio), an increase in BTX, anisole, and phenol formation accompanies the effect of HDO on GUA flow rate. In principle, this is due to the amount of hydrogen produced by alkane DeH per aromatic ring in guaiacol, as well as the ratio of catalyst active sites to aromatic rings. Therefore, the heavy HDO product increased in proportion to the liquid flow rate, indicating that hydrogen was in short supply. In addition, the hydrogen limitation inhibited the elimination of the hydroxy group from phenol, which was compensated for by methylation. According to Bui et al., methylation is a potential route for ex-situ HDO [155]. Methane radicals are produced during demethylation (DME), while the hydrogenolysis of phenol and catechol require shorter residence time, which lead to the formation of methyl catechol and cresol as shown in R5 and R7 in Figure 4.14. In in-situ via alkane DeH, methylation significantly increases since methane radicals are produced from the non-selective DeH of ethane (cracking to methane). Cresol undergoes further methylation to produce methyl cresol, which if hydrodeoxygenated, xylenes are formed.

4.5.2.2 The effects of time-on-stream

In a single experiment, HDO of guaiacol declines with time on stream, as illustrated in Figure 4.15. The concentration of unreacted GUA present in the liquid product increased from 24% (30 min) to 29% (S3) in 90 min operation. During the run, BTX, phenol and catechol yields decreased with time, indicating that HDO has declined due to deactivation of the catalytic bed or the limited hydrogen available for HDO. Hydrogen formation declined due to the deactivation of ethane DeH resulting from the saturation of the catalytic surface with

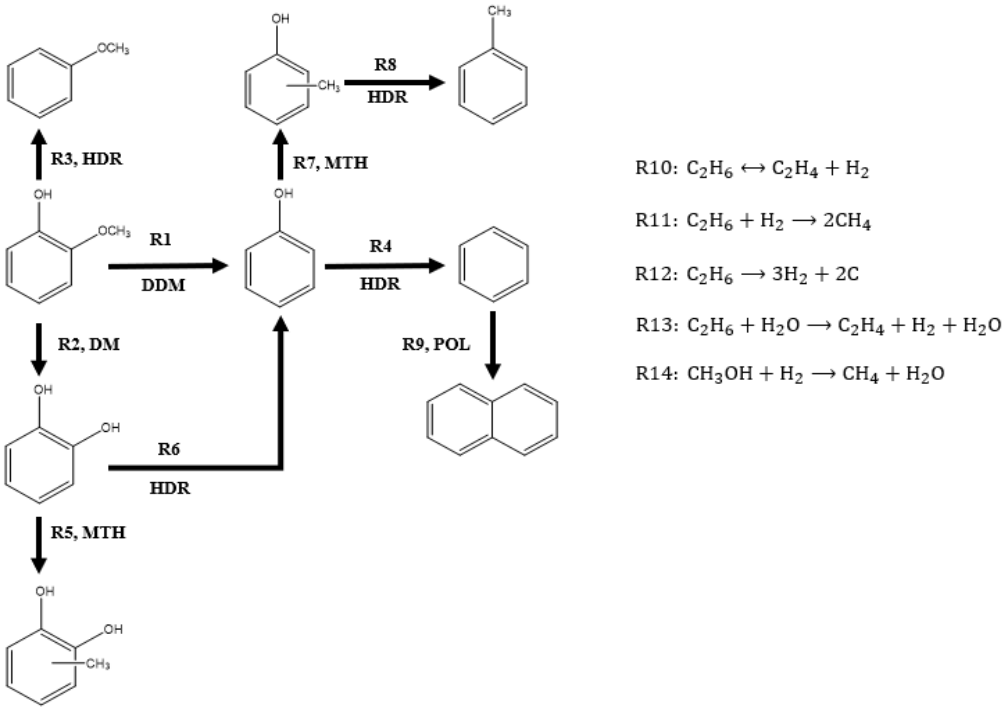


Figure 4.14: Proposed reaction network for guaiacol HDO using hydrogen produced from ethane DeH. DDM: Direct demethoxlyation, HDR:hydrogenolysis (dehydroxylation), DME: demethylation, MTH: methylation, POL: polymerisation

phenolic compound covering the active sites. Yet, hydrogen was still detected in the gas outlet. As illustrated in Figure 4.15, phenol selectivity is three-fold that of catechol in the first three samples. However, by the end of the experiment, phenol and catechol selectivities are comparable, suggesting that the catalytic bed was completely deactivated. In such a case, the reaction is dominated by thermodynamic effects, which favours demethylation forming more catechol since the dissociation energy of aromatic-OCH_3 is less than -OCH_3. Furthermore, methylation increased by the end of the reaction (120 min), showcased by the increase in catechol yields which subsequently undergoes further conversion producing methane radicals. Additionally, methane is produced from alkane DeH with no guaiacol since the selectivity toward DeH is limited to 75 vol% due to the presence of Ni, which activates C-C cleavage. The deactivation of the catalytic system is ascribed to carbon formation from both reactions, as well as the condensation of phenolic compounds as observed by [123]. During the co-processing of both reactions on a mesopore catalytic material such as alumina-supported active sites, the presence of phenolic compounds leads to blockage of the active sites due to the formation of a condensate. Coke formation is possibly initiated from the feedstock (guaiacol), and other phenolic compounds [156]. Therefore, the flow-rate of HDO feed contributes to the reaction performance as previously explained in

Figure 4.13. However, ethylene formation can be maintained by the ability of the smaller compound ethane to reach to the active sites. As Ni active sites for alkane DeH, the acidity of the catalyst caused by the support accelerates coke formation for guaiacol HDO [156].

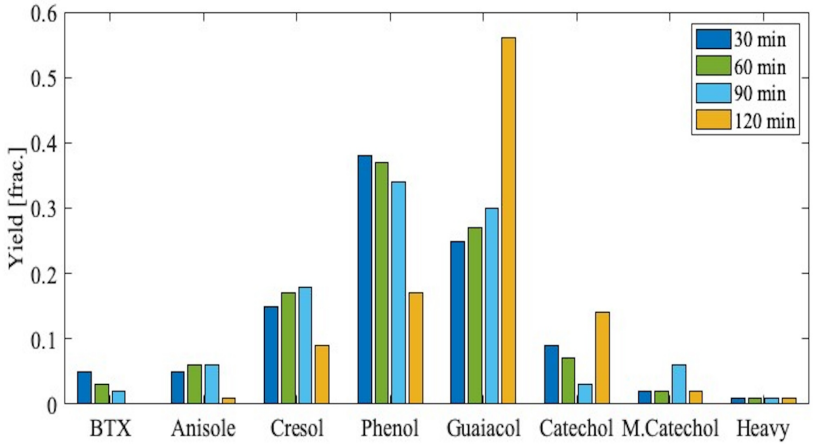


Figure 4.15: HDO of guaiacol via in-situ hydrogen generation from ethane DeH using PNi-MoAl at atmospheric pressure, 550 °C and gas flow of 0.27 mol·g_{cat}^{-1}·h^{-1}.

The DeH-HDO integration aims to attain a higher ethylene-to-ethane ratio in the gaseous product stream to demonstrate a shift in thermodynamic equilibrium. The DeH-HDO integration improved the ethylene-to-ethane ratio in all reported cases, as shown in Figure 4.16. The decrease in ethylene selectivity relative to ethane DeH experiment was caused by the formation of additional methane from HDO through direct demethylation. Also, the presence of minimal methanol in the product stream indicates that mainly guaiacol HDO undergoes demethylation to generate catechol, followed by hydrogenolysis to generate phenol. If active sites remain reactive, phenol and methyl phenol will eventually convert to BTX. This mechanism is consistent with the rapid drop in BTX, followed by the production of phenol and cresol and an increase in catechol.

In addition, Figure 4.16 demonstrates that lower GUA flow rates, at 0.054 mol·g_{cat}^{-1}·h^{-1}, resulted in an initial decrease in ethylene production. However, this phenomenon was followed by a spike after 60 min on the stream. This change in performance is a consequence of the exposure and deactivation of active sites to HDO, DeH, or both simultaneously. The lower GUA flow rate results in a prolonged residence time, which may account for the higher ethylene production and selectivity (greater ethane conversion) observed. Increasing the residence time by increasing the catalytic bed from 1.0 g to 3.0 g did not increase ethylene production or selectivity over the course of the entire reaction cycle. This suggests that HDO promotes ethane DeH in the low flow-rate experiment, wherein not all active sites

were blocked by HDO condensate. The sudden decline at the end could be attributed to the limitation of ethane diffusion caused by the accumulation of condensate on the active sites after 100 min.

Table 4.4: Overall atmospheric pressure HDO performance using PNiMoAl at 550 °C and gas flow of 0.27 mol g_{cat}^{-1} h^{-1} for 120-minute run.

Gas feed	GUA flow ($mol \cdot g_{cat}^{-1} \cdot h^{-1}$)	O/Aromatic (selectivity)	O/Aromatic (yield)	carbon formation[b] (g/g_{cat})	Condensate[a] (g/g_{cat})
H_2	0.54	1.30	1.61	0.508	0.0912
N_2	0.54	1.28	1.60	-	-
C_2H_6	0.54	1.29	1.55	0.516	0.481
C_2H_6	0.27	1.30	1.57	0.640	0.518
C_2H_6	0.13	1.20	1.50	0.471	0.415
C_2H_6	0.054	1.32	1.63	0.414	0.378

[a] From TGA - the weight accumulated on the catalyst: up to 500 °C N_2 flow.
[b] From TGA - the weight accumulated on the catalyst: 500-850 °C air flow.

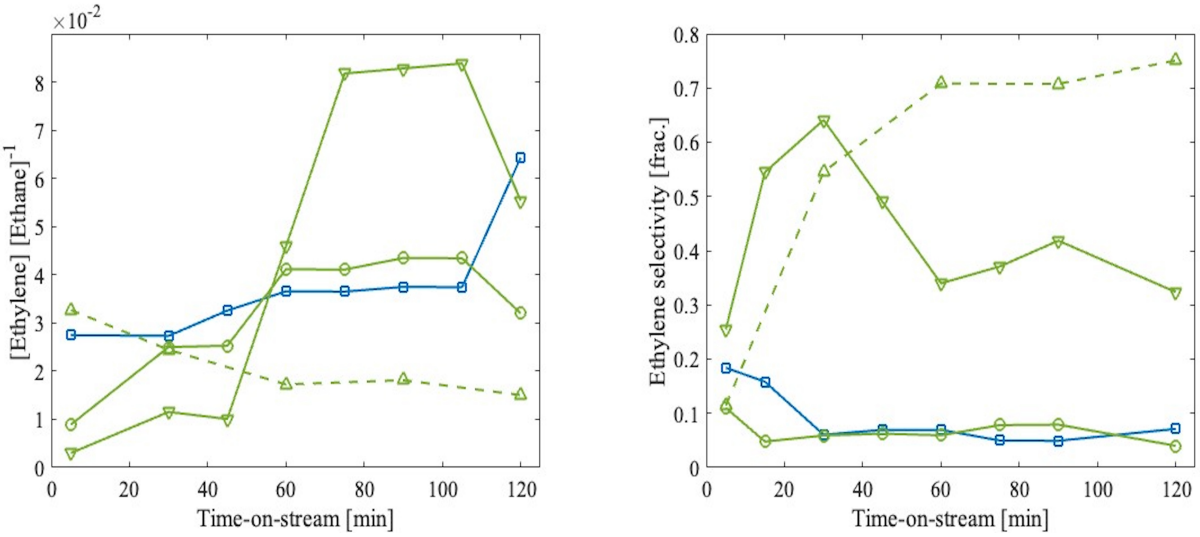


Figure 4.16: Composition of gas product stream of DeH-HDO integration for guaiacol and ethane on PNiMoAl catalyst at 550 °C, an atmospheric pressure: No GUA only ethane DeH (△), 0.05 $mL \cdot g_{cat}^{-1} \cdot h^{-1}$ GUA and 1.0 g_{cat},(▽), 0.27 $mol \cdot g_{cat}^{-1} \cdot h^{-1}$ GUA and 1.0 g_{cat} (□), and 0.09 $mol \cdot g_{cat}^{-1} \cdot h^{-1}$ GUA and 3.0 g_{cat} (○).

In general, under the investigated operating conditions, neither in-situ nor ex-situ has exhibited the saturation of the aromatic ring of guaiacol using Ni-Mo-based catalyst. This observation is consistent with literature findings of ex-situ under atmospheric pressure [25], [142], [157], indicating hydrogen availability is not the limiting factor in saturating the aromatic ring relative to other operating conditions. A study that considered ex-situ of phenol at different temperature at atmospheric pressure over Ag/TiO_2 concluded that regardless of the phenol conversion, which varied with reaction temperature, the product mostly consists of benzene above 90% on selectivity [85]. Unlike operating at higher pressures where aromatic saturation is an intermediate step for HDO [158], [159]. This achieved since the

activation energy for -OH group is lower if it is associated with hexane in comparison to benzene. However, this pathway requires excessive hydrogen at operating temperature to hydrogenate the aromatic ring. Moreover, this pathway requires a catalytic system that is capable of hydrogenation-and-DeH as well as HDO, which led to the development of bifunctional catalytic system for ex-situ. Therefore, operating at atmospheric pressure adds a significant benefit, as it promotes alkane DeH and limits the saturation of aromatic rings.

4.6 Eliminating the effects of Ni and acidic support using unsupported MoO_3

Recently, MoO_3 has received considerable attention for HDO [24], [91], [129], [130], [160]. MoO_3 was considered in this work to eliminate the effect of Ni and acidic support, and understand the role of Mo in these reactions. In addition to the promotion of the dissociation of carbon and heteroatoms as previously discussed, Ni negatively contributes in C-C cleavage that affects ethylene selectivity and consequently HDO. G.Wang et al. reviewed the mechanisms of Ni-based catalysts on light alkane DeH [141]. Several reported studies in the review conclude that unlike alkane DeH leading catalysts based on Pt, Ni active sites undergo multiple C-C dissociation phases during the desorption of reacting light alkanes at the active sites [141]. This mechanism is known as hydrogenolysis since two atoms are required to complete methane formation in particular from ethane. Consequently, the use of ethane in DeH-HDO would have reverse effect since it consumes hydrogen. Another study confirms computationally and experimentally that Ni-Mo has better selectivity toward ethylene than Pt based catalyst for ethane DeH [161]. Yet, to eliminate all the effect of Ni, MoO_3 was considered to validate the potential for in-situ HDO over ex-situ HDO.

Figure 4.17 illustrates a comparison of in-situ and ex-situ HDO of GUA in presence of MoO_3. In this study, an analysis of ex-situ at lower temperature was investigated to include a perspective of the performance of most investigated temperatures in literature for HDO (350 °C). In-situ HDO has exhibited BTX formation close to ex-situ HDO at the higher temperature study, but four-fold higher than ex-situ HDO at the conventional temperature as shown in Figure 4.17. In addition, in-situ HDO demonstrated less heavy hydrocarbon formation, which could be attributed to the presence of active hydrogen from alkane DeH. Furthermore, in-situ HDO achieved better selectivity towards phenolic compounds and anisole. In comparison to ex-situ HDO at a lower temperature, the operating condition in this work has

less catechol formation, improving the degree of HDO. Therefore, as indicated in Table 4.5, and similar to NiMo catalytic system, MoO_3 catalytic system has improved the O-to-aromatic ratio.

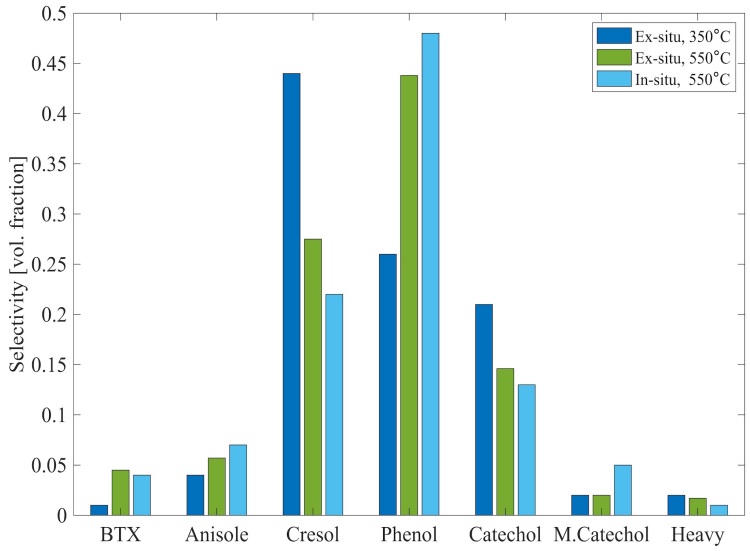


Figure 4.17: Catalytic atmospheric HDO of guaiacol using MoO_3: gas flow of 0.18 mol·g_{cat}^{-1}·h^{-1}, with catalyst weight of 1.5 g. Ex-situ using molecular hydrogen, in-situ using hydrogen produced from alkane DeH.

Table 4.5: Overall atmospheric pressure HDO performance using MoO_3 at 550 °C and gas flow of 0.18 mol·g_{cat}^{-1}·h^{-1} for 120-minute run.

Experiment	GUA flow	O/Aromatic (yield)	O/Aromatic (selectivity)	carbon formation (g/g_{cat})	Condensate (g/g_{cat})
H_2 -350 °C	0.13	1.47	1.23	0.0186	0.0197
H_2	0.13	1.45	1.19	0.211	0.182
C_2H_6	0.27	1.60	1.28	0.390	0.641
C_2H_6	0.13	1.39	1.17	0.238	0.374

Furthermore, despite the lower heavies produced by the use of ethane, still high amount of condensation and carbon formation were observed at the catalytic surface. Both condensation and carbon formation significantly increases at processing higher guaiacol flow of 0.27 mol·g_{cat}^{-1}·h^{-1} at constant gas flow. Similar phenomena was observed in using NiMo at different guaiacol flows in the previous section. Interestingly, HDO occurred even when guaiacol molar rate is higher than that of ethane, which is attributed to hydrogen generated from condensation and carbon formation that yield H atom re-distribution.

The use of MoO_3 has two main advantages over NiMo, especially, for in-situ HDO via alkane DeH. Firstly, the selectivity of MoO_3 towards ethylene formation is higher in comparison to Ni-Mo, limiting the acceleration of coke formation and promoting the formation of valuable alkenes (ethylene). Consequently, methylation effects are reduced as shown in Figure 4.18,

where the selectivities of cresol and methyl cresol are lower than that of phenol. This was also observed in the in-situ HDO condition used in Figure 4.17 relative to ex-situ HDO. Previous results indicated that Ni-Mo promoted methylation in general, and in the comparison in-situ HDO and ex-situ HDO. Secondly, for 120 min TOS, guaiacol conversion maintained a stable value.

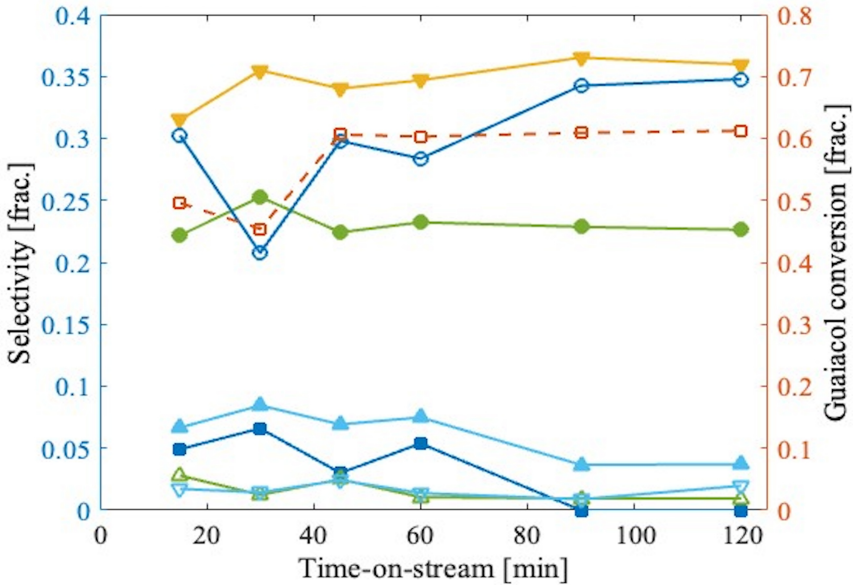


Figure 4.18: Atmospheric HDO of guaiacol via in-situ hydrogen generation from ethane DeH using MoO_3 at 550 °C and gas flow of 0.18 mol·g_{cat}^{-1}·h^{-1}: [Right axis] Guaiacol conversion (□), [Left axis] BTX (■), phenol(●), anisole (▲), cresol and methyl cresol (▼), catechol (○), methyl catechol (▽), and Heavy (△) selectivity.

4.7 DeH-HDO based on alkane DeH catalyst Cr_2O_3/Al_2O_3 (CrAl)

4.7.1 Catalytic ethane DeH

4.7.2 Catalyst characterisation

The Cr catalyst employed in this chapter reveals a high loading of 36 wt%, as previously shown in Table 4.3, in order to expedite the conversion through C-H dissociation. This is due to the fact that Cr serves as the primary non-noble active site. The characterisation of alumina-supported chromium has been extensively studied in the literature [162]–[165]. As depicted in Figure 4.5, the elevated concentration of chromium oxide leads to an increase in the crystallinity of the active sites. The presence of γ-alumina is primarily identified by the peaks at 47° and 68°, while the majority of the other peaks are attributed to chromium oxide. However, it is likely that multiple phases of Cr oxide are present. Initially, there is a significant amount of Cr^{+6} attached to the support, followed by the presence of dispersed microcrystalline Cr^3 oxide on the catalyst surface. Ultimately, this leads to the formation of

crystalline Cr_2O_3, as proposed by Cavani et al. [163], particularly when the loading exceeds 11%. Additional research has verified the presence of a crystalline structure when the loading exceeds 12%. However, this is accompanied by the presence of additional phases, specifically Cr^{+6} and Cr^{+3}, as reported in previous studies [162], [164], [165].

4.7.3 Catalytic ethane DeH

Chromium-based catalysts are recognised as the primary and commercially used catalysts for alkane DeH [82]–[84]. In this section, DeH catalyst is investigated due to the critical importance of preserving reactive hydrogen for HDO. The reduction in active hydrogen leads to a decrease in the extent of HDO, as previously addressed in the preceding sections concerning Mo-based catalysts. While Cr on alumina has been extensively studied as a catalyst for alkane DeH, with a particular focus on ethane, it is essential to ensure that the catalyst remains in an active state for highest reactivity.

Hence, we explore the impact of reducing the chromium-based catalyst in Figure 4.19, with the absence of guaiacol flow. Chromium oxide catalysts may exist in different oxidation states, including +3, +5, and +6. During the reduction process, Cr^{+5} and Cr^{+6} are converted to the active state of +3. However, Figure 4.19 reveals different behaviour during the alkane DeH experiment, where the reduced catalysts exhibited poor performance compared to the untreated catalytic bed at various GHSV.

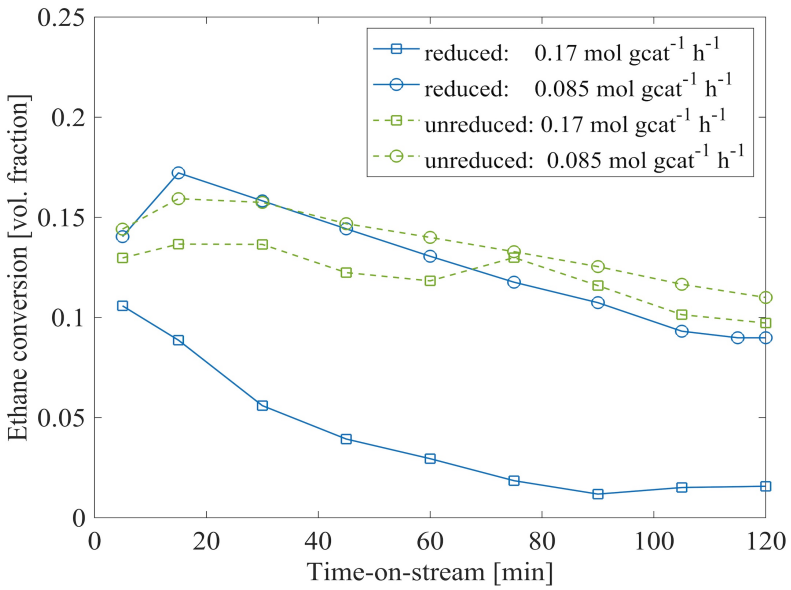


Figure 4.19: Catalytic ethane DeH of ethane using $CrAl_2O_3$ at different space velocity and activation procedure: GHSV of 0.17 mol·g_{cat}^{-1}·h^{-1} (□) and 0.085 mol·g_{cat}^{-1}·h^{-1} (○). Reduction occur at the reaction temperature using H_2 flow of 0.26 mol·h^{-1} for 120 min.

This observation aligns with the findings from XRD in Figure 4.5 and Table BET analysis,

indicating that the catalyst is predominantly composed of the crystalline structure of Cr_2O_3. In Figure 4.5, the crystallinity is indicated by the sharp characteristic peaks, showing that the large Cr structure aligns with surface area analysis as shown in Table 4.1, where the surface area is relatively small due to agglomerated Cr-active sites. This suggests that further reduction exceeds sintering effects by promoting the migration of less reduced states within the catalyst to the crystalline structure. Egorova et al. have concluded that the presence of the crystalline +3 state stabilises the performance of butane DeH by bonding with the available amorphous +3 and +6 states [166], which may explain the steady performance of the reduced catalyst at 0.17 $mol \cdot g_{cat}^{-1} \cdot h^{-1}$ at the last 60 min. The initial decline in activity of the catalysts may be attributed to the migration of the amorphous +3 state, forming polychromate or chromate species through migration to the support [166]. The catalysts employed in this study undergo a continuous cycle of reduction and oxidation. Reduction takes place through the utilisation of generated hydrogen from the reaction itself or external hydrogen during the pre-treatment phase. Likewise, oxidation occurs during the reaction through HDO feed and product, catalysed by adsorption at the catalyst surface or through external air or oxygen during catalyst regeneration. Therefore, the performance of this redox cycle is of utmost importance. Nazimov et al. have highlighted several reported findings in the literature that support the irreversibility of chromium oxide catalysts to their original state [167], indicating that for DeH-HDO using Cr-based catalysts, regeneration of the initial active state may not be feasible. Therefore, to maintain active sites, it is suggested that the reduction of Cr catalysts considered in this chapter be avoided.

4.7.4 Catalytic DeH-HDO on alkane DeH catalyst

In-situ and ex-situ were investigated, as well as temperature and catalyst loading. As shown in Table 4.6, in general, BTX was barely detectable; instead, the yield of double aromatic ring components (heavy) increased in comparison to other catalysts. Lowering the guaiacol flow to catalyst weight ratio (F_L/W_{cat}) by using a high catalyst load of 1.5 g resulted in improved cresol and catechol selectivity and decreased phenol production. This indicates that the alkylation step follows HDO.

In comparison to ex-situ (C), in-situ hydrogen (B) generation using CrAl generates less phenol and more cresol from guaiacol using ethane as the hydrogen source, as demonstrated in Figure 4.6. Consequently, the degree of HDO is not improved by using ethane since O-to-aromatic (O:A) favours the use of hydrogen in terms of yield and selectivity. In terms

of O:A yield (selectivity), B is 1.55 (1.30), while C is 1.51 (1.24). To further improve HDO, a temperature increase to 600 °C was investigated since the temperature improves alkane DeH as well as HDO as illustrated in previous sections. 600 °C demonstrates both better BTX and degree of HDO but still does not reach the performance of ex-situ, unlike Mo-based catalysts where in-situ produced improved results.

Table 4.6: Atmospheric pressure HDO of guaiacol using hydrogen or ethane at 0.17 $mol{\cdot}g_{cat}^{-1}{\cdot}h^{-1}$ in a CrAl catalytic bed

		Case A	Case B	Case C	Case D
Temperature	°C	550	550	550	600
GUA flow	$mol{\cdot}g_{cat}^{-1}{\cdot}h^{-1}$	0.13	0.09	0.09	0.09
Hydrogen source		C_2H_6	C_2H_6	H_2	C_2H_6
GUA conversion	(vol%)	66.2	64.8	64.1	73.0
		Selectivity			
BTX	vol%	-	0.21	1.01	0.43
Anisole	vol%	3.00	2.32	3.08	3.61
Phenol	vol%	13.1	8.71	17.3	16.2
Cresol	vol%	44.4	47.8	44.8	38.8
Catechol	vol%	27.0	33.3	26.7	33.1
Methyl catechol	vol%	7.05	2.58	2.52	2.69
Heavy	vol%	5.61	5.21	5.11	5.08

Despite the limited production of BTX, the decrease in GHSV results in relatively higher BTX yields, transitioning from no BTX formation in scenario A to slightly improved performance in scenarios B and D, particularly at higher temperatures. This phenomenon could be attributed to the reduced limitation of ethane access to active sites for DeH when guaiacol is present in lower quantities, consequently leading to higher levels of reactive hydrogen. This is supported by the reduced formation of heavy fractions, which is expected in scenarios with higher levels of reactive hydrogen. Thus, the in-situ approach necessitates the generation of more active hydrogen to promote increased BTX formation while restricting the formation of heavy hydrocarbons.

4.7.5 Optimising the processing parameters to maximise BTX yield

The preceding section provides evidence that ethane can effectively substitute hydrogen as a hydrogen source through alkane DeH. However, the production of BTX either fails to materialise, remains negligible, or diminishes within a short runtime. When employing guaiacol as the HDO model compound, the primary mechanism for HDO entails hydrogenolysis (direct HDO) of oxygenated functional groups, leading to the direct formation of phenol, anisole, and benzene following the removal of hydroxy and methoxy groups. Nevertheless, two addi-

tional competing mechanisms contribute to the formation of catechol, alkyl-catechol, cresol, toluene and xylenes through methylation. To investigate these mechanisms, several experimental runs' focus is narrowed to a single oxygenated aromatic compound, phenol. Phenol is selected since it represents a considerable fraction of lignin-derivatives and the removal of its methoxy group is the limiting step for complete HDO.The rationale behind selecting CrAl for processing phenol into BTX with ethane lies in the catalyst's failure to produce BTX from phenol. This characteristic simplifies the exploration of potential improvements in BTX.

As depicted in Figure 4.20, phenol demonstrates the capability to yield BTX up to 24% at 600 °C. However, this initial increase in yield at 30 min is followed by a sharp decline to 7% after 75 min, ultimately leading to near-complete deactivation. To achieve this result, the flow rate of phenol had to be reduced below 0.13 and 0.09 $mol \cdot g_{cat}^{-1} \cdot h^{-1}$, which are the most extensively investigated values in this chapter using guaiacol, achieved by increasing the catalyst weight to 2.0 g and decreasing the volumetric flow rate. Operating phenol at the standard guaiacol flow rate detailed in this chapter results in less than 5% BTX production within 30 min.

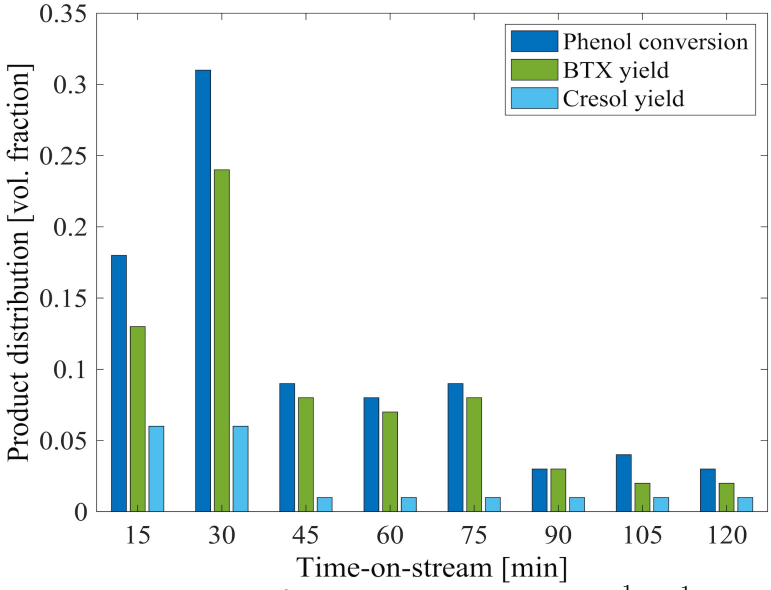


Figure 4.20: Atmospheric HDO of phenol at 0.03 $mol \cdot g_{cat}^{-1} \cdot h^{-1}$ and ethane as hydrogen source at 0.13 $mol \cdot g_{cat}^{-1} \cdot h^{-1}$ using at CrAl catalyst at 600 °C

Examining Figure 4.20, it is evident that although DeH-HDO processes occur, converting phenol into BTX, excessive methylation results in a selectivity of 90% for BTX at 15 and 30 min. However, beyond this runtime, toluene becomes the sole BTX product alongside cresol. The formation of toluene can be elucidated by the methyl radical interacting with a benzene radical generated through hydrogenolysis of hydroxyl (-OH) groups, leading to the

formation of water (H_2O), or by adsorbed -OH groups at the catalyst surface. The emergence of cresol suggests that methylation is not solely instigated by methane radicals produced from HDO, but that DeH also significantly influences this mechanism. Excessive methylation (formation of methyl-cresol and xylenes) was limited with phenol, which contributed to the absence of methyl group from the model compound, phenol unlike guaiacol. These observations further imply the occurrence of chemical species transfer between the two reactions, in addition to the presence of more reactive hydrogen.

4.8 Conclusions

The findings in this chapter concerning atmospheric hydrogen HDO align with recent literature, indicating no saturation of the aromatic ring. This supports the feasibility of conducting HDO at atmospheric pressure using molecular hydrogen, termed "ex-situ" HDO. Elevating the pressure up to 25 bar proves that no ring saturation (hydrogenation) occurs in guaiacol conversion at investigated catalysts and operating conditions, and the HDO is governed by the hydrogenolysis of methoxy and hydroxy groups.

Investigation into a single metal oxide (MoO_3) for HDO confirms the potential superiority of in-situ hydrogen generation (using ethane) HDO over ex-situ HDO at both low and high temperatures. Similarly, NiMo-based catalysts exhibited high degrees of HDO using ethane instead of externally-supplied hydrogen. However, the alkane DeH catalysts, such as CrAl, showed slightly better ex-situ performance due to the relatively low conversion for guaiacol HDO, attributed to the absence of HDO active sites.

Nonetheless, ex-situ HDO resulted in more prominent BTX production due to excess hydrogen availability. Conversely, in-situ HDO led to lower BTX formation but favoured the production of heavy hydrocarbons, primarily comprising naphthalene-like compounds formed by two aromatic rings attached. This suggests that in-situ performance is limited by active hydrogen adsorbed at the catalyst surface, leading to BTX formation at the initial stages, followed by further polymerisation of aromatic rings due to insufficient reactive hydrogen, resulting in heavy hydrocarbon condensate deposition on the catalyst and subsequent coke deposition.

In the gas stream, all reported cases showed a high ethylene-to-ethane ratio with HDO initially. However, this improvement decreases as DeH activity reduces due to coke forma-

tion, indicating rapid active site deactivation by the condensation of phenolic compounds, affecting both reactions and limiting ethane diffusion to active sites.

Alkylation in "ex-situ" HDO is expected from guaiacol demethylation (-OCH_3), where formed methane radicals may react excessively to form additional methylation. In “in-situ" conditions, alkylation increases due to additional methane radicals from ethane cracking, especially with PNiMoAl. Therefore, selective alkane DeH sites are necessary to enhance hydrogen and ethylene yields. In conclusion, while in-situ HDO shows promise over ex-situ HDO, further research is needed to deepen our understanding of reaction mechanisms and develop an improved catalytic system that ensures sustained performance over extended time-on-stream periods before catalyst regeneration.

Chapter 5

Optimising DeH-HDO with Synergistic Dual Catalyst System

5.1 Introduction

This chapter aims to extend the assessment of ethane DeH as a hydrogen source for bio-oil HDO, using guaiacol as a model compound. Findings in the previous chapter showed that the limited hydrogen produced within the catalytic bed exhibits superior reactivity and comparable or better HDO performance than molecular hydrogen. In this chapter, the same catalysts are utilised but configured differently to include both alkane DeH and bio-oil HDO functionalities within a single catalytic bed to improve product quality. We focus on investigating two catalytic systems: P-NiMo/Al_2O_3 combined with Cr/Al_2O_3 and MoO_3 combined with Cr/Al_2O_3. The primary objective is to enhance alkane DeH performance, particularly hydrogen production, by incorporating the Cr-based catalyst. This enhancement aims to improve the extent of HDO by increasing the supply rate of reactive hydrogen. As in the previous chapter, we evaluate the two catalytic systems by comparing externally-supplied molecular hydrogen (referred to as "ex-situ") and in-situ produced hydrogen (shortened to "in-situ" for simplicity), while taking into account different process parameters at atmospheric pressure.

The conversion of ethane via DeH is dominated by the reaction kinetics, as its thermodynamic limits ethane conversion at the targeted operating temperature of 600 °C as shown in Chapter 4. On the other hand, HDO is a catalytic reaction whose selectivity depends on the catalyst, as explored in Chapter 2. Thus, in order to couple both reactions, the catalytic bed must contain the required active sites and catalytic support to optimise the productivity. Although a limited number of active sites have been identified and studied for both reactions, the distinct mechanistic requirements make it difficult to find a suitable commercially available and well-studied catalyst. Therefore, this chapter suggests employ-

ing a mixed catalytic bed approach that is based on the catalysts utilised in Chapter 4. This concept originated from the HDO catalysts, which exhibited superior performance in DeH-HDO processes compared to the use of molecular hydrogen for HDO. However, their ability to perform alkane DeH was limited. Furthermore, the utilisation of a chromium-based catalyst for alkane DeH in the DeH-HDO process did not surpass the performance of the conventional HDO method. Nevertheless, its alkane DeH was acceptable. Hence, mixing both mechanisms by physical catalytic mixing approach might materialise some degree of synergy.

5.1.1 Background

5.1.2 The utilisation of dual catalytic system for DeH-HDO

The literature has explored the use of physical mixing of two heterogeneous catalysts to enhance the reactivity and selectivity of a complicated mechanism network. This approach has been discussed in several studies [168]–[176]. Examples are conventional hydroprocessing applications and the integration of a hydrogen-shift catalyst with 1-butene hydroisomerisation catalysts since the 1980s [168], [169]. Furthermore, for instance, Fang et al. conducted a study exploring the enhancement of hydrogenation through a DeH mechanism by using a hydrophobic absorbent that was physically combined with Co-based catalysts, similar to the setting of DeH-HDO [170]. The goal was to simulate the reaction mechanism of a membrane in a specific local environment at the particle level in a fixed-bed reactor. The ongoing extraction of water through absorption enhanced the specific transformation. In addition, physical mixing was employed to combine a Fischer-Tropsch (FT) catalyst with a hydroprocessing catalyst in a single hybrid catalytic system. This was done to enable the direct conversion of syngas into transportation fuel using a two-step process in a single reactor. Furthermore, several works [171], [172], [174], [175] investigated the HDO of bio-oil derivatives in physically mixed catalytic systems, uncovering intriguing findings about the synergistic effects.

To maximise the HDO of phenol, guaiacol, and cresol and to raise the total HDO reactivity, Safaghat et al. used a physical mixture of palladium on carbon with a zeolite catalyst [177]. It was reported that the hydrogenation (HYD) of aromatic compounds occurs through direct HDO via hydrogenolysis (HDR) at metal-active sites, whereas dehydration (DeHD), hydrocracking (HDC), and alkylation/dealkylation mechanisms are regulated by acidic zeolite

[177]. When utilising zeolite alone in the case of phenol HDO, DeHD becomes difficult because phenol necessitates the saturation of the aromatic ring to form cyclohexanol through the metal active site. The DeHD mechanism involves the use of acidic zeolite, which results in a synergistic effect due to the combination of catalysts. Prabhudesai and colleagues showed that platinum supported on activated carbon exhibits superior HDO activity compared to other noble catalysts, resulting in the production of propyl cyclohexane. This activity was further enhanced by mixing the catalyst with acidic zeolite [174].

Physically mixed catalysts can be generated in several ways, such as particle mixing, powder mixing, or pelltizing or extruding, to create a single catalytic particle. Alternatively, the catalysts can be suspended in an aqueous phase, depending on the specific reaction requirements and kind of reactor. In this work, mechanically mixed catalysts are prepared by crushing and sieving commercial catalysts to an identical particle range to ensure uniform mixing. This chapter studies a 1:1 weight ratio of mixed catalysts in a single catalytic bed.

5.1.3 The potential role of dual active sites for DeH-HDO

This section explores the processes of alkane DeH-assisted HDO (in-situ) and conventional HDO (ex-situ) for MoO_3 and Cr/Al_2O_3 with a weight ratio of 1:1, which is consistent with the preceding chapter. Every catalyst has undergone extensive review in the literature for its respective reaction, as documented in Chapter 2 (Cr-based catalyst for alkane DeH and MoO_3 for HDO). The objective of coupling both reactions is to facilitate hydrogen transfer by establishing a synergy between the two reactions. This involves the utilisation of a single catalytic bed where both exothermic and endothermic reactions occur, allowing for efficient heat exchange in addition to H-transfer. However, a mix of two catalysts is hypothesised to introduce an additional synergistic dimension at a catalytic level, as illustrated in Figure 5.1. The presence of oxygen vacancies on the MoO_3 catalyst surface facilitates the HDO mechanism where oxygenated functional groups are adsorbed [96]. An effective method to promote the formation of vacancies in the catalyst is hydrogen reduction to extract surface oxygen by forming water.

On the other hand, the activity of the catalytic bed containing an active Cr-based catalyst may be impeded by excessive reduction, as experimentally demonstrated in Chapter 4. This inactivity is caused by H atoms attached to the metal active site instead of available oxygen, assuming a heterocatalytic dissociation of hydrogen where the split hydrogen atoms are

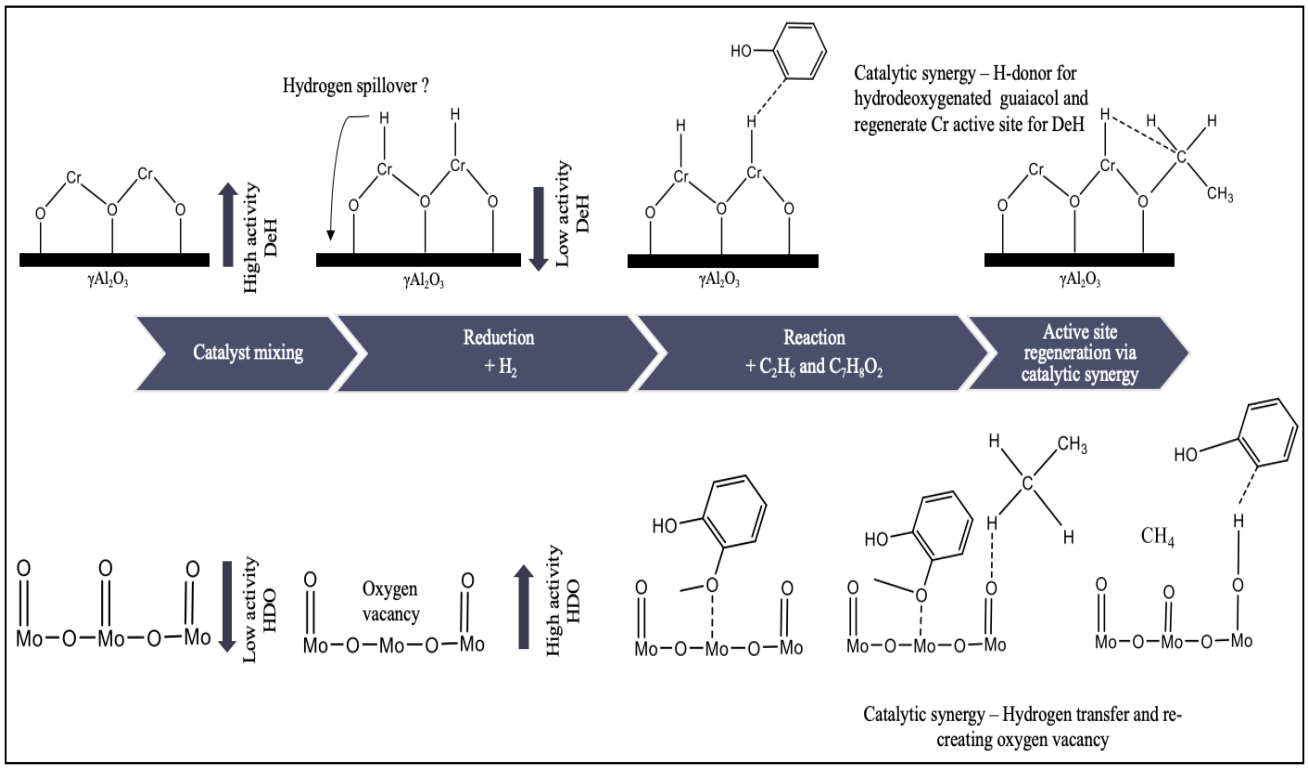


Figure 5.1: Targeted synergistic effects of mixing HDO and alkane DeH catalysts in a single catalytic bed

attached to the active sites and not the support [178]. Due to the absence of oxygen defects in the alumina-based support, it may be challenging for hydrogen linked to Cr to undergo H-spillover phenomena from the active site to the support. However, this phenomenon is controversial in regard of H-spillover to oxygen defect-free support. Prins claims H-spillover is energetically impossible in non-reducible support, but it can be developed with carbon formation or catalyst surface impurities [179]. However, Shen et al., in their review on the magic of hydrogen spillover, reported a study showing the possibility of H-spillover only near the active sites, unlike on reducible support, where spillover covers a larger distance [180].

It can be assumed that spillover does not occur at the beginning of the experiment, yet it happens via two mechanisms during the reaction. First, a dense layer of coke builds up as the reaction progresses. Secondly, the hydrogen atom that is adsorbed at the active site of Cr may react with the hydrodeoxygenated product that is produced on the surface of MoO_3. This mechanism recovers the activity of the Cr active sites for DeH. In addition, we can anticipate a reaction synergy on MoO_3, where the alkane DeH capabilities of the Mo active site can regenerate oxygen vacancy by selectively targeting the oxides in a redox catalytic cycle, as seen in Figure 5.1. Despite CrAL activity decreasing after hydrogen reduction, as illustrated in Chapter 7 Figure 4.19, an unreduced HDO catalyst yields a significant reduc-

tion in performance. Therefore, in this chapter, the catalytic system is reduced before the reaction and regulated by synergistic effects to reactivate the catalyst during the reaction.

5.1.4 Chapter structure

This chapter commences with a brief review of relevant literature regarding the utilisation of mixed catalytic systems for coupled reaction system in Section 5.1.1. Experimentally, this chapter explores the behaviour of mixed MoO_3-Cr_2O_3/Al_2O_3 (MoO_3-Cr) under various operational conditions, including alterations in flow rates and particle sizes as well as the extent of HDO for in-situ and ex-situ approaches, detailed in Section 5.2, where ex-situ and in-situ refer to the use of molecular hydrogen, and ethane DeH as hydrogen source, respectively. Subsequently, Section 5.3 investigates the impact of in-situ (DeH-HDO) for guaiacol and phenol across diverse operational conditions using PNiMo/Al_2O_3-Cr_2O_3/Al_2O_3 (PNiMo-Cr). In order to understand the causes for catalyst deactivation, Section 5.4 employs SEM to investigate the formation of coke deposition on CrAl and PNiMo-Cr. Section 5.6 provides a summary of the proposed reaction pathways, drawing insights from both Chapters 4 and 5. The chapter concludes by illustrating the integration of multiple reactors arranged in series, employing the cyclic operating method to achieve continuous catalyst regeneration in Section 5.7.

5.2 MoO_3-Cr catalytic system

In the evaluation of MoO_3-Cr catalytic system different operating condition were investigated as shown in Table 5.1. Case A is regarded as the reference point based on the optimised reaction parameters determined in Chapter 4.

HDO has exhibited exceptional performance for a duration of 120 min, with a molar ratio of 2.0 for ethane to guaiacol (Case A). However, the selectivity of BTX is limited to only 0.2%. Guaiacol conversion reaches over 95% within 20 min, but then decreases significantly to an average of 82% as depicted in Figure 5.2a. The system exhibited a high level of selectivity, resulting in the production of single-oxygenated aromatic compounds: phenol, anisole and cresol. The selectivity of these compounds was initially measured at 80%, with an average selectivity of 76% throughout the run. This results in a decrease in O/aromatic of 38%. However, the majority of the output does not consist of phenol due to methylation (MTH). The MTH of phenol exhibits a positive correlation with the progress of the reaction.

Table 5.1: Guaiacol conversion and liquid product selectivity of DeH-HDO using MoO_3-Cr catalytic system with total catalyst loading of 2.5 g

	Case A	Case B	Case C	Case D	Case E	Case F[1]
Liquid flow	GUA	GUA	GUA	GUA	GUA	GUA
$mol \cdot g_{cat}^{-1} \cdot h^{-1}$	0.054	0.054	0.054	0.027	0.054	0.054
Gas flow	C_2H_6	H_2	H_2	C_2H_6	C_2H_6	C_2H_6
$mol \cdot g_{cat}^{-1} \cdot h^{-1}$	0.10	0.16	0.10	0.05	0.10	0.05
Particle size, μm	150-212	150-212	150-212	106-150	106-150	106-150
GUA conversion, vol%	82.0	63.9	78.2	40.2	85.4	92.1
Product selectivity	vol%					
BTX	0.20	1.27	1.49	0.0	0.5	0.7
Phenol	28.5	24.9	21.4	22.1	19.1	80.9
Anisole	2.44	3.11	4.17	5.80	4.10	5.70
Cresol	32.4	30.8	34.1	34.1	33.8	5.05
M.Cresol	11.3	12.6	11.0	11.3	11.6	0.4
Catechol	20.3	23.1	23.4	23.1	26.1	1.32
M.catechol	2.03	2.46	2.58	0.9	2.80	2.53
Heavy	1.72	1.88	1.84	2.70	1.50	0.43

[1] catalyst weight is 5.0 g

Echeandia et al. explain the mechanism of methylation and de-methylation by attributing it to the presence of an acidic active site [177]. In this particular catalytic system, based on the literature the Cr active site is acidic. MTH in the coupled DeH-HDO reaction is initiated by an abundance of methyl radicals, which are produced through three distinct routes. The first route involves the direct demethoxylation (DDM) of guaiacol to produce methanol. However, under the given operating conditions, methanol may undergo DeHD, resulting in the formation of methane or dimethyl ether. Dimethyl ether was not detected in the experimental results; however, the mass balance indicates that the excess production of methane can be attributed to the presence of HDO. Secondly, methane is derived from HDO, and its presence can be detected when the production of gas grows over time due to the increased production of catechol through guaiacol demethylation. The third route is that ethane undergoes an undesired pathway either because of the catalyst active site or extended carbon formation, which results in thermal cracking.

5.2.1 The effect of replacing molecular hydrogen to ethane DeH

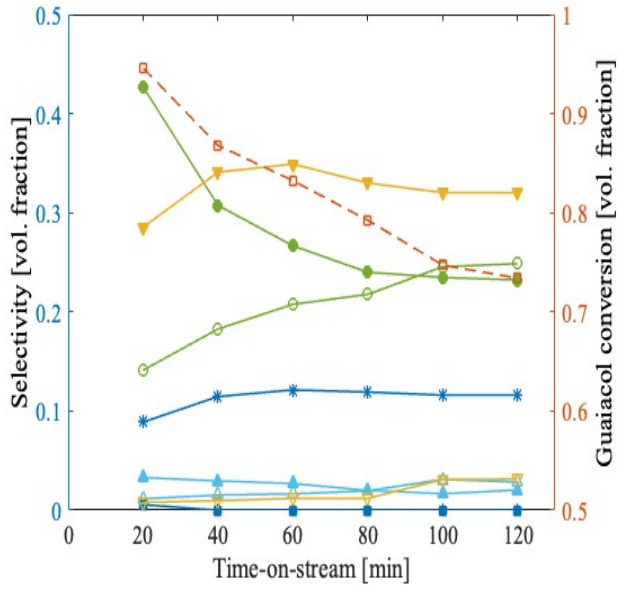
Continuing from the previous chapter, the assessment of in-situ versus ex-situ approaches is examined in Cases A-C. While the prior chapter confirmed the superior HDO performance of the in-situ approach over ex-situ using HDO catalysts within a single catalyst configuration. However, the same configuration reveals no discernible advantage in utilising an

in-situ approach for the alkane DeH catalyst, CrAl.

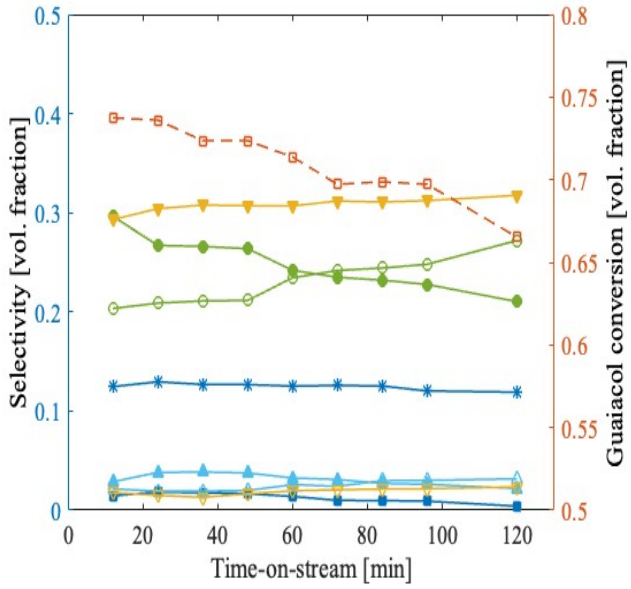
For the dual catalysts configuration, at similar liquid-to-gas flow (Case C) and catalytic bed conditions, in-situ hydrogen generation (Case A) has demonstrated better guaiacol conversion by 4.6% and less heavy hydrocarbon generation by 9.3% despite the limited hydrogen generation from ethane DeH in comparison to supplied molecular hydrogen, as shown in Table 5.1.

Furthermore, in terms of HDO, DeH-HDO (in-situ Case A) has resulted in 5.4% improvement over ex-situ (Case C) in terms of product selectivity, considering the total product yield, raising the improvement to 10.4% on an O/aromatic basis. This is proof of the higher reactivity of hydrogen available at the active sites. Another indication is the accumulation of heavy hydrocarbons, which is caused by limited HDO as a precursor for condensate and coke formation. These heavy hydrocarbons can be resulted from both phenolic compounds adsorbed and accumulated at the catalyst surface, or accumulated BTX leading to less observed BTX in the liquid product samples. Therefore, less BTX formation can be attributed to the rapid deactivation of in-situ hydrogen generation via alkane DeH which resulted in BTX growth to polycyclic aromatic (PAH). Therefore, BTX appears only at the beginning of each run and disappears, which reduced the average of 120 min to 0.2% in comparison to 1.5% at start of run (SOR).

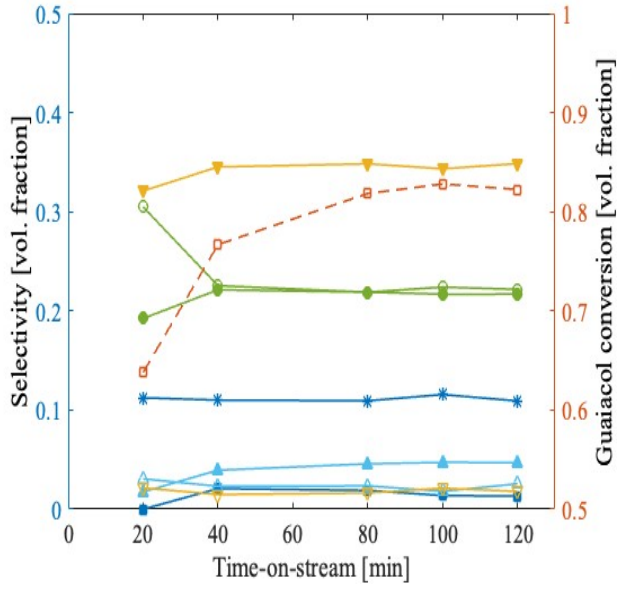
Furthermore, in terms of HDO, the DeH-HDO process (in-situ Case A) has shown a 5.4% enhancement in product selectivity compared to ex-situ (Case C), considering total product yield, translating to a 10.4% improvement on an O/aromatic basis. This underscores the higher reactivity of hydrogen accessible at the active sites. Another indicator is the accumulation of heavy hydrocarbons, a result of limited HDO as a precursor for condensate and coke formation. These heavier hydrocarbons may stem from phenolic compounds adsorbed and accumulated at the catalyst surface, or from accumulation of linked BTX forming PAH. The latter leads to reduced BTX observed in the liquid product samples. Consequently, diminished BTX formation can be attributed to the swift deactivation of in-situ hydrogen generation via alkane DeH, resulting in phenolic compounds and BTX growth to PAH. As a consequence, BTX is only present at the initial stages of each run and diminishes over time, reducing from 1.5% at SOR to an average of 0.2% after a 120-min run.



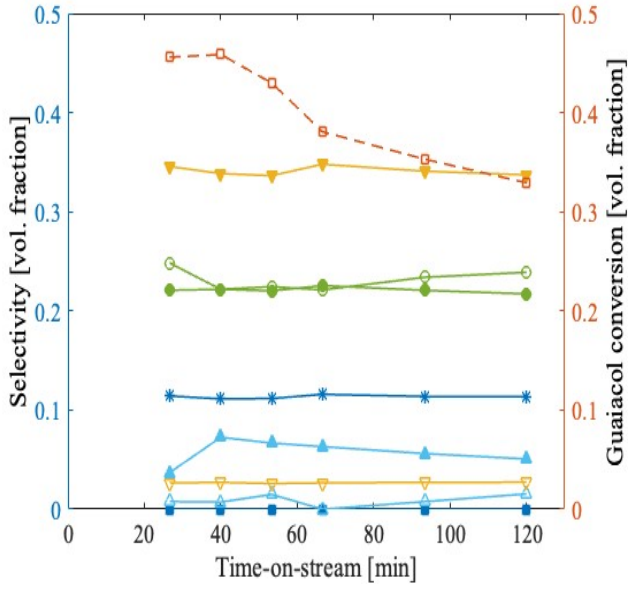
(a) Case A: Ethane 0.10, GUA 0.05 mol·g_{cat}^{-1}·h^{-1}



(b) Case B: H_2 0.16, GUA 0.05 mol·g_{cat}^{-1}·h^{-1}



(c) Case C: H_2 0.10 GUA 0.05 mol·g_{cat}^{-1}·h^{-1}



(d) Case D:Ethane 0.10 GUA 0.027 mol·g_{cat}^{-1}·h^{-1}

Figure 5.2: Atmospheric pressure HDO using MoO_3-Cr at 600 °C: [Right axis] Guaiacol conversion (□), [Left axis] BTX (■), Phenol(●), anisole (▲), cresol (▼), methyl cresol (★), catechol (○), methyl catechol (▽), and Heavy (△) selectivity.

To properly assess in-situ, several parameters were tested to improve the ex-situ to have a solid baseline and to understand the reaction routes. One approach was to increase hydrogen flow by 50% in Case B to reduce heavy and coke formation, which might lead to better BTX and HDO. A drastic reduction in conversion was observed, which is expected due to the short residence time, which limits guaiacol contact time to the catalyst surface. Yet, BTX and methylation were reduced. The former observation suggests that BTX requires longer residence time for oxygen removal due to the importance of the catalytic role. The latter observation, MTH, is attributed to transalkylation, where the methyl group in guaiacol is

re-positioned itself during or after HDO due to the absence of an external methane radical formed from ethane DeH in ex-situ approach. In short, in-situ performance in comparison to ex-sit suggests that MoO_3 has demonstrated a good degree of HDO with the provided hydrogen from Cr-based alkane DeH. However, still, ex-situ has 1% higher BTX on a selectivity basis. This BTX limitation is attributed due to the shorter residence for the coupled DeH-HDO, which requires longer time to accommodate both reactions, since both are catalytic.

5.2.2 Particle size effects

A further optimisation approach for the catalytic system involved reducing the particle size in order to eliminate mass transfer limitations for ethane, hence enhancing hydrogen production. Two catalyst ranges were examined in addition to the baseline range of 150-212 μm in order to evaluate the mass transfer restriction for DeH-HDO. These ranges are 106-150 μm and 45-106 μm. The latter range has exhibited severe pressure drop and catalyst blockage, leading to 106-150 μm (Case E) being the lowest possible particle range for DeH-HDO. The reduction in particle size lower than 106-150 μm led to a 3.0 bar rise in pressure drop across the catalytic bed within the initial 30 min of the reaction, which was comparable to the increase in pressure drop observed in the DeH alone run. The modification of the particle size of the catalytic bed to 106-150 μm led to favourable results in alkane DeH and HDO.

The guaiacol conversion reaches full completion within the first 60 min for particles ranging from 106-150 μm (Case E), but subsequently decreases significantly. Yet, the smaller particle size run has an overall higher guaiacol conversion by 4.1%, and more than double BTX selectivity. However, the overall selectivity of HDO in terms of oxygen-to-aromatic decreased due to the higher catechol formation, but there is a slight increase in yield due to the higher conversion of guaiacol. Moreover, lowering the particle size range has no additional effect on MTH, but a reduction in heavy formation was observed. The reported observation indicates a slight mass transfer resistance operating at the standard particle size. Therefore, moving forward 106-150 μm is used as the particle size for DeH-HDO.

5.2.3 Space velocity effect

In order to demonstrate the space velocity effects, an experiment was conducted with a lower space velocity (resulting in a longer residence time). This was achieved by reducing the flows of guaiacol and ethane by half while maintaining the same catalytic loading as in

Case D. Nevertheless, the overall HDO decreased as a result of guaiacol conversion, despite employing an identical gas-to-liquid molar ratio. As indicated previously, the conversion in guaiacol is to the liquid phase, which means a higher overall conversion of guaiacol is achieved, but to undesirable gas and solid production with 38% liquid recovery. Other runs have liquid recovery in the range of 72-81% caused by the loss of methyl and hydroxy groups as well as coke formation. To summarise, experimental observations have shown that a longer residence period when using alkane DeH might lead to the unwanted development of coke and undesirable methane formation. Hence, it is crucial to strategically configure the reaction parameter to maximise efficiency.

5.2.4 Molar ratio effect

To enhance performance, the catalytic bed was increased to 5.0 g (Case F), while maintaining a guaiacol flow rate of 0.05 mol·g_{cat}^{-1}·h^{-1}. The larger catalytic bed enhances the selectivity of guaiacol conversion towards a single oxygenated aromatic compounds. However, there has been no substantial variation observed in BTX generation, highlighting the challenging nature of converting phenol into BTX, which is also reported in the literature. Additionally, the difficulty in HDO of phenol also appears in the impact of ethylene formation; DeH was hindered due to the strong attachment of phenolic compounds on the catalytic surface, which eliminates ethane accessibility as shown in Figure 5.3.

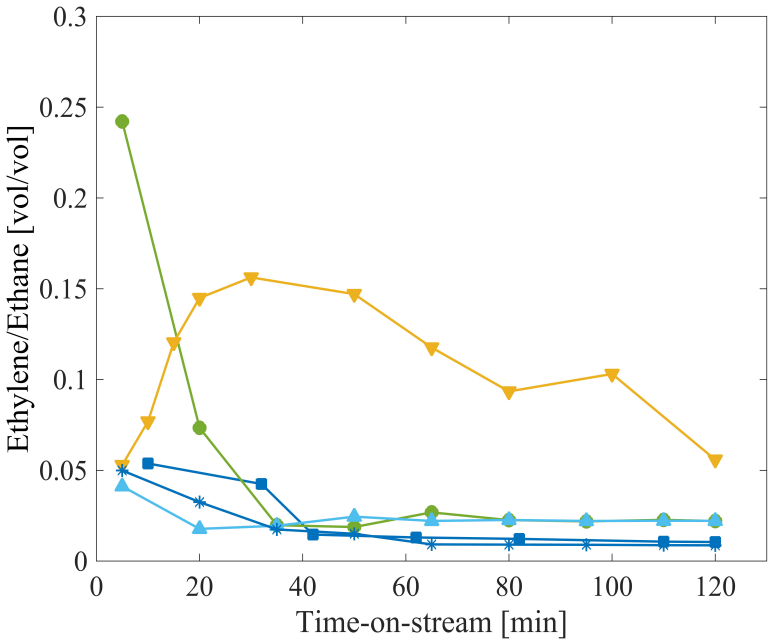


Figure 5.3: Ethylene-to-ethane ratio DeH and DeH-HDO using MoO_3-Cr at atmospheric pressure and 600 °C for (all flows in mol·g_{cat}^{-1}·h^{-1}): No guaiacol only 0.10 ethane (▼), guaiacol 0.027 and ethane 0.10 (●), 0.027 phenol and 0.05 ethane (★), 0.054 guaiacol and 0.1 ethane (■), 0.054 guaiacol and 0.1 ethane small particle size (▲)

Figure 5.3 presents the ethylene-to-ethane ratio under varying operating conditions for the MoO3-Cr catalytic system. All cases examined involve DeH-HDO, except for a reference case using only ethane for DeH. In the DeH-HDO cases, ethylene formation consistently declined, whereas DeH with 0.1 mol·gcat^{-1}·h^{-1} ethane initially exhibited an increase in ethylene production, followed by a gradual decline, primarily due to catalyst deactivation. Notably, the addition of 0.027 mol·gcat^{-1}·h^{-1} guaiacol to ethane resulted in a five-fold increase in initial ethylene formation; however, this was followed by a rapid decline to levels below those observed in the ethane-only DeH experiment. This rapid drop is attributed to quick deactivation caused by condensates, a common phenomenon across various catalytic systems. Doubling the guaiacol flow to 0.054 mol·gcat^{-1}·h^{-1} did not improve ethylene yield, likely due to the higher guaiacol-to-ethane ratio, highlighting the importance of ensuring sufficient hydrogen formation for HDO. Despite the sharp decline, the lower guaiacol-to-ethane ratio yielded better results. The influence of smaller particle size on the ethylene-to-ethane ratio demonstrated slight improvements during extended runs, despite moderate initial performance. This suggests that improving ethane accessibility to active sites by minimising mass transfer limitations could enhance performance, despite increased coke formation.

Limiting ethane access to the active site reduces ethylene formation in all cases investigated in Figure 5.3 under standard operating conditions compared to the non-guaiacol experiment. However, during experiments with longer residence times, initially, ethylene formation exceeded ethane DeH. This phenomenon could be attributed to improved hydrogen transfer resulting in higher ethane conversion. Nevertheless, this effect was significantly diminished due to severe coke formation reported in Case D. After 40 minutes, ethylene formation remains low and stable. The lower particle size range and longer residence time show slightly higher ethylene formation. Although the increase in ethylene formation is negligible, it underscores the importance of ethane accessibility to the active site, as these experiments are designed for enhanced contact with active sites. Therefore, to fully leverage the potential of coupling DeH-HDO, understanding and mitigating heavy hydrocarbon and coke deposition are crucial.

5.3 DeH-HDO in PNiMo-Cr catalytic system

5.3.1 Thermal and HDO catalytic effects

5.3.1.1 Guaiacol upgrading improvement with HDO active sites for DeH-HDO

HDO catalyst was mechanically mixed with alkane DeH catalyst in a 1:1 weight ratio with an overall catalytic bed of 2.5 g. This approach was considered to maximise the outputs of both reactions. In the comparison between the catalytic and thermal effects of a mechanically mixed catalytic system, the thermal effect experiment is represented by a total of 2.5 g of SiC and CrAl with a weight ratio of 1:1 (no HDO catalyst). The results are shown in Table 5.2. The results are classified in term of O/aromatic for the liquid yield and for the product (selectivity) at two stages for complete 120-min and 15-min runs. Overall, the reported result indicate the significant role of HDO catalyst over non-HDO system to improve oxygen removal mainly determined by increasing guaiacol conversion. Additionally, the HDO catalysts promote the selectivity towards phenol instead of catechol route.

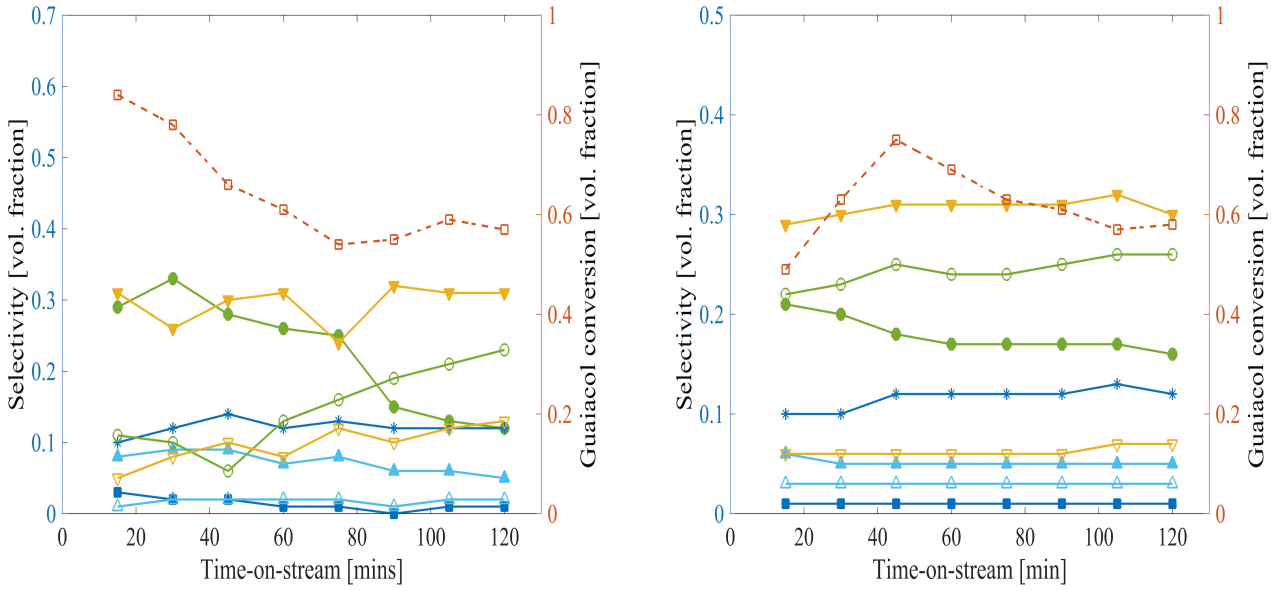
Table 5.2: Atmospheric pressure DeH-HDO of guaiacol at different catalytic systems at 600 °C with ethane flow of 0.10 mol·g_{cat}^{-1}·h^{-1} and guaiacol flow of 0.05 mol·g_{cat}^{-1}·h^{-1}

Catalytic system*	O/aromatic (yield)	O/aromatic (selectivity)	SOR[a] (yield)	SOR (Selectivity)
MoO_3-Cr	1.36	1.22	1.30	1.15
PNiMo-Cr	1.42	1.27	1.24	1.19
SiC-Cr	1.55	1.26	1.60	1.21

* The catalytic systems are compared on a mass basis.
[a] Start of run sample at 15-min.

The ability to adsorb oxygen at the catalyst active sites, the HDO catalyst—one of the two Mo-based catalysts—generally causes an increase in O/aromatic and HDO degrees in catalytic systems. However, as the process goes on, these oxygenated active sites saturate, reducing the amount of DDM (-OCH_3) and providing an easier path for demethylation (DME) (-CH_3). As a result, catechol selectivity rises as clearly shown in Figure 5.4 for PNiMo-Cr and SiC-Cr. With the presence of HDO active sites (PNiMo), phenol reduces and catechol builds up, whereas in "thermal" (SiC-Cr) where no HDO active sites are present, catechol is dominant. This indicates HDO active sites play a significant role along with reactive hydrogen in the extent of HDO. This proves the two routes HDO from guaiacol: (1) DDM and (2) DME followed by HDR.

Yet, the importance of HDO active sites, reduces with time despite its higher rate of hydrogen



(a) PNiMoAl-CrAl **(b)** SiC-CrAl

Figure 5.4: HDO of guaiacol via in-situ hydrogen generation from ethane DeH using PNiMo/Al_2O_3 -Cr/Al_2O_3 at atmospheric pressure, 600 °C and ethane flow of 0.1 mol·g_{cat}^{-1}·h^{-1} and guaiacol flow of mol·g_{cat}^{-1}·h^{-1} : [Right axis] Guaiacol conversion (□), [Left axis] BTX (■), Phenol(•), anisole (▲), cresol (▼), methyl cresol (★), catechol (○), methyl catechol (▽), and heavies (△) selectivity.

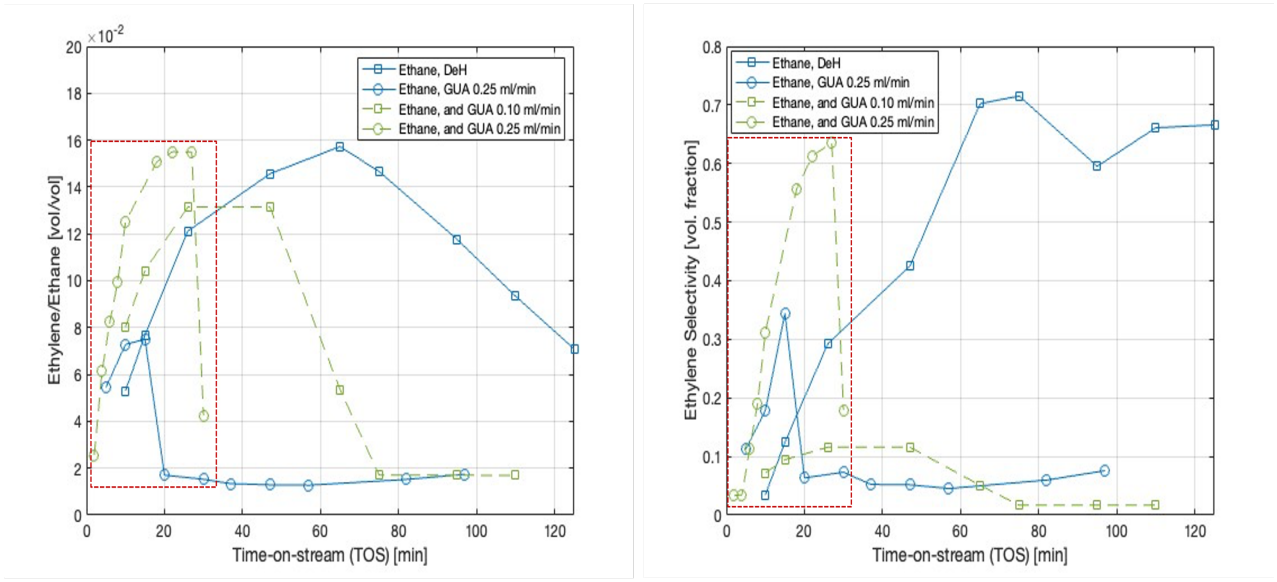
formation. At the end of 120-min both SiC-Cr and PNiMo-Cr have almost similar results. This similarity develops over time as the catalyst deactivates and hydrogen formation reduces. Therefore, both the rate of the production of reactive hydrogen and the availability of HDO sites are crucial to enhance the extent of HDO.

Overall, it is evident that the catalytic system with more HDO active sites (MoO_3) more active towards HDO as all of the catalytic systems in Table 5.2 have the same loading for alkane DeH. However, as previously mentioned Ni features HDR in HDO, thus, at the start of reaction (SOR) PNiMo-Cr exhibits a higher extent of HDO, which can be attributed to the presence of Ni, which also causes hydrogen formation via cracking mechanisms. As Ni active sites deactivate, HDO performance remains on thermal and molybdenum-based active sites which leads to lower HDO for the overall 120-min run.

5.3.1.2 Ethylene formation improvement with DeH-HDO

Alkane DeH was evaluated for the selected catalyst bed to determine hydrogen formation as well as the progress of ethylene/ethane. Initially, the ethylene/ethane ratio was low, which was related to ethylene selectivity led by methane formation. Methane was formed from the hydrotreating catalyst since the CrAL catalyst is selective. The initial value for the ethylene/ethane ratio was improving until it peaked at roughly 65 min. The ethylene

selectivity started below 10% due to the existence of Ni, which dominated and accelerated C-C cleavage, and coke formation, which blocked the active sites from ethane DeH. Therefore, ethylene selectivity couldn't exceed 70%.



(a) [Ethylene][Ethane]$^{-1}$ ratio **(b)** Ethylene-to-hydrocarbon selectivity

Figure 5.5: Atmospheric HDO of guaiacol using ethane DeH as a hydrogen donor reaction at 600 °C: Guaiacol 0.05 mol·g_{cat}^{-1}·h^{-1} and ethane 0.10 mol·g_{cat}^{-1}·h^{-1} through a 2.5 g catalytic bed of PNiMo-Cr (1:1 weight ratio)

Flowing guaiacol into the system to remove hydrogen via HDO increased the ethylene-to-ethane ratio at 0.25 and 0.1 mL·min^{-1} at the beginning of the experiment, as illustrated in Figure 5.5. Feed saturation at the catalytic bed active site caused a sharp reduction in the ethane/ethylene ratio because it restricts ethane accessibility to the active sites. The decline was shifted on time with lowering GUA flow from 0.25 to 0.1 mL·min^{-1}. With more frequent sampling at the start of the experiment, the increase in ethylene/ethane was clearly seen at 0.25 mL·min^{-1}. In addition, similarly, the DeH with guaiacol improved ethylene selectivity, and the sharp decline can be reasoned by the increase in methane formation from the HDO of GUA. Yet this limitation has not totally blocked ethane DeH as produced ethylene is more than that formed from thermal DeH. When comparing DeH-HDO to only DeH, the in-situ hydrogen contribution in HDO is evident in the hydrogen-to-ethane ratio.

5.3.2 DeH-HDO improvement via reducing partial pressure?

In the previous sections, it was hypothesised that the fundamental cause for the limited synthesis of BTX is the lack of sufficient reactive hydrogen. This hypothesis was based on the observation that runs with excess molecular hydrogen (ex-situ) showed slightly better

formation of BTX, but in-situ has greater extent of overall HDO. The decrease in BTX is gradual and is similarly linked to the decrease in ethane conversion, resulting in a decrease in reactive hydrogen on the active sites of the catalyst. Consequently, to improve the production of ethylene and hydrogen ethane partial pressure reduction is employed by utilising nitrogen as an inert gas. This approach is employed to favours the thermodynamic pressure for ethane DeH.

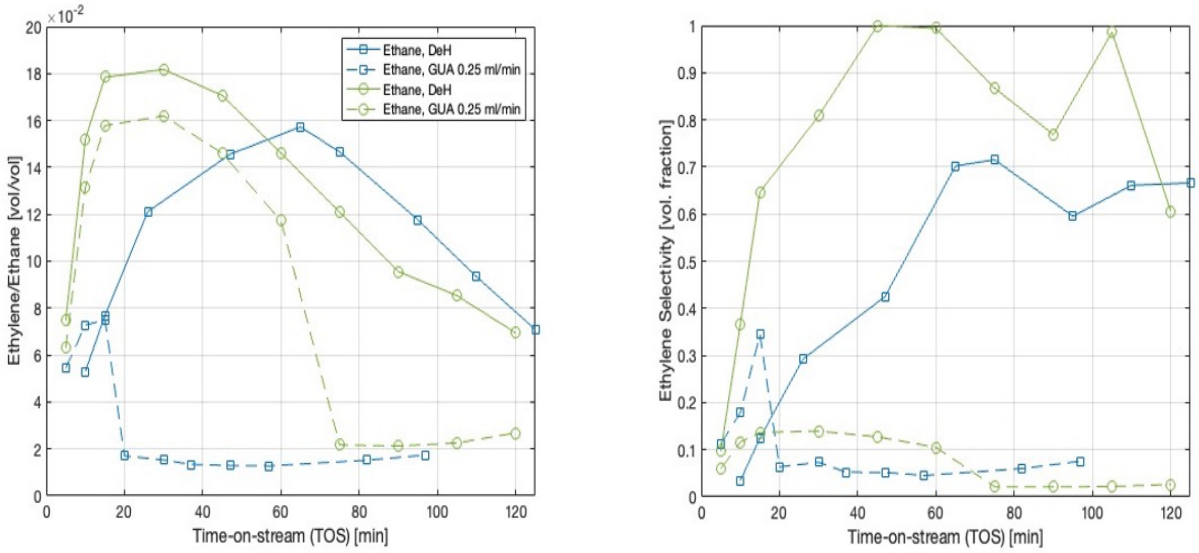
Table 5.3 demonstrates the effectiveness of conducting alkane DeH in an inert atmosphere, as opposed to a non-diluted ethane experiment, utilising Cr-based catalysts. The presence of nitrogen enhances the conversion of ethane and the selectivity towards ethylene. As a result, the ratio of ethylene to ethane is improved.

Table 5.3: The effectiveness of operating alkane DeH at reduced ethane partial pressure for PNiMo-Cr catalytic system at 600 °C in nitrogen environment.

Catalytic system		PNiMo-Cr	CrAL	CrAL
C_2H_6 inlet flow	$mol{\cdot}g_{cat}^{-1}{\cdot}h^{-1}$	0.1	0.1	0.05
C_2H_6 partial pressure	bar	0.4	0.4	1.0
C_2H_4 conv.	vol%	13.7	18.1	13.3
C_2H_4 selec.	vol%	79.6	96.7	83.6
C_2H_4/C_2H_6	vol/vol	0.126	0.222	0.129

The non-improved conditions for ethane DeH mechanism used in DeH-HDO yields the formation of methane, where ethane DeH favours reduced pressures. However, the purpose of initiating the ethane flow at atmospheric pressure is to accommodate reactions that have varied preferred pressure conditions. The addition of PNiMo catalyst to the catalytic system decreases the average ethylene conversion for a 120-min run. This is because the presence of Ni at the start of the reaction causes deactivation, which initiates a C-C cleavage mechanism resulting in the formation of methane. This phenomena reduces as Ni active sites is blocked be carbon formation. The incorporation of a CrAL catalyst with the PNiMo-Cr system is crucial for sustaining the DeH mechanism involved in the synthesis of ethylene and reactive hydrogen. As shown in Figure 5.6, the PNiMo-Cr catalytic system is also employed under atmospheric pressure to evaluate its efficacy for DeH-HDO, even though the CrAL catalyst is preferred for ethane DeH. As demonstrated by earlier observations, DeH-HDO temporarily increases DeH before quickly deactivating due to coke deposition.

Additionally, as shown in Figure 5.6, lowering ethane partial pressure with an inert increases ethane DeH when guaiacol is absent. This first enhances ethylene rates but is later

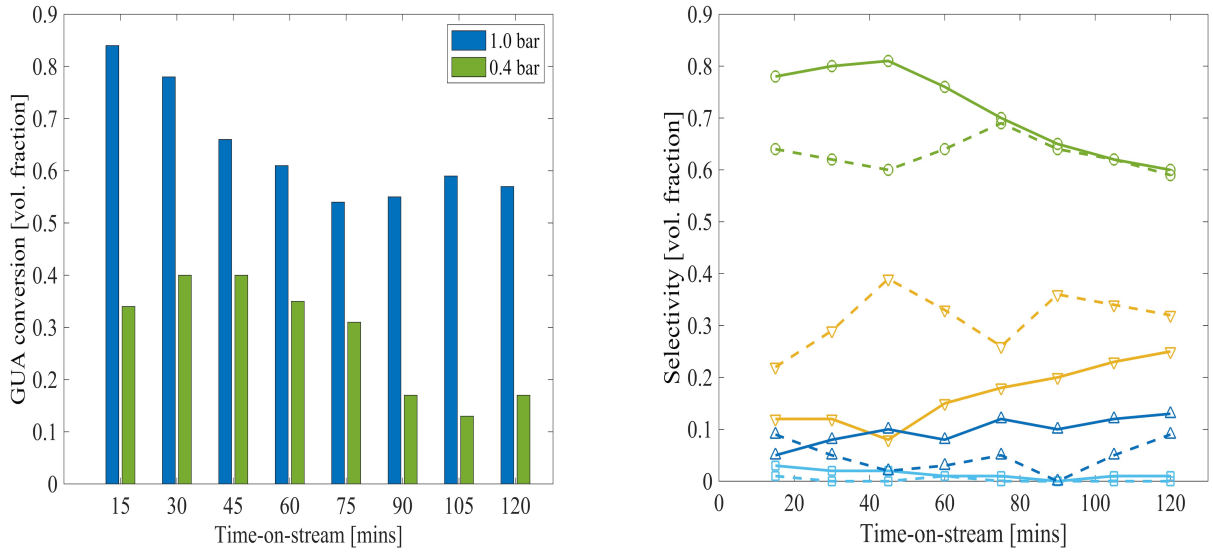


(a) [Ethylene][Ethane]$^{-1}$ ratio **(b)** Ethylene selectivity

Figure 5.6: Atmospheric HDO of guaiacol using ethane DeH as a hydrogen donor reaction at 600 °C: Guaiacol 0.05 mol·g_{cat}^{-1}·h^{-1} and ethane 0.10 mol·g_{cat}^{-1}·h^{-1} through a 2.5 g catalytic bed with of PNiMo-Cr (1:1 weight ratio). [Green] Diluting in nitrogen at ethane partial pressure 0.4 bar, whereas [Blue] no nitrogen.

hindered by condensate and coke formation. Though guaiacol showed promise overall in terms of gas production, the improvement in ethane DeH disappeared when it was introduced at a lower reaction partial pressure. Nitrogen addition causes the conversion to take place earlier and the sharp ethylene reduction to be delayed by 60 min, indicating that lowering the partial pressure reduces coke formation for the DeH and DeH-HDO. As seen in Figure 5.7, this delay is ascribed to the decreased degree of HDO brought on by operating at a lower pressure and the shorter residence time. The produced liquid indicated considerable effects on both selectivity to single oxygen per aromatic ring (SOAr) and guaiacol conversion. When the ethane partial pressure dropped and the selectivity of double oxygen per aromatic ring (DOAr) rose, the guaiacol conversion fell by 56%. Consequently, when operating at reduced ethane partial pressure, there is a trade-off between maximising DeH and HDO.

While there was a notable enhancement in ethylene formation observed in DeH-HDO processes, operating at atmospheric pressure had adverse effects on HDO selectivity towards SOAr and BTX, as discussed in Chapter 4. Elevated pressure experiments had better presence for BTX, yet with limited guaiacol conversion. Low partial pressures, explored in this section, also led to further HDO selectivity. Nonetheless, DeH-HDO with ethane remains preferable to the use of molecular hydrogen. Furthermore, HDO conversion does not dis-



(a) GUA conversion **(b)** HDO selectivity

Figure 5.7: Atmospheric pressure HDO of guaiacol via in-situ hydrogen generation from ethane DeH using PNiMo-Cr at 600°C, ethane flow of 0.1 mol·g_{cat}^{-1}·h^{-1}, 0.05 mol·g_{cat}^{-1}·h^{-1}: [Right figure] BTX (□), SOAr (◯), DOAr (▽) and HOHC (△) selectivity: [Solid] 1.0 bar and [Dashed] 0.4 bar

play detrimental effects with low pressure across all investigated cases, as the targeted mechanisms do not entail hydrogenating the aromatic ring, typically necessitating higher pressure. Instead, targeted de-methylation and demethoxylation rely on active site availability and reactive hydrogen. The reduction in demethoxylation suggests competition between both mechanisms at the active site, thus highlighting the potential for improved reaction performance with enhanced demethoxylation activity.

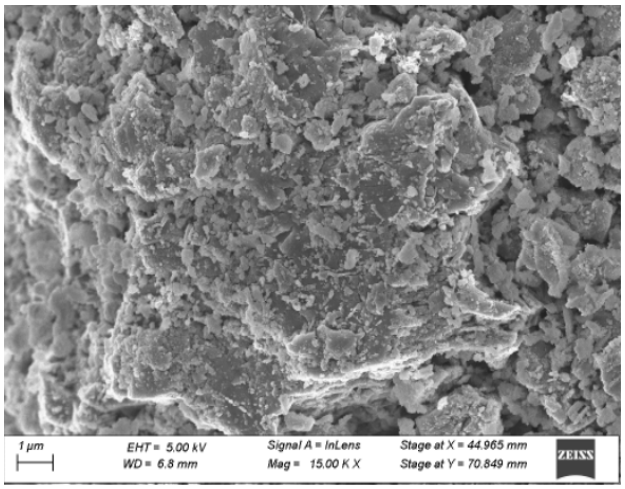
5.4 Coke formation investigation under SEM

TGA analysis confirmed the substantial deposition of coke and condensate on the catalytic surface. Yet, SEM was utilised to gain further insight on the spent catalysts of alkane DeH and DeH-HDO for CrAl and PNiMo-Cr catalytic system as depicted in Figure 5.8 and Figure 5.9.

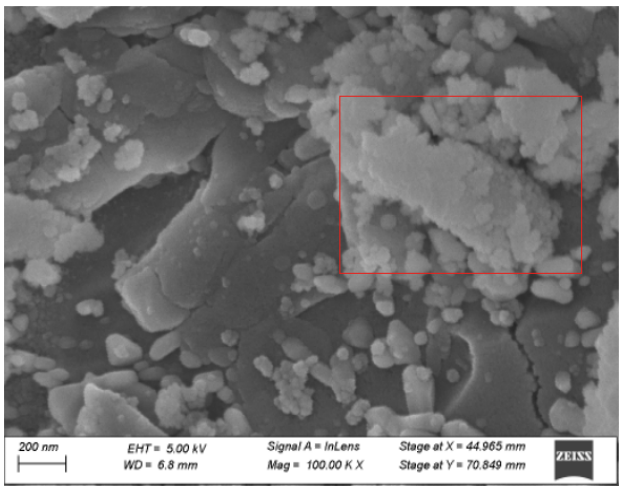
5.4.1 Coke formation on CrAl in a single catalytic system

In the case of ethane DeH spent catalysts, the SEM images revealed the presence of chromate clusters and/or amorphous coke. The clustering of active chromium oxide sites underscores the dominance of crystalline Cr_2O_3/Al_2O_3 on the alumina support. Furthermore, since chromium serves as the active site for DeH, these clusters of metal active sites may have been coated by coke, thus inhibiting their reactivity, as shown in Figure 5.8b. The clustering itself leads to reduced activity by diminishing the total surface area of active sites.

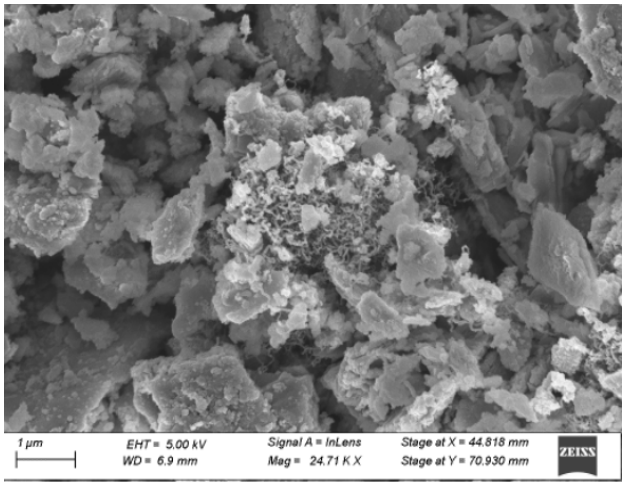
Additionally, filamentous coke was also observed in the ethane DeH experiment without HDO, as depicted in Figure 5.8c and 5.8d. This type of coke, formed by methane and alkanes, occurs when carbon diffuses through the metal active sites during the adsorption and dissociation process [181]. Filamentous coke anchors the active sites and forms condensed networks, indicating the extent of carbon formation. However, this phenomenon was not as easily observed in the P-NiMo catalyst, which will be discussed in the next section.



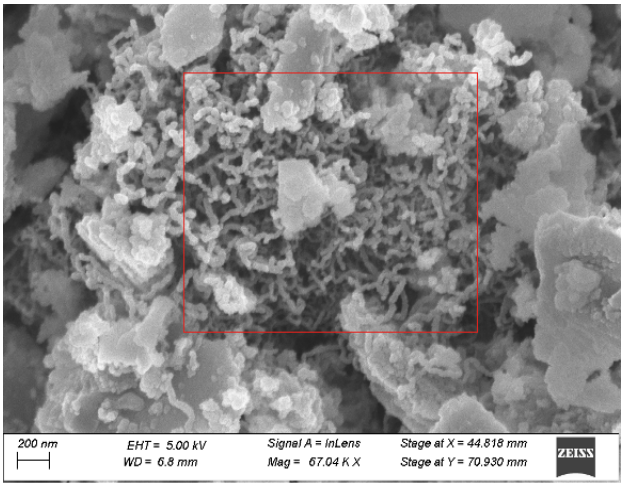
(a) DeH Spent catalyst



(b) DeH Spent catalyst



(c) DeH-HDO Spent catalyst

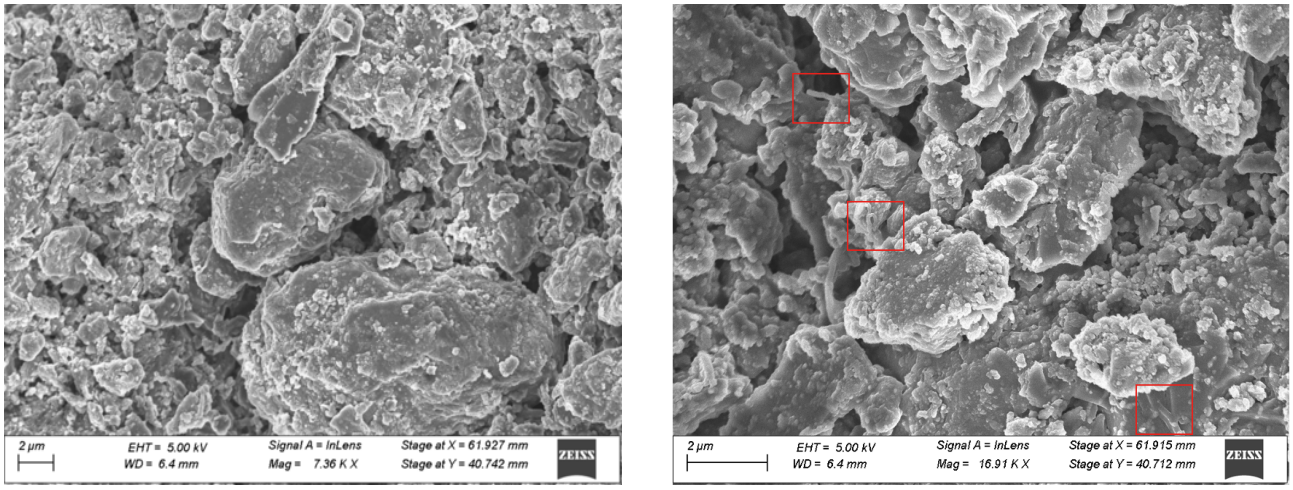


(d) DeH-HDO Spent catalyst

Figure 5.8: SEM Images of spent catalysts of atmospheric pressure ethane DeH using CrAl at GHSV of 0.17 mol·g_{cat}^{-1}·h^{-1}

For the DeH-HDO run, clustering and filamentous coke were challenging to detect, despite the presence of a large coke content as indicated by TGA. This observation suggests the presence of a third type of coke, likely resulting from interactions with heavy aromatic structures, such as pyrolytic coke. Pyrolytic coke may encompass the condensed aromatic network on the catalyst surface, including the active sites and support. This observation is supported by the condensed polyaromatic rings and coke observed in the DeH-HDO experiment. Furthermore, Figure 5.9b reveals several spots where filamentous coke appears to

be impeded on the surface, most likely forming a layer of pyrolytic coke. This layer, covering the entire catalyst's surface, significantly reduces the conversion of both DeH and HDO, as access to the active sites becomes limited. Additionally, the catalytic role of the acidic alumina support diminishes as the layer thickness increases with higher deposition rates.



(a) DeH Spent catalyst **(b)** DeH Spent catalyst

Figure 5.9: SEM Images of spent catalyst of atmospheric pressure DeH-HDO using CrAl at ethane and guaiacol for 0.17 mol·g_{cat}^{-1}·h^{-1}, 0.17 mol·g_{cat}^{-1}·h^{-1}, respectively.

Energy Dispersive X-ray Spectroscopy EDS is commonly employed to ascertain the distribution of active sites and the deposition of coke. Specifically, elemental composition was quantified by analysing various spots within 20 μm areas, as indicated in Table 5.4. The high level of carbon observed by SEM-EDS aligns with the TGA findings indicating that the amount of carbon formed exceeds 0.3 g per g of catalyst. This high coke production demonstrates the coke accumulating on both active site and support. Additionally, another mechanism can be identified by measuring the weight-based ratio of Cr/C. A larger value suggests a greater number of active sites for Cr at a specific location, providing evidence for the proposed process of catalyst sintering with reduced surface area for carbon deposition. Spot 4, and 5 indicates two and nearly twelve times increase in Cr/C ratio, respectively, based on the average of 0.22. Thus, to summarise, much carbon formation occurs during DeH-HDO, similar to typical hydroprocessing processes. Consequently, the reduction of coke formation becomes a crucial objective for the success of coupling DeH-HDO.

5.4.2 Coke formation on PNiMo-Cr catalytic system

The catalytic system of PNiMo-Cr on alumina comprises two distinct catalysts that are mechanically combined. The preceding section examined the Cr_2O_3/Al_2O_3 compound using SEM. Thus, this section specifically concentrates on PNiMo in the PNiMo-Cr catalytic sys-

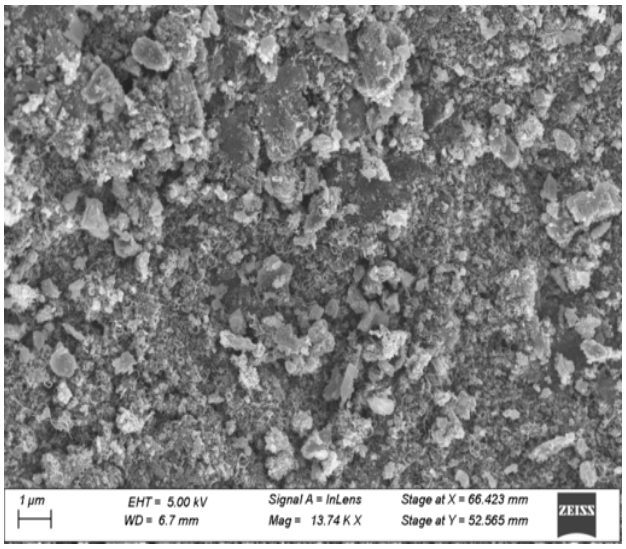
Table 5.4: EDS Elemental composition on a DeH-HDO spent catalyst using Cr_2O_3/Al_2O_3 at 600 °C, in wt%.

Spot	C	O	Al	Cr	Cr/C (wt/wt)
1	35.2	40.7	15.2	8.14	0.23
2	31.3	48.5	14.4	5.17	0.17
3	30.4	45.0	15.7	6.88	0.23
4	37.6	30.3	11.8	19.8	0.53
5	15.5	25.3	19.9	39.3	2.53
6	32.0	43.5	16.9	7.01	0.22

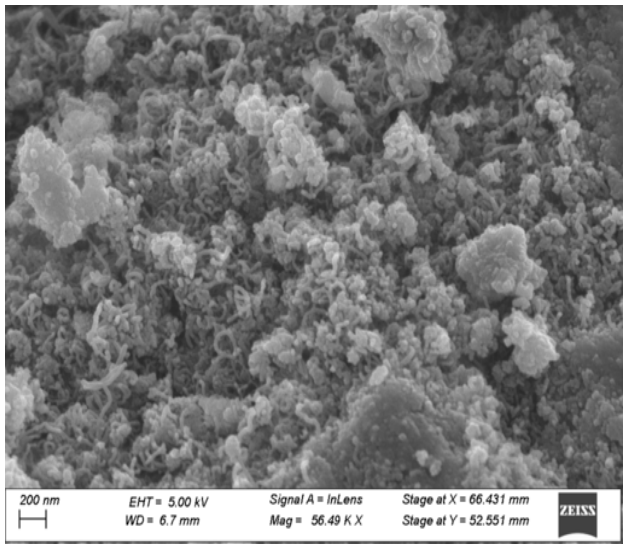
tem identified using SEM spot using EDS. Consequently, EDS was employed to precisely identify the PNiMo catalyst particles for SEM imaging and to gain an understanding of the uniformity of Ni and Mo active sites on the alumina support. EDS verifies the homogeneous dispersion of active sites in NiMo, as confirmed by Anastassia's research [146], which includes SEM images of the catalyst in its initial state. The present study did not examine the fresh catalyst due to the adverse charging impact caused by its excessive metal loading. The attempt to coat Pt was unsuccessful in resolving the issue, resulting in the production of a low-quality image.

In contrast to the CrAL catalyst, the SEM pictures of PNiMo reveal substantial filament coke formation during ethane DeH without guaiacol run, leading to a significant change in the catalyst morphology. This phenomenon is primarily attributed to the existence of a Ni active site, where comparable behaviour has been extensively investigated in the context of steam and catalytic biomass reforming [182], [183]. Furthermore, the phenomenon of clustering is evident in Figure 5.8b as areas of lighter agglomerated spots. These spots consist of either clusters of metal active sites that are covered by coke or metal active sites that have evolved on filamentous coke generated from the dissociation of C-C bonds. Ochoa et al. conducted a review on coke derived from catalytic reforming of biomass. They concluded that in the process of ethylene generation, amorphous and encapsulating coke serve as intermediate stages before filament coke is formed [182]. This mechanism explains the reduced development of filamentous coke when using CrAL catalyst in single-metal oxide runs, with amorphous coke being the predominant form. Although there are variations in the active sites, the spent catalyst of Cr was examined for a run at 550 °C, while this observation was made on PNiMo at 600 °C. Typically, filament coke is identified in processes that occur at rather high temperatures.

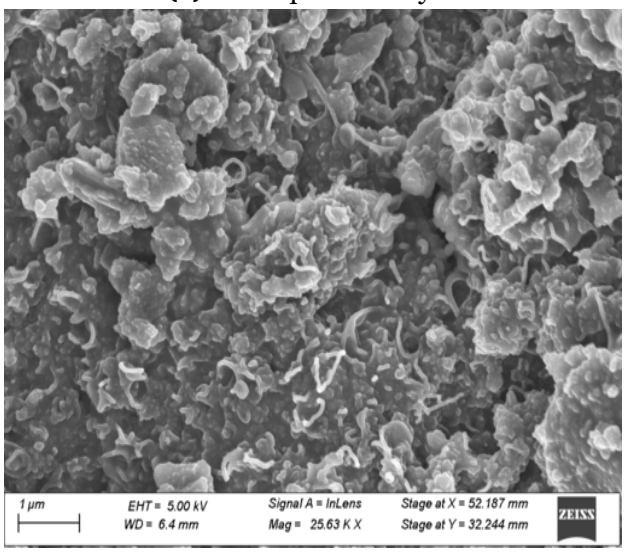
From the reaction perspective, the significant increase in filament coke formation is the



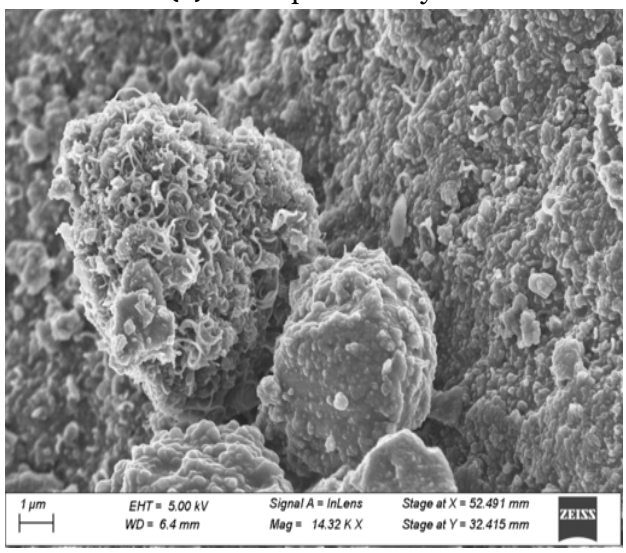
(a) DeH spent catalyst



(b) DeH spent catalyst



(c) DeH-HDO spent catalyst



(d) DeH-HDO spent catalyst

Figure 5.10: SEM Images of spent catalyst of PNiMo-Cr with 1:1 weight ratio: atmospheric pressure ethane DeH (a and b), and guaiacol HDO with alkane DeH as hydrogen donor for (c and d).

main reason for the noticeable decrease in ethane conversion when utilising the PNiMo catalyst. This decrease is attributed to the dissociation of C-C bonds, which is supported by the strong initial production of methane that limits the selectivity towards ethylene. When employing DeH-HDO, as depicted in Figures 5.10c and 5.10d, filament coke is still observed, albeit at a reduced density compared to ethane DeH. This observation is consistent with the Cr-active site, despite the variation in intensity. Therefore, this observation indicates that the formation of pyrolytic coke, which originates from the HDO feed and builds up on both the catalyst support and active sites, reduces the presence of other types of coke and mitigates its detrimental impact on reactivity.

As indicated in Table 5.5, TGA quantifies the increased coke production seen in SEM. Ap-

parently, for a 120-minute run, ethane DeH has minimum coke deposition on investigated catalysts in comparison with the coupled DeH-HDO. CrAl yields 0.047 g of carbon per g of catalyst, whereas the catalytic system of PNiMo-Cr has 0.063. This aligns with the hypothesis that Ni presence contributes to C-C cleavage and accelerates the deactivation by coke deposition. According to DeH-HDO, guaiacol flowing at 0.02 or 0.05 mol·g_{cat}^{-1}·$h^{-1}h^{-1}$ produces comparable coke deposition, meaning that even at low guaiacol flow rates, coke deposition saturated the catalyst surface. No further reduction in guaiacol was investigated. Nonetheless, the results of the 30-minute short-run experiment showed that the carbon deposition rate did not correlate linearly with time-on-stream (TOS), with a higher deposition rate at the beginning of the run yielding 0.188 g of carbon per g of catalyst. As a result, the short-term cyclic catalyt regeneration process DeH-HDO could decrease the challenges associated with carbon deposition and ensuing carbon losses.

Table 5.5: Quantification of coke and condensate deposition on PNiMo-Cr using TGA for guaiacol flow of 0.05 mol·g_{cat}^{-1}·h^{-1} and ethane 0.1 mol·g_{cat}^{-1}·h^{-1} with 2.5 g catalytic bed

Catalyst	PNiMo-Cr[a] DeH-HDO	PNiMo-Cr DeH-HDO	PNiMo-Cr[b] DeH-HDO	PNiMo-Cr DeH	CrAL DeH
Condensate, g/g_{cat}	0.102	0.128	0.256	-	-
Coke, g/g_{cat}	0.427	0.477	0.188	0.063	0.047

[a] Guaiacol flow 0.02 mol·g_{cat}^{-1}·h^{-1}
[b] short run 30-min

5.5 Discussion on the production of BTX and its limitations

The primary objective of upgrading lignin-derived bio-oil to chemicals through HDO is the production of high-value BTX. This has been achieved in several published works through using external hydrogen, with reported limitations. Furthermore, in the preceding chapter, it was documented that BTX was detected at a comparatively low pressure (25 bar) when compared to standard HDO pressure of 100-200 bar. Furthermore, operating at unfavourable HDO conditions where pressure is reduced to atmospheric makes the production of BTX challenging. However, this does not imply that the conversion of HDO to BTX cannot happen. It just requires a suitable catalytic system to ensure that the desired product selectivity is directed towards BTX. The creation of BTX is directly influenced by the degree of HDO, which is catalytically driven. This relationship has been experimentally demonstrated in the previous section, utilising various catalysts or catalytic systems. Figure 5.11 depicts the decrease in BTX production over time using MoO_3-Cr_2O_3/Al_2O_3 (Case B in Table 5.1). Similar behaviour was observed in the previous chapter: working at elevated pres-

sure, BTX formation reduces with time, where the catalytic active surfaces suffer complete or partial deactivation. In Figure 5.11, in 120 min, the selectivity of BTX was reduced by 73%. Considering a short run for 60 mins, the overall BTX selectivity increases by 2.5% but at different compositions.

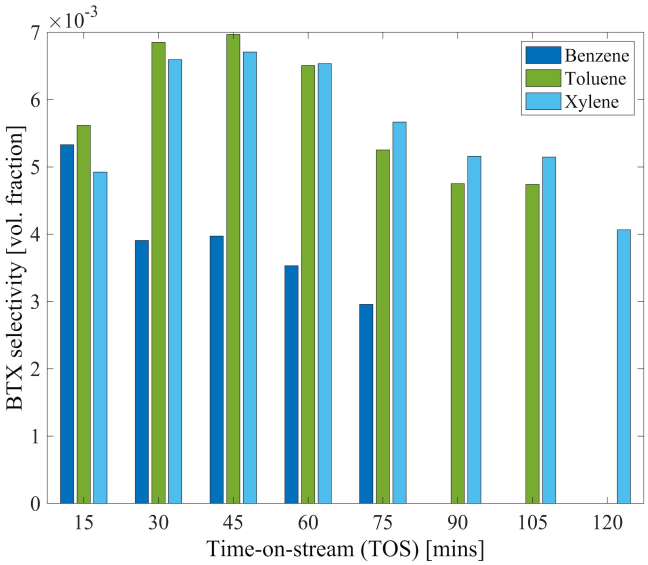


Figure 5.11: Atmospheric pressure HDO of guaiacol via ex-situ using MoO_3-Cr catalytic system at 600 °C

When examining BTX, it is seen that each compound has a distinct rate of decay. The elimination of benzene is not caused by the termination of the degree of HDO towards non-oxygenated aromatic compounds. Instead, transalkylation has become the dominant mechanism. The transkylation process continues to be active since HDO exhibits enhanced selectivity towards catechol as the reaction proceeds, which is an undesirable route. This implies that methane radicals are still being produced by the cleavage of O-CH_3 in the guaiacol methoxy group even after 120 min, contributing to more transalkylation. Transalkylation reactions typically persist even when oxygenated aromatics like phenol and catechol are involved, resulting in the formation of cresol, methyl cresol, and methyl catechol. The transalkylation of BTX is not a significant concern in terms of HDO. However, it becomes crucial when aiming for chemical production, as the value and downstream processing of these chemicals vary.

Table 5.6 includes different BTX selectivity at different stages of the reaction. As with ex-situ, there is a drop in BTX in-situ as well, but this drop is significant. The lack of hydrogen needed to facilitate HDO for BTX production is assumed to be the root cause of this decrease. After the catalyst surface is saturated by heavies, the formation of reactive hydrogen from

ethane DeH becomes constrained due to reduced accessibility of active sites. The hydrogen generation remains constrained to thermal cracking of ethane.

Table 5.6 shows a severe reduction of BTX selectivity in PNiMo-Cr or MoO_3-Cr catalytic systems via in-situ, where ex-situ reduction is gradual. As shown in Table 5.6, the PNiMo-Cr catalytic system has better BTX formation in in-situ, which is also linked to a higher rate of heavy hydrocarbons. Since heavies are double aromatics with one or less oxygen per aromatic, this indicates greater extent to HDO limited by reactive hydrogen that reduced the coupling of these aromatic ring molecules. Therefore, improving the accessibility to reactive hydrogen yields a potential for higher BTX and reduction of heavies.

Table 5.6: BTX, double aromatic (Heavy) products in term of selectivity and coke production at different catalytic systems using a gas feed flow, and guaiacol flow of 0.10 and 0.05 $mol{\cdot}g_{cat}^{-1}{\cdot}h^{-1}$, respectively

Catalytic system*	Flow	SOR[a] %	MOR[b] %	EOR[c] %	Heavy %	Condensate g/g_{cat}	Coke g/g_{cat}
PNiMo-Cr	C_2H_6	3.44	1.03	1.05	4.65	0.128	0.477
MoO_3-Cr	H_2	0.0	2.30	1.32	1.81	0.0214	0.208
MoO_3-Cr[d]	H_2	1.44	1.66	0.41	1.88	-	-
MoO_3-Cr	C_2H_6	0.55	-	-	1.83	0.197	0.184

* The catalytic systems are compared on a mass basis.
[a] SOR sample at 15-min, [b] middle of run (MOR) sample, [c] end of run (EOR) at 120-min.
[d] H_2 0.16 $mol{\cdot}g_{cat}^{-1}{\cdot}h^{-1}$

5.6 Proposed reaction pathway for DeH-HDO

Figure 5.12 depicts the potential pathways reported in the literature and this study. The operating conditions of this investigation did not detect any aromatic ring hydrogenation, and the HDO was terminated by the formation of BTX. The formation of anisole indicates that guaiacol undergoes HDR, despite the fact that the elimination of the methoxy group requires less energy.

This observation implies that active sites contribute to HDO, which is reduced by catalytic deactivation at the conclusion of the reaction, as depicted in Figure 4.15 and Figure 4.18 for the two catalytic systems Ni-Mo/Al_2O_3 and MoO_3, respectively. Therefore, the catalytic activity may directly produce phenol from guaiacol via DDM. DDM induces the formation of methanol at a negligible rate under the studied operating conditions. Methane formation in the gas stream confirms that DME is the dominant pathway, as suggested by the formation of catechol and a small amount of methanol. Ex-situ MTH was observed via re-distribution of the methyl group; in-situ MTH is promoted to a greater degree by alkane DeH. The elimi-

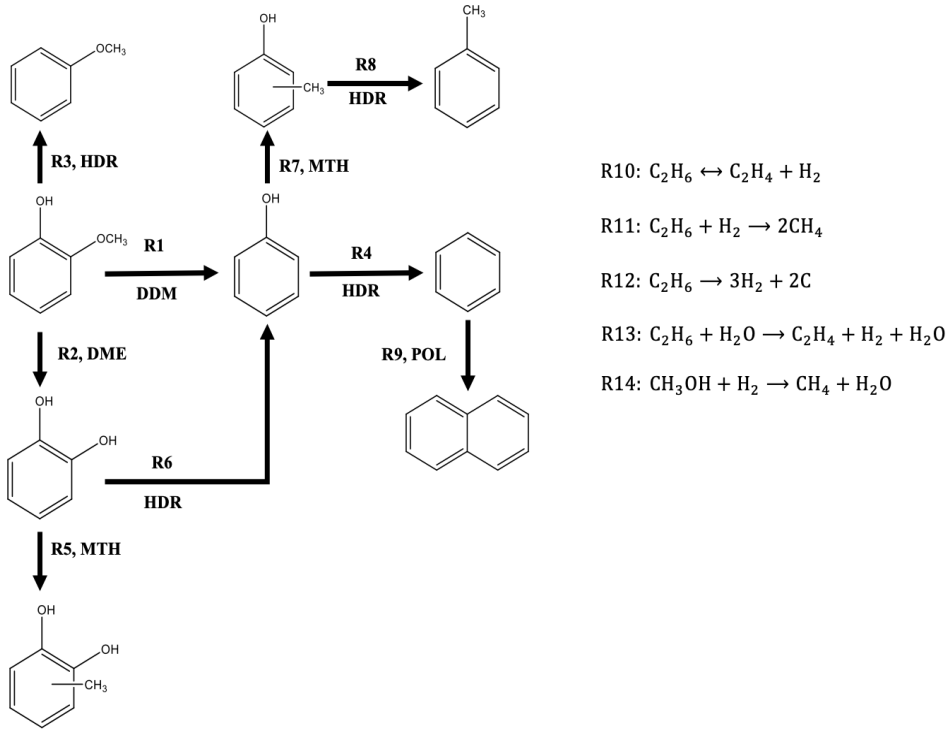


Figure 5.12: Proposed reaction network for guaiacol HDO using hydrogen produced from ethane DeH. DDM: direct demethoxlyation, HDR: hydrogenolysis (dehydroxylation), DME: demethylation, MTH: methylation, POL: polymerisation.

nation of the hydroxy group is accompanied by the formation of water. The presence of water can explain the enhancement of ethylene production by steam cracking of ethane; however, this enhancement may be minimal as the investigated temperature was considerably below the steam cracking temperature of 800 °C. Therefore, the only reasonable explanation for the improved ethylene formation is the continuous removal of hydrogen, which led to shifting the ethane DeH equilibrium for high ethane conversion.

The condensation of aromatic and oxygenated aromatics on the catalytic surface, which has been observed to play a significant role in deactivating alkane DeH, may affect HDO distribution. It was observed in other work, which refers to it as a surface pool [142] caused by adsorbed reactants and products. This accumulation of condensate may resemble microbatching processing at the catalytic surface, which, with time, continues to polymerise and form coke with the lack of reactive hydrogen.

5.7 Experimental results from an industrial perspective

Based on the experimental findings, producing BTX is feasible, though additional efforts are required to enhance its extraction from bio-oil. This entails addressing the issue of

excessive coke generation, which hinders the catalytic process essential for BTX formation. The accumulation of coke impeded the increase in ethylene output during the reaction. However, this may be attributed to the fact that the reaction ran for an extended period of 120 min at an extreme temperature and low pressure and was not viable. As previously stated, performance degradation typically diminishes with time in almost all cases. The performance peak could be achieved within a 30-min operation. Hence, if the coupled DeH-HDO is intended for 30-min operations, followed by coke gasification for energy generation, then catalyst regeneration is performed prior to resuming DeH-HDO.

In industrial contexts, the frequent cyclic process is commercially employed for propane and butane DeH (CATOFIN process) because the catalytic bed becomes deactivated after about 10 min of operation. Thus, implementing the identical cyclic process enables DeH-HDO to enhance its potential. Coke gasification can be used to convert the surplus of condensate and the accumulation of carbon into energy, or biogas. The development of a regenerative catalytic bed allows for the exploration of noble-based catalysts, even though Clariant already produces non-noble catalysts for the commercialised CATOFIN process. Thus, Figure 5.13 represents a proposed system consisting of a two-stage sequence reaction, which is based on experimental results obtained at a 30-min time-on-stream.

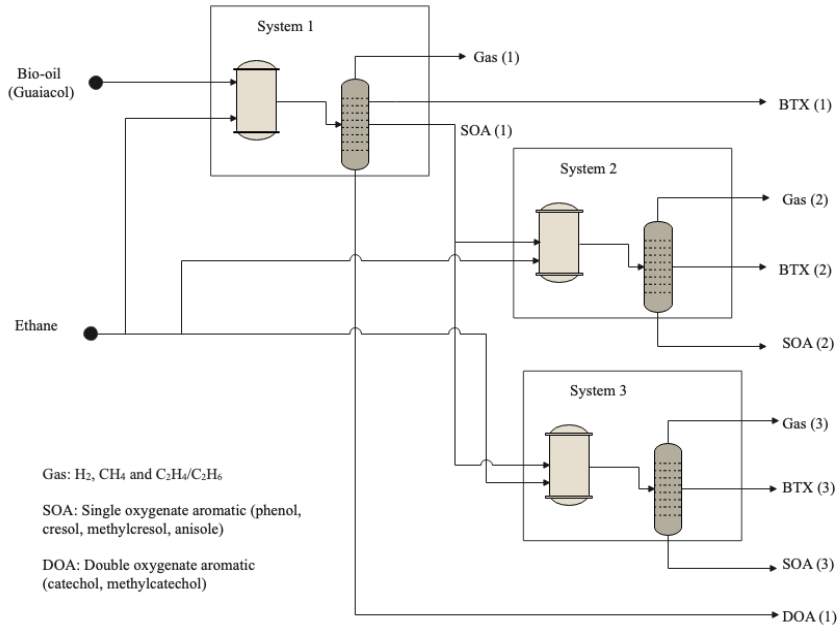


Figure 5.13: Integration of catalytic systems to improve BTX formation based on experimental results

The recommended catalytic systems to be included in this study are Cr-MoO_3, which will be operated at a guaiacol and ethane flow rate of 0.05 mol·g_{cat}^{-1}·h^{-1}, and at a temperature

of 600 °C. This catalytic system has a selectivity of 93% specifically towards the formation of single oxygen aromatic compounds, with phenol accounting for 90% of the total fraction. The catalyst weight used in this experiment was 5.0 g (Case F in Table 5.1), leading to a guaiacol conversion of 92%. However, the selectivity of BTX is limited to only 1%.

This suggests that achieving full HDO is feasible, but it would require a series of reactors for continuous processing. In the first stage, the O:A ratio was found to be 1.01 reduced from 2.0 (start from guaiacol) followed by processing a single oxygen aromatic, predominantly phenol, in three identical systems (2A, 2B, and 2C) using a Cr/Al_2O_3 bed. With molar ratio of 2.0 for ethane-to-guaiacol, this resulted in a further reduction of the O:A ratio to 0.90 due to the increase of BTX yield to 10%. Substituting the catalytic system in system 2 with $PNiMo/Al_2O_3$ results in an O:A ratio of 0.88. However, the overall conversion of ethylene to ethane is higher in the former case. Table 5.7 illustrates the mass balance for the integrated systems that have been studied.

Table 5.7: Mass balance for integration of catalytic systems for BTX and HDO improvement based on experimental findings

Parameter	Unit	Inlet	outlet
Guaiacol	$g\ h^{-1}$	33.3	2.56
Gas	$g\ h^{-1}$	32.1	32.04
BTX	$g\ h^{-1}$	-	2.71
SOAr	$g\ h^{-1}$	-	19.28
DOAr	$g\ h^{-1}$	-	1.13
HOHC	$g\ h^{-1}$	-	0.12
Methanol, water	$g\ h^{-1}$	-	0.3,4.04
Coke, condensate	$g\ h^{-1}$	-	4.71

The integration demonstrates the viability of synthesising a catalytic system or HDO process that can primarily produce phenol and BTX. However, at this point, although there has been an improvement in the level of HDO the production of ethylene is not yet improved. This is because when phenol is processed in the system, the conversion of ethane and the selectivity of ethylene are maintained at 22% and 11%, respectively. The increase in ethane conversion over time in System 2 resulted from the cracking mechanism, resulting in the formation of methane. In the integration, methane is mostly made through alkane DeH processing, since phenol HDO processing does not make methane because it does not have a methoxy group as guaiacol.

5.8 Conclusions

This chapter explores the utilisation of catalytic systems containing two catalysts: a bio-oil HDO catalyst and an alkane DeH catalyst. The aim of this approach is to enhance the performance of a single catalyst catalytic bed by boosting the efficiency of both catalytic reactions. The results in this chapter validate the findings in Chapter 4 by confirming the two hypotheses: the continuous removal of hydrogen leads to higher alkane conversion, and hydrogen produced by DeH exhibits higher reactivity at the catalytic surface than externally-supplied hydrogen. These hypotheses were proven using the HDO catalyst (PNiMo/Al_2O_3 or MoO_3). The assisted alkane DeH for guaiacol HDO (in-situ) exhibited a 20% higher O/aromatic ratio after a 15-min run and a 12% increase after a 120-min run over the use of molecular hydrogen (ex-situ). The decrease in performance is attributable to the excessive accumulation of condensate coke, which hinders ethane access to active sites for the DeH mechanism.

The limitation in the production of BTX is attributed to the lack of reactive hydrogen on the catalyst surface. As a result, BTX appears and then gradually diminishes over time. Moreover, the deficiency of reactive hydrogen results in the accumulation of condensate and coke, as evidenced by the formation of several types of cokes in both the active site and support observed in the SEM. In SEM, when running only catalytic DeH, a significant amount of filamentous coke is noticed. However, when running DeH-HDO, less filamentous coke is observed because layers of condensate coke are formed, as determined by TGA, indicating that HDO is the main condensate accumulation. The challenge of HDO of phenolic compounds was evident in the phenol runs. Despite increasing the catalytic bed and reducing the flow rate by four times of the slandered guaiacol runs, only 18% of phenol was converted in a 30-min period. However, this conversion exhibited a high selectivity of nearly 95% towards BTX. It is important to note that this selectivity significantly decreased with prolonged time-on-stream. To summarise, the two aforementioned hypotheses have been validated, but more enhancement is necessary to fully use the potential of DeH-HDO. One of the constraints identified in this chapter is the presence of nickel, which has a beneficial impact on the HDR of Ar-OCH_3 (422 kJ·mol^{-1}) and Ar-OH (468 kJ·mol^{-1}) [37], but has a detrimental effect on ethane DeH, as the dissociation energy of the C-C bond is relatively low at 368 kJ·mol^{-1}. Consequently, the production of methane rises as the catalyst surface becomes saturated with condensate, leading to the elimination of DeH and the initiation of ethane cracking. Another constraint in using the mixed metal catalytic system

is the spatial separation between the HDO and DeH active sites, which could hinder the efficient transfer of reactive hydrogen (adsorbed) by the formed molecular hydrogen during the reactions. This suggests additional improvement through catalyst synthesis with dual non-noble metal active sites on a single support to enhance hydrogen transfer and further improve the DeH-HDO process.

Chapter 6

Tailored Catalyst Synthesis for Enhanced DeH-HDO Coupling

6.1 Introduction

The achieved viability of utilising in-situ aided HDO through ethane DeH, shown in earlier chapters, eliminates the necessity for high-pressure hydrogen HDO. Nevertheless, the formation of BTX, which are the intended products of bio-oil HDO to chemicals, was limited to the start of the run and decayed as the reaction progressed. Three reasons were highlighted for the low BTX at the beginning of a run: (1) limited catalytic HDO reactivity on phenolic compounds; (2) insufficient utilisation of DeH-produced hydrogen; and (3) rapid catalytic deactivation for both DeH and HDO caused by sever formation of phenolic condensate. As reaction progresses, the main limitation of DeH-HDO is the excessive carbon deposition blocking active sites, which was verified through TGA and SEM analysis. This chapter seeks to resolve the former two reasons via modification of the catalytic system. Consequently, it investigates the efficacy of various catalysts utilising Mo and Cr active sites. Similar to the previous chapter, alumina is considered the base catalyst support; yet in this chapter, alumina acts as a substrate for both active sites for ideal synergistic effects.

Alumina oxide is commonly used as a support for these reactions, ethane DeH in particular, while zirconia and zeolites have also been investigated as alternatives. These alternative supports have been well investigated with prominent active sites (Cr and Pt) for alkane DeH [140], [184]–[186]. Additionally, Ni and Mo metal oxides studied in the preceding chapter have been taken into consideration in the literature for guaiacol HDO, along with alternate supports such zeolites [187], [188], activated carbon [189], titanium oxide [86], and silica [90].

6.1.1 Chapter structure

This chapter commences by explaining the rational of selecting zeolite as an alternative support to replace alumina in Section 6.1.2, since it is not addressed in Chapter 2. The experimental results for Cr and Mo on alumina-supported catalysts are presented in Section 6.2. The DeH-HDO reactivity on zeolite-supported Cr and Mo results are presented in Section 6.3. In both sections, alkane DeH serves as a screening assessment for a range of synthesised catalysts, examining single or dual active sites and their loadings. Selected catalysts are then employed for DeH-HDO, with a focus on producing high-value chemicals such as ethylene and hydrogen, and benzene in the case of zeolite-based catalysts.

6.1.2 Why zeolite for DeH-HDO?

The choice of catalyst support and active metal oxide sites plays a critical role in the ethane and guaiacol DeH and HDO reactions. From a reaction coupling perspective, zeolite catalysts for ethane DeHA are further utilized in a coupled system with CO_2 conversion via the reverse water gas-shift (RWGS) reaction. The study by Gomez et al. highlights the thermodynamic conversion gain from CO_2 to aid ethane DeHA, particularly using P-modified Ga/ZSM-5 [190]. This gain is supported by both density functional theory (DFT) and experimental findings, showing increased conversion and ethylene formation with certain variations of Ga/ZSM-5. The study key conclusion, supported by $^{13}CO_2$ isotope experiments, is that the continuous consumption of H_2 via CO_2 conversion enhances ethylene formation. However, fully leveraging CO_2 as a carbon source requires catalyst modification for its activation and transformation, adding value to the product stream.

Zeolite is, therefore, the most widely used substitute support for the two reactions. Furthermore, zeolite is a well-established catalytic system from industrial perspective for alkane DeHA [191], [192] and catalytic cracking [193], [194]. Thus, the following section will address using zeolite for DeH-HDO. Zeolites, in particular, have found widespread use as catalyst supports due to their structural versatility. They offer a large surface area for improved reactant adsorption and metal oxide dispersion [192]. Furthermore, zeolites can be modified to suit various reaction requirements, including acidity adjustments, by controlling the Al/Si ratio [195]. This makes them valuable for catalytic cracking and hydrocarbon conversion. Zeolites are also known for their shape-selective catalytic properties, making them suitable for isomerization and DeHA [140].

This chapter focuses on zeolite-supported catalysts, exploring the incorporation of a DeHA mechanism into the DeH-HDO coupling process. Two main pathways for DeHA have been extensively studied with zeolite-supported molybdenum oxide catalysts. The first pathway involves direct DeHA of ethane into benzene, while the second pathway involves ethane cracking into methane radicals, followed by DeHA to produce benzene. Zeolites can facilitate both pathways due to their ability to perform ethane DeHA and ethane cracking. Thus, tuning zeolite properties is crucial for desired product outcomes. Although the project aims to improve the catalytic system's selectivity towards both BTX and alkenes (specifically ethylene). Prioritising higher BTX formation over alkenes from alkane is acceptable due to the value of both molecules and their ease of separation under ambient conditions. At this stage, the main focus is delivering reactive hydrogen for HDO as well as valuable byproducts. The direct conversion pathway, as illustrated in Reaction 8, is favoured for HDO due to its higher hydrogen yield per ethane molecule in comparison with ethane DeH. The two-step ethane pathway demands hydrogen for the first step Reaction 9, and higher energy for aromatization process in the second step as illustrated in Reaction 10.

$$3\,C_2H_6 \leftrightarrow C_6H_6 + 6\,H_2 \qquad \Delta H = 377\,kJ^{-1} \tag{R8}$$

$$C_2H_6 + H_2 \leftrightarrow 2\,CH_4 \qquad \Delta H = -64.9\,kJ\,mol^{-1} \tag{R9}$$

$$6\,CH_4 \leftrightarrow C_6H_6 + 9\,H_2 \qquad \Delta H = +531\,kJ^{-1} \tag{R10}$$

From a catalytic perspective, ethane and guaiacol react on the same catalytic surface in zirconia and alumina-based catalysts. However, zeolites offer a crucial distinction in their catalytic behaviour with both reactants. Ethane, with a kinetic diameter of 0.44 nm [196], can diffuse into the zeolite for DeH or DeHA because it is smaller than the ZSM-5 pore size, which is 0.59 nm [197], [198]. In contrast, guaiacol, with a larger kinetic diameter of 0.67 nm [197], is restricted to the outer catalytic surface. This limitation may reduce the yield of BTX products due to excessive coke formation. It is worth noting that other investigated zeolites for the HDO of guaiacol have larger pore diameters, potentially leading to different mechanisms. Exploring the differential surface interactions of these two reactants is crucial in this section, especially considering that the blockage of active sites on alumina-supported

metal oxides significantly impacted the ethylene-to-ethane ratio.

6.2 Alumina support

6.2.1 Catalyst synthesis and bed preparation

A series of alumina-supported catalysts containing Mo, Cr and both as active sites were synthesised to be investigated for "in-situ" HDO. Alumina was selected since both reactions are heavily considered using alumina based catalysts. Alumina-supported Cr and Mo-based catalysts were investigated using two synthesis approaches: (1) sequential impregnation and (2) single-step impregnation. In sequential impregnation, an ethanol solution containing a Mo- precursor (ammonium tetrathiomolybdate, from Sigma-Aldrich) was mixed with an ethanol solution of γ-Al_2O_3. To achieve uniform mixing, the solution was agitated for four hours at 1000 RPM, followed by 48 hours of evaporation in an 80 °C water bath. After the sample was dried, the obtained powder was subjected to four hours of calcination at 600 °C. The calcination occurs in atmospheric chamber furnace with programmed heating and cooling at 10 °C·min^{-1}. The Mo-based catalyst is identified as xxMoAl, where xx represents the weight proportion of metal oxide. The Mo-based catalyst was re-impregnated with a Cr (chromium (III) nitrate nonahydrate, supplied by Sigma Aldrich) suspension in ethanol, then subjected to identical mixing, drying, and calcination processes. The catalyst produced is identified as xxCr-xxMoAl.

The Cr and Mo precursors were added to the support-ethanol solution for the single-step impregnation, followed by the identical mixing, drying, and calcination stages. For the single step impregnation, sodium molybdate was used as the Mo precursor, supplied by Sigma-Aldrich. The catalysts for the single-step impregnation are specified as xxCrxxMoAl.

Table 6.1 lists the catalysts investigated in this section with metal oxide loading based on XRF. Three samples of each synthesised catalyst are quantified to verify the uniformity of the metal oxide distribution. Appendix C contains examples of metal oxide distributions that are not uniform. All the catalysts investigated in this section are combined with SiC in a 1:1 weight ratio within a 2.5 g catalytic bed, with particle sizes ranging between 106-212 μm. Additionally, this chapter examines previously investigated supplied catalysts CrAl and PNiMo at similar catalyst preparation and testing conditions for comparison.

Table 6.1: Elemental analysis of catalysts used in this chapter using XRF

Metal oxide composition (%)		Al (Al_2O_3)	Ni (NiO)	Mo (MoO_3)	Cr (Cr_2O_3)
Ni-Cr_2O_3/Al_2O_3	4Ni8CrAl	88.2	4.2	-	7.8
Cr_2O_3/Al_2O_3	8CrAl	92.6	-	-	7.4
MoO_3/Al_2O_3	40Mo/Al	58.9	-	41.1	-
Cr_2O_3-MoO_3/Al_2O_3	8Cr-40MoAl	51.2	-	40.9	8.1
Cr_2O_3/Al_2O_3[1]	CrAL	63.6	-	-	36.4
P-NiMo/Al_2O_3[2]	PNiMoAl	54.0	9.2	33.6	-

[1] supplied catalyst not synthesised studied as alkane DeH catalyst in previous chapter added for comparison with synthesised catalyst.
[2] supplied catalyst not synthesised studied as guaiacol HDO catalyst in previous chapter added for comparison with synthesised catalyst, the remaining 3.2% is for P.

6.2.2 Ethane DeH on Cr and Mo in Al_2O_3 supported catalysts

6.2.2.1 Ethane DeH conversion improvement with particle size and Ni effects

In the previous chapter, a key discovery was the detrimental impact of Ni on ethylene selectivity, leading to reduced DeH adsorbed hydrogen and accelerated active site deactivation. Consequently, this chapter, centred on synthesised catalytic systems, starts by substantiating the adverse effects of Ni. To enhance the evaluation of Ni presence at active sites, a lower particle size range is explored to assess mass transfer limitations. The impact of nickel oxide would be readily apparent. The new investigated particle size range is 45-106 μm for 8CrAl and 4Ni8CrAl, as depicted in Figure 6.1.

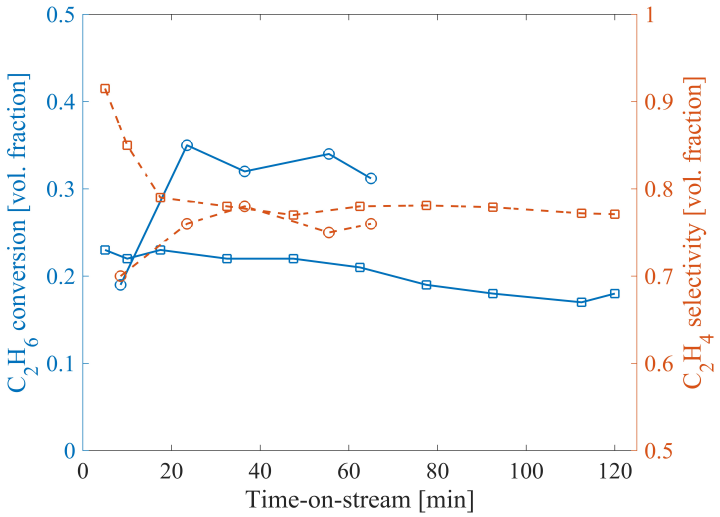


Figure 6.1: Atmospheric ethane DeH at 600 °C using low particle size using GHSV of 0.17 mol·g_{cat}^{-1}·h^{-1}: (○) 4Ni8CrAl, and (□) 8CrAl, [solid-line] Ethane conversion, [dashed-line] Ethylene selectivity

Both catalysts tested within the smaller particle size range exhibit intriguing ethane con-

version, as depicted in Figure 6.1. Specifically, the smaller particle size range demonstrates higher ethane conversion for CrAl compared to the standard particle size range (106-150 μm), indicating the presence of some degree of mass transfer limitations within this range. However, both Ni-containing and Ni-free catalysts resulted in a significant pressure drop across the catalyst bed. It is noteworthy that the experimental protocol is designed to terminate the run at a pressure drop of 3.0 bar, leading to experimental termination before reaching a 120-minute TOS.

The presence of nickel increases conversion but has noticeable decreasing selectivity at the beginning of the run , suggesting its involvement in C-C cleavage. The selectivity of both catalyst stabilise at the same value and the one with Ni with have higher ethylene yield, the acceleration of coke formation in Ni catalyst contributes to the rise in pressure drop, reaching 3.0 bar within 60 min. Therefore, the run was terminated.

Considering that accommodating guaiacol would further expedite coke formation and exacerbate the pressure drop, the standard particle size investigated in the previous chapter was also applied to all the catalysts synthesised in this chapter. Additionally, to mitigate the influence of nickel, the synthesised catalysts comprised only chromium and molybdenum oxides as active sites for acDeH and acHDO, respectively.

6.2.2.2 Ethane DeH conversion with Cr and Mo active sites

The CrAL catalyst examined in the previous chapters has a significant chromium content. Although the ethane DeH catalyst shows strong activity in terms of conversion and selectivity, studies indicate that catalysts with reduced chromium loadings exhibit better performance. Therefore, a chromium catalyst with decreased loading was synthesised and tested for its ethane DeH performance, as detailed in Table 6.1. Furthermore, in order to get a similar amount of Mo active sites as in the supplied studied non-supported MoO_3 and PNiMoAl, the Mo loading was set at 30-40 MoO_3 on alumina, as specified in Table 6.1. The higher loading of Mo also ensures that the synthesised catalyst has a similar crystalline phase, as shown in Figure 6.2. This phase was not apparent when molybdenum was added to CrAl, but it was clear in the reverse synthesis.

An experiment was conducted utilising a blank SiC run to evaluate catalysts in comparison to SiC as an inert medium, aiming to improve temperature uniformity across the catalytic bed. SiC shows inert behaviour at 600 °C, with a conversion of merely 0.9%, likely due to

thermal conversion. Consequently, it can be said that SiC is an inert medium.

Table 6.2: Atmospheric ethane DeH results for alumina-supported catalysts for Cr and Mo active sites at 600 °C with ethane GHSV of 0.1 mol·g_{cat}^{-1}·h^{-1}, all the catalyst are physically mixed with SiC in 1:1 weight ratio

Catalytic system	Ethane conversion (vol%)	Ethylene selectivity (vol%)	C_2"/C_2[1] (vol/vol)
PNiMoAl[2]-SiC	50.2	6.97	0.021
CrAl[3]-SiC	30.6	82.7	0.141
8CrAl-SiC	41.6	85.0	0.125
40MoAl-SiC	35.1	43.4	0.03
SiC	0.90	64.7	0.004

[1] ethylene-to-ethane ratio
[2] supplied catalyst as indicated in Table 6.1
[3] supplied catalyst as indicated in Table 6.1

At the standard operating condition with a GHSV of 0.1 mol·g_{cat}^{-1}·h^{-1}, Cr-based catalysts dominate DeH, as shown in Table 6.2. The synthesised catalyst superior performance as a predictable outcome, yielding a 11% increase ethane conversion and a 2% rise in ethylene selectivity in comparison to the supplied catalyst (CrAl). However, this improvement does not align with the ethylene-ethane ratio due to coke formation. The heightened conversion with 8CrAl, which contains less Cr loading, suggests enhanced dispersion of Cr active sites, mitigating clustering induced by high loading. Nonetheless, increased activity leads to higher coke production, indicating a larger active surface area in the low catalyst loading, as confirmed by BET analysis in Table 6.3. The synthesised 8CrAl boasts a three times larger surface area (152.9 m^2/g) compared to the supplied CrAl (53.5 m^2/g), probably as a result of a better dispersion of small loading Cr_2O_3 in 8CrAl, as evidenced by its amorphous form in XRD analysis (Figure 6.2). Furthermore, the crystalline form of the supplied CrAl was not observed, even in the synthesis of CrAl with a 16wt% loading of Cr_2O_3.

Table 6.3: Physicochemical properties of synthesised alumina supported Cr and Mo catalysts

Catalyst	BET surface area (m^2/g)	Average volume of pores (m^3/g)	Average pore diameter (nm)
8CrAl	152.9	0.264	5.51
8Cr-40MoAl	19.25	0.095	17.8

The utilisation of Mo sites for HDO in ethane DeH demonstrates a conversion of 35.1%, which is comparable to that of CrAl. However, 40MoAl significantly impacts ethylene selectivity. Nevertheless, 40MoAl exhibits overall superior performance in terms of ethylene yield compared to the supplied PNiMoAl-SiC as both considered HDO catalysts. The supplied resulted in the higher ethane conversion compared to all the investigated catalysts.

However, it conversion mainly targeted C-C cleavage. It worth mentioning that the thermal ethane conversion using on SiC has a better ethylene selectivity indicating the active sites' role in reducing the selectivity towards less ethylene in 40MoAl and PNiMoAl. This observation underscores the detrimental effect of Ni presence in ethane DeH. However, it is important to note that Ni plays a crucial role in HDO, necessitating a thorough investigation into developing a catalytic system.

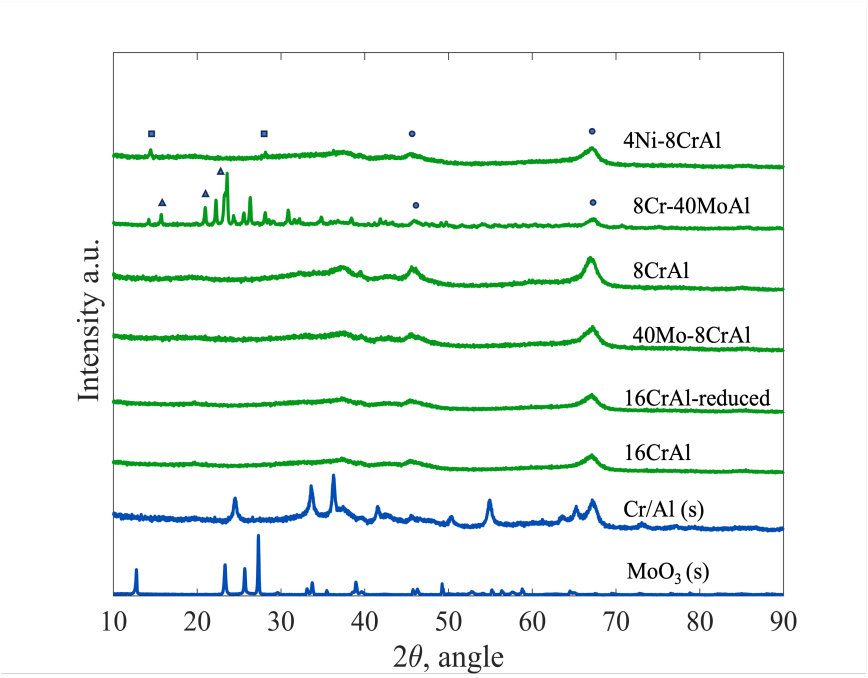


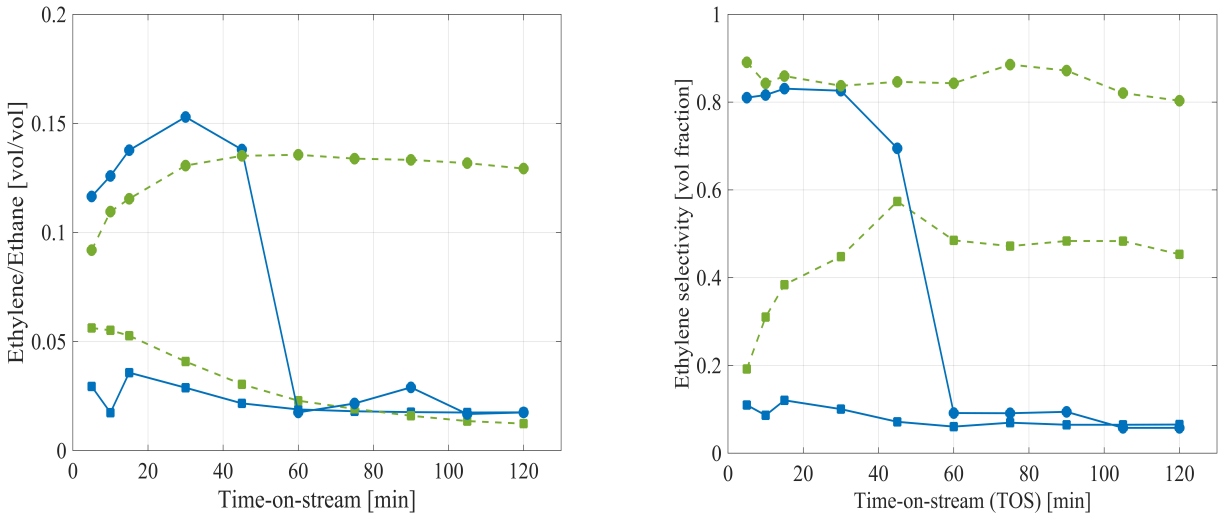
Figure 6.2: XRD patterns for included catalysts in this section: (s) refers to supplied catalysts used in the previous chapters: (■) NiO, (●) Cr_2O_3, and (▲) MoO_3

6.2.3 Reactivity test performance: Guaiacol and ethane DeH-HDO on Cr and Mo in Al_2O_3 supported catalysts

In this section, guaiacol HDO for DeH-HDO using the synthesised catalysts was examined and compared with single catalyst catalytic system using the supplied catalyst at the standard operating conditions.

6.2.3.1 Effect of the presence of guaiacol on DeH

In investigating the ethane DeH process, the absence and presence of guaiacol play crucial roles in understanding the catalytic behaviour, as there is no HDO without guaiacol. Two catalysts were investigated with and without guaiacol: 8CrAl and 40MoAl as shown in Figure 6.3. Ethane DeH without guaiacol resulted in an average ethylene-to-ethane ratio of 0.125 over a 120-minute run for the 8CrAl catalyst, as shown in Figure 6.3. With its stable ethylene selectivity, 8CrAl indicates a noticeable increase in ethylene formation at the beginning of the run, reaching a steady state after 30 min.



(a) [alkane][alkene]$^{-1}$ ratio **(b)** Ethane selectivity-to-hydrocarbons

Figure 6.3: Ethylene formation for atmospheric HDO of guaiacol via ethane DeH as a hydrogen donor reaction at 600 °C: Guaiacol 0.05 mol·g$_{cat}^{-1}$·h^{-1} and ethane 0.1 mol·g$_{cat}^{-1}$·h^{-1} through a 2.5 g catalytic bed with 50wt% SiC: 8CrAl (∘) and 40MoAl (□), [—] for ethane DeH with the absence of guaiacol, [-] with the presence of guaiacol

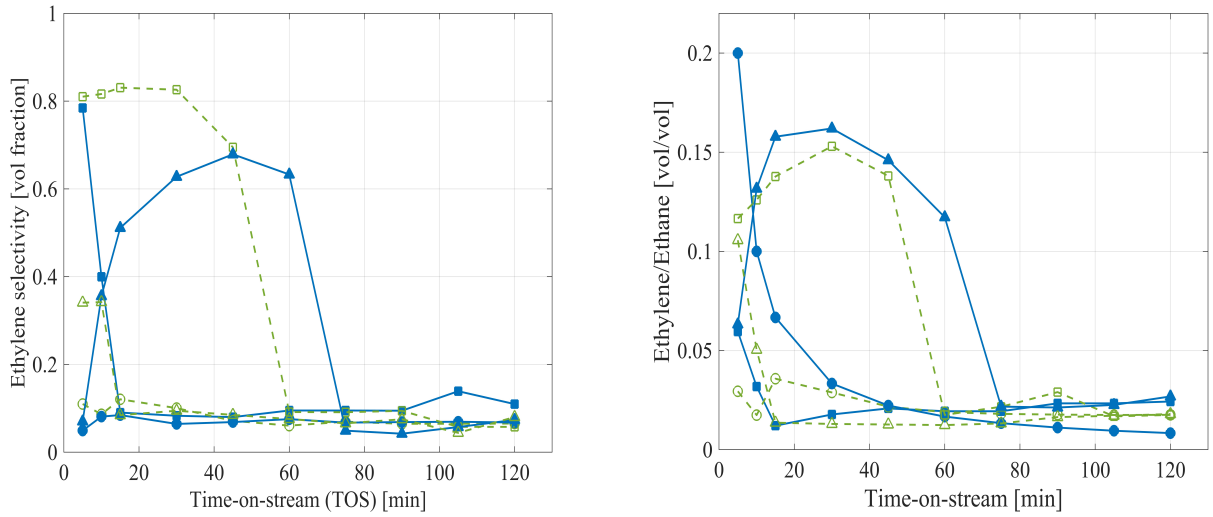
Note that all catalytic runs underwent a reduction step in a hydrogen environment to eliminate oxidation mechanisms, developed by oxidative DeH by metal oxide. However, a slight decline in conversion was observed towards the end of the experiment due to catalyst deactivation. As expected from Cr-based catalysts, ethane DeH exhibited high selectivity to ethylene, 85%, optimising hydrogen formation.

For 8CrAl, remarkably, co-feeding guaiacol improved ethylene formation, following the same increasing trend as without guaiacol for the first 40 min as shown in Figure 6.3 . However, a sudden reduction in ethylene selectivity occurred due to expected rapid carbon deposition and heavy condensation on the catalyst surface, blocking DeH active sites. The ethylene selectivity of DeH-HDO is further reduced due to methane formation from guaiacol demethylation. Regarding 40MoAl, there was a roughly 40% reduction in ethylene formation initially upon guaiacol injection. However, ethylene-to-ethane ratio reduced for both with and without guaiacol over time. However, the reduction rate with guaiacol presence was lower resulting in slightly higher ethylene-to-ethane ratio with guaiacol by the end of the experiment, as illustrated in Figure 6.3.

This performance is expected since MoO_3 active sites have less DeH activity, yielding 20-50% ethylene selectivity without guaiacol. Therefore, to achieve ethane conversion improvement towards ethylene, the catalytic system must be selective for DeH to increase hydrogen for-

mation and consumption (reactive hydrogen). The presence of reactive hydrogen limits coke accumulation and prevents rapid reduction due to the inhibition of the DeH mechanism. The delayed in rapid reduction with guaiacol using 8CrAl indicates at the beginning the available reactive hydrogen ethane DeH resisting the formation of condensate and carbon deposition. Once undesirable condensate and carbon deposition occur, a rapid decline in ethylene formation happens indicating limited accessibility to active sites. with absence of guaiacol, the active site in 8CrAl is capable for maintaining a stable performance for 120-minute.

To confirm the linkage between the lack of reactive hydrogen, carbon deposition, and condensate Figure 6.4 illustrates 8CrAl performance in comparison to CrAl and PNiMoAl-Cr, which were explored in previous chapters to have high hydrogen formation. The PNiMoAl-Cr catalytic system operates at 0.4 bar, as indicated in the indicated in the previous chapter, which indicates better performance than atmospheric pressure.



(a) Ethylene selectivity **(b)** [Ethylene][Ethane]$^{-1}$ ratio

Figure 6.4: Atmospheric HDO of guaiacol via ethane DeH as a hydrogen donor reaction at 600 °C: Guaiacol 0.05 mol·g_{cat}^{-1}·h^{-1} and ethane 0.1 mol·g_{cat}^{-1}·h^{-1} through a 2.5 g catalytic bed with 50wt% SiC: (△), 8CrAl (□), 40MoAl (○), PNiMoAl-Cr at 0.4 bar (▲), CrAl (■), 8Cr-40MoAl (●)

8CrAl and PNiMoAl-Cr indicate an improvement in ethylene formation, which can be attributed to continuous hydrogen removal by HDO, thereby delaying deactivation as shown in Figure 6.4. Running PNiMo-Cr under partial pressure exhibited better runtime and ethylene-to-ethane ratio, but with lower selectivity due to the catalyst's different nature. The better delay in rapid reduction in PNiMoAl-Cr system can be attributed to the presence of HDO active sites, which reduces the formation of undesirable heavies from HDO. How-

ever, 8CrAl indicates overall higher ethylene formation. Therefore, as both ethane DeH and guaiacol HDO are expected to benefit each other, they negatively affect each other's performance. Thus, an improved integrating condition is targeted to unlock the full potential of DeH-HDO coupling.

6.2.3.2 the effects of synthesised catalyst for DeH-HDO on guaiacol upgrading

The liquid fractions of the catalytic systems synthesised in this section have revealed promising insights when compared to the catalysts supplied in the previous chapters. Overall, the extent of HDO based on liquid fraction selectivity follows the order: 8Cr-MoAl > 40MoAl > CrAl > PNiMo > 8CrAl, as listed in Table 6.4. Furthermore, in terms of the liquid fraction HDO yield, the sequence is: PNiMo > 40MoAl > 8CrAl > 8Cr-MoAl > CrAl. Both CrAl and PNiMo were the supplied catalysts investigated in the previous chapter in different configurations. In this chapter, they were mixed with SiC in a 1:1 weight ratio, akin to the synthesised catalysts.

Table 6.4: Atmospheric DeH-HDO results for alumina-supported catalysts with Mo and Cr active sites at 600 °C and 0.1 and 0.05 mol·g_{cat}^{-1}·h^{-1} ethane and guaiacol flow, respectively

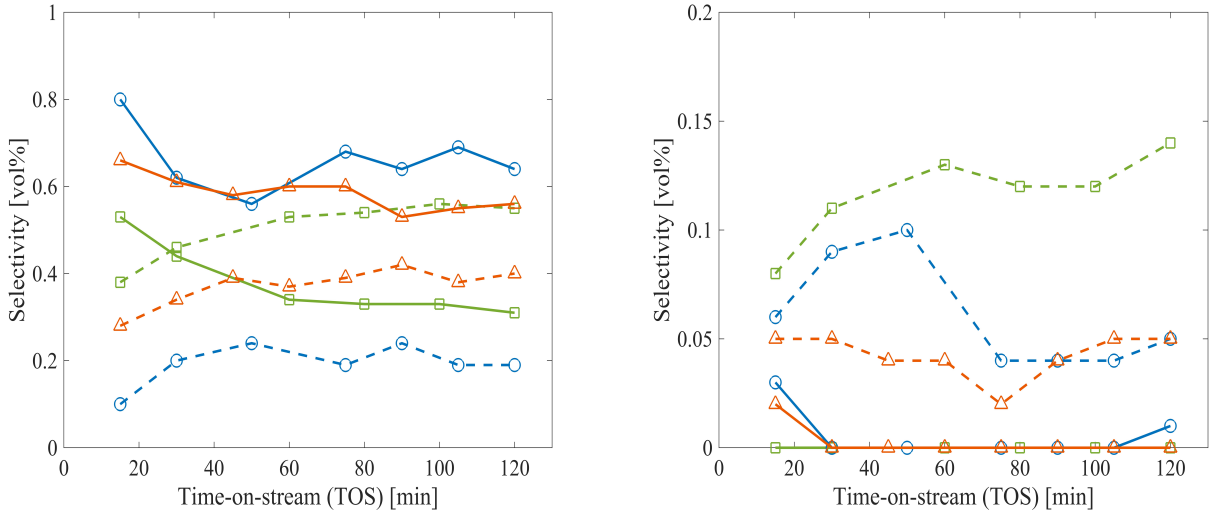
Catalyst	C_2"/C_2[a] vol/vol	O:A[b] select.	O:A[b] yield	Condensate g/g_{cat}	Coke g/g_{cat}
8CrAl-SiC	0.077 (0.125)	1.50	1.52	0.030 (0.011)	0.243 (0.008)
40MoAl-SiC	0.022 (0.032)	1.17	1.46	0.223 (0.015)	0.213 (0.112)
8Cr-40MoAl-SiC	0.027	1.16	1.57	0.227	0.267
CrAl-SiC	0.026	1.20	1.61	0.469	0.218
PNiMo-SiC	0.0223	1.25	1.40	0.083	0.297

[a] values within parentheses for ethane DeH with absence of guaiacol for ethylene-to-ethane ratio
[b] O:A refers to oxygen atom per aromatic ring in the selectivity indicates only for the products, in yield includes unconverted guaiacol

In both assessments, the benefits of the synthesised catalysts were realised, where they outperformed the supplied HDO and DeH catalysts. This indicates the importance of engineering the catalyst for these coupled reactions. In terms of guaiacol conversion, PNiMoAl outperformed the synthesised Mo and Cr-based catalysts due to the existence of Ni, which promotes HDR. However, its selectivity remains below that of 40MoAl and 8Cr-40MoAl, which are synthesised to accommodate HDO. The HDO selectivity of 8CrAl is weakest, which is attributed to the lack of HDO active sites despite its higher hydrogen formation and improvement in ethylene formation. The difference in performance between CrAl (supplied)

and 8CrAl is in the Cr loading. The supplied CrAl has ahigh loading of Cr, which shows a crystalline structure as shown in Figure 6.2.

The results for Cr catalysts, indicate the possibility of the support (alumina) contribution to the HDO conversion. Where the acidity of the support favours DME, which yields the formation of catechol from guaiacol. This observation agrees with one of Wu et al. conclusions on atmospheric guaiacol HDO using Ni_2P at different supports [87]. They concluded that the acidity of the alumina support prefers the DME route for forming catechol. Since 8CrAl contains a larger surface of acidic support that favours catechol formation instead of phenol, which could be activated at the chromium active sites, Therefore, Figure 6.5a illustrates that 8CrAl forms more DOAr, mainly catechol and methyl catechol, than SOAr. This is completely the opposite for all other investigated systems in this chapter and previous chapters, since they have a higher metal oxide loading, including 40MoAl.



(a) SOAr (-), DOAr (- - -) **(b)** BTX (-) , HOHC (- - -)

Figure 6.5: Liquid fraction of atmospheric HDO of guaiacol via ethane DeH as a hydrogen donor reaction at 600 °C: Guaiacol 0.05 mol·g_{cat}^{-1}·h^{-1} and ethane 0.1 mol·g_{cat}^{-1}·h^{-1} through a 2.5 g catalytic bed with 50wt% SiC and 50wt%: PNiMo (△), 40MoAl (○) and 8CrAl (□)

This observation also explains the improvement in ethylene-to-ethane ratio for 8CrAl in comparison with the absence of guaiacol. The reduced dispersed active sites delayed the deactivation as well as the conversion of guaiacol to catechol is relatively easier in term of bond dissociation. Figure 6.2 illustrates that 40MoAl exhibits a crystalline structure due to the high loading intentionally targeted to emulate a similar phase as the investigated unsupported MoO_3 and PNiMo. In its active state at the beginning of the experiment (15 min), 40MoAl has demonstrated remarkable HDO, yielding the highest BTX and SOAr selectivity, reaching 83%. Despite the reduction in SOAr selectivity, it remains the top-performing

catalyst. The addition of chromium active sites to 40MoAl has shown a slight improvement in O:A selectivity, but no enhancement in overall yield. Additionally, the ethylene ratio improved, which can be attributed to the presence of Cr active sites.

6.2.3.3 Coke formation

Produced HOHC in the liquid fraction and condensate in the solid deposition are the main precursors for coke formation. Therefore, mitigating the formation of HOHC and condensation suppresses coke formation and consequently delays catalyst deactivation. The formation of HOHC in the liquid fraction indicates a degree of HDO but due to the lack of reactive hydrogen, two aromatics are linked to each other. This explains the variation in the selectivities in Figure 6.5. Once SOAr decreases, there is an increase in HOHC, proving that HOHC are mainly phenolic or/and completely HDO compounds. Furthermore, in 40MoAl Figure 6.3 shows that ethylene formation increases with time, which causes the reduction in HOHC in Figure 6.5b unlike 8CrAl which has the opposite trend.

The condensate is the further polymerised HOHC adsorbed at the catalytic surface, forming a dense layer on the catalyst surface, including both the support and active sites as illustrated in the previous chapter using SEM. Table 6.4 clearly shows that guaiacol conversion is correlated to condensation formation. Guaiacol conversion can be realised from the differences in O:A yield and selectivity, where the smaller the difference indicates high conversion. The higher the conversion, which is near completion for 8CrAl (synthesised), yields low condensation, while CrAl (supplied) yields high condensation with the lowest guaiacol conversion. For Cr-based catalysts, despite having similar ethane DeH performance in the absence of guaiacol, the metal oxide form and dispersion resulted in different results with guaiacol, which favours the low-loading catalyst. Furthermore, with the absence of guaiacol, CrAl has decaying conversion, whereas 8CrAl has stable conversion despite the overall similar conversion on average. Hence, dispersed chromium oxide ensures stability in producing reactive hydrogen by minimizing the impact on active site agglomeration and reducing the total active site area.

Generally, the high condensation refers to the different residence times between the two reactions. High conversion of ethane producing reactive hydrogen in 8CrAl, or the presence of Ni that accelerates HDO, delays the accumulation of condensate. The role of Mo active sites in HDO by adsorbing oxygenated function groups requires a longer residence time that

yields the formation of a pool of condensates.

The degree of HDO using Cr-MoAl has demonstrated its potential based on O:A ratio selectivity. Similar to previously investigated catalytic systems, phenol, catechol, and their methylation derivatives are the main products, along with anisole. However, in the synthesised catalysts, HOCH has a notable increase in its selectivity, as shown in Figures 6.5b and 6.6, reaching up to 20%. Since HOHC mainly consists of naphthalene and 1-naphthol, it indicates that the lack of reactive hydrogen limits BTX and phenolic formation as the reaction progresses. Figure 6.6 shows an increase in HOCH selectivity and a decrease in BTX due to the reduction in hydrogen formation, consequently reducing reactive hydrogen. Therefore, limiting the formation of HOCH would increase BTX formation as well as the degree of HDO, and reduce total solid deposition.

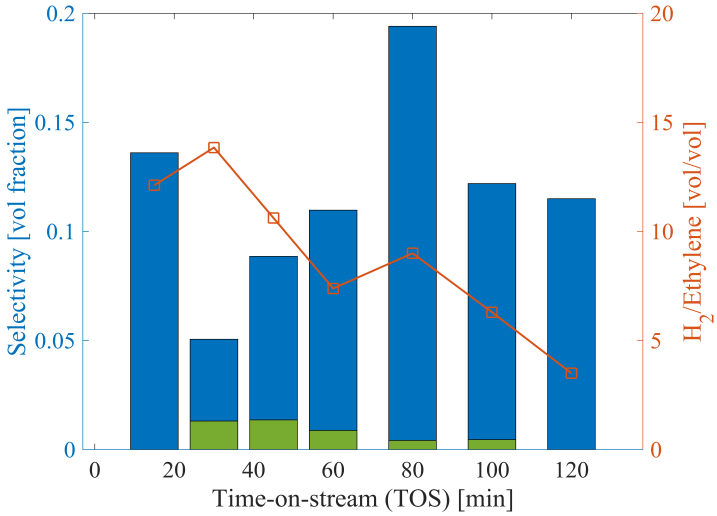


Figure 6.6: Atmospheric DeH-HDO at 600 °C using Cr-MoAl at 0.10 and 0.05 mol·g_{cat}^{-1}·h^{-1}, respectively: [Blue] HOHC and [Green] BTX

In summary, achieving an efficient catalytic system for DeH-HDO necessitates catalytic engineering to withstand phenolic condensation, a phenomenon that impedes the activity of both reactions by restricting the accessibility of reactants to active sites. As demonstrated in this section, enhancing ethylene production can be achieved through continuous hydrogen removal with a well-dispersed chromium catalyst. However, the acidity of the alumina support surface does not favour DDM, thus limiting HDO activity. Therefore, exploring alternative catalyst supports becomes crucial. Wu et al. showed that the presence of SiO_2 favours the DDM route, consequently increasing BTX formation [87]. Hence, the subsequent section will address the investigation of alternative supports incorporating SiO_2.

6.3 Zeolite support

6.3.1 Catalyst synthesis

Various zeolite-based catalysts with Mo and/or Cr active sites in oxide form were synthesised to assess the potential of including zeolite hydrocracking and DeHA mechanisms into the DeH-HDO coupling process. Ammonium tetrathiomolybdates for Mo and chromium (III) nitrate nonahydrate for Cr oxides were purchased from Sigma Aldrich, and ZSM-5 with a Si/Al ratio of 25 was supplied from Zeolyst as the catalyst support. The used solvent, ethanol, was purchased from Sigma Aldrich.

Incipient wetness impregnation (IWI) is used as the synthesis technique, where the targeted metal oxide's precursor is dissolved in an H-ZSM-5 ethanol solution. The mixture is agitated at 800 RPM for four hours. Next, the mixture evaporates in a water bath at 80 °C for 48 hours. After drying, the resultant powder is calcined at 600 °C for four hours. A second IWI step is used to produce zeolite-based catalysts with two active sites, where the second precursor is added to the calcined powder dissolved in ethanol. The two-step IWI synthesis process is denoted as sequential IWI. The catalysts are labelled as xCr-yMoZ, with x and y representing the weight percentage of the active metal loading in oxide form. The precursor order in the catalyst name signifies the sequence of impregnation. Using a Mo precursor during the initial impregnation is denoted by Cr-MoZ.

6.3.2 Catalyst preparation and characterisation

Characterising synthesised catalysts involves determining the metal oxide content. XRF analysis was conducted after each metal oxide impregnation step in a dual metal oxide catalytic system. The zeolite-supported catalysts studied in this chapter are detailed in Table 6.5. The measurements for both impregnated and non-impregnated ZSM-5 validate the specified Si/Al ratio of 25.0.

To prepare the catalytic bed, the catalysts need to be crushed, sieved, and pelletised into fine powder particles, typically ranging from 150 to 212 µm in size. The zeolite structure integrity is carefully preserved during this process by using a Specase Atlas manual hydraulic press, with a pressing force of up to 5 tonnes. This method has no adverse effects on the zeolite structure, as demonstrated by the nitrogen physisorption isotherms in Figure 6.7. These isotherms confirm the utilisation of zeolite microporosity, with the mean pore size and Type

Table 6.5: Elemental analysis of all the catalysts used in this work using XRF.

Metal oxide composition (%)		Al (Al_2O_3)	Si (SiO_2)	Mo (MoO_3)	Cr (Cr_2O_3)
ZSM-5	-	4.4	95.6	-	-
15Mo/Z		3.9	81.9	14.0	-
10Mo/Z		4.1	86.2	9.7	-
5Mo/Z		4.3	90.5	5.2	-
6Cr/Z		4.2	89.7	-	6.1
4Cr/Z		4.4	91.1	-	4.5
2Cr/Z		4.6	92.9	-	2.2
6Cr-15Mo/Z		3.5	74.5	16.1	5.9

IV physisorption isotherms providing clear evidence. The presence of H4 loop hysteresis is a result of the organised silica structure within the zeolite.

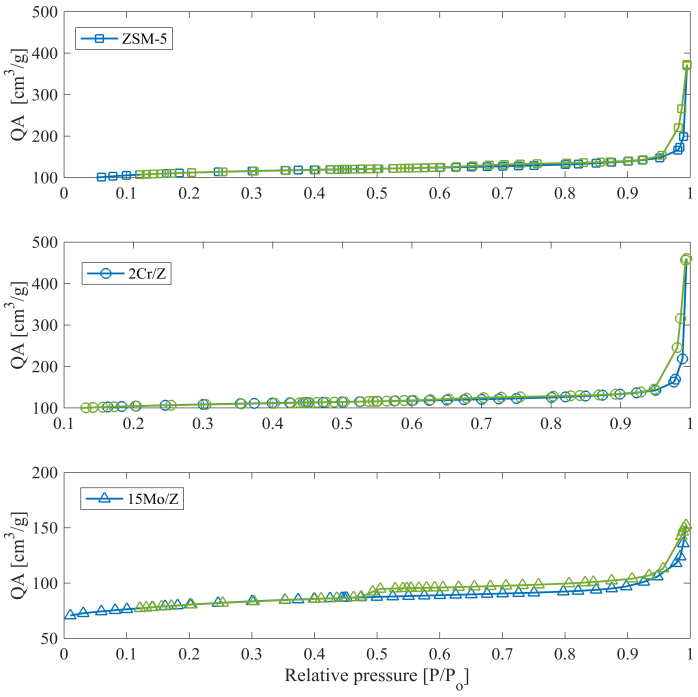


Figure 6.7: Nitrogen physisorption isotherms for ZSM-5 catalysts with Cr and Mo active sites. QA refers to quantity adsorbed at FT.

Furthermore, Figure 6.7 illustrates that the nitrogen physisorption isotherms indicate a reduction in adsorbed nitrogen in the zeolite micropores with a higher loading of MoO_3. This reduction is attributed to the migration of Mo oxides within the catalytic structure. This conclusion is supported by the 28% reduction in surface area and the 29% decrease in average pore volume compared to ZSM-5. However, when using a modest loading of Cr oxides, the amount of nitrogen adsorbed is significantly higher than that of ZSM-5, primarily due to a slight enlargement in the average pore size. This phenomenon can be attributed to the infiltration of larger Cr_2O_3 particles into the zeolite microporous structure.

Table 6.6: Physicochemical properties of synthesised zeolite supported Cr and Mo catalysts

	BET surface area (m^2/g)	Average volume of pores (m^3/g)	Average pore diameter (nm)
ZSM-5	387.8	0.257	2.65
15Mo/Z	277.8	0.182	2.63
2Cr/Z	361.0	0.251	2.78

6.3.3 Cr and Mo in zeolite supported catalysts for ethane DeH

The experiment involves developing various Mo and Cr oxide active sites on a ZSM-5 support in order to determine the most effective loading for the DeH-HDO catalytic system. Zeolite support is utilised in various applications, such as catalytic cracking and hydrocracking. It is noteworthy that the application of MoO_3 on zeolite induces methane and light alkane dehydroaromatization. Figure 6.8 depicts the performance in relation to ethylene selectivity and ethylene-to-ethane ratio. Catalysts containing chromium (Cr) exhibit moderate conversion of ethane to ethylene. The Cr_2O_3 active site is essential for alkane DeH since there is a direct relationship between the amount of chromium loaded in oxide form and the level of ethylene generation. However, the ethylene selectivity is only 30% because the zeolite cracking mechanism produces methane as the main component. The stable productionof ethylene is due to the chromium oxides being well-dispersed on the zeolite. This is done by keeping the loads low to avoid active site agglomeration. This approach differs from the high-loading chromium catalysts studied in previous chapters. The acidity of the support causes the cracking mechanism, leading to a decrease in selectivity.

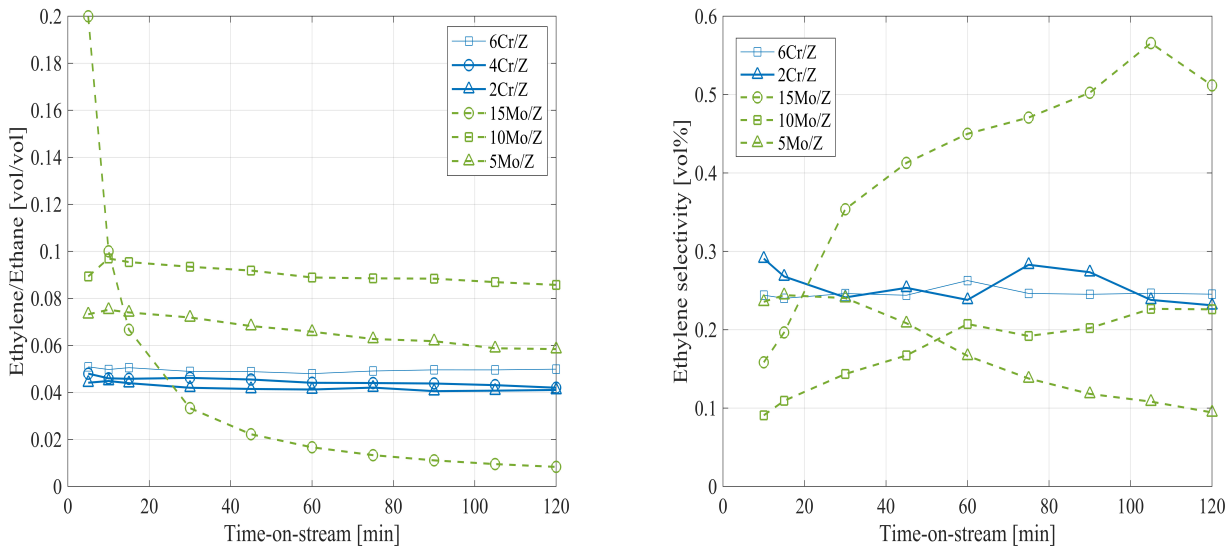


Figure 6.8: Ethane DeH using Mo and Cr zeolite catalysts at 600 °C.

When the loading of MoO_3 catalysts increases from 5% to 10%, a rise in ethylene production is observed. Nonetheless, an equivalent decrease in performance is observed over a duration of 120 min, during which Cr-based catalysts exhibit consistent stability. While there is a clear reduction in ethane conversion (ethylene-to-ethane), catalysts containing molybdenum demonstrate a direct relationship between the active site loading used and the selectivity towards ethylene. According to this discovery, the addition of MoO_3 lessens the effect of zeolite cracking. Increasing the Mo loading to 15% initially boosts conversion at the beginning of the reaction, but subsequently leads to a rapid decrease in ethylene formation caused by ethane conversion to DeH, despite, the increase in selectivity. Uslamin et al. found that there was a simultaneous decrease in conversion and an increase in selectivity when employing MoZ [199] for ethane DeHA and DeH. The unique mechanism of ethane aromatization using the Mo active site was observed in comparison to Ga. According to previous studies, it has been suggested and agreed upon that the utilisation of Mo does not result in the production of ethylene as an intermediate for benzene production [199]. Therefore, this indicates that low ethylene selectivity is not attributed to high ethane conversion to benzene. Furthemore, the large formation of methane indicates no or limited benzene formation since methyl radical is the intermediate step for ethane DeHA using Mo-based zeolite as reported by Uslamin et al. [199].

The loading of 15MoZ demonstrates an average molar ratio of 1.03 for hydrogen-to-ethane. Nevertheless, the ratio rises to 1.9 and 1.8 for 5MoZ and 10MoZ, respectively, as evidenced by the production of hydrogen, validating these discoveries. The elevated hydrogen molar ratio arises from the synthesis of benzene or excessive dehydroaromatization, resulting in the formation of aromatic-based coke, despite hydrogen being consumed by methane. According to the reports, the application of Mo on ZSM-5 catalysts leads to the synthesis of benzene, but only at temperatures over 600 °C [199], [200]. This observation is expected because of the necessary endothermicity of benzene compared to ethylene derived from ethane, as demonstrated in Reaction 8 and Reaction 9. Therefore, it can be assumed that the production of benzene is negligible, and the increase in the molar ratio of hydrogen to ethylene is generated by coke formation.

Furthermore, the combination of Cr-Mo was investigated for alkane DeH to require Cr active sites for ethane DeH with Mo oxides for HDO as shown in Figure 6.9. The combination also aim to maintain the good alkane DeH in a single active site run using MoO_3. The use of

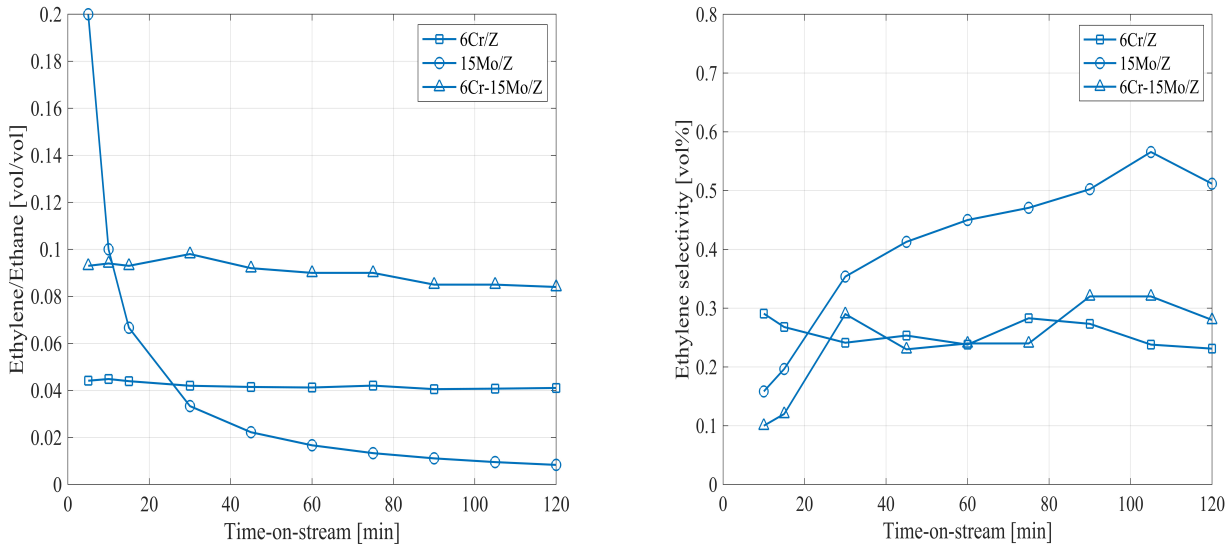


Figure 6.9: Ethane DeH using Mo and Cr zeolite catalysts at 600 °C.

6Cr15MoZ maintains similar performance for ethane-to-ethylene to 10Mo, not including the sharp decline as of 15MoZ. Furthermore, ethylene selectivity also increased with the 10MoZ, but with relatively better performance compared to the results of chromium-loaded selectivity as well as hydrogen formation rate with a hydrogen to ethylene molar ratio of 0.5. This suggests the incorporation of Cr limits DeHA and eventually carbon formation.

6.3.4 Cr and Mo in zeolite supported catalysts for ethane and guaiacol DeH-HDO

Figure 6.10 illustrates that the introduction of guaiacol initially decreases the production of ethylene, but with a higher degree of selectivity. As the reaction proceeds, the generation of ethylene increases, albeit with less selectivity due to the excessive formation of methane caused by the zeolite cracking of ethane and guaiacol HDO.

The application of zeolite for DeH-HDO in the synthesis of gaseous compounds demonstrates clear variations in performance over time when compared to catalysts supported by alumina. At first, the production of ethylene is low, but it gradually increases with time, as shown in Figure 6.10. When using a chromium-based catalyst, the use of guaiacol slightly enhances the selectivity of ethylene to hydrocarbons. Conversely, when MoO_3 is utilised in zeolite, there is a complete selectivity towards ethylene at 15 min, which dramatically decreases to 9% as reaction progress. The increase in ethylene output can be linked to the influence of dehydroaromatization. Figure 6.10 demonstrates that the addition of guaiacol initially reduces ethylene synthesis of ethylene, but with increased selectivity. During

the progression of the reaction, the production of ethylene intensifies,however, its selectivity decreases due to the excessive formation of methane resulting from the zeolite-induced cracking of ethane and guaiacol HDO.

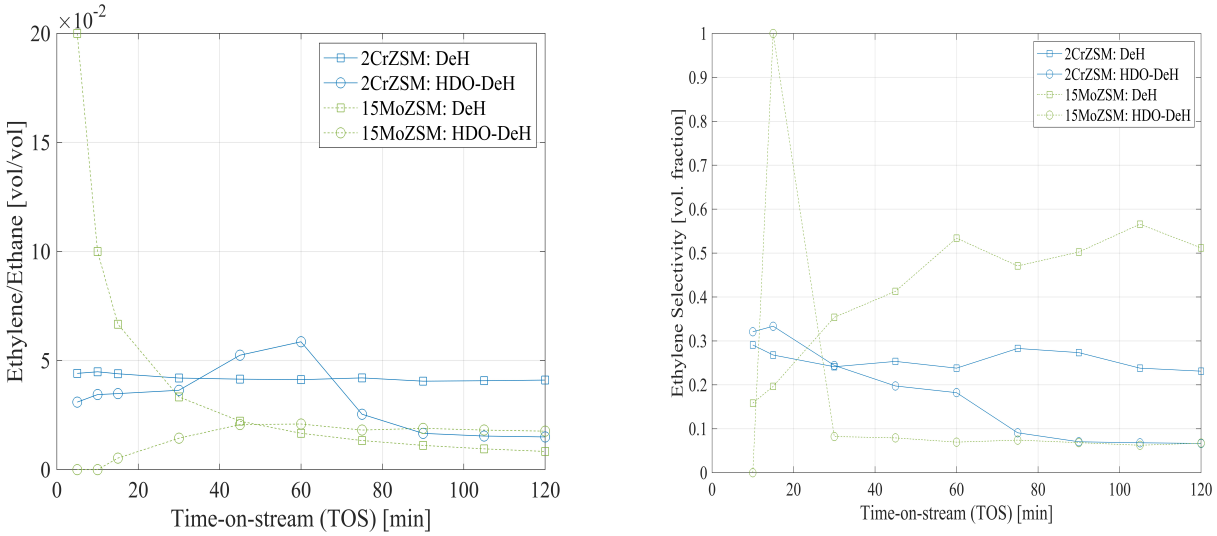


Figure 6.10: DeH-HDO using Mo and Cr zeolite catalysts at 600 °C

The gas produced by DeH-HDO and DeH suggests that the addition of guaiacol resulted in hydrogen consumption via HDO, as depicted in Figure 6.11. The decrease in the mol/mol ratio of hydrogen-to-ethylene, as compared to DeH, suggests that both hydrogen transfer processes are taking place inside the same catalytic bed for both Cr and Mo-based catalysts. As mentioned earlier, the Cr-zeolite exhibits reduced selectivity towards ethylene as a result of the zeolite acidic properties, causing cracking mechanisms, in particular, at the investigated low Cr loading. Nevertheless, the incorporation of guaiacol resulted in the consumption of H_2, leading to a significantly reduced H_2-to-ethylene ratio, which is $\ll$1.0. In the case of the Mo-zeolite catalyst for DeH-HDO, the molar ratio was not calculated in the first 30 min due to the absence of ethylene production and the presence of excess hydrogen production. This trend remained for 60 min, with the molar ratio remaining above 1.0 compared to DeH. This implies that the addition of guaiacol may have altered the ethane conversion mechanism, leading to the formation of benzene and coke. Figure 6.11 illustrates the H_2 consumption using guaiacol for HDO over the past 60 min. However, the rate of H_2 consumption is comparatively slower when using a Cr-based catalyst at the studied loadings.

The liquid product of DeH-HDO in zeolite-based catalysts yields similar products to alumina-supported catalysts but with varying yields. Both Cr and Mo active sites exhibit higher SOAr than DOAr. Zeolite catalysts generate significant amounts of heavy molecules, char-

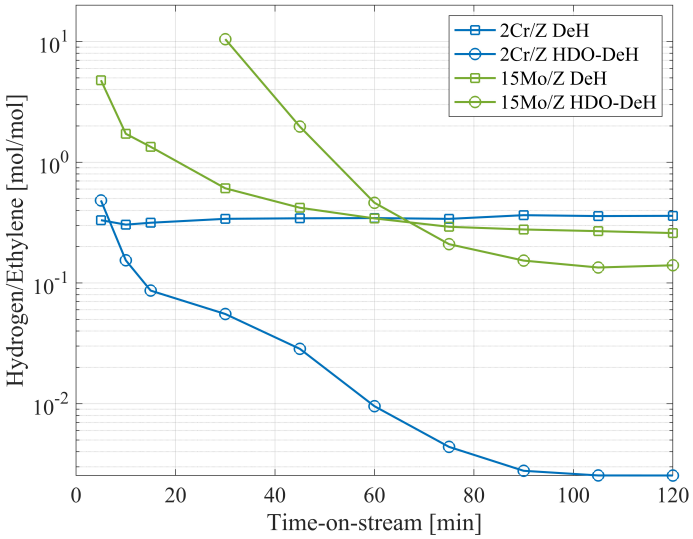


Figure 6.11: Hydrogen transfer in DeH-HDO using Mo and Cr zeolite catalysts at 600 °C

acterised by two aromatic rings with one or fewer oxygen atoms per aromatic ring. The formation of heavies may result from aromatic polymerisation due to insufficient reactive hydrogen, as evidenced by the high guaiacol conversion observed for both Mo (79%) and Cr (80%) on average over a 120-minute run. Despite Mo showing lower hydrogen consumption (23%) compared to Cr (76%) in DeH-HDO, indicating less HDO. Mo-based catalysts exhibit a higher presence of heavy hydrocarbons in the collected liquid resulting on a higher condensation rate at the catalyst surface. In contrast, Cr catalysts exhibit lower condensation with a reduced condensate of 0.13 g/g catalyst, attributed to the abundance of reactive hydrogen reducing precursor heavies in the liquid phase. However, CrZ catalysts report higher carbon deposition due to excessive DeH.

Table 6.7: Atmospheric pressure DeH-HDO coupling at 600 °C using zeolite-supported Cr and Mo oxides

Catalyst	Reaction	H_2/ethylene (vol/vol)	HDO selectivity	HDO yield	Carbon (g/g_{cat})	Condensation (g/g_{cat})
2CrZ	DeH	0.34	-	-	0.002	0.006
	DeH-HDO	0.08	0.96	0.97	0.22	0.13
15MoZ	DeH	1.03	-	-	0.039	0.005
	DeH-HDO	1.34	1.303	1.402	0.16	0.40

Although MoZ catalysts produce hydrogen at a higher rate relative to ethylene, this does not facilitate HDO. Reactive hydrogen availability is crucial. These observations suggest that the reactive hydrogen necessary for improving DeH-HDO is derived from catalytic ethane DeH adsorbed at the catalytic site. Therefore, further catalytic engineering is needed to achieve enhanced outcomes in the catalytic coupling of DeH-HDO.

6.4 Conclusions

The choice of catalyst support plays a crucial role in the development of active sites in reaction mechanisms. This chapter investigates alumina and zeolite as supports for Cr and Mo active sites. The synthesised catalysts demonstrate their potential to facilitate DeH-HDO in terms of ethylene formation and the degree of HDO. Both Cr on zeolite and alumina exhibit higher ethylene formation in the presence of guaiacol compared to runs without guaiacol. Despite rapid deactivation after 60 min, increased ethylene correlates with higher hydrogen consumption, indicating H-transfer to HDO. This enhancement in ethylene formation and hydrogen consumption leads to almost complete guaiacol conversion for both Cr-based catalysts, as well as relatively low condensate deposition. The difference between the two supports lies in selectivity. The alumina catalyst favours the DME route, whereas the zeolite cracking characteristic plays a role in improving HDR, yielding 28% at the start of the run.

Mo-active sites for HDO yield different outcomes on alumina and zeolite. Alumina reduces ethylene formation due to rapid deactivation, which is attributed to minimal hydrogen formation and accelerated coke formation. Conversely, zeolite exhibits higher ethylene formation towards the reaction end, with lower hydrogen/ethylene, suggesting increased selectivity towards DeH over DeHA, supported by the absence of guaiacol run. The addition of Cr and Mo in a single support has demonstrated similar effects to MoAl, which is attributed to the high loading of molybdenum oxide, yet a slight improvement caused by the existence of chromium oxide was observed. In the zeolite catalyst, the integration of Cr and Mo yielded higher ethylene formation compared to single-active-site catalysts. However, further research is required to understand the distribution of active sites and the associated synergistic effects.

Chapter 7

Techno-Economic Feasibility for Integrating Alkane DeH with Bio-Oil HDO Processes

7.1 Introduction

Considerable emphasis has been devoted to valorising lignocellulosic biomass to produce high-value green chemicals. A crucial aspect of transitioning the chemical industry towards bio-based feedstock is efficiently converting lignin-derived bio-oil into environmentally-friendly chemicals while ensuring economic viability in biorefineries. The objective is to provide hydrocarbon building blocks that can be effectively integrated into the chemical industry's value chain, thereby meeting the worldwide demand for chemicals in an environmentally sustainable manner. To achieve this objective, HDO has been identified in this work as the primary process in biorefineries. Previous chapters have explored the potential of catalytic HDO of bio-oil model compounds via in-situ hydrogen generation by alkane DeH. Experimentally, the developed concept has proven promising from a technological standpoint. Nevertheless, it is imperative that the economic aspects of the process also must be sufficiently appealing for implementation.

7.1.1 Chapter structure

This chapter investigates the techno-economic assessment (TEA) of various approaches used for coupling HDO and ethane DeH in a single catalytic bed, termed as in-situ and DeH-HDO, to assess its feasibility compared to externally produced hydrogen, referred to as ex-situ or conventional HDO. This chapter commences by briefly highlighting the recent published economic evaluation of HDO processes in Section 7.1.2. For this work, Section 7.2 evaluates the economic potential of substituting molecular hydrogen for HDO with hydrogen generated via ethane DeH, utilising experimental data and historical pricing. The aim of

this section is to provide insights into the TEA at the current experimental stage. Section 7.4 examines the economic viability of substituting hydrogen sources based on findings from highly cited publications. This section explores the TEA after the anticipated development of the DeH-HDO process, drawing on published research. Finally, this chapter concludes by offering perspectives on the benefits of scaling up DeH-HDO processes and their potential integration in Section 7.5.

7.1.2 The industrial implication of coupling DeH-HDO

Numerous studies have delved into the techno-economic aspects of upgrading bio-oil into viable fuels or transforming it into high-value chemicals. The United States and European Union have achieved great milestones in bio-oil upgrading for fuel and chemical production [201]. A comprehensive study was conducted by Kumar et al. in 2013 to highlight the progress in commercialising biomass upgrading using different approaches, including thermochemical and biochemical conversion [201]. The increasing number of published studies investigating the economic potential of HDO of bio-oil into upgraded fuels exhibits interest in moving from experimental findings into commercialisation [202]. Despite the revealed positive economic outcomes and environmental advantages of bio-oil to reduce and eventually eliminate petroleum-based fuels, commercialisation efforts are minimal [201], [203]. The assessments of biomass processing are varied and lack certainty due to the complexity of the feed material. They are based on specific biomass types, upgrading processes, and operating conditions, which limits their applicability beyond certain parameters. However, these assessments offer valuable indications of the potential for biomass processing for chemical production.

Sorunmu et al. evaluated the technological readiness level (TRL) of reported technologies for upgrading bio-oil into high-value fuels and chemicals in terms of TEA, life cycle assessment (LCA), and green house gas (GHG) emissions [203]. Since the evaluated technologies are still under development, the minimum product selling price for most of them remains above the conventional process threshold. However, the global warming indicator shows positive values below the conventional process threshold. Despite the economic disadvantages at this stage for the investigated technologies (mainly for upgraded fuels), better economics could be achieved by focusing on the production of biomass-derived chemicals instead of bio-oil, as they have higher selling prices. Definitely, these prices have to satisfy the complex processing requirements for producing high-value commodity chemicals such as BTX

and phenol. Most of the technologies under investigation rely on molecular hydrogen for upgrading, which inevitably impacts the technology's attractiveness by driving up the feedstock cost. Therefore, the present work on DeH-HDO presents a promising avenue for enhancing the economics of bio-oil HDO, as discussed in the subsequent sections.

7.2 Techno-economic (TEA) based on experimental findings

7.2.1 Economic Potential

The calculation of the EP of the process is derived from the evaluation of the selling prices of both the feedstock and the products. The selling prices are derived from commercially established conventional processes and serve as a means to provide insight into the economic feasibility of the process. The economic potential does not incorporate capital and operation expenditures, as these expenses are already factored into the selling prices, as shown in Equation 1.

$$EP = \sum((F_{\mathrm{i,out}} - F_{\mathrm{i,in}})_{\mathrm{DeH\text{-}HDO}} \cdot P_{\mathrm{i}}) - \sum((F_{\mathrm{i,out}} - F_{\mathrm{i,in}})_{\mathrm{HDO}} \cdot P_{\mathrm{i}}) \qquad \text{(Equation 1)}$$

In this work, this analysis provides an insight into the present state of the DeH-HDO approach compared to conventional HDO, based on experimental data. The experimental data utilised for both DeH-HDO and HDO hydrogen analysis are derived from the same catalytic system and operating conditions. The experimental data selected for this analysis is based on a 1:1 mixed catalytic bed of Cr_2O_3 supported on alumina and unsupported MoO_3 at 600°C and atmospheric pressure. The reported yields are based on an average of 120 min of operation. The mass balances considered for this analysis are listed in Table 7.1.

Given the observed volatility of commodity chemicals in correlation to fluctuations in crude oil prices [204], various pricing scenarios were taken into account in Figure 7.1 to analyse the process's economic viability. It is assumed that the product prices are highly correlated to the feedstock prices, which vary based on geographical location. Some countries have access to cheap biomass and/or ethane, while others rely on expensive imports. Therefore, the EP was considered for a range of feedstock prices. The analysis in Figure 7.1 considers the economic potential of converting the conventional HDO processes to an DeH-HDO

Table 7.1: Material balance of guaiacol processing via conventional HDO and DeH-HDO based on experimental findings. Scaled-up to a guaiacol processing capacity of 99.1 ton·hr^{-1}

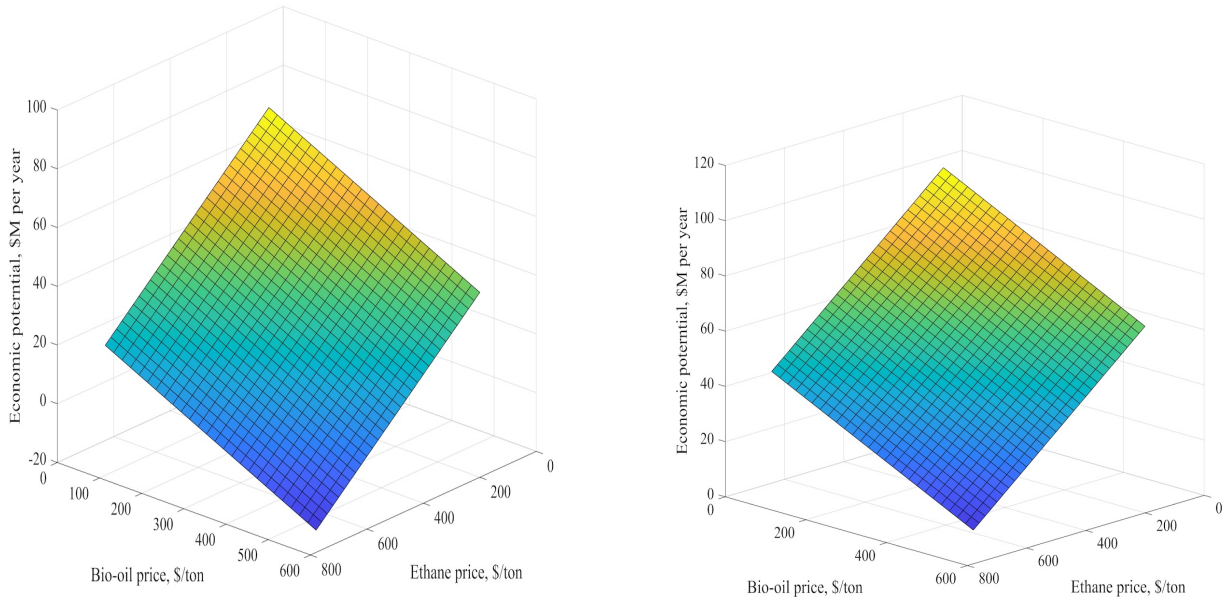
Component	DeH-HDO		conventional HDO	
	Inlet (ton·hr^{-1})	Outlet (ton·hr^{-1})	Inlet (ton·hr^{-1})	Outlet (ton·hr^{-1})
Ethane	48.1	38.9	-	-
Ethylene	-	3.17	-	-
Hydrogen	-	0.19	3.21	1.86
Methane	-	3.17	-	3.42
Guaiacol	99.1	11.9	99.1	23.8
Phenol	-	22.0	-	12.0
Anisole	-	2.25	-	2.37
Cresol	-	24.5	-	22.1
M.cresol	-	9.21	-	8.05
Catechol	-	13.6	-	16.0
M.catechol	-	1.18	-	1.92
Water	-	8.82	-	8.29
Methanol	-	3.4	-	0.36
Heavy	-	0.91	-	1.37

approach, which means hydrogen prices heavily contribute to EP. Therefore, in this analysis, two hydrogen values were considered to distinguish the effects based on the hydrogen source. 1000 \$·ton^{-1} is used for grey hydrogen that is generated from methane reforming processes, while 3000 \$·ton^{-1} is used to consider the use of hydrogen generated from renewable sources such as electrolysis.

Table 7.2: Chemical prices used for EP calculation based on historical data.

Component	AVG price \$·ton^{-1}	StD price \$·ton^{-1}	Min. price \$·ton^{-1}	Max. price \$·ton^{-1}
Hydrogen[1]	-	-	1,000	3,000
Ethane	435.0	163	110	760.0
Ethylene	1,055	238	800	1,600
Methane	265.0	-	-	-
Phenol	960.0	236	800	1,400
Cresol	1,314	540	341	2,500
Benzene	659.0	168	280	1,100
Toluene	803.0	191	440	1,330
Xylenes[2]	694.0	147	407	1,020
Anisole	1,152	283	960	1,680
Lignin (bio-oil)	380.0	60.0	260	500.0
Biomass	80.00	-	-	-
Heavies	162.0	6.00	87.0	237.0
Methanol	369.0	71.0	223	475.0

[1] Based fossil fuel or renewable sources
[2] Average of p-xylene, o-xylene and m-xylene



(a) Hydrogen $1000/ton **(b)** Hydrogen $3000/ton

Figure 7.1: Economic potential for using alkane DeH for HDO of bio-oil at different feedstock and product prices.

Based on historical chemical prices, the economic potential indicates a higher potential for DeH-HDO over conventional HDO using experimental yields obtained in this investigation, as shown in Table 7.1. Positive EP, which appears to be dominant for high and low hydrogen prices, is essential to deeply investigate this approach. Yet, for the fixed product prices, the increase in the price of ethane and biomass with low-cost hydrogen might lead to no or a negative advantage of using DeH-HDO approach. This becomes crucial for gas-importing countries; however, this analysis comes with a low experimental conversion of ethane caused by carbon deposition. Therefore, advancing the performance of the coupled system will lead to enhanced economic potential. Figure 7.2 shows the value distribution of the outlet stream based on the experimental findings. The distribution shows a low contribution of hydrogen and ethylene prices, which is caused by the limited metric yield. However, since the liquid product streams are similar for for HDO with molecular hydrogen and DeH-HDO processes, the difference in EP is controlled by the gas distribution.

The positive EP values demonstrate enough promise to thoroughly examine the techno-economic aspects, including capital expenditure (CapEx) and operational expenditure (OpEx), inside the EP equation in order to mitigate uncertainties. In particular, although the liquid products of DeH-HDO and HDO have shown similarity, DeH-HDO generates valuable ethylene. However, it is crucial to address the separation of ethane and ethylene due to the

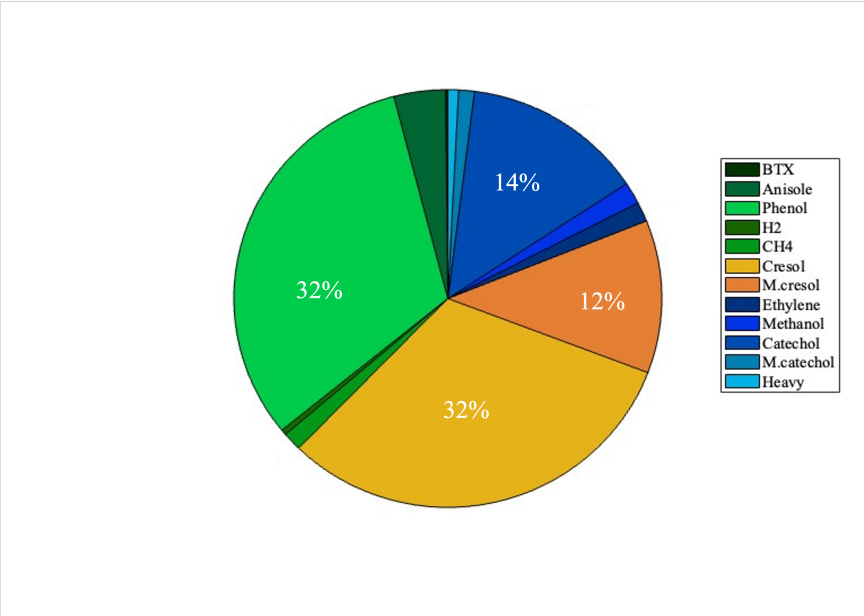


Figure 7.2: The product distribution in the economic potential of DeH-HDO approach

impact of coke production on ethylene yield during DeH-HDO. This separation process is known to be energy-intensive and requires significant investment. Therefore, DeH-HDO has been evaluated as a standalone technology and integrated with the state-of-the-art steam cracking of ethane

7.3 DeH-HDO process synthesis for TEA

7.3.1 Process boundary limits

The synthesis of biomass-to-chemical processes relies heavily on the biomass source and the sequence of conversion and extraction steps required to obtain the desired product streams. In this evaluation, the focus lies on comparing conventional HDO with coupled DeH-HDO. The process boundary limit begins with the supplied lignin-derived bio-oil via lignin pyrolysis and extends to the purified gas and liquid chemical streams, as depicted in Figures 7.3 and 7.4.

In conventional HDO, after the conversion step, any unreacted hydrogen from the HDO process is recycled back to the HDO conversion unit through gas separation processing, yielding recycled hydrogen and fuel gas. The generated fuel gas stream is then utilised for energy generation during HDO conversion and its subsequent separation. The resulting HDO upgraded liquid fraction is further separated to yield BTX and phenols, which are then sold for further processing outside the boundary limit (OBL). The non-upgraded fraction of bio-oil is recycled for further upgrading. It is assumed that the DeH-HDO approach follows a similar conversion process to the conventional HDO approach in terms of capital

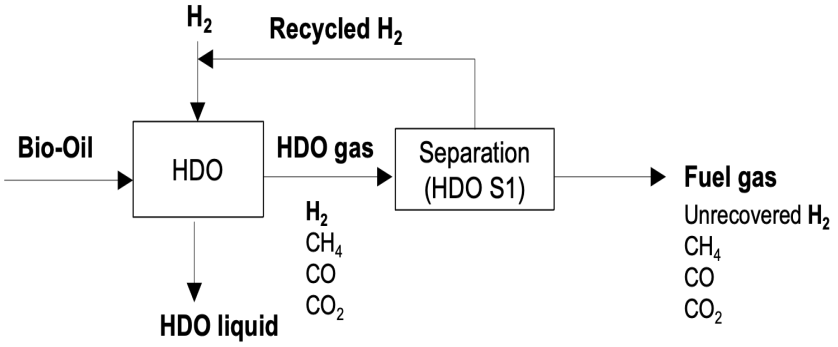


Figure 7.3: BFD of conventional HDO using external (ex-situ) hydrogen source defined as HDO

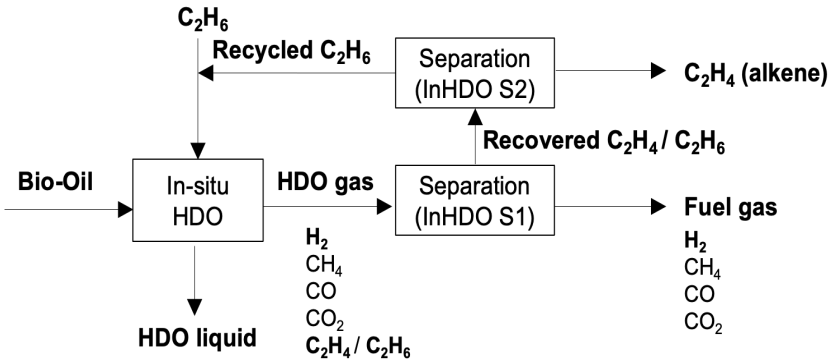


Figure 7.4: BFD of HDO using ethane DeH (in-situ) as hydrogen source defined as DeH-HDO

expenditure CapEx. However, the implementation of DeH-HDO approach requires additional gas separation steps, including the energy-intensive separation between ethane and ethylene. Consequently, the economic viability of the DeH-HDO process may be impacted by the hydrogen donor reaction. Nonetheless, integrating the DeH-HDO concept with steam cracking, a key process in the chemical industry, could lead to better utilisation of existing plant CapEx. As illustrated in Figure 7.8, state-of-the-art ethane steam cracking can be integrated with bio-oil HDO in the separation section.

In terms of process flexibility, the separation section of steam cracking is designed to separate C_2-C_4 alkanes and alkenes and may include a BTX separation train depending on the cracked feed. For instance, naphtha steam cracking processes typically include a BTX separation train, whereas C_2 and C_3 are often not separated. However, mixed cracking feed exists since each cracker comprises several independent furnaces where the cracked gases are mixed in the quenching section. This flexibility often necessitates a BTX separation train in most steam cracking processes, obviating the need for new installations in existing plants.

7.3.2 HDO conversion section

In the TEA flowchart incorporates HDO conversion, which is reliant on empirical data for quantifying liquid and gas products, with solid products determined through TGA analysis. However, the content of water was not measured. To compensate for this, we implemented a reaction network, as illustrated in Figure [Reaction network], to ensure that the overall mass balance is maintained and to calculate the conversion for each individual reaction, as outlined in Table 7.3. These conversion values were determined for the flowchart analysis in this study due to the absence of a kinetic model for the complex reaction network.

This reaction network assumes that alkane DeH and HDO occur within the same catalytic system but independently, as a mixed catalyst bed is used. This implies that Cr active sites are likely responsible for the DeH, while HDO takes place on the Mo oxide active sites. Nonetheless, the fundamental concept in this project is that HDO relies on adsorbed hydrogen radicals at the active sites and/or the support. It's important to note that both HDO mechanisms may be observed, with both hydrogen radicals and molecular hydrogen playing significant roles in HDO, primarily due to the differences in residence time between the two reactions. Alkane DeH has a shorter residence time, which means that molecular hydrogen could be regenerated before HDO is completed.

Furthermore, it's worth mentioning that alkane DeH might occur in the gas phase at high operating temperatures. This suggests that with the missing adsorbed medium, which facilitates hydrogen transfer between ethane and bio-oil, molecular hydrogen can be formed. This especially occurred due to the excessive accumulation of carbon formation as well as the small catalytic loading ranges examined in comparison to the published guaiacol-to-catalytic ratio. Therefore, it is reasonable to assume that each reaction operates independently for the flow-sheeting analysis.

7.3.3 HDO liquid separation section

HDO of bio-oil derivatives into high-value chemicals generates valuable mono-aromatics as well as valuable alcohols that contribute to the overall positive economics of the process. However, to realise the potential value of these compounds, the product HDO liquid stream has to be processed to separate BTX, single oxygenated aromatics, double oxygenated aromatics, heavies, water, and alcohols from each other. Since many different species exist in the HDO liquid stream, the separation process will impact the overall economics of both

Table 7.3: Used conversion of developed reaction network based on experimental findings.

Rxn	Process	Reaction	Conversion
1	De-methoxylation	$C_7H_8O_2 + H_2 \rightarrow C_6H_5OH + CH_3OH$	64.1
2	De-methylation	$C_7H_8O_2 + H_2 \rightarrow C_6H_4(OH)_2 + CH_4$	21.3
3	Hydrogenolysis	$C_7H_8O_2 + H_2 \rightarrow C_6H_5OCH_3 + H_2O$	2.60
4	De-methoxylation	$C_6H_5OCH_3 + H_2 \rightarrow C_6H_6 + CH_3OH$	0.00
5	Methylation	$C_6H_4(OH)_2 + CH_4 \rightarrow C_6H_3(OH)_2CH_3 + H_2$	5.80
6	Hydrogenolysis	$C_6H_4(OH)_2 + H_2 \rightarrow C_6H_5OH + H_2O$	21.5
7	Hydrogenolysis	$C_6H_5OH + H_2 \rightarrow C_6H_6 + H_2O$	2.10
8	Polymerization	$C_6H_6 \rightarrow Coke + 3\,H_2$	100
9	Methylation	$C_6H_5OH + CH_4 \rightarrow C_6H_4CH_3OH + H_2$	48.5
10	Hydrogenolysis	$C_6H_4CH_3OH + H_2 \rightarrow C_6H_5CH_3 + H_2O$	0.52
11	Methylation	$C_6H_4CH_3OH + CH_4 \rightarrow C_6H_3(CH_3)_2OH + H_2$	14.2
12	Hydrogenolysis	$C_6H_3(CH_3)_2OH + H_2 \rightarrow C_6H_3(CH_4)_2 + H_2O$	0.00
13	Methylation	$C_6H_5OH + 2\,CH_4 \rightarrow C_6H_3(CH_3)_2OH + 2\,H_2$	6.87
14	Dehydrogenation	$C_2H_6 \rightarrow H_2 + C_2H_4$	2.00
15	Cracking	$C_2H_6 \rightarrow CH_4 + H_2 + C$	24.8

$C_7H_8O_2$:guaiacol (GUA), C_6H_5OH:phenol (PHL), $C_6H_4(OH)_2$:catechol (CAT),
$C_6H_4CH_3OH$:cresol (CRSL), $C_6H_5OCH_3$:Anisole (ANS), $C_6H_5CH_3$:toluene (TOL)

CapEx and OpEx perspectives. Therefore, this EP is considered crucial for the overall process economics. The separations are based on the physical properties as well as the binary interaction between the components present. In addition, separation heuristics were employed to obtain an optimised separation sequence. The main components are phenol, cresol, methylcresol, methanol, heavy hydrocarbons, catechol, and unconverted feed. In addition, the product contains water. Figure 7.5 shows a separation block flow diagram designed by taking into account that guaiacol and aromatic with two oxygenated functional groups will be sent back for further HDO. The available binary mixtures were studied for the level of difficulty of separation as well as the existence of azeotropes. The designed separation train was established in Aspen Hysys to ensure the technological ability of obtaining the product at the market specification. Yet for this analysis, ethane and ethylene separation were not considered due to the low conversion rate. However, this was considered in the next sections.

In the flowsheet the process recycled catechol, guaiacol and m.catechol to result the the product listed in Table 7.4 satisfying market specification. Detailed equipment specification and process flow diagram is available in [205].

7.3.4 Economic evaluation

Detailed process flow diagram based on Aspen Hysys flowsheet is available in Appendix C. The flowsheet includes the conversion and separation sections to estimate the working and

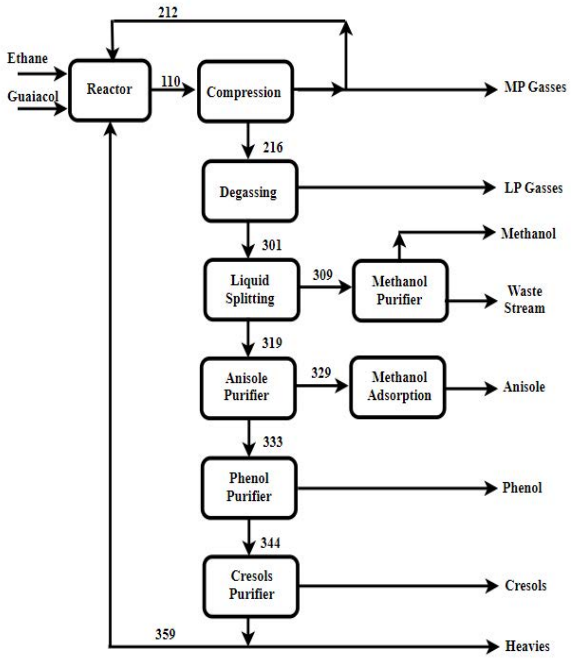


Figure 7.5: Proposed separation sequence based on experimental findings [205]

Table 7.4: Net production mass balance from the Aspen flowsheet for the production of 200 kta phenol.

Component	Mass Balance, ton·hr^{-1}	Net Production, ton·hr^{-1}
Guaiacol	99.12	99.1
Ethane	17.5	17.5
Total Raw Materials	116.6	116.6
Gases[1]	12.1	9.97
Methanol	12.3	12.23
Wastewater	3.45	-
Anisole	2.44	2.44
Phenol	25.4	25.4
Cresols[2]	28.5	28.5
Heavies	27.6	27.6
Carbon	4.81	0
Recycle		10.4
Total Products	116.6	116.2

[1] Includes hydrogen, methane and ethylene
[2] Includes m-cresol

fixed capital investment requirements to scale up DeH-HDO. The equipment purchase cost is estimated to be $49.5M based on aspen process economic analyser (APEA) for all the operation units except reactor and continuous catalyst regeneration (CCR) system, which were estimated from literature. The detailed capital investment cost was estimated based on the criteria used by Wright et al. to be $269M [206]. Table 7.5 illustrates the fixed capital investment breakdown. The revenue generated based on the production rate shown in Tables 7.1 and 7.2 leads to an annual gross profit (revenue - cash flow) of $35M. In this scenario, no ethane and ethylene separation was implemented due to the enrichment of

ethane in the ethane/ethylene stream caused by the small conversion.

Table 7.5: Total capital investment breakdown.

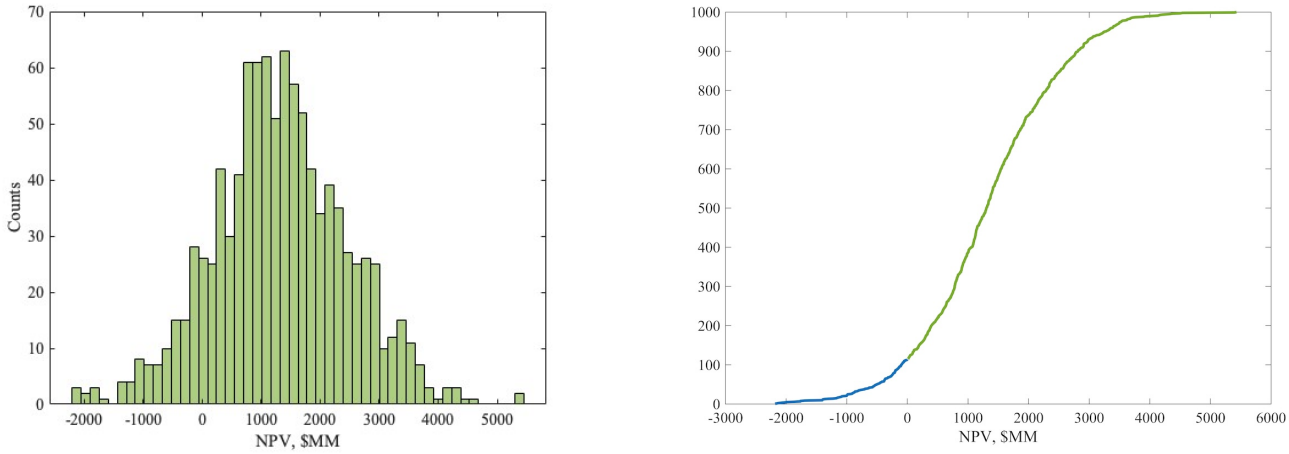
Total purchased equipment cost	F_{PC}	\$MM	49.5
Total installed cost (direct cost)	F_{DIR}	\$MM	148
Indirect cost	F_{IND}	\$MM	44.0
Total direct and indirect costs	F_{cost}	\$MM	193
Contingency		\$MM	38.5
Fixed capital investment	F_{FC}	\$MM	231
Working capital	F_{WC}	\$MM	37.6
Total capital investment	F_{TCI}	\$MM	269

For NPV calculation, the process was assumed to have a lifetime of 20 years with three establishments. The capital investment during the first three years was divided as follows: (year 1) 30% of fixed capital; (year 2) 60% of fixed capital; (year 3) 10% of fixed capital plus the working capital. The NVP was evaluated at 30%, 5%, tax rate, and discount rate, respectively, to yield a 20-year NVP of \$1.6B. The selected tax rate was based on a common and average global corporate tax rate that ranges from 25-45% depending on the location. No subsidy or credit for the production of bio-based products was considered in the analysis since this type of incentive is expected to change as the bio-based chemical industry matures.

7.3.5 Monte-Carlo and economic sensitivity analysis

The chemical industry operates in a landscape of consistent price fluctuations in both commodities and energy resources. These fluctuations are predominantly attributed to the inherent volatility in chemical prices and the disruptions in supply and demand. To navigate this complex terrain, the Monte Carlo analysis method has emerged as a critical tool. It allows for the exploration of a wide array of potential scenarios driven by ever-fluctuating factors, most notably energy and commodity prices. This method leverages an extensive historical dataset, making it particularly valuable in situations where historical data is scarce, a common challenge when dealing with certain chemical substances. In this analysis, the NPV was computed based on the mean prices of chemicals and utilities. However, recognising the intricate economic risks associated with the chemical process, we conducted a comprehensive examination. This involved an in-depth analysis that considered an extensive range of process options, as outlined in Table 7.6. We conducted a total of one thousand simulations as part of this study.

The intriguing finding, illustrated in Figure 7.6, is that, despite a strong NPV generated in the base scenario, a negative NPV remains a plausible outcome. In fact, our analysis indicates a 88% likelihood of a positive result when subjected to one thousand simulations involving variations in chemical and utility prices. The simulated NPV outcomes range from -$2.0B to $4.0B, encompassing the entire price spectrum, from feedstock and product to utilities. This is a remarkable observation, given the typically high correlation observed in petroleum-based chemicals, where an increase in ethane prices, a key feedstock, often aligns with increased ethylene prices, the primary end product. It is crucial to emphasise the Monte-Carlo analysis's ability to reflect price variations driven by different geographical locations, a factor significantly impacting feedstock pricing. For instance, ethane prices in the Middle East, the United States, and Europe stand at $90, $250, and $760 per tonne, respectively. Therefore, conducting a Monte Carlo study provides a reliable gauge of the economic outlook for the DeH-HDO process. In summary, the Monte Carlo simulation results point to an estimated NPV of approximately $1.6 billion, with a standard deviation of $1.2 billion. This insight underscores the economic dynamics in play, highlighting the importance of comprehensive analysis in the chemical industry.



(a) **(b)**

Figure 7.6: Monte Carlo analysis for DeH-HDO's NPV for 20 years with 30% tax and 5% discount rate

Figure 7.7 presents a comprehensive sensitivity analysis of the Net Present Value (NPV) aimed at maximising the economic performance of the DeH-HDO process. This sensitivity analysis is standardised using the baseline NPV of $1.61 billion and relies on data sourced from various published references. The variations in these values are influenced not only by historical fluctuations but also by the scale of activity. When it comes to feedstock costs, specifically ethane and guaiacol, any price fluctuations in these inputs can impact the NPV

calculations. Reducing the cost of ethane, particularly in regions like the Middle East, can have a positive effect on NPV. However, the need to import lignin-based oil can negatively affect cash flow. In certain regions, the use of lignin-based bio-oil may offer benefits but also pose challenges, such as the cost of importing ethane. Consequently, the cost of feedstock for this process is entirely dependent on the geographical location of the plant. An anticipated cumulative impact of 20% on the total NPV is projected due to these factors.

In terms of products, the price of cresol plays a significant role in NPV due to its large production volume and substantial economic price fluctuations. To maintain a strong NPV, it is crucial to minimise these price fluctuations for cresol. Anisole and methanol, on the other hand, have a minor impact, contributing less than five percent to the total revenue generated by the entire process. The influence of ethylene variation is also minimal due to its relatively low production rate. Addressing this requires an increase in DeH-HDO to enhance the economic viability of the process and mitigate any negative fluctuations in product value.

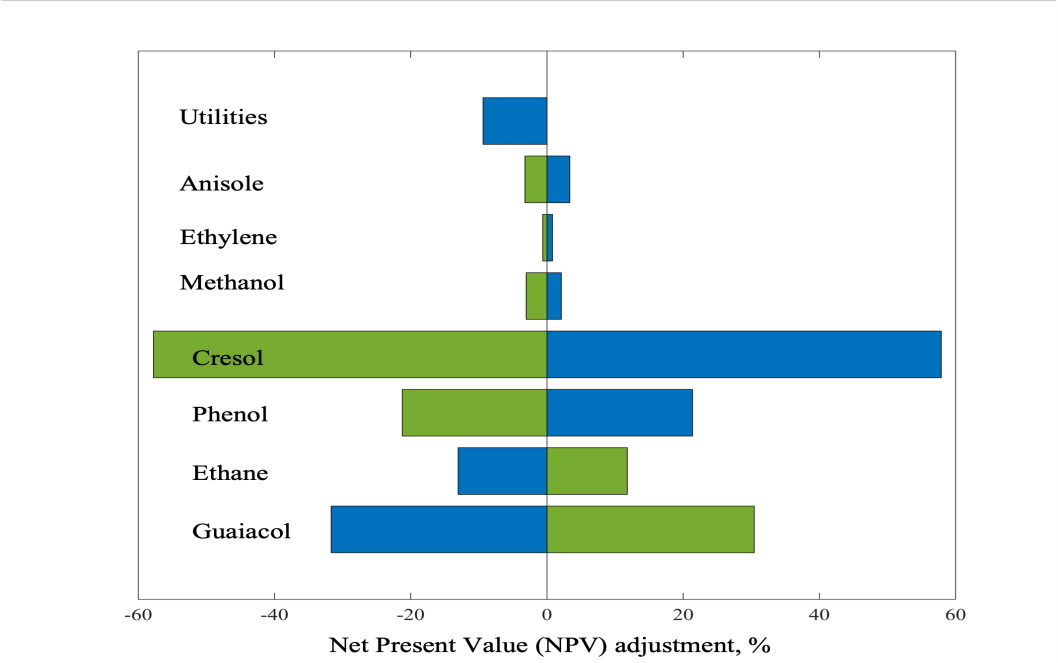


Figure 7.7: NPV sensitivity analysis based on feedstock,product and utilities value variation by a stander deviation: $+\sigma$ (green) and $-\sigma$ (blue).

7.3.6 Sensitivity analysis: Improved ethane DeH

In pursuit of enhancing the overall economic prospects of the integrated DeH-HDO process, which aims to elevate the product value by generating alkenes, a hypothetical improvement in alkane DeH was explored to improve the product stream and establish a target for the technological advancement of DeH-HDO. Referring to reactions RXN 14 and 15 in Table 7.3,

it is important to note that both generate hydrogen through distinct mechanisms. RXN 14 follows a targeted alkane DeH mechanism, primarily driven by kinetics. In the absence of a catalytic bed, it leads to a limited conversion based on the thermodynamic equilibrium conversion of ethane. The second reaction (RXN 15) is a cracking mechanism dominated by thermal effects. Despite the simplified representation of ethane conversion reactions, they explain the distribution of gaseous products. However, it is essential to acknowledge the presence of water generated from HDO, along with other oxygenated compounds resulting from ethane conversion reactions such as reforming, contributing to RXN 15 products.

It is worth mentioning that the experimental findings in this study are based on a mixed catalyst bed comprising a Cr-based catalyst for ethane DeH and a Mo-based catalyst for the HDO of bio-oil. Over a two-hour run, alkane DeH accounts for approximately 2% of the total, while cracking is estimated to be around 25%. Consequently, improvements in ethane conversion were categorised based on these two reactions, as outlined below. These performance improvements were selected to cover different possible catalytic systems. Based on this work, Case A represents the dominant cracking mechanism involved from HDO that does not support DeH, similar to the investigated PNiMoAl excluding the influence of bio-oil (guaiacol) condensates. Case B, where DeH is partially improved by the addition of DeH active site similar to the catalytic system PNiMo-Cr. In Case C, it is based on improved catalysts for DeH and HDO maintaining the selective DeH, CrAl catalyst, while having HDO performance. From the literature, these values are representative for alkane DeH with Mo-based catalysts, where the alkene selectivity ranges from 38-84% [84]. Alkane DeH for Cr-based catalysts was reviewed by Saito et al. showing 19-41% with the absence of CO_2 [140].

Table 7.6: Monte-Carlo statistical analysis for a thousand-simulation run for DeH-HDO improvement via boosting alkane DeH performance.

Indicator		Base case	Case A	Case B	Case C
Gross profit	$MM/year	219	223	230	233
Mean NPV	20-year $B	1.31	1.31	1.38	2.61
STD NVP	20-year $B	1.18	1.16	1.19	1.17
Min. NVP	20-year $B	-3.53	-2.18	-2.18	-1.60
Max. NVP	20-year $B	5.70	4.92	5.00	6.43
Probability (>0)	%	87.3	87.5	88.3	98.7

Case A: Balanced conversion favours cracking (11.0% DeH and 15.7% cracking)
Case B: Balanced conversion favours DeH (15.0% DeH and 10% cracking)
Case C: Complete dehydrogenation of 20.0%

Balancing cracking and DeH products has demonstrated limited improvement due to the

challenge posed by the increased production of ethylene, coupled with the reduction in the energy-based stream, encompassing methane and unreacted hydrogen produced from both DeH mechanisms and HDO reactions. Another reason for the modest economic improvement stemming from ethylene production lies in the prevailing ethane prices, which render the difference between ethylene and ethane less attractive. As previously mentioned, this challenge can be mitigated by reducing the ethane price range used in this study, especially by considering geographical areas where ethane pricing is more justified. However, it's important to note that since no specific geographical location was selected, a general overview was provided. The probability of achieving a positive NPV saw a significant increase, reaching 98.7% in Case C, where the value of ethylene production compensated for the value of energy stream production. Nonetheless, the improvement in gross profit was relatively modest, reaffirming that even a slight improvement in feedstock prices could significantly boost the NPV for all cases.

7.3.7 DeH-HDO Integration to the chemical Industry

The previous section detailed the scaling up of the integrated DeH-HDO process to handle 790 kta of bio-oil, resulting in the production of 200 kta of phenol. This output accounts for approximately 1.5% of the current global phenol capacity. The chosen capacity aligns with Cespsa and INEOS production capacities, as they boast the largest capacities for bio-oil processing and phenol production, respectively [39], [40]. INEOS, the largest phenol manufacturer, has an overall production capacity of 4,000 kta, with its MOBILE, USA site initially holding a capacity of 400 kta [40]. Utilising half of this site's capacity is justified by the differing process feed for phenol production between petrochemical and bio-oil feed. Cespsa, claims its largest second-generation bio-fuels from bio-oil, has a capacity of 1,000 kta [39]. Therefore, these chosen capacities are deemed reasonable since the largest bio-oil processing facility is not exceeded, with a conservative phenol capacity.

The ultimate goal of this technology is to further improve it for the production of olefins and BTX to be scaled to the ethylene market capacity. Achieving this presents challenges, particularly due to limited ethylene production, which affects the allocation of feedstock for such a process with a significant recycled stream resulting from low alkane conversion. In the improvement scenario discussed earlier, ethylene production reaches 100 kta, which is less than 0.1% of the current ethylene market capacity. However, reaching this goal requires further work and innovation. Therefore, integrating DeH-HDO into existing processes is

seen as a way to improve the overall economic outlook and leverage its bio-based feed to advance the integrated process towards carbon neutrality, particularly for the production of olefins, BTX, and other high-value chemicals such as phenol. The challenge lies in the fact that the DeH-HDO process requires a petroleum-based feed (ethane) for alkane DeH. Two possible integration approaches have been considered: (1) integrating with a conventional refinery in a biorefinery setting or (2) integrating with a petrochemical facility that uses ethane or LPG (liquefied petroleum gas) as a feedstock as shown in Figure 7.8. In the former case, an extracted stream from the refinery's FCC (fluid catalytic cracking) unit would be directed toward the DeH-HDO process, but this would necessitate the installation of an energy-intensive ethane/ethylene separation unit. Alternatively, the integration of DeH-HDO with steam cracking, which utilises ethane, LPG, or naphtha for the production of alkenes and aromatics, presents significant advantages. The steam cracking process has been explored for various routes towards carbon neutrality, including the use of heat pumps and electrified crackers, aligning with the industry's commitment to carbon neutrality.

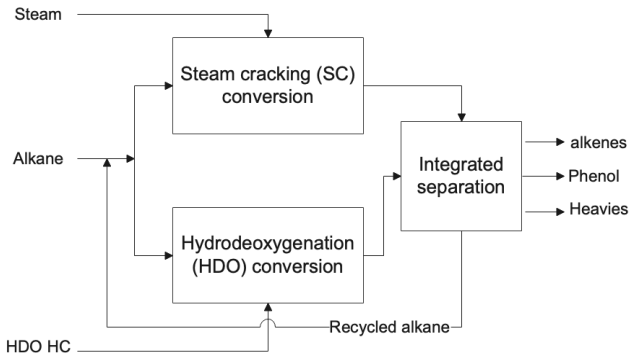


Figure 7.8: Block Flow Diagram (BFD) of conventional HDO

The integration of DeH-HDO with SC (integration option 2) involves diverting a fraction of allocated ethane (ethane-cut) from the steam cracker feed to the HDO reactor, as illustrated in Figure 7.9. The product stream from the HDO process is first purified to remove oxygenated compounds before being merged with the separation train of the steam cracking process. Steam cracking includes the separation of alkanes and alkenes in multiple distillation columns, and depending on the feedstock, it can also produce BTX compounds. In the case of feeding natural gas liquefied (NGL), LPG or a mixture, the products would be olefins. However, the use of naphtha includes BTX formation depending on the the naphtha source and physical properties. The content of naphtha is estimated by using oil quality characterisation factor as following:

$$k = \frac{(18 \cdot T_K)^{\frac{1}{3}}}{d} \qquad \text{(Equation 2)}$$

Where T is the boiling point in K, and d is the relative density. k values less than 12.0 makes more aromatic [207]. Therefore, steam cracker for naphtha feed contains a recovery section that includes BTX fractionation due to the production of 10-15 wt% of BTX based on the cracking severity [207]. In summary, This integration holds great potential as it can incorporate the advancements achieved by HDO in generating more de-oxygenation which yield more BTX.

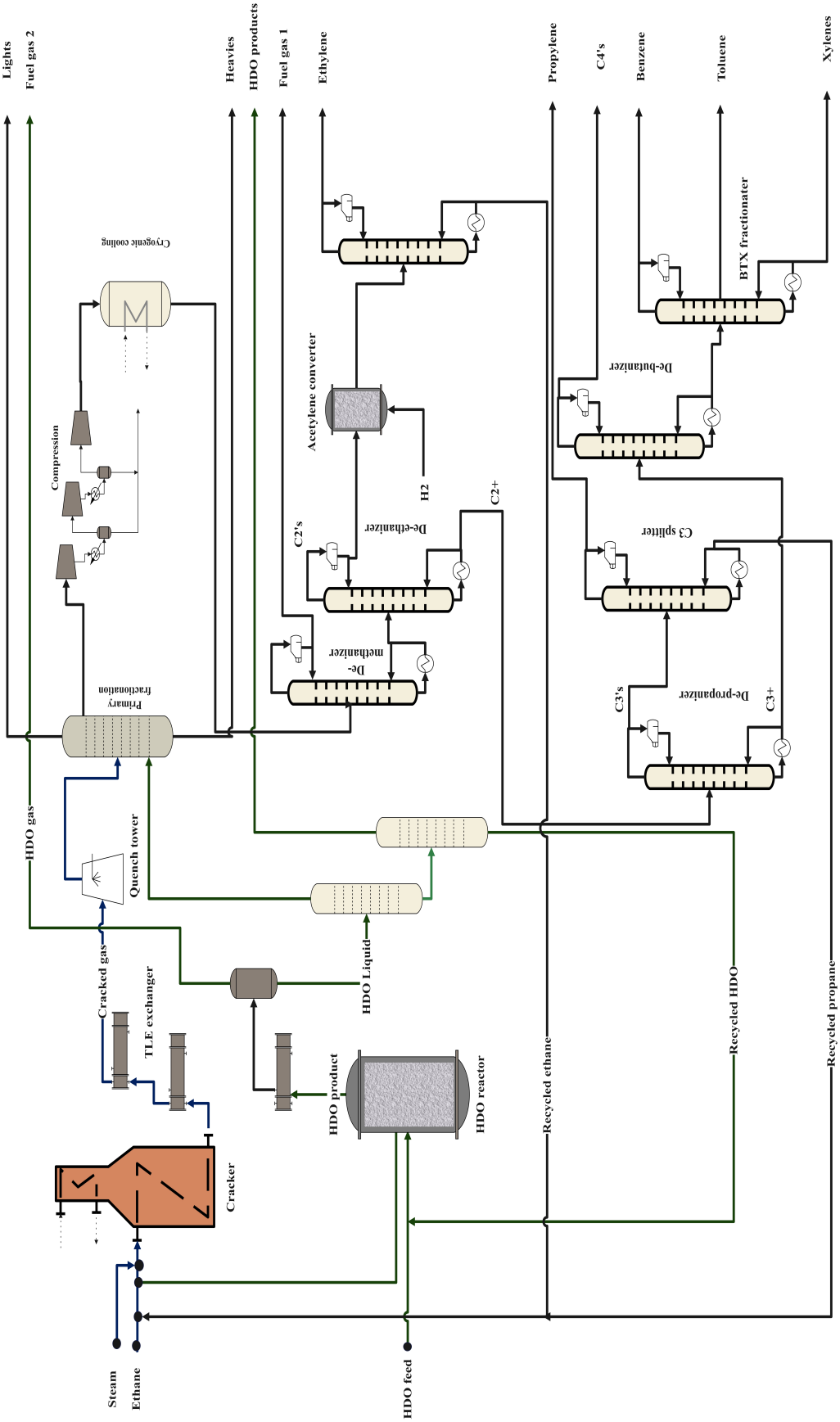


Figure 7.9: Simplified PFD of the integration of DeH-HDO with steam cracking.

In this work, ethane is selected as the feed to utilise experimental findings as well as avoid the complexity of naphtha feed composition, despite the advantage of generating BTX from naphtha cracking. A comprehensive flowsheet was developed to evaluate the energy changes per ton of ethylene and the overall economic viability of the integration in terms of the value of product streams. The techno-economic aspects of the steam cracking process have been extensively investigated in various studies. The developed flowsheet to investigate steam cracking and DeH-HDO has been designed to produce an ethylene capacity of 1,200 kta, which is a commercial ethane SC capacity. Thus, the flowsheet has a fresh ethane flow of 185 MMton·hr^{-1} for 8000 annual operational hours, as indicated in Table 7.7.

Table 7.7: Production rate based on DeH-HDO process using Aspen Plus flowsheet

Ethane cut to HDO		0	5%	10%	15%	20%
Fresh ethane	ton·hr^{-1}	185	185	185	185	185
Recycled ethane	ton·hr^{-1}	128.3	125.3	117.5	110.5	103.6
Produced ethylene	ton·hr^{-1}	151	140	133	124	116
Reduction in ethylene	%	0	7.2	12.0	18.0	22.9
Produced HDO liquid	ton·hr^{-1}	0	88.4	172	252	330

An investigated allocated fraction of ethane for DeH-HDO (ethane-cut) was employed to address the mass balance and energy balance impacts. The allocation of ethane into HDO led to slightly higher ethylene production; for example, an allocation of 5% led to 7.2% reduction in ethylene production. The additional reduction is attributed to process losses caused by the designed parameters used for the unit operation in the flowsheet. However, the reduction in HDO liquid yields contains valuable products such as phenol, cresol, and methanol, as discussed in the earlier section of this chapter. This allocation leads to 88.4 ton·hr^{-1} from processing 93.4 ton·hr^{-1} of bio-oil (guaiacol as a model compound). The standalone HDO discussed in the earlier section was designed for 99.1 ton·hr^{-1} for annual production of 250 kta of phenol, along with the other targeted products.

In principle, the increased allocation of ethane-cut for HDO improved HDO liquid leading to enhanced economic feasibility, as shown in Table 7.10. Yet, the increase in the ethane-cut is controlled by market needs and demand, therefore, based on the current global market size shown in Table 7.8, an ethane-cut of 5-10% is targeted. More than 20% ethane-cut yields a large reduction of valuable ethylene as a building block chemical for the chemical industry. Note that a 20% allocation contributes to the production of 614 kta of phenol, which is the maximum reported phenol production capacity in a single plant. Therefore, the ethane-cut controls the trade-off between HDO profitability and market demand.

Table 7.8: Global market capacity for DeH-HDO product streams as of 2022.

Chemical	Annual market capacity, Mt	ACGR[1] %	Ref.
Ethylene	224	>6	[208]
Propylene	150	6.2	[209]
Methanol	93.0	4.5	[210], [211]
Benzene	60.2	2.9	[212]
Toluene	31.2	3.1	[213]
Xylene	46.0	6.3	[214]
Phenol	12.1	2.7	[215]

[1] Annual Compounded Growth Rate (ACGR).

In addition to the significant mass gain from HDO liquid, the integration results in energy savings per tonne of ethylene produced, as outlined in Table 7.10. These energy savings stem from various sources, including the steam cracker, compression, recovery system, and fuel gases (methane and hydrogen) generated from both steam cracking (SC) and DeH-HDOydration (DeH-HDO) processes.

Table 7.9: DeH-HDO with ethane steam cracking integration flowsheet summary and economic evaluation at different ethane cut from steam cracking feed using the experimental results in Table 7.1.

Ethane cut		0	5%	10%	15%	20%
Cracking	$GJ{\cdot}ton^{-1}$	15.4	15.5	15.2	15.1	14.9
Compression	$GJ{\cdot}ton^{-1}$	1.46	1.54	1.56	1.61	1.65
Recovery	$GJ{\cdot}ton^{-1}$	1.51	1.52	1.55	1.57	1.58
Generated	$GJ{\cdot}ton^{-1}$	12.5	13.6	14.1	14.8	15.6

For the energy analysis, the energy requirement per tonne of ethylene in the steam cracker was derived from the reactor and feed heating, while the compression energy was obtained from the compressor duty. Within the recovery system, including all distillation columns, energy calculations were based on the difference between condensation and reboiling energy requirements, with the assumption of employing heat pumps for efficient energy conservation. The fuel gases produced were considered as input for combustion, although there is potential to sell valuable natural gas hydrogen as a commodity chemical for steam reforming and other upgrading processes to enhance the overall stream value. This approach would be particularly feasible in environments where significant electrification efforts in steam cracking have been accomplished.

The energy consumption study reveals that by raising the ethane cut, energy may be conserved in all sections of the integrated process due to a reduction in flow capacity. However, the calculated energy values based on the production of ethylene exhibit variations, as il-

lustrated in Table 7.10. The need for cracker feed decreases as the cut increases, as a result of the marginal increase in ethylene production from the complete integration of SC with HDO-DeH. This implies that by integrating the process, there will be a notable decrease in the amount of energy needed, since the synthesis of ethylene is enhanced in the HDO process. This is a hopeful benefit, considering that the energy required for steam cracking is influenced by the highly endothermic nature of the cracking reactions. The compression and recovery systems have exhibited an elevation in energy demand per metric tonne, resulting from the alteration in the composition of the gas stream through the combination of SC and DeH-HDO mixtures. As the amount of ethane is increased, there is a corresponding increase in methane and hydrogen, while the ratio of ethylene to ethane decreases. This leads to a more efficient separation process using a de-methanizer and C_2 splitter, with a reduced difference in energy consumption. However, while assessing the decrease in energy based on the production of ethylene, it was found that there was a greater demand compared to the base scenario. The fuel gas streams produced are combusted for energy purposes in the established flowsheet for analysis. The combustion streams serve as fuel for the cracker, functioning similarly to the existing traditional steam cracking furnaces. Theoretical calculations in the flowsheet, without accounting for heat losses, indicate that an ethane cut of 16% fulfils the energy requirements for the cracker and feed heating, as shown in Table 7.10.

Table 7.10: DeH-HDO with ethane steam cracking integration flowsheet summary and economic evaluation at different ethane cut from steam cracking feed using the experimental results in Table 7.1.

Ethane cut		0	5%	10%	15%	20%
Cracking	$GJ{\cdot}ton^{-1}$	15.4	15.5	15.2	15.1	14.9
Compression	$GJ{\cdot}ton^{-1}$	1.46	1.54	1.56	1.61	1.65
Recovery	$GJ{\cdot}ton^{-1}$	1.51	1.52	1.55	1.57	1.58
Generated	$GJ{\cdot}ton^{-1}$	12.5	13.6	14.1	14.8	15.6

By considering several aspects of energy analysis, such as incorporating the recycling stream heating and the quenching and fractionation of the cracker gas output, the expansion of the cracking boundary reveals a clear trend of energy reduction, as depicted in Figure 7.10. The base case, which simply includes steam cracking without DeH-HDO, yields an energy consumption of 6.1 $GJ{\cdot}ton^{-1}$ of ethylene. The model demonstrates that there is no further reduction in energy per metric tonne of ethylene beyond a threshold of 5%. Beyond this point, the combustion energy increases linearly due to the additional gases generated by HDO, as indicated by the solid green line in Figure 7.10. However, the intriguing supple-

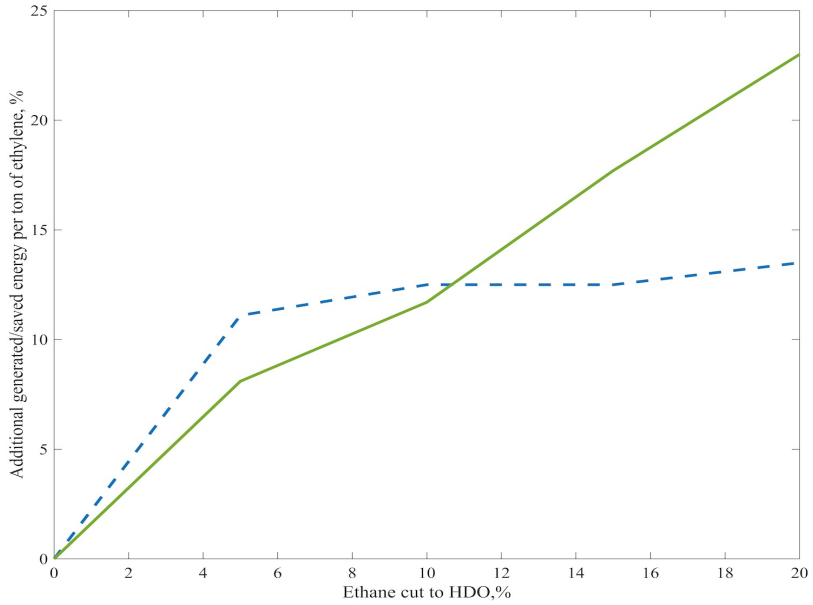


Figure 7.10: Saved energy from steam cracking (cracker) [dashed-line] and additional generated energy from combustion gases [solid-line]by ethane cut to HDO reactor(s).

mentary energy derived from the fuel gas stream has a detrimental impact on the overall production of ethylene, hence directly influencing the chemical industry downstream in the creation of important compounds. Within the specified boundary of this study, the economic worth of the streams enhances the overall value, even though the valuable ethylene is reduced due to the value of phenolic HDO products. The baseline was increased by approximately 50%, and at an applied reduction of 20% as shown in Table 7.11. Nevertheless, the improvement of the cut is influenced by the market demand for the targeted and downstream products, taking into account the material, energy, and economic gains.

Table 7.11: DeH-HDO economic evaluation at different ethane cut from steam cracking feed using the experimental results in Table 7.1.

Ethane cut		0	5%	10%	20%
HDO stream value	$MM	0	223	468	668
Overall value	$MM	852	992	1,182	1,247

The integration has demonstrated significant potential for managing a wide range of chemical streams from both biorefinery and traditional refinery sources, resulting in economic and energy benefits. The strategic deployment of integration also yields environmental benefits by reducing the mass required for steam cracking, resulting in a decrease in greenhouse gas emissions from furnace fire. According to reports, one metric tonne of ethylene produces an equivalent of 1-1.6 tonnes of CO_2 emissions, depending on the source of the feedstock [207]. Keller et al. conducted a study to determine the global warming potential associated

with the production of one tonne of olefins, primarily ethylene, from a shale gas ethane stream. The study found that this process results in the emission of 3.01 tonnes of CO_2 [216]. Excluding the emissions related to the extraction and refining processes, which are not included within the scope of this study, the estimated value is around 1.5 metric tonnes of CO_2.

The influence of climate change on ethylene yields results in a reduction of around 90 kta, leading to a 5% decrease in CO_2 emissions. Mynko et al. conducted a life cycle assessment on several advancements in steam cracking in order to mitigate the emissions linked to it [217]. The utilisation of biogas furnaces in all steam cracking processes has been determined to result in a 21% decrease in carbon footprint [217]. This reduction has been predicted to amount to 116 million metric tonnes per year. This highlights the significance of combining steam cracking with biorefinery. However, in the specific experimental situation being studied, this integration cannot be realised due to the insufficient energy provided to operate the furnace. With a 20% reduction, the biogas produced from HDO is measured at 1.46 GJ·ton^{-1}, representing 18.3% of the necessary fuel gas. However, by expanding the HDO boundary limit to encompass biomass (specifically lignin) pyrolysis, it is possible to meet the biogas cracker demand while maintaining the same operational capacity. This will be further explained in the following section. Thus, integrating HDO into the SC process enhances research and development endeavours to minimise emissions and supplement other technological advancements, such as cracker electrification, in order to attain carbon neutrality objectives.

7.4 DeH-HDO implementation in HDO-FCC process integration

7.4.1 The economic potential of replacing HDO by DeH-HDO in HDO-FCC integration

Wright et al. have proven the potential of biomass conversion into bio-based hydrocarbons in comparison to chemicals and bio-fuels in three different processing schemes. The represented chemicals for each scheme are gasoline and diesel for bio-fuel, asphlt binder, dextrose, calcium, and acetate for biomass-derived chemicals, and aromatics and olefins for bio-hydrocarbons [206]. The results indicate that the capital investment associated with biofuel is higher and produces the lowest revenue due to product prices. This evalua-

tion approves the advantages of transitioning biomass towards chemical production [206]. Developed Monte-Carlo analysis indicates that hydrocarbon scheme (Bio-oil-to-chemical) always have a positive NPV, despite the change in chemical prices [206].

To prove the merit of replacing hydrogen as HDO agent due to its cost, Wright et al. prove that after biomass cost, hydrogen has the highest operating cost (20% of the total OpEx) [206]. Hence, replacing hydrogen with an on-purpose DeH approach would further increase the profitability of the entire process. In Section 7.2, EP was determined based on experimental findings. These experiments revealed the possibility of negative economic potential in specific situations where ethane prices are high and hydrogen prices are low. This occurrence is rare because most chemicals today are closely tied to crude oil prices, and renewable hydrogen generation methods are currently more expensive than traditional steam reforming.

To extend our understanding beyond these experimental findings, we explored an integrated approach involving a biorefinery and refinery process to convert biomass into various chemicals as illustrated in Figure 7.11. This integration, developed by Vispute et al., transforms water-soluble bio-oil into alkanes, alkenes, aromatics, and bio-oil. Wright et al. expanded the scope of this process to begin directly with biomass and compared it with other schemes from an economic standpoint. This expanded process underscores the importance of separating high-value chemicals, specifically alkanes and alkenes, to unlock their full potential. These findings suggest the merits of using in-situ, on-purpose hydrogen generation via HDO for future implementations. By using alkanes in the feed to generate hydrogen for HDO and alkenes in the integrated HDO with FCC process, the attractiveness can be as alkene production increases, and separating alkanes from alkenes becomes essential in the baseline scenario. Figure 7.11 displays Wright et al. process and Vispute et al. integration as well as the in-situ hydrogen generation concept (DeH-HDO), which proved its potential from the experimental and economic perspectives.

7.4.1.1 Hydrogen availability

The EP of in-situ hydrogen generation DeH-HDO is fully explored by investigating the use of ethane under ideal operating conditions for hydroprocessing, followed by FCC operation for olefin and aromatic production. The primary challenge for alkane dehydrogenation lies in its ability to supply sufficient hydrogen under thermally harsh operating conditions. Despite

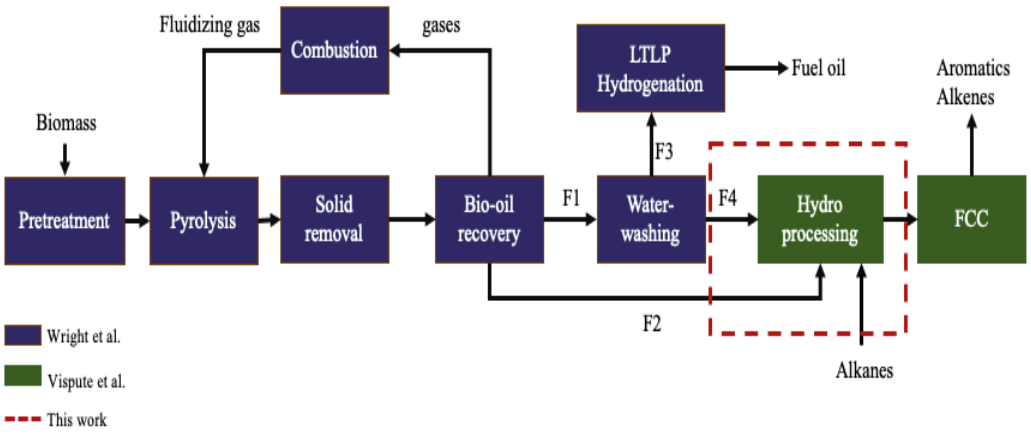
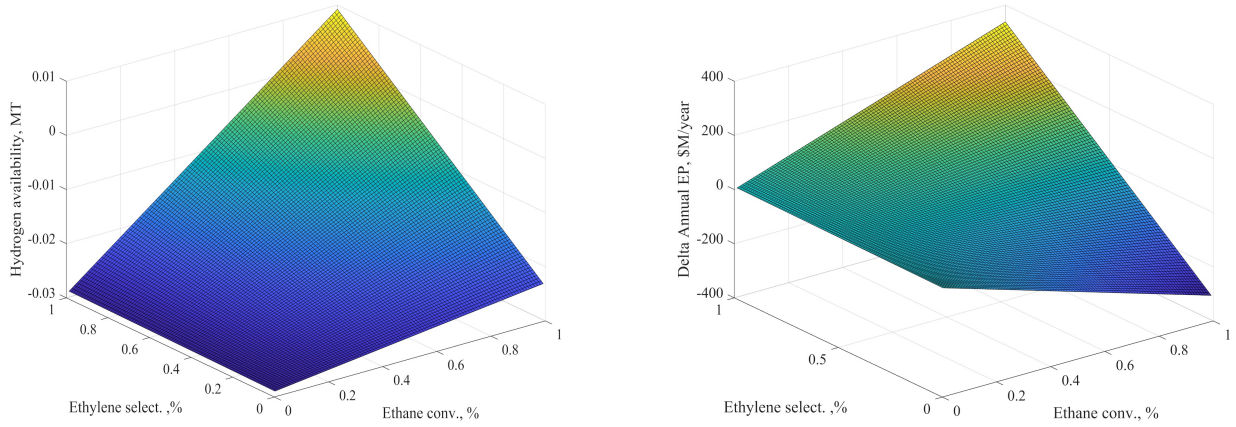


Figure 7.11: Block Flow Diagram (BFD) of biomass processing to chemicals implemented by Wright et al. including a hydroprocessing and FCC integration by Vispute et al. [206], [218].

the high operating temperature required for alkane DeH, it is a kinetically driven reaction for selectively producing ethylene and hydrogen. Therefore, it is important to establish a baseline for hydrogen requirements derived from alkane DeH for achieving full conversion to aromatic and alkene cases. This baseline is established based on ethane conversion, ethylene selectivity, and aromatic composition in bio-oil



(a) Hydrogen availability for HDO **(b)** EP difference

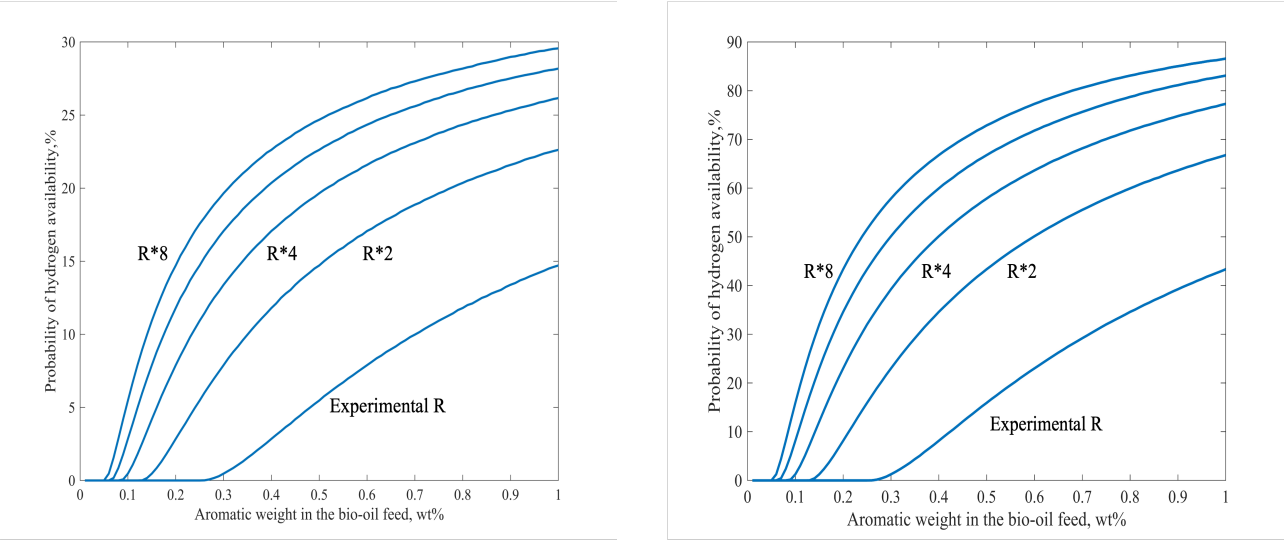
Figure 7.12: Investigating required alkane DeH conversion and selectivity to perform Vispute et al. HDO-FCC integration at range of ethane-to-aromatic ratio

Figure 7.12 demonstrates the conversion and selectivity of alkane DeH to produce sufficient hydrogen for HDO based on experimental flow conditions. At zero, HDO has just the needed hydrogen for HDO, where positive values mean additional hydrogen is generated, which also makes the EP higher for using additional hydrogen as an energy source or a by-product, depending on its production rate. However, negative values mean hydrogen deficiency, which leads to the accumulation of heavy hydrocarbons or coke formation, which negatively affects

EP. Therefore, Figure 7.12 shows a rare possibility for hydrogen sufficiency at the experimental condition unless near-complete conversion and selectivity can be achieved, which is not applicable for alkane dehydrogenation as well as state-of-the-art steam cracking. Therefore, adjustments to the operating conditions for the techno-economic assessment have to be made prior to further investigation. Regardless of hydrogen availability, the EP has a considerable probability of being negative. Therefore, in the next step, hydrogen generation will be adjusted by increasing ethane flow and, consequently, the ethane-to-bio-oil ratio.

Figure 7.13 maps different operating ethane-to-aromatic flow ratios (R) and aromatic ratios in bio-oil to draw a line for the hydrogen requirement for sufficient HDO. The probability of hydrogen availability in Figure 7.13 is defined by the probability of sufficient hydrogen at a range of ethane conversion and ethylene selectivity based on aromatic weight in bio-oil. The reactions involved in each alkane conversion approach are listed in Table 7.12. The low probabilities mean that alkane DeH has to have superior performance to be suitable for integration. Nevertheless, the analysis in 7.13a shows low probability as only it considers ethane cracking as a byproduct, whereas 7.13b includes another undesirable reaction, which is ethane to carbon and hydrogen. Although this approach results in a higher probability of hydrogen availability, it comes with a trade-off between carbon efficiency and valuable chemicals. Eventually, low carbon efficiency leads to low EP, especially in cases where ethane is an expensive commodity chemical. Increasing R increases the probability, which also gives shorter residence time for meeting a satisfactory conversion but also may limit undesirable methane cracking, which actually consumes hydrogen. Therefore, further in the flowsheet analysis and techno-economic assessment, R = 5 is used.

The required ethane flow per aromatic in the bio-oil is set based on the experiment conditions developed in this work since it has proven its potential to generate similar or better performance to conventional HDO, which is 5.8 in weight basis (ethane-to-aromatic). However, since this EP study processes a full bio-oil stream, the cases presented in Figure 7.13 based on the aromatic weight present for the total bio-oil weight. In the case of enriched aromatic bio-oil (80wt%), a stable ethane conversion of 20wt% requires at least a catalytic selectivity of 80wt% towards ethylene to have sufficient hydrogen. At full ethane conversion, still a selectivity of 67% has to be achieved. This observation indicates the significant role of the catalytic system in achieving certain performance for the in-situ hydrogen generation approach. The importance of improving selectivity becomes more profound in the



(a) Ethane dehydrogenation **(b)** Propane Dehydrogenation

Figure 7.13: Probability of hydrogen availability via alkane DeH performance at different aromatic content in bio-oil as well as ethane-to-aromatic ratio (R).

case of low-quality bio-oil in terms of aromatic quantity. In terms of 40wt% aromatic in bio-oil, ethane conversion of 20% and complete conversion require selectivity of 95% and 70%, respectively, to deliver sufficient hydrogen for HDO. Therefore, the DeH-HDO has to be improved from a catalytic perspective to achieve hydrogen yield and limit its declines due to coke formation.

7.4.2 Economic incentive of integrating DeH-HDO to FCC

The economic incentive of HDO as an alternative fuel and chemical production process remains challenging due to the technical limitations of biomass conversion. Although several studies report that HDO has produced promising outcomes in terms of aromatic and olefin production, the variation of feed composition remains a constrain for developing a robust process. Beside the bio-oil or biomass feedstock flexibility requirement, hydrogen economic and environmental costs remain an obstacle. A number of published works have considered the production of hydrogen within the process boundary limit as a potential to reduce the overall operation cost [219]–[221]. Therefore, previous section has drawn a baseline for alkane DeH performance to suitable alternative for process implementation, which is economically measured in this section.

Experimentally, ethane has proven its potential as a hydrogen replacement for HDO. Yet, the coupling is not improved to unlock the process potential of increasing BTX and alkenes, and the reaction coupling is in its early technological stages. However, moving forward, several parameters have to be re-adjusted to ensure better performance, as previously explained.

To reflect the progress in this work and the full potential of HDO presented in published works, a baseline was drawn in terms of the reaction performance of H-donor to boost BTX and alkene formation. First of all, the ethane-to-bio-oil feed ratio has to be adjusted based on the aromatic composition of bio-oil or its derivatives. For this evaluation, the aromatic content in bio-oil was set to 0.63 since guaiacol was selected as a model compound in this work. The selection of guaiacol as a bio-oil model compound in the simulation is good since it represents the poor and rich aromatic fractions in bio-oil. It is poor due to its high O/C based on the classification by Xiong et al. [222]. However, containing an aromatic structure makes it a rich fraction, as shown in the summary represented by Xiong et al. [222].

Feed-to-bio-oil requirements are subject to reaction performance in terms of conversion and selectivity. Therefore, a correction factor was introduced, which increased the increase from the investigated experimental condition. Alkane (ethane or propane) requires a higher correction factor to generate sufficient hydrogen; therefore, the flows were accordingly adjusted in the model. Ethane conversion was set at 30% for using a Pt-based zeloite catalyst investigated by Vispute et al. [218]. However, in the presence of hydrogen, ethane undergoes C-C cleavage, which consumes hydrogen to form undesirable methane. Therefore, undesirable methane and carbon formation were included with a total selectivity of 70% towards ethylene. The same methodology is used for propane dehydrogenation, except that operating at the same temperature as ethane would slightly increase the conversion based on equilibrium conversion.

Table 7.12: Alkane conversion reactions for the production of hydrogen, alkenes and aromatics, and parameters requirement to achieve sufficient hydrogen for DeH-HDO integration with FCC.

Feed	Pathway	Reactions	Feed/Bio-oil kg/kg	Corr. F
Ethane	Dehydrogenation Cracking	$C_2H_6 \leftrightarrow C_2H_4 + H_2$ $C_2H_6 \rightarrow CH_4 + H_2 + C$	1.45	5.0
Ethane	DeHA cracking	$3\,C_2H_6 \rightarrow C_6H_6 + 6\,H_2$ $C_2H_6 + H_2 \rightarrow 2\,CH_4$ $8\,C_2H_6 \rightarrow C_{16}H_{10} + 19\,H_2$	0.58	2.0
Propane	Dehydrogenation Cracking	$C_3H_8 \leftrightarrow C_3H_6 + H_2$ $C_3H_8 \rightarrow CH_4 + C_2H_4$ $C_3H_8 \rightarrow 4\,H_2 + 3\,C$	1.45	5.0

Since the integrated HDO-FCC used Pt and Ru-based catalysts, the ethane DeHA mechanism has to be employed as it forms BTX. The DeHA mechanism occurs within the micro-

pore structure of zeolite [140]. It was also considered since it produces valuable BTX and hydrogen, which suit the product streams generated from HDO. Since, on a molar basis, ethane produces more hydrogen via DeHA, the correction factor for sufficient hydrogen was calculated to be 1.6. Therefore, in the model, a correction factor of 2.0 was used. In principle, from a catalytic perspective, the low residence time favours alkene formation, whereas a higher residence time allows for alkene aromatization in the micropore structure [140]. Consequently, that leads to higher ethane conversion. In the case of excessive aromatization, coke formation was identified as pyrene. Therefore, Table 7.13 shows different gas feed-to-bio-oil ratios for the different mechanisms, which resulted in different overall BTX and alkene production, as shown in Table 7.12.

Due to the utilisation of Pt and Ru based catalysts in the combined HDO-FCC process, the ethane DeHA mechanism must be applied, as it results in the formation of BTX. The DeHA mechanism takes place within the micropore structure of zeolite [140]. It was also deemed suitable because of its production of valuable BTX and hydrogen, which are compatible with the product streams generated from HDO. Based on a molar basis, ethane generates a greater amount of hydrogen through DeHA. Consequently, the correction factor required to ensure an adequate supply of hydrogen was determined to be 1.6. Thus, a correction factor of 2.0 was employed in the model. From a catalytic standpoint, a shorter residence time promotes the production of alkenes, whereas a longer residence time facilitates the conversion of alkenes into aromatic compounds within the micropore structure [140]. As a result, this results in an increased ethane conversion rate. When there is an excessive process of converting substances into aromatic compounds, the production of coke is determined to be pyrene. Table 7.13 displays varying feed-to-bio-oil ratios for different processes, leading to distinct overall BTX and alkene production as presented in Table 7.12.

The energy requirement is a significant parameter in comparing different processes. These processes are compared in terms of energy requirements per ton of produced products, as illustrated in Table 7.13. Since the processed biomass has the same volume in the three investigated cases, the energy is primarily based on the conversion of the inlet gas feedstock, which consists of ethane and propane, as well as the energy needed for feedstock heating. Despite the approximately 2.5-fold reduction in ethane processing in the DeHA case compared to the DeH case, it is more endothermic. This indicates that DeHA likely requires less energy, and the energy of the reaction is mostly recovered by other streams.

Additionally, the proportionality of fuel gas formed in the case of DeHA helps to offset the energy requirement.

Table 7.13: Aspen Plus process results for the integration of DeH-HDO with FCC of processing 3,300 tpd

Parameter		Ethane DeH	Ethane DeHA	Propane DeH
Production	kta	436	298	576
Alkene/Aromatics	$kg{\cdot}kg^{-1}$	6.15	1.06	8.44
Energy requirement	$GJ{\cdot}ton^{-1}$	9.89	2.54	6.67
Economic potential[a]	$/year	1.02	1.07	1.37

[a] Calculated based on the difference of feedstock and product values

However, since the production from DeHA results in aromatics, unreacted ethane, and hydrogen, it involves a straightforward separation process that does not require extensive equipment, unlike the ethylene and propylene recovery, which necessitates complex C_2 and C_3 splitters. Furthermore, in the DeHA process, most of the outlet stream bypasses the compression unit, which is used for gas separation. Therefore, as discussed in the previous section, the integration of DeH-HDO with steam cracking becomes essential since alkane/alkene separation is a critical step in the process. This integration addresses the challenges faced by standalone DeH-HDO, especially in cases of low DeH performance where the separation process is not economically justified. Table 7.13 EP suggests that the DeHA route has the highest potential per metric tone; however, its revenue heavily depends on benzene. The cases have better economics derived from the higher production rate of alkenes, as shown in Figure 7.11. Nevertheless, the cases employed showed that the integration of petroleum-based streams with biorefinery streams rich in hydrocarbons can utilise existing infrastructure while maintaining economic feasibility. Improving the catalytic to yield 21% of ethylene or benzene is a benchmark for the ethane valorization experimental phase to move this integration into the next technological readiness level. In the case of propane, a minimum yield is the benchmark.

$$C_2H_6(g) \rightarrow C_2H_6(g) + H_2(g), \Delta H = 137\,kJ{\cdot}mol^{-1} \quad \text{(R11)}$$

$$3\,C_2H_6(g) \rightarrow C_6H_6(l) + 6\,H_2(g), \Delta H = 337\,kJ{\cdot}mol^{-1} \quad \text{(R12)}$$

Another important factor in processing 3,300 tpd of biomass for chemical and fuel purposes

is the reduction of the overall carbon footprint per metric tonne of product. In the case of propane dehydrogenation as H-donor, the product stream is 32% bio-based, where ethane DeH and DeHA are 42% and 62%, respectively. Yet, a detailed investigation is required to realise the non-monetary incentive associated with the integration.

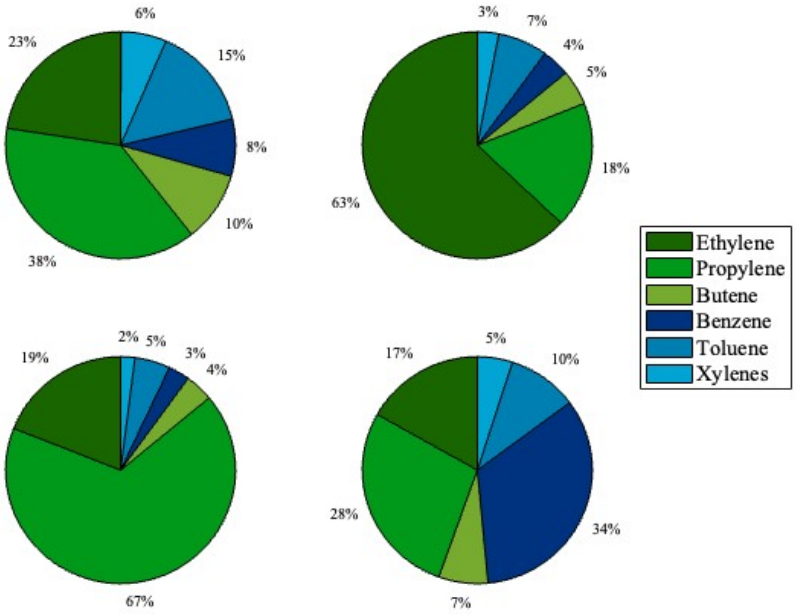


Figure 7.14: Product distribution from the integration of in-situ hydrogenation via H-donor reactions and FCC from Aspen flowsheet using the parameters in Table 7.12. [Top-left] base case, [Top-right] with improved ethane DeH, [Bottom-left] improved propane DeH, [Bottom-right] improved ethane DeHA

7.5 Conclusion: HDO Industrial scalability and process integration

The primary objective of this chapter was to assess the economic feasibility of up-scaling the experimental results to a commercial scale. Initially, the coupled reactions involving HDO and DeH demonstrated a favourable economic outlook, with positive NPV outcomes observed in over 88% of Monte Carlo simulations for a planned plant with a phenol production capacity of 200 kta. However, it is noteworthy that the product stream was not improved to attain the targeted levels of alkenes and BTX. Subsequently, various scenarios were investigated to explore the potential for enhancing the catalytic performance of alkane DeH. These improvement scenarios were formulated based on experimental data that evaluated DeH with no HDO feed (Cases A and B) to remove the effects of HDO heavy condensate on the catalytic bed. Furthermore, Case C was an investigation under the assumption of initial reaction performance without any degradation caused by coke formation. The Monte

Carlo analysis indicated that a catalytic system yielding a 20% ethylene yield could serve as a benchmark, demonstrating a nearly positive NPV across different price variations in the chemical market.

Next, this chapter studied the commercial implementation of DeH-HDO and its integration with steam cracking, where a large stream of ethane exists and can be split with DeH-HDO. Steam cracking was selected because it is a common feed and it contains an alkane/alkene recovery system, which might hinder the implementation of DeH-HDO standalone due to the expensive energy requirements for the separation. The integration generated an increase in economic incentive that reaches a 50% increase in product stream value for 20% ethane split to DeH-HDO. Overall, energy savings per metric tonne of ethylene are caused by the additional ethylene from HDO as well as additional bio-fuel that can be used for cracking instead of petroleum-based fuel gas. Environmentally, steam cracking is associated with high emissions, which can be offset by processing 3,300 tpd of biomass for 7% ethane cut in a negative or low emission rating processing to bio-oil.

Furthermore, a second step in the improvement process involved enhancing the performance of HDO within the coupled reactions. This improvement was guided by previously published experimental data and was complemented by a separate study that encompassed the entire process, from biomass conversion to the production of aromatics and alkanes. Traditional HDO was enhanced using a two-step zeolite/H_2 processing method for bio-oil. In this study, hydrogen generated from alkane dehydrogenation was considered, assuming comparable HDO performance to molecular hydrogen. This assumption was experimentally validated in earlier chapters using various catalytic beds, including zeolite-based ones. The primary objective of this chapter was to determine the necessary DeH performance to generate the required hydrogen through various reaction feeds and mechanisms.

The developed Aspen flowsheet took into account the utilisation of a recovery system generated from steam cracking to process 1,400 kta of ethane, or LPG. Another approach considered DeHA as the hydrogen source, given that the catalyst used was zeolite-based. The resulting alkane/aromatic ratios exceeded current and anticipated market capacities by more than twofold. On the other hand, ethane DeHA approaches led to a threefold reduction from a market capacity ratio of 3.34 to 1.06. Therefore, initially, the catalytic development route was needed to investigate the ideal path for further development.

The environmental aspect of moving towards carbon neutrality held great importance and served as a decision factor in future catalytic advancements. This was due to the variation in biomass to petroleum-based chemical production across the three different cases. Ethane DeHA, for instance, resulted in greater biochemical production due to its reduced reliance on petroleum-based feedstock.

To summarise, the incorporation of biorefineries into the chemical sector offers significant promise, resulting in a rising number of studies focusing on technoeconomics and life cycle assessments, especially when compared to crude refineries. While the implementation of a coupled reaction approach is still in its initial phases, it holds the potential to improve performance and play a crucial role in advancing the industry's journey towards carbon neutrality.

Table 7.14: Summary of current advantages and disadvantages for the process integration, as well as future potential and technical challenges.

	DeH-HDO	DeH-HDO+SC	DeH-HDO+FCC
Current advantages	• Positive economic potential in comparison to the use of molecular hydrogen. • The production of alkenes (ethylene) beside biogas the increase the profitability of gas stream	• Reduction on energy requirement per ton of produced ethylene. • Formation of biogas that be in steam cracker to lower CO_2 production per ethylene.	• Additional production of bio-ethylene from sustainable carbon source. • Maximising BTX formation with FCC catalysts
Disadvantages	• Large recycle stream due to ethane low DeH conversion. • Limited BTX formation at this stage based on this work.	• Limited BTX formation at this stage based on this work.	
Potential	• Proven to have similar or better hydrodeoxygenation products than expensive molecular hydrogen • Reducing carbon footprint	• HDO generated biogas can be used in SC furnaces • Increasing BTX with better catalyst and reactor configuration	• Produces relatively bio-aromatics that can be utilised in other processes not constrained to phenol market Challenges • Reduces SC CO_2 consumption per ton of ethylene.
Technical challenges	• Catalyst yields high ethane conversion to reduce recycle stream. • Catalyst eliminate high coke formation, and sustain conversion and selectivity.	• Study process integration with existing SC plants • HDO feed variability may effect the outlet steam which might disturb the integration.	• It has to be experimentally validated for using ethane as hydrogen donor instead of molecular hydrogen • the use of zeolite catalyst might increase cracking activity on ethane

Chapter 8

Conclusions

This thesis investigated the possibility of substituting molecular hydrogen with on-purpose ethane DeH for bio-oil HDO. The aim is to improve the feasibility of bio-oil HDO by reducing the demand for costly hydrogen. This approach is encouraged by the high demand for hydrogen as an energy source and feedstock across various applications. Furthermore, the coupling of HDO and DeH could establish an integration between conventional refineries, downstream petrochemical processing, and bio-refineries to reduce the carbon footprint per tonne of produced chemicals. Despite operating under disparate thermodynamic conditions, the catalytic coupling of these reactions offers the potential for a synergistic effect, improving overall performance by producing valuable building block chemicals: alkenes and aromatics.

This thesis is founded on three hypotheses explored across four chapters. First, the continuous removal of hydrogen from DeH via HDO was hypothesised to enhance DeH conversion by driving the reaction towards ethylene production. This observation was proven in catalytic systems and operating conditions with relatively high ethane DeH conversion to ethylene, which increased with the introduction of guaiacol, such as using synthesised Cr-based catalysts on zeolite and alumina support. These catalytic systems facilitated ethane DeH, generating reactive hydrogen that mitigated catalyst surface condensation, thereby preventing ethane from reaching active sites. Consequently, catalytic systems that did not promote ethane DeH in the absence of guaiacol exhibited rapid condensate formation when introducing guaiacol due to the absence of reactive hydrogen. This leads to a diminished observation of high ethylene formation with guaiacol. This observation was also observed with running alkane DeH catalysts, PNiMo, operating at low ethane pressure. Therefore, a selective catalyst for alkane DeH is essential for the DeH-HDO.

The second hypothesis proposed that adsorbed hydrogen produced by DeH (in-situ) on the

catalytic surface would exhibit greater reactivity than molecular hydrogen (ex-situ). Experimental findings substantiated the superiority of the "in-situ" approach over the "ex-situ", despite its lower hydrogen per guaiacol molar ratio. This superiority was observed through a higher degree of HDO with ethane compared to molecular hydrogen across all catalytic systems, except for the single catalyst system utilising Cr_2O_3/Al_2O_3. This discrepancy can be attributed to the lack of HDO active sites as well as the limited alkane DeH caused by high Cr loading. Furthermore, the increase in ethylene formation in the presence of guaiacol provides additional evidence of reactive hydrogen at the active surface, thus supporting the findings of the first hypothesis.

Using HDO to fully convert bio-oil (guaiacol) to BTX, which can be done by operating in a series of reactors to resemble a CSTR operation mode, requires a long residence time. This approach was confirmed where guaiacol (double oxygenated per aromatic) could easily generate a single oxygenated aromatic. However, further HDO of single oxygenated aromatics (ex. phenol) into BTX has shown a low conversion of 14%, indicating that a complete conversion of guaiacol is possible, but at an extended reaction zone. The dual catalyst (HDO and DeH catalysts in a single bed) experiments demonstrated higher conversion of guaiacol near completion, significantly reducing time for both ex-situ and in-situ and indicating that molecular hydrogen activation also requires active sites. Therefore, operating at atmospheric pressure, more molar molecular hydrogen does not increase HDO unless more active sites are available. This observation increases H-donors' potential to replace hydrogen since active sites are the main constraint in both mechanisms.

The techno-economics chapter explores different scenarios of implementing DeH-HDO: as a standalone technology with the current status generated in this work or as an integrated technology with a steam cracking process. Furthermore, as found in the literature, this integration with steam cracking improved HDO performance. These approaches indicate that thermal, material, and synthetic effects play a significant role in achieving an overall optimised economy from a process perspective. The reduction in energy requirement for the coupled DeH-HDO per tonne of hydrocarbon stream proves the third hypothesis. However, the sensitive analysis indicates reactive hydrogen availability in-situ is crucial to ensuring optimised HDO.

A primary challenge of this reaction coupling is the rapid formation of coke due to phenolic

condensation, which hinders feedstock access to active sites. Overcoming this limitation is critical for commercial implementation, necessitating various strategies, from catalytic system design to alternative reactor configurations such as membrane reactors. Mitigating rapid phenolic compound condensation is critical not only for the DeH-HDO coupling but also for individual HDO and DeH conversions for each process to be economically viable. In conclusion, while the DeH-HDO-coupled reactions show significant promise, further extensive research and collaborations are imperative to address existing challenges and fully realise their potential.

Chapter 9

Future Prospects

HDO of bio-oil coupled with alkane DeH (DeH-HDO) has validated its potential compared to conventional HDO using expensive molecular hydrogen at elevated pressures. However, the coupled DeH-HDO must be improved to increase its technological attractiveness and facilitate its commercialisation as a standalone technology or integrated into existing chemical facilities. From a technological standpoint, HDO via ethane DeH necessitates a long, stable processing time with sufficient product yield to fix downstream processing (separation or additional conversion steps).

Despite the concept economic attractiveness, rapid deactivation hinders its commercial viability as frequent catalyst activation steps are required. Therefore, the rapid decline in ethylene conversion necessitates further investigation to understand the underlying causes and develop approaches to eliminate or slow the rate of decline. Addressing this issue is critical for improving the HDO process, as ethylene conversion via DeH generates the hydrogen required for effective deoxygenation. An approach to address this issue involves scaling down the experimental setup and conducting shorter runs with more frequent sampling, enabling a more detailed and systematic analysis of the conversion decline. Furthermore, DeH-HDO necessitates expanding the investigation of this concept in terms of operating conditions, material selection (catalytic system), reactor design, and process integration.

9.1 Processing parameters

Operating parameters can be investigated in terms of which reaction is aided by the other by adjusting the feed flow rates. While the primary objective of this thesis was to evaluate how alkane DeH can improve HDO, it is essential to recognise the potential of the reverse mechanism. As demonstrated in this study, ethane DeH can be improved by introducing relatively small injections of guaiacol as an oxidant. Small injections of guaiacol may help mitigate the drawbacks associated with conventional oxidative dehydrogenation of ethane using oxygen

or air, which often leads to reduced carbon efficiency due to the undesirable formation of carbon oxides. Moreover, these guaiacol injections can be further improved to replace CO_2-assisted alkane DeH, where CO_2 serves as a sustainable oxidant. The advantage of utilising bio-oil, particularly guaiacol, instead of CO_2 lies in its lower oxygen-to-carbon ratio, which contributes to increasing the value of the outlet stream by producing valuable BTX. Hence, adjusting the ethane-to-guaiacol flow ratio presents a promising avenue for enhancing the potential of the DeH-HDO coupling.

Relevant to this work, to improve DeH-HDO for assisting HDO by DeH, additional research could be conducted for assisted alkane DeH via HDO. In theory, achieving a flexible technology dependent on the market supply and demand for aromatics and alkenes will substantially enhance the desirability of DeH-HDO. In addition, ethane was used as the alkane agent in this study; however, it would be advantageous to expand this research to include other alkanes that could benefit from a reduction in operating temperature while achieving a considerable conversion. For instance, higher alkanes such as propane and butane can be candidates for lowering the operating temperature because their equilibrium conversion is greater than that of ethane at a particular pressure and temperature. An example proofing the potential of this approach is demonstrated by Gorte et al. in dehydrogenating hexane while HDO cresol, which led to exceeding dehydrogenation equilibrium conversion [21]. Furthermore, an advanced approach to consider would be the use of a mix of LPG or another bio-alkane mixture, which can be considered an effective hydrogen donor for HDO while producing high-value chemicals. This approach can add another perspective to integrating biorefineries with conventional ones since low-value streams can be processed without costly separation processes.

Additionally, H-transfer from saturated cyclic hydrocarbons, such as cyclohexane, to oxygenated aromatics boosts non-oxygenated aromatics. This DeH-HDO generated by cyclohexane dehydrogenation can be desirable because both reactions favour a similar temperature regime. This reaction coupling can link hydroprocessing petroleum refining and biomass refining. Hydrogen is used for hydrocracking heavy oil streams where aromatic saturation occurs at elevated pressures. Hydrocracking can be further processed for in-situ hydrogen generation through the DeH of cyclic hydrocarbons. Furthermore, this DeH-HDO integration can be targeted and investigated for green bio-based chemicals by considering alkanes and saturated cyclic hydrocarbons that can be generated from sustainable sources, such

as biomass pyrolysis or recycled waste plastics produced by hydrocracking waste plastics.

9.2 Catalytic system

From a catalytic perspective, both computational and experimental investigations are necessary to identify the optimal catalytic system, with the goal of minimising carbon formation and reducing the frequency of catalytic bed regeneration. Among the potential candidates, noble metal-based catalysts, especially Pt-based systems, stand out due to their distinct active sites and demonstrated superiority over Mo- and Cr-based catalysts. Pt catalysts, in particular, have been extensively studied and recognised for their effectiveness in both HDO and ethane DeH reactions. The presence of Pt active sites is crucial for the dissociation of oxygenated functional groups from aromatics during HDO, and Pt has shown exceptional capability in prolonging HDO lifetime while enhancing selectivity toward light aromatics derived from pine pyrolysis vapour [88].

Moreover, Pt-based catalysts have emerged as leading candidates for ethane DeH, comparable to Cr-based systems [223]. Utilising a Pt catalyst supported on zeolite holds promise for achieving synergistic effects at single active sites, thus avoiding challenges associated with dual active sites that may hinder hydrogen transfer. The selection of zeolite is attributable to the interesting observations observed at the end of this thesis.

9.3 Reactor configuration

This work demonstrated the potential of this coupling in a packed-bed reactor, which is hindered by the rapid coke formation that results from operating HDO at relatively higher temperatures (600 °C) than conventional HDO, which operates at temperatures of approximately 350 °C. Since both reactions occur on the same catalytic bed, both reactions will be affected by accumulated coke formation, or the exponential growth of coke formation caused by the lack of sufficient reactive hydrogen from alkane DeH. Therefore, another reactor type or configuration might play a role in enhancing product selectivity. Several literature findings have reported improved BTX yield in a pack-bed reactor at different operating conditions with higher molar H_2 to aromatic ring in the feed. Applying these conditions requires a specific injection procedure or reactor design for bio-oil feed to on-purpose alkane DeH. Another approach is to consider multiple packed-bed reactors in series.

Alternative to the packed-bed reactor, a membrane reactor might play an optimal advantage

since the integration of DeH-HDO potential is controlled by mass transfer (H-transfer) and heat transfer, as shown in Figure 9.1. A membrane shell-and-tube reactor can maximise the benefits of both reactions by minimising adverse effects. In principle, alkane DeH takes place on the shell side, which must directly contact the heat source to attain the required endothermicity. The tube side of the reactor is designed for HDO, where hydrogen diffuses from the reactive membrane on the shell side to the tube side. Additionally, heat transfers from the shell to the tube side. Since HDO operates at a lower temperature, a radial temperature decrease from the shell to the tube can be tolerated and even encouraged by HDO exothermicity. Therefore, integrating both reactions into a single membrane shell and tube reactor reveals significant potential.

In literature, on-purpose alkane DeH of C_2-C_4 has been considered in membrane reactors to achieve continuous hydrogen removal, resulting in increased dehydrogenation conversion [19], [20], [224]–[228]. This approach can be further advanced by the separation and continuous hydrogen consumption via HDO reactions. This is consistent with Hughes et al.'s mathematical model, which concluded that the addition of a reactive reaction for hydrogen facilitates its removal [224]. In a study, Caro et al. investigated coupling ethane DeH in a membrane reactor by oxidant transfer [20]. To maximise the benefits of operating each reaction separately, several aspects of this concept must be extensively investigated, including the possibility of using a membrane-packed-bed reactor in which additional catalytic packing is added to increase the reactivity. Each section, shell and tube can have its catalytic bed, eliminating the need for a bi-functional catalytic bed. However, H-transfer via membrane catalytic behaviour remains a fundamental principle for improving reactivity in comparison to molecular hydrogen. Furthermore, in the literature, membrane reactors were considered for dehydrogenation of potentially generated chemicals from renewable biomass streams such as cyclohexane and ethanol [229]–[231]. These findings enable DeH-HDO in a membrane reactor to have significant potential for relatively smaller-scale biorefineries.

9.4 Process integration

The practical application of DeH-HDO needs a thorough examination, both in terms of its compatibility with other processes and its viability as a standalone technology. Additionally, the economic aspects of implementing this approach in existing facilities (brownfields) or entirely new ones (greenfields) should be carefully assessed, as they could either be constrained or enhanced by these factors. Consequently, extensive research is required to ex-

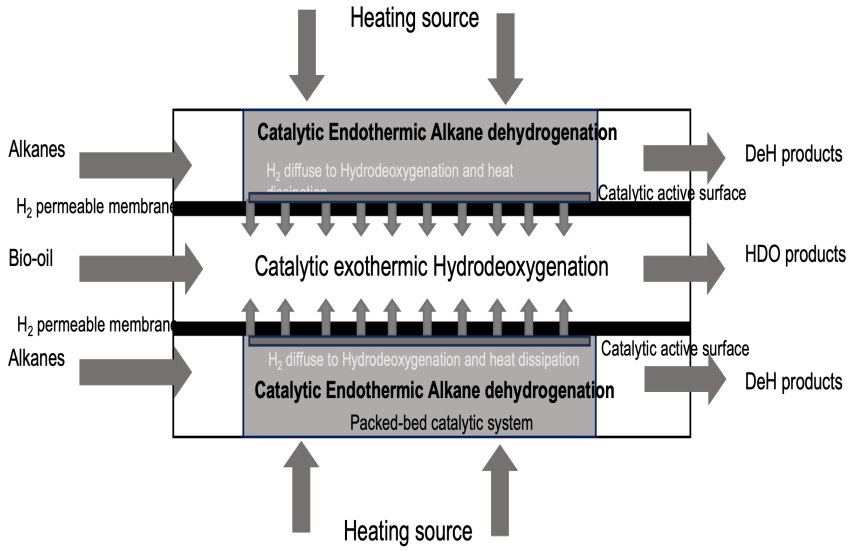


Figure 9.1: Conceptual membrane reactor for DeH-HDO

plore how DeH-HDO can be integrated into conventional refineries or petrochemical plants. One significant challenge to integrating DeH-HDO is the need to import certain chemicals, especially in regions with abundant biomass resources but limited petroleum reserves. To make DeH-HDO more appealing, it is worth investigating its potential within independent bio-refineries. This approach would facilitate a complete shift from petroleum-based chemicals to biochemicals within a single facility.

Rather than focusing solely on incorporating HDO into petroleum-based feedstocks like LPG or processes such as steam cracking and reforming, attention should also be given to converting first- and second-generation alcohols, such as ethanol and methanol. This can result in hydrogen production for HDO. Dehydration of ethanol can be an adequate replacement for ethane DeH to produce high-value ethylene, as shown in Reaction 13; however, the required hydrogen is lacking. Ethanol steam reforming is promising since it produces six molars of hydrogen with one mole of bioethanol, as appears in Reaction 14.

$$C_2H_5OH \rightarrow C_2H_4 + H_2O \tag{R13}$$

$$C_2H_5OH + 3\,H_2O \rightarrow {}_2CO_2 + 6\,H_2 \tag{R14}$$

Therefore, a membrane reactor for bio-oil HDO via in-situ hydrogen generation from ethanol

reforming for bio-aromatics is an exciting topic. Ultimately, the inclusion of bio-ethanol in bio-ethylene could improve the economics of the entire process to generate bio-based building block chemicals for the industry, as illustrated in Figure 9.2. This integration offers numerous advantages and can elevate and accelerate the technology readiness level. In conclusion, the scientific community has several dimensions to explore for developing a more sustainable chemical industry in terms of fulfilling population needs while eliminating environmental risks.

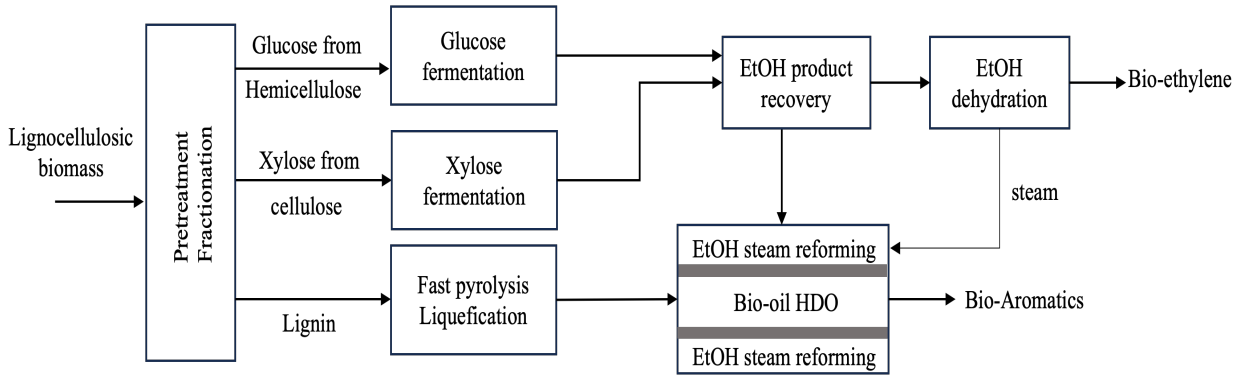


Figure 9.2: BFD of lignocellulosic biomass (non-food biomass) maximum utilisation for bio-based building block chemical production for the chemical industry. This route include the integration of Ethanol reforming and bio-oil HDO in a membrane reactor technology. Cellulose and hemicellulose routes extracted from [29].

Bibliography

[1] Zhiguo Hou and Daniel F. Brady, "Market insights on the crude-to-chemicals trend: Refining the product slate," ExxonMobil Chemical Company and Tree Line Consulting, Inc., Tech. Rep., 2018.

[2] The catalyst group resources, "Oil-to-chemicals: Technological approaches and advanced process configurations," TCGR, Tech. Rep., 2017.

[3] Intenrational Energy Agency, "The future of petrochemicals," Paris, Tech. Rep., 2018.

[4] R. J. Chang, "Crude oil to chemicals: Industry development and strategic implications," in *Industrial Arene Chemistry*, Wiley, Jun. 2017, pp. 43–69, ISBN: 9783527827992. DOI: 10.1002/9783527827992.ch3.

[5] International Energy Agency, "Renewables 2022," IEA, Tech. Rep., 2022.

[6] T. Gül, L. Cozzi, and P. Havlik, "What does net-zero emissions by 2050 mean for bioenergy and land use?" IEA, Paris, Tech. Rep., 2021.

[7] A. Kumar, M. Jindal, S. Maharana, and B. Thallada, "Lignin biorefinery: New horizons in catalytic hydrodeoxygenation for the production of chemicals," *Energy & Fuels*, vol. 35, no. 21, pp. 16 965–16 994, Nov. 2021, ISSN: 0887-0624. DOI: 10.1021/acs.energyfuels.1c01651.

[8] W. Deng, Y. Feng, J. Fu, *et al.*, "Catalytic conversion of lignocellulosic biomass into chemicals and fuels," *Green Energy & Environment*, vol. 8, no. 1, pp. 10–114, Feb. 2023, ISSN: 24680257. DOI: 10.1016/j.gee.2022.07.003.

[9] P. Lahijani, M. Mohammadi, A. R. Mohamed, F. Ismail, K. T. Lee, and G. Amini, "Upgrading biomass-derived pyrolysis bio-oil to bio-jet fuel through catalytic cracking and hydrodeoxygenation: A review of recent progress," *Energy Conversion and Management*, vol. 268, p. 115 956, Sep. 2022, ISSN: 01968904. DOI: 10.1016/j.enconman.2022.115956.

[10] K. Mano, "Industry Outlook : Creative Disruptions (Part 2)," KPMG, Tech. Rep., 2019.

[11] European Bioplastics e.V., "Global Production capacities of bioplastics 2023-2028," EUBP, Berlin, Tech. Rep., 2023.

[12] H. Shafaghat, I. G. Lee, J. Jae, S. C. Jung, and Y. K. Park, "Pd/C catalyzed transfer hydrogenation of pyrolysis oil using 2-propanol as hydrogen source," *Chemical Engineering Journal*, vol. 377, p. 119 986, Dec. 2019, ISSN: 13858947. DOI: 10.1016/j.cej.2018.09.147.

[13] Y. Xiang, X. Li, C. Lu, L. Ma, J. Yuan, and F. Feng, "Reaction performance of hydrogen from aqueous-phase reforming of methanol or ethanol in hydrogenation of phenol," *Ind. Eng. Chem. Res*, vol. 50, p. 28, 2011. DOI: 10.1021/ie101411h.

[14] J. Remón, J. Arauzo, L. García, *et al.*, "Bio-oil upgrading in supercritical water using Ni-Co catalysts supported on carbon nanofibres," *Fuel Processing Technology*, vol. 154, pp. 178–187, Dec. 2016, ISSN: 03783820. DOI: 10.1016/j.fuproc.2016.08.030.

[15] R. O. Canıaz and C. Erkey, "Process intensification for heavy oil upgrading using supercritical water," *Chemical Engineering Research and Design*, vol. 92, no. 10, pp. 1845–1863, Oct. 2014, ISSN: 02638762. DOI: 10.1016/j.cherd.2014.06.007.

[16] T. Yan, J. Xu, L. Wang, Y. Liu, C. Yang, and T. Fang, "A review of upgrading heavy oils with supercritical fluids," *RSC Advances*, vol. 5, no. 92, pp. 75 129–75 140, Aug. 2015, ISSN: 2046-2069. DOI: 10.1039/C5RA08299D.

[17] J. M. Thomas and W. J. Thomas, *Principles and practice of heterogeneous catalysis*. 2015, p. 767, ISBN: 978-3-527-31458-4.

[18] R. J. Clews, "Front matter," in *Project Finance for the International Petroleum Industry*, Elsevier, Jan. 2016, p. iii. DOI: 10.1016/B978-0-12-800158-5.00024-4.

[19] S. Dangwal, R. Liu, and S.-J. Kim, "High-temperature ethane dehydrogenation in microporous zeolite membrane reactor: Effect of operating conditions," *Chemical Engineering Journal*, vol. 328, pp. 862–872, Nov. 2017, ISSN: 13858947. DOI: 10.1016/j.cej.2017.07.108.

[20] H. Jiang, Z. Cao, S. Schirrmeister, T. Schiestel, and J. Caro, "A coupling strategy to produce hydrogen and ethylene in a membrane reactor," *Angewandte Chemie International Edition*, vol. 49, no. 33, pp. 5656–5660, Aug. 2010, ISSN: 1433-7851. DOI: 10.1002/anie.201000664.

[21] C. Wang, G. R. Wittreich, C. Lin, R. Huang, D. G. Vlachos, and R. J. Gorte, "Hydrodeoxygenation of m-Cresol over Pt-WOx/C using H_2 Generated in situ by n-hexane dehydrogenation," *Catalysis Letters*, vol. 150, no. 4, pp. 913–921, Apr. 2020, ISSN: 1011-372X. DOI: 10.1007/s10562-019-03027-8.

[22] G. W. Huber and A. Corma, "Synergies between bio- and oil refineries for the production of fuels from biomass," *Angewandte Chemie International Edition*, vol. 46, no. 38, pp. 7184–7201, Sep. 2007, ISSN: 1433-7851. DOI: 10.1002/anie.200604504.

[23] I. D. Mora-Vergara, L. Hernández Moscoso, E. M. Gaigneaux, S. A. Giraldo, and V. G. Baldovino-Medrano, "Hydrodeoxygenation of guaiacol using NiMo and CoMo catalysts supported on alumina modified with potassium," *Catalysis Today*, vol. 302, pp. 125–135, Mar. 2018, ISSN: 09205861. DOI: 10.1016/j.cattod.2017.07.015.

[24] G. Zhou, P. A. Jensen, D. M. Le, N. O. Knudsen, and A. D. Jensen, "Atmospheric hydrodeoxygenation of biomass fast pyrolysis vapor by MoO_3," *ACS Sustainable Chemistry & Engineering*, vol. 4, no. 10, pp. 5432–5440, Oct. 2016, ISSN: 2168-0485. DOI: 10.1021/acssuschemeng.6b00757.

[25] X. Zhu, L. L. Lobban, R. G. Mallinson, and D. E. Resasco, "Bifunctional transalkylation and hydrodeoxygenation of anisole over a Pt/HBeta catalyst," *Journal of Catalysis*, vol. 281, no. 1, pp. 21–29, Jul. 2011, ISSN: 00219517. DOI: 10.1016/j.jcat.2011.03.030.

[26] M. A. Gonzalez-Borja and D. E. Resasco, "Anisole and guaiacol hydrodeoxygenation over monolithic Pt–Sn catalysts," *Energy & Fuels*, vol. 25, no. 9, pp. 4155–4162, Sep. 2011, ISSN: 0887-0624. DOI: 10.1021/ef200728r.

[27] D. Gao, Y. Xiao, and A. Varma, "Guaiacol hydrodeoxygenation over platinum catalyst: Reaction pathways and kinetics," *Industrial & Engineering Chemistry Research*, vol. 54, no. 43, pp. 10 638–10 644, Nov. 2015, ISSN: 0888-5885. DOI: 10.1021/acs.iecr.5b02940.

[28] F. Cherubini, "The biorefinery concept: Using biomass instead of oil for producing energy and chemicals," *Energy Conversion and Management*, vol. 51, no. 7, pp. 1412–1421, Jul. 2010, ISSN: 01968904. DOI: 10.1016/j.enconman.2010.01.015.

[29] C. E. Wyman, "Ethanol from lignocellulosic biomass: Technology, economics, and opportunities," *Bioresource Technology*, vol. 50, no. 1, pp. 3–15, Jan. 1994, ISSN: 09608524. DOI: 10.1016/0960-8524(94)90214-3.

[30] E. de Jong and G. Jungmeier, "Biorefinery concepts in comparison to petrochemical refineries," in *Industrial Biorefineries & White Biotechnology*, Elsevier, Jan. 2015, pp. 3–33, ISBN: 9780444634535. DOI: 10.1016/B978-0-444-63453-5.00001-X.

[31] F. G. Calvo-Flores and F. J. Martin-Martinez, "Biorefineries: Achievements and challenges for a bio-based economy," *Frontiers in Chemistry*, vol. 10, Nov. 2022, ISSN: 2296-2646. DOI: 10.3389/fchem.2022.973417.

[32] R. Olcese, M. Bettahar, D. Petitjean, B. Malaman, F. Giovanella, and A. Dufour, "Gas-phase hydrodeoxygenation of guaiacol over Fe/SiO_2 catalyst," *Applied Catalysis B: Environmental*, vol. 115-116, pp. 63–73, Apr. 2012, ISSN: 09263373. DOI: 10.1016/j.apcatb.2011.12.005.

[33] E. De Jong, H. Stichnothe, G. Bell, and H. Jørgensen, "Bio-based chemicals a 2020 update bio-based chemicals with input from: (pdf version) published by IEA bioenergy," International Energy Agency Bioenergy, Tech. Rep., 2020.

[34] A. Khosravanipour Mostafazadeh, O. Solomatnikova, P. Drogui, and R. D. Tyagi, "A review of recent research and developments in fast pyrolysis and bio-oil upgrading," *Biomass Conversion and Biorefinery*, vol. 8, no. 3, pp. 739–773, Sep. 2018, ISSN: 2190-6815. DOI: 10.1007/s13399-018-0320-z.

[35] A. Pawar, N. L. Panwar, and B. L. Salvi, "Comprehensive review on pyrolytic oil production, upgrading and its utilization," *Journal of Material Cycles and Waste Management*, vol. 22, no. 6, pp. 1712–1722, Nov. 2020, ISSN: 1438-4957. DOI: 10.1007/s10163-020-01063-w.

[36] R. Sahu, B. J. Song, J. S. Im, Y.-P. Jeon, and C. W. Lee, "A review of recent advances in catalytic hydrocracking of heavy residues," *Journal of Industrial and Engineering Chemistry*, vol. 27, pp. 12–24, Jul. 2015, ISSN: 1226086X. DOI: 10.1016/j.jiec.2015.01.011.

[37] E. Furimsky, "Catalytic hydrodeoxygenation," *Applied Catalysis A: General*, vol. 199, no. 2, pp. 147–190, Jun. 2000, ISSN: 0926860X. DOI: 10.1016/S0926-860X(99)00555-4.

[38] J. Fortuin and H. Waterman, "Production of phenol from cumene," *Chemical Engineering Science*, vol. 2, no. 4, pp. 182–192, Aug. 1953, ISSN: 00092509. DOI: 10.1016/0009-2509(53)80040-0.

[39] *Cepsa & Bio-Oils build the largest 2G biofuel plant*.

[40] *Sites | INEOS Phenol*.

[41] R. Shu, R. Li, B. Lin, C. Wang, Z. Cheng, and Y. Chen, "A review on the catalytic hydrodeoxygenation of lignin-derived phenolic compounds and the conversion of raw

lignin to hydrocarbon liquid fuels," *Biomass and Bioenergy*, vol. 132, p. 105 432, Jan. 2020, ISSN: 0961-9534. DOI: 10.1016/J.BIOMBIOE.2019.105432.

[42] F. Cherubini, G. Jungmeier, M. Wellisch, *et al.*, "Toward a common classification approach for biorefinery systems," *Biofuels, Bioproducts and Biorefining*, vol. 3, no. 5, pp. 534–546, Sep. 2009, ISSN: 1932-104X. DOI: 10.1002/bbb.172.

[43] "Opportunities for the fermentation-based chemical industry | Deloitte | Chemicals," Deloitte, Tech. Rep.

[44] A. Rafiee, K. Rajab Khalilpour, D. Milani, and M. Panahi, "Trends in CO_2 conversion and utilization: A review from process systems perspective," *Journal of Environmental Chemical Engineering*, vol. 6, no. 5, pp. 5771–5794, Oct. 2018, ISSN: 22133437. DOI: 10.1016/j.jece.2018.08.065.

[45] Y. Gao, J. Jiang, Y. Meng, F. Yan, and A. Aihemaiti, "A review of recent developments in hydrogen production via biogas dry reforming," *Energy Conversion and Management*, vol. 171, pp. 133–155, Sep. 2018, ISSN: 01968904. DOI: 10.1016/j.enconman.2018.05.083.

[46] H. Xu, Z. Wang, J. Huang, and Y. Jiang, "Thermal Catalytic Conversion of Biomass-Derived Glucose to Fine Chemicals," *Energy & Fuels*, vol. 35, no. 10, pp. 8602–8616, May 2021, ISSN: 0887-0624. DOI: 10.1021/acs.energyfuels.1c00715.

[47] A. Corma, S. Iborra, and A. Velty, "Chemical Routes for the Transformation of Biomass into Chemicals," *Chemical Reviews*, vol. 107, no. 6, pp. 2411–2502, Jun. 2007, ISSN: 0009-2665. DOI: 10.1021/cr050989d.

[48] Y. Zhang, H. Lei, Z. Yang, D. Duan, E. Villota, and R. Ruan, "From glucose-based carbohydrates to phenol-rich bio-oils integrated with syngas production via catalytic pyrolysis over an activated carbon catalyst," *Green Chemistry*, vol. 20, no. 14, pp. 3346–3358, Jul. 2018, ISSN: 1463-9262. DOI: 10.1039/C8GC00593A.

[49] J. A. Rodriguez, P. Liu, D. J. Stacchiola, S. D. Senanayake, M. G. White, and J. G. Chen, "Hydrogenation of CO_2 to methanol: Importance of metal–oxide and metal–carbide interfaces in the activation of CO_2," *ACS Catalysis*, vol. 5, no. 11, pp. 6696–6706, Nov. 2015, ISSN: 2155-5435. DOI: 10.1021/acscatal.5b01755.

[50] Carbon Recycling International, *World's largest CO_2-to-methanol plant starts production*, 2022.

[51] C. Chen, X. Zhu, X. Wen, *et al.*, "Coupling N_2 and CO_2 in H_2O to synthesize urea under ambient conditions," *Nature Chemistry*, vol. 12, no. 8, pp. 717–724, Aug. 2020, ISSN: 1755-4330. DOI: 10.1038/s41557-020-0481-9.

[52] Y. Wang and D. J. Darensbourg, "Carbon dioxide-based functional polycarbonates: Metal catalyzed copolymerization of CO_2 and epoxides," *Coordination Chemistry Reviews*, vol. 372, pp. 85–100, Oct. 2018, ISSN: 0010-8545. DOI: 10.1016/J.CCR.2018.06.004.

[53] Z. Zhou, D. Liu, and X. Zhao, "Conversion of lignocellulose to biofuels and chemicals via sugar platform: An updated review on chemistry and mechanisms of acid hydrolysis of lignocellulose," *Renewable and Sustainable Energy Reviews*, vol. 146, p. 111 169, Aug. 2021, ISSN: 13640321. DOI: 10.1016/j.rser.2021.111169.

[54] S. I. Mussatto, "Biomass pretreatment, biorefineries, and potential products for a bioeconomy development," in *Biomass Fractionation Technologies for a Lignocellulosic Feedstock Based Biorefinery*, United States: Elsevier, 2016, p. 1, ISBN: 0128023236.

[55] J. J. Bozell and G. R. Petersen, "Technology development for the production of biobased products from biorefinery carbohydrates—the US Department of Energy's "Top 10" revisited," *Green Chemistry*, vol. 12, no. 4, p. 539, 2010, ISSN: 1463-9262. DOI: 10.1039/b922014c.

[56] E. M. H. Jhuma Sadhukhan Kok Siew Ng, "Introduction," in *Biorefineries and Chemical Processes*, Wiley, Oct. 2014, ch. 1, pp. 1–41, ISBN: 9781118698129. DOI: 10.1002/9781118698129.ch1.

[57] A. M. Ribeiro, A. I. Santos, F. Veiga, and A. Figueiras, "Lignin nanoparticle–based nanocomposite hydrogels for biomedical applications," in *Functional Nanocomposite Hydrogels*, Elsevier, Jan. 2023, pp. 69–90, ISBN: 9780323996389. DOI: 10.1016/B978-0-323-99638-9.00003-4.

[58] A. Alzagameem, B. E. Khaldi-Hansen, D. Büchner, *et al.*, "Lignocellulosic Biomass as Source for Lignin-Based Environmentally Benign Antioxidants," *Molecules*, vol. 23, no. 10, p. 2664, Oct. 2018, ISSN: 1420-3049. DOI: 10.3390/molecules23102664.

[59] L. A. Dodge, R. M. Kalinoski, L. Das, *et al.*, "Sequential extraction and characterization of lignin-derived compounds from thermochemically processed biorefinery lignins," *Energy and Fuels*, vol. 33, no. 5, pp. 4322–4330, May 2019, ISSN: 15205029. DOI: 10.1021/acs.energyfuels.9b00376.

[60] N. Mahmood, Z. Yuan, J. Schmidt, and C. Xu, "Depolymerization of lignins and their applications for the preparation of polyols and rigid polyurethane foams: A review," *Renewable and Sustainable Energy Reviews*, vol. 60, pp. 317–329, Jul. 2016, ISSN: 1364-0321. DOI: 10.1016/J.RSER.2016.01.037.

[61] M. Saidi, F. Samimi, D. Karimipourfard, T. Nimmanwudipong, B. C. Gates, and M. R. Rahimpour, "Upgrading of lignin-derived bio-oils by catalytic hydrodeoxygenation," *Energy Environ. Sci.*, vol. 7, no. 1, pp. 103–129, 2014, ISSN: 1754-5692. DOI: 10.1039/C3EE43081B.

[62] R. Venderbosch and W. Prins, "Fast pyrolysis technology development," *Biofuels, Bioproducts and Biorefining*, vol. 4, no. 2, pp. 178–208, Mar. 2010, ISSN: 1932-104X. DOI: 10.1002/bbb.205.

[63] A. C. Garcia, S. Cheng, and J. S. Cross, "Solvolysis of Kraft Lignin to Bio-Oil: A Critical Review," *Clean Technologies*, vol. 2, no. 4, pp. 513–528, Dec. 2020, ISSN: 2571-8797. DOI: 10.3390/cleantechnol2040032.

[64] S. BAUMLIN, F. BROUST, F. BAZERBACHI, *et al.*, "Production of hydrogen by lignins fast pyrolysis," *International Journal of Hydrogen Energy*, vol. 31, no. 15, pp. 2179–2192, Dec. 2006, ISSN: 03603199. DOI: 10.1016/j.ijhydene.2006.02.016.

[65] Z. Luo, K. Lu, Y. Yang, S. Li, and G. Li, "Catalytic fast pyrolysis of lignin to produce aromatic hydrocarbons: optimal conditions and reaction mechanism," *RSC Advances*, vol. 9, no. 55, pp. 31 960–31 968, 2019, ISSN: 2046-2069. DOI: 10.1039/C9RA02538C.

[66] S. S. Toor, L. Rosendahl, and A. Rudolf, "Hydrothermal liquefaction of biomass: A review of subcritical water technologies," *Energy*, vol. 36, no. 5, pp. 2328–2342, May 2011, ISSN: 03605442. DOI: 10.1016/j.energy.2011.03.013.

[67] D. Castello, T. H. Pedersen, and L. A. Rosendahl, "Continuous Hydrothermal Liquefaction of Biomass: A Critical Review," *Energies*, vol. 11, no. 11, 2018, ISSN: 1996-1073. DOI: 10.3390/en11113165.

[68] G. Fogassy, N. Thegarid, G. Toussaint, A. C. van Veen, Y. Schuurman, and C. Mirodatos, "Biomass derived feedstock co-processing with vacuum gas oil for second-generation fuel production in FCC units," *Applied Catalysis B: Environmental*, vol. 96, no. 3-4, pp. 476–485, Jun. 2010, ISSN: 09263373. DOI: 10.1016/j.apcatb.2010.03.008.

[69] F. Broglia, L. Rimoldi, D. Meroni, S. De Vecchi, M. Morbidelli, and S. Ardizzone, "Guaiacol hydrodeoxygenation as a model for lignin upgrading. Role of the support

surface features on Ni-based alumina-silica catalysts," *Fuel*, vol. 243, pp. 501–508, 2019, ISSN: 00162361. DOI: 10.1016/j.fuel.2019.01.157.

[70] Z. Chen, R. G. Kukushkin, P. M. Yeletsky, A. A. Saraev, O. A. Bulavchenko, and M. Millan, "Coupling hydrogenation of guaiacol with in situ hydrogen production by glycerol aqueous reforming over Ni/Al_2O_3 and Ni-X/Al_2O_3 (X = cu, mo, p) catalysts," *Nanomaterials*, vol. 10, no. 7, pp. 1–21, 2020, ISSN: 20794991. DOI: 10.3390/nano10071420.

[71] A. Gutierrez, R. Kaila, M. Honkela, R. Slioor, and A. Krause, "Hydrodeoxygenation of guaiacol on noble metal catalysts," *Catalysis Today*, vol. 147, no. 3-4, pp. 239–246, Oct. 2009, ISSN: 09205861. DOI: 10.1016/j.cattod.2008.10.037.

[72] A. Oasmaa and S. Czernik, "Fuel oil quality of biomass pyrolysis oils state of the art for the end users," *Energy & Fuels*, vol. 13, no. 4, pp. 914–921, Jul. 1999, ISSN: 0887-0624. DOI: 10.1021/ef980272b.

[73] Q. Zhang, J. Chang, T. Wang, and Y. Xu, "Review of biomass pyrolysis oil properties and upgrading research," *Energy Conversion and Management*, vol. 48, no. 1, pp. 87–92, Jan. 2007, ISSN: 0196-8904. DOI: 10.1016/J.ENCONMAN.2006.05.010.

[74] S. Xiu, A. Shahbazi, V. Shirley, and D. Cheng, "Hydrothermal pyrolysis of swine manure to bio-oil: Effects of operating parameters on products yield and characterization of bio-oil," *Journal of Analytical and Applied Pyrolysis*, vol. 88, no. 1, pp. 73–79, May 2010, ISSN: 0165-2370. DOI: 10.1016/J.JAAP.2010.02.011.

[75] S. Xiu and A. Shahbazi, "Bio-oil production and upgrading research: A review," *Renewable and Sustainable Energy Reviews*, vol. 16, no. 7, pp. 4406–4414, Sep. 2012, ISSN: 13640321. DOI: 10.1016/j.rser.2012.04.028.

[76] H. A. Baloch, S. Nizamuddin, M. T. Siddiqui, *et al.*, "Recent advances in production and upgrading of bio-oil from biomass: A critical overview," *Journal of Environmental Chemical Engineering*, vol. 6, no. 4, pp. 5101–5118, Aug. 2018, ISSN: 2213-3437. DOI: 10.1016/J.JECE.2018.07.050.

[77] H. Setiabudi, M. Aziz, S. Abdullah, L. Teh, and R. Jusoh, "Hydrogen production from catalytic steam reforming of biomass pyrolysis oil or bio-oil derivatives: A review," *International Journal of Hydrogen Energy*, vol. 45, no. 36, pp. 18 376–18 397, Jul. 2020, ISSN: 03603199. DOI: 10.1016/j.ijhydene.2019.10.141.

[78] R. Trane, S. Dahl, M. Skjøth-Rasmussen, and A. Jensen, "Catalytic steam reforming of bio-oil," *International Journal of Hydrogen Energy*, vol. 37, no. 8, pp. 6447–6472, Apr. 2012, ISSN: 03603199. DOI: 10.1016/j.ijhydene.2012.01.023.

[79] R. Davda, J. Shabaker, G. Huber, R. Cortright, and J. Dumesic, "A review of catalytic issues and process conditions for renewable hydrogen and alkanes by aqueous-phase reforming of oxygenated hydrocarbons over supported metal catalysts," *Applied Catalysis B: Environmental*, vol. 56, no. 1-2, pp. 171–186, Mar. 2005, ISSN: 09263373. DOI: 10.1016/j.apcatb.2004.04.027.

[80] A. Bridgwater, "Review of fast pyrolysis of biomass and product upgrading," *Biomass and Bioenergy*, vol. 38, pp. 68–94, Mar. 2012, ISSN: 09619534. DOI: 10.1016/j.biombioe.2011.01.048.

[81] M. Al-Sabawi, J. Chen, and S. Ng, "Fluid catalytic cracking of biomass-derived oils and their blends with petroleum feedstocks: A review," *Energy & Fuels*, vol. 26, no. 9, pp. 5355–5372, Sep. 2012, ISSN: 0887-0624. DOI: 10.1021/ef3006417.

[82] M. M. Bhasin, J. H. Mccain, B. V. Vora, T. Imai, and P. R. Pujadó, "Dehydrogenation and oxydehydrogenation of paraffins to olefins," *Applied Catalysis A: General*, vol. 221, pp. 397–419, 2001.

[83] Z. Nawaz, "Light alkane dehydrogenation to light olefin technologies: a comprehensive review," *Reviews in Chemical Engineering*, vol. 31, no. 5, pp. 413–436, Jan. 2015, ISSN: 2191-0235. DOI: 10.1515/revce-2015-0012.

[84] J. J. H. B. Sattler, J. Ruiz-Martinez, E. Santillan-Jimenez, and B. M. Weckhuysen, "Catalytic dehydrogenation of light alkanes on metals and metal oxides," *Chemical Reviews*, vol. 114, no. 20, pp. 10613–10653, Oct. 2014, ISSN: 0009-2665. DOI: 10.1021/cr5002436.

[85] M. Heuchel, F. Reinhardt, N. Merdanoğlu, E. Klemm, and Y. Traa, "Co-catalytic cracking of n-decane and 2-ethylphenol over a variety of deactivated zeolites for the conversion of fossil- and bio-based feeds in Co-FCC," *Microporous and Mesoporous Materials*, vol. 254, pp. 59–68, Dec. 2017, ISSN: 1387-1811. DOI: 10.1016/J.MICROMESO.2017.05.005.

[86] A. Aqsha, L. Katta, and N. Mahinpey, "Catalytic hydrodeoxygenation of guaiacol as lignin model component using Ni-Mo/TiO_2 and Ni-V/TiO_2 catalysts," *Catalysis Letters*, vol. 145, no. 6, pp. 1351–1363, Jun. 2015, ISSN: 1011-372X. DOI: 10.1007/s10562-015-1530-7.

[87] S.-K. Wu, P.-C. Lai, Y.-C. Lin, H.-P. Wan, H.-T. Lee, and Y.-H. Chang, "Atmospheric hydrodeoxygenation of guaiacol over alumina-, zirconia-, and silica-supported nickel phosphide catalysts," *ACS Sustainable Chemistry & Engineering*, vol. 1, no. 3, pp. 349–358, Mar. 2013, ISSN: 2168-0485. DOI: 10.1021/sc300157d.

[88] M. M. Yung, G. S. Foo, and C. Sievers, "Role of Pt during hydrodeoxygenation of biomass pyrolysis vapors over Pt/HBEA," *Catalysis Today*, vol. 302, pp. 151–160, Mar. 2018, ISSN: 09205861. DOI: 10.1016/j.cattod.2017.03.014.

[89] H. Zhou, H. Wang, A. D. Sadow, and I. I. Slowing, "Toward hydrogen economy: Selective guaiacol hydrogenolysis under ambient hydrogen pressure," *Applied Catalysis B: Environmental*, vol. 270, p. 118 890, Aug. 2020, ISSN: 09263373. DOI: 10.1016/j.apcatb.2020.118890.

[90] T. He, X. Liu, Y. Ge, *et al.*, "Gas phase hydrodeoxygenation of anisole and guaiacol to aromatics with a high selectivity over Ni-Mo/SiO_2," *Catalysis Communications*, vol. 102, pp. 127–130, Dec. 2017, ISSN: 15667367. DOI: 10.1016/j.catcom.2017.09.011.

[91] T. Prasomsri, M. Shetty, K. Murugappan, and Y. Román-Leshkov, "Insights into the catalytic activity and surface modification of MoO_3 during the hydrodeoxygenation of lignin-derived model compounds into aromatic hydrocarbons under low hydrogen pressures," *Energy Environ. Sci.*, vol. 7, no. 8, pp. 2660–2669, Jul. 2014, ISSN: 1754-5692. DOI: 10.1039/C4EE00890A.

[92] C.-J. Chen, W.-S. Lee, and A. Bhan, "Mo_2C catalyzed vapor phase hydrodeoxygenation of lignin-derived phenolic compound mixtures to aromatics under ambient pressure," *Applied Catalysis A: General*, vol. 510, pp. 42–48, Jan. 2016, ISSN: 0926860X. DOI: 10.1016/j.apcata.2015.10.043.

[93] J. Sun, A. M. Karim, H. Zhang, *et al.*, "Carbon-supported bimetallic Pd–Fe catalysts for vapor-phase hydrodeoxygenation of guaiacol," *Journal of Catalysis*, vol. 306, pp. 47–57, Oct. 2013, ISSN: 0021-9517. DOI: 10.1016/J.JCAT.2013.05.020.

[94] Y. Wu, X. Xu, Y. Sun, *et al.*, "Gas-phase hydrodeoxygenation of guaiacol over Ni-based HUSY zeolite catalysts under atmospheric H_2 pressure," *Renewable Energy*, vol. 152, pp. 1380–1390, Jun. 2020, ISSN: 09601481. DOI: 10.1016/j.renene.2020.01.117.

[95] H. Pourzolfaghar, F. Abnisa, W. M. A. Wan Daud, and M. K. Aroua, "Atmospheric hydrodeoxygenation of bio-oil oxygenated model compounds: A review," *Journal of*

Analytical and Applied Pyrolysis, vol. 133, pp. 117–127, Aug. 2018, ISSN: 01652370. DOI: 10.1016/j.jaap.2018.04.013.

[96] T. Prasomsri, T. Nimmanwudipong, and Y. Román-Leshkov, "Effective hydrodeoxygenation of biomass-derived oxygenates into unsaturated hydrocarbons by MoO_3 using low H_2 pressures," *Energy & Environmental Science*, vol. 6, no. 6, pp. 1732–1738, May 2013, ISSN: 17545692. DOI: 10.1039/C3EE24360E.

[97] Z. Yuan, B. Chen, and R. Gani, "Applications of process synthesis: Moving from conventional chemical processes towards biorefinery processes," *Computers & Chemical Engineering*, vol. 49, pp. 217–229, Feb. 2013, ISSN: 00981354. DOI: 10.1016/j.compchemeng.2012.09.020.

[98] P. M. de Souza, R. C. Rabelo-Neto, L. E. P. Borges, *et al.*, "Effect of zirconia morphology on hydrodeoxygenation of phenol over Pd/ZrO_2," *ACS Catalysis*, vol. 5, no. 12, pp. 7385–7398, Dec. 2015, ISSN: 2155-5435. DOI: 10.1021/acscatal.5b01501.

[99] P. M. de Souza, R. C. Rabelo-Neto, L. E. P. Borges, *et al.*, "Hydrodeoxygenation of phenol over Pd catalysts. Effect of support on reaction mechanism and catalyst deactivation," *ACS Catalysis*, vol. 7, no. 3, pp. 2058–2073, Mar. 2017, ISSN: 2155-5435. DOI: 10.1021/acscatal.6b02022.

[100] G. J. Stiegel and M. Ramezan, "Hydrogen from coal gasification: An economical pathway to a sustainable energy future," *International Journal of Coal Geology*, vol. 65, no. 3-4, pp. 173–190, Jan. 2006, ISSN: 01665162. DOI: 10.1016/j.coal.2005.05.002.

[101] A. Arregi, M. Amutio, G. Lopez, J. Bilbao, and M. Olazar, "Evaluation of thermochemical routes for hydrogen production from biomass: A review," vol. 165, pp. 696–719, Jun. 2018, ISSN: 01968904. DOI: 10.1016/j.enconman.2018.03.089.

[102] K. Liu, C. Song, and V. Subramani, *Hydrogen and syngas production and purification technologies*. Wiley, 2010, p. 533, ISBN: 978-0-471-71975-5.

[103] J. R. Bartels, M. B. Pate, and N. K. Olson, "An economic survey of hydrogen production from conventional and alternative energy sources," *International Journal of Hydrogen Energy*, vol. 35, no. 16, pp. 8371–8384, Aug. 2010, ISSN: 03603199. DOI: 10.1016/j.ijhydene.2010.04.035.

[104] "Commodity Pricing Index," IHS, Tech. Rep., 2014.

[105] L. O. Alemán-Vázquez, P. Torres-Mancera, J. Ancheyta, and J. Ramírez-Salgado, "Use of hydrogen donors for partial upgrading of heavy petroleum," *Energy & Fuels*, vol. 30,

no. 11, pp. 9050–9060, Nov. 2016, ISSN: 0887-0624. DOI: 10.1021/acs.energyfuels.6b01656.

[106] A. Guo, C. Wu, P. He, *et al.*, "Low-temperature and low-pressure non-oxidative activation of methane for upgrading heavy oil," *Catalysis Science & Technology*, vol. 6, no. 4, pp. 1201–1213, Feb. 2016, ISSN: 2044-4753. DOI: 10.1039/C5CY00947B.

[107] C. Ovalles, A. Hamana, I. Rojas, and R. A. Bolívar, "Upgrading of extra-heavy crude oil by direct use of methane in the presence of water," *Fuel*, vol. 74, no. 8, pp. 1162–1168, Aug. 1995, ISSN: 00162361. DOI: 10.1016/0016-2361(95)00071-C.

[108] C. Ovalles, E. Filgueiras, A. Morales, C. E. Scott, F. Gonzalez-Gimenez, and B. Pierre Embaid, "Use of a dispersed iron catalyst for upgrading extra-heavy crude oil using methane as source of hydrogen," *Fuel*, vol. 82, no. 8, pp. 887–892, May 2003, ISSN: 00162361. DOI: 10.1016/S0016-2361(02)00406-4.

[109] P. He, W. Shan, Y. Xiao, and H. Song, "Performance of Zn/ZSM-5 for in-situ catalytic upgrading of pyrolysis bio-oil by methane," *Topics in Catalysis*, vol. 59, no. 1, pp. 86–93, Jan. 2016, ISSN: 1022-5528. DOI: 10.1007/s11244-015-0508-4.

[110] A. Hart, M. Adam, J. P. Robinson, S. P. Rigby, and J. Wood, "Tetralin and decalin H-donor effect on catalytic upgrading of heavy oil inductively heated with steel balls," *Catalysts*, vol. 10, no. 4, p. 393, Apr. 2020, ISSN: 2073-4344. DOI: 10.3390/catal10040393.

[111] S. H. Kim, K. D. Kim, H. Lee, and Y. K. Lee, "Beneficial roles of H-donors as diluent and H-shuttle for asphaltenes in catalytic upgrading of vacuum residue," *Chemical Engineering Journal*, vol. 314, pp. 1–10, 2017, ISSN: 13858947. DOI: 10.1016/j.cej.2016.12.119.

[112] A. Hart and J. Wood, "In situ catalytic upgrading of heavy crude with CAPRI: Influence of hydrogen on catalyst pore plugging and deactivation due to coke," *Energies*, vol. 11, no. 3, p. 636, Mar. 2018, ISSN: 1996-1073. DOI: 10.3390/en11030636.

[113] C. A. Fisk, T. Morgan, Y. Ji, M. Crocker, C. Crofcheck, and S. A. Lewis, "Bio-oil upgrading over platinum catalysts using in situ generated hydrogen," *Applied Catalysis A: General*, vol. 358, no. 2, pp. 150–156, May 2009, ISSN: 0926860X. DOI: 10.1016/j.apcata.2009.02.006.

[114] V. Palma, C. Ruocco, M. Cortese, and M. Martino, "Bioalcohol reforming: An overview of the recent advances for the enhancement of catalyst stability," *Catalysts*, vol. 10, no. 6, p. 665, Jun. 2020, ISSN: 2073-4344. DOI: 10.3390/catal10060665.

[115] C. A. Schwengber, H. J. Alves, R. A. Schaffner, *et al.*, "Overview of glycerol reforming for hydrogen production," *Renewable and Sustainable Energy Reviews*, vol. 58, pp. 259–266, May 2016, ISSN: 13640321. DOI: 10.1016/j.rser.2015.12.279.

[116] X.-d. Fan, Y.-j. Wu, Z.-y. Li, *et al.*, "Benzene, toluene and xylene (BTX) from in-situ gas phase hydrodeoxygenation of guaiacol with liquid hydrogen donor over bifunctional non-noble-metal zeolite catalysts," *Renewable Energy*, vol. 152, pp. 1391–1402, Jun. 2020, ISSN: 09601481. DOI: 10.1016/j.renene.2020.01.015.

[117] V. L. Yfanti and A. A. Lemonidou, "Mechanistic study of liquid phase glycerol hydrodeoxygenation with in-situ generated hydrogen," *Journal of Catalysis*, vol. 368, pp. 98–111, Dec. 2018, ISSN: 0021-9517. DOI: 10.1016/J.JCAT.2018.09.036.

[118] M. Zhang, Y. Wu, X. Han, Y. Zeng, and C. C. Xu, "Upgrading pyrolysis oil by catalytic hydrodeoxygenation reaction in supercritical ethanol with different hydrogen sources," *Chemical Engineering Journal*, vol. 446, p. 136 952, Oct. 2022, ISSN: 13858947. DOI: 10.1016/j.cej.2022.136952.

[119] M. T. Timko, A. F. Ghoniem, and W. H. Green, "Upgrading and desulfurization of heavy oils by supercritical water," *The Journal of Supercritical Fluids*, vol. 96, pp. 114–123, Jan. 2015, ISSN: 08968446. DOI: 10.1016/j.supflu.2014.09.015.

[120] A. Vutolkina, I. Baigildin, A. Glotov, *et al.*, "Hydrodeoxygenation of guaiacol via in situ H_2 generated through a water gas shift reaction over dispersed NiMoS catalysts from oil-soluble precursors: Tuning the selectivity towards cyclohexene," *Applied Catalysis B: Environmental*, vol. 312, p. 121 403, Sep. 2022, ISSN: 09263373. DOI: 10.1016/j.apcatb.2022.121403.

[121] C. Miao, O. Marin-Flores, T. Dong, *et al.*, "Hydrothermal catalytic deoxygenation of fatty acid and bio-oil with in-situ H_2," *ACS Sustainable Chemistry & Engineering*, vol. 6, no. 4, pp. 4521–4530, Apr. 2018, ISSN: 2168-0485. DOI: 10.1021/acssuschemeng.7b02226.

[122] W. Jin, L. Pastor-Pe, J. J. Villora-Pico, A. Sepuíveda-Escribano, S. Gu, and T. R. Reina, "Investigating New Routes for Biomass Upgrading: "H 2-Free" Hydrodeoxygenation Using Ni-Based Catalysts," 2019. DOI: 10.1021/acssuschemeng.9b02712.

[123] L. Gueudré, N. Thegarid, L. Burel, *et al.*, "Coke chemistry under vacuum gasoil/bio-oil FCC co-processing conditions," *Catalysis Today*, vol. 257, pp. 200–212, Nov. 2015, ISSN: 09205861. DOI: 10.1016/j.cattod.2014.09.001.

[124] I. Graça, J. Lopes, M. Ribeiro, F. Ramôa Ribeiro, H. Cerqueira, and M. de Almeida, "Catalytic cracking in the presence of guaiacol," *Applied Catalysis B: Environmental*, vol. 101, no. 3-4, pp. 613–621, Jan. 2011, ISSN: 09263373. DOI: 10.1016/j.apcatb.2010.11.002.

[125] S. W. Benson, "III-bond energies," *Journal of Chemical Education*, vol. 13, p. 502, 2024.

[126] M. W. Nolte and B. H. Shanks, "A perspective on catalytic strategies for deoxygenation in biomass pyrolysis," *Energy Technology*, vol. 5, no. 1, pp. 7–18, Jan. 2017, ISSN: 2194-4288. DOI: 10.1002/ente.201600096.

[127] V. M. Whiffen and K. J. Smith, "Hydrodeoxygenation of 4-methylphenol over unsupported MoP, MoS_2, and MoO_x catalysts," *Energy and Fuels*, vol. 24, no. 9, pp. 4728–4737, Sep. 2010, ISSN: 08870624. DOI: 10.1021/EF901270H/ASSET/IMAGES/LARGE/EF-2009-01270H{_}0008.JPEG.

[128] S. Boullosa-Eiras, R. Lødeng, H. Bergem, M. Stöcker, L. Hannevold, and E. A. Blekkan, "Catalytic hydrodeoxygenation (HDO) of phenol over supported molybdenum carbide, nitride, phosphide and oxide catalysts," *Catalysis Today*, vol. 223, pp. 44–53, Mar. 2014, ISSN: 09205861. DOI: 10.1016/j.cattod.2013.09.044.

[129] D. R. Moberg, T. J. Thibodeau, F. G. Amar, and B. G. Frederick, "Mechanism of hydrodeoxygenation of acrolein on a cluster model of MoO_3," *Journal of Physical Chemistry C*, vol. 114, no. 32, pp. 13 782–13 795, Aug. 2010, ISSN: 19327447. DOI: 10.1021/jp104421a.

[130] D. Mei, A. M. Karim, and Y. Wang, "Density functional theory study of acetaldehyde hydrodeoxygenation on MoO_3," *The Journal of Physical Chemistry C*, vol. 115, no. 16, pp. 8155–8164, Apr. 2011, ISSN: 1932-7447. DOI: 10.1021/jp200011j.

[131] A. M. Robinson, J. E. Hensley, and J. W. Medlin, "Bifunctional catalysts for upgrading of biomass-derived oxygenates: A review," *ACS Catalysis*, vol. 6, no. 8, pp. 5026–5043, Aug. 2016, ISSN: 2155-5435. DOI: 10.1021/acscatal.6b00923.

[132] J. Védrine, "Heterogeneous catalysis on metal oxides," *Catalysts*, vol. 7, no. 11, p. 341, Nov. 2017, ISSN: 2073-4344. DOI: 10.3390/catal7110341.

[133] H. Yang, L. Xu, D. Ji, Q. Wang, and L. Lin, "The catalytic dehydrogenation of C_2H_6 to C_2H_4 under non-oxidative conditions over the $6Cr/\gamma$-Al_2O_3 catalyst," *Reaction Kinetics and Catalysis Letters*, vol. 76, no. 1, pp. 151–159, 2002, ISSN: 01331736. DOI: 10.1023/A:1015633915938.

[134] E. Heracleous and A. A. Lemonidou, "Homogeneous and heterogeneous pathways of ethane oxidative and non-oxidative dehydrogenation studied by temperature-programmed reaction," *Applied Catalysis A: General*, vol. 269, no. 1-2, pp. 123–135, Aug. 2004, ISSN: 0926860X. DOI: 10.1016/j.apcata.2004.04.007.

[135] R. Yao, J. E. Herrera, L. Chen, and Y. H. C. Chin, "Generalized mechanistic framework for ethane dehydrogenation and oxidative dehydrogenation on molybdenum oxide catalysts," *ACS Catalysis*, vol. 10, no. 12, pp. 6952–6968, Jun. 2020. DOI: 10.1021/ACSCATAL.0C01073.

[136] A. Siahvashi, D. Chesterfield, and A. A. Adesina, "Nonoxidative and oxidative propane dehydrogenation over bimetallic Mo–Ni/Al_2O_3 catalyst," *Industrial & Engineering Chemistry Research*, vol. 52, no. 11, pp. 4017–4026, Mar. 2013, ISSN: 0888-5885. DOI: 10.1021/ie302392h.

[137] T. Wang, X. Cui, K. T. Winther, F. Abild-Pedersen, T. Bligaard, and J. K. Nørskov, "Theory-aided discovery of metallic catalysts for selective propane dehydrogenation to propylene," *ACS Catalysis*, vol. 11, no. 10, pp. 6290–6297, May 2021, ISSN: 2155-5435. DOI: 10.1021/acscatal.0c05711.

[138] T. Wang, G. Li, X. Cui, and F. Abild-Pedersen, "Identification of earth-abundant materials for selective dehydrogenation of light alkanes to olefins," *Proceedings of the National Academy of Sciences*, vol. 118, no. 11, e2024666118, Mar. 2021, ISSN: 0027-8424. DOI: 10.1073/pnas.2024666118.

[139] W. Shen, Y. Wang, X. Shi, *et al.*, "Catalytic nonoxidative dehydrogenation of ethane over Fe-Ni and Ni catalysts supported on Mg(Al)O to produce hydrogen and easily purified carbon nanotubes," *Energy and Fuels*, vol. 21, no. 6, pp. 3520–3529, Nov. 2007, ISSN: 08870624. DOI: 10.1021/ef7004018.

[140] H. Saito and Y. Sekine, "Catalytic conversion of ethane to valuable products through non-oxidative dehydrogenation and dehydroaromatization," *RSC Advances*, vol. 10, no. 36, pp. 21 427–21 453, 2020, ISSN: 20462069. DOI: 10.1039/d0ra03365k.

[141] G. Wang, S. Zhang, X. Zhu, C. Li, and H. Shan, "Dehydrogenation versus hydrogenolysis in the reaction of light alkanes over Ni-based catalysts," *Journal of Industrial and Engineering Chemistry*, vol. 86, pp. 1–12, Jun. 2020, ISSN: 1226086X. DOI: 10.1016/j.jiec.2020.02.025.

[142] X. Xu, E. Jiang, Y. Du, and B. Li, "BTX from the gas-phase hydrodeoxygenation and transmethylation of guaiacol at room pressure," 2016. DOI: 10.1016/j.renene.2016.04.094.

[143] S. Ted Oyama, T. Onkawa, A. Takagaki, *et al.*, "Production of phenol and cresol from guaiacol on nickel phosphide catalysts supported on acidic supports," *Topics in Catalysis*, vol. 58, no. 4-6, pp. 201–210, Apr. 2015, ISSN: 1022-5528. DOI: 10.1007/s11244-015-0361-5.

[144] T. Nimmanwudipong, R. C. Runnebaum, D. E. Block, and B. C. Gates, "Catalytic conversion of guaiacol catalyzed by platinum supported on alumina: reaction network including hydrodeoxygenation reactions," *Energy & Fuels*, vol. 25, no. 8, pp. 3417–3427, Aug. 2011, ISSN: 0887-0624. DOI: 10.1021/ef200803d.

[145] I. Graça, J. D. Comparot, S. Laforge, *et al.*, "Effect of phenol addition on the performances of H–Y zeolite during methylcyclohexane transformation," *Applied Catalysis A: General*, vol. 353, no. 1, pp. 123–129, Jan. 2009, ISSN: 0926-860X. DOI: 10.1016/J.APCATA.2008.10.032.

[146] A. Sivena, "Hydrocracking Reaction Pathways of 1-Methylnaphthalene in a Continuous Fixed-Bed Reaction," Ph.D. dissertation, Imperical College London, 2015.

[147] I. Graa, A. Fernandes, J. M. Lopes, *et al.*, "Bio-oils and FCC feedstocks co-processing: Impact of phenolic molecules on FCC hydrocarbons transformation over MFI," *Fuel*, vol. 90, no. 2, pp. 467–476, Feb. 2011, ISSN: 0016-2361. DOI: 10.1016/J.FUEL.2010.09.028.

[148] S. Mukundan, D. Boffito, A. Shrotri, L. Atanda, J. Beltramini, and G. Patience, "Thermocatalytic hydrodeoxygenation and depolymerization of waste lignin to oxygenates and biofuels in a continuous flow reactor at atmospheric pressure," *ACS Sustainable Chemistry & Engineering*, vol. 8, no. 35, pp. 13 195–13 205, Sep. 2020, ISSN: 2168-0485. DOI: 10.1021/acssuschemeng.0c02102.

[149] L. R. Mentasty, O. F. Gorriz, and L. E. Cadus, "Chromium oxide supported on different Al_2O_3 supports: Catalytic propane dehydrogenation," *Industrial & Engineering Chemistry Research*, vol. 38, no. 2, pp. 396–404, Feb. 1999, ISSN: 0888-5885. DOI: 10.1021/ie9802562.

[150] D. Zhang, A. Duan, Z. Zhao, *et al.*, "Preparation, characterization and hydrotreating performances of ZrO_2–Al_2O_3-supported NiMo catalysts," *Catalysis Today*, vol. 149, no. 1-2, pp. 62–68, Jan. 2010, ISSN: 09205861. DOI: 10.1016/j.cattod.2009.04.012.

[151] M. Ayala-G, E. Puello P, P. Quintana, G. González-García, and C. Diaz, "Comparison between alumina supported catalytic precursors and their application in thiophene hydrodesulfurization: $(NH_4)_4[NiMo_6O_{24}H_6]\cdot 5H_2O/\gamma\text{-}Al_2O_3$ and $NiMoO_x/\gamma\text{-}Al_2O_3$ conventional systems," *RSC Advances*, vol. 5, no. 124, pp. 102 652–102 662, 2015, ISSN: 2046-2069. DOI: 10.1039/C5RA17695F.

[152] P. Sangnikul, C. Phanpa, R. Xiao, *et al.*, "Role of copper- or cerium-promoters on $NiMo/\gamma\text{-}Al_2O_3$ catalysts in hydrodeoxygenation of guaiacol and bio-oil," *Applied Catalysis A: General*, vol. 574, pp. 151–160, Mar. 2019, ISSN: 0926860X. DOI: 10.1016/j.apcata.2019.02.004.

[153] V. Sundaramurthy, A. Dalai, and J. Adjaye, "The effect of phosphorus on hydrotreating property of $NiMo/\gamma\text{-}Al_2O_3$ nitride catalyst," *Applied Catalysis A: General*, vol. 335, no. 2, pp. 204–210, Feb. 2008, ISSN: 0926860X. DOI: 10.1016/j.apcata.2007.11.024.

[154] G.-N. Yun, S.-J. Ahn, A. Takagaki, R. Kikuchi, and S. T. Oyama, "Hydrodeoxygenation of γ-valerolactone on bimetallic NiMo phosphide catalysts," *Journal of Catalysis*, vol. 353, pp. 141–151, Sep. 2017, ISSN: 00219517. DOI: 10.1016/j.jcat.2017.07.006.

[155] V. N. Bui, D. Laurenti, P. Afanasiev, and C. Geantet, "Hydrodeoxygenation of guaiacol with CoMo catalysts. Part I: Promoting effect of cobalt on HDO selectivity and activity," *Applied Catalysis B: Environmental*, vol. 101, no. 3-4, pp. 239–245, Jan. 2011, ISSN: 09263373. DOI: 10.1016/j.apcatb.2010.10.025.

[156] A. Centeno, E. Laurent, and B. Delmon, "Influence of the support of CoMo sulfide catalysts and of the addition of potassium and platinum on the catalytic performances for the hydrodeoxygenation of carbonyl, carboxyl, and guaiacol-type molecules," *Journal of Catalysis*, vol. 154, no. 2, pp. 288–298, Jul. 1995, ISSN: 00219517. DOI: 10.1006/jcat.1995.1170.

[157] X. Lan, E. J. Hensen, and T. Weber, "Hydrodeoxygenation of guaiacol over Ni_2P/SiO_2 reaction mechanism and catalyst deactivation," *Applied Catalysis A: General*, vol. 550, pp. 57–66, Jan. 2018, ISSN: 0926860X. DOI: 10.1016/j.apcata.2017.10.018.

[158] J. Lu, X. Liu, G. Yu, *et al.*, "Selective hydrodeoxygenation of guaiacol to cyclohexanol catalyzed by nanoporous nickel," *Catalysis Letters*, vol. 150, no. 3, pp. 837–848, Mar. 2020, ISSN: 1011-372X. DOI: 10.1007/s10562-019-02967-5.

[159] Z. Si, X. Zhang, C. Wang, L. Ma, and R. Dong, "An overview on catalytic hydrodeoxygenation of pyrolysis oil and its model compounds," *Catalysts*, vol. 7, no. 6, p. 169, Jun. 2017, ISSN: 2073-4344. DOI: 10.3390/catal7060169.

[160] I. Graa, A. Fernandes, J. M. Lopes, *et al.*, "Effect of phenol adsorption on HY zeolite for n-heptane cracking: Comparison with methylcyclohexane," *Applied Catalysis A: General*, vol. 385, no. 1-2, pp. 178–189, Sep. 2010, ISSN: 0926-860X. DOI: 10.1016/J.APCATA.2010.07.011.

[161] E. Heracleous, A. F. Lee, K. Wilson, and A. A. Lemonidou, "Investigation of Ni-based alumina-supported catalysts for the oxidative dehydrogenation of ethane to ethylene: structural characterization and reactivity studies," *Journal of Catalysis*, vol. 231, no. 1, pp. 159–171, Apr. 2005, ISSN: 0021-9517. DOI: 10.1016/J.JCAT.2005.01.015.

[162] B. Grzybowska, J. Słoczyński, R. Grabowski, *et al.*, "Chromium oxide/alumina catalysts in oxidative dehydrogenation of isobutane," *Journal of Catalysis*, vol. 178, no. 2, pp. 687–700, Sep. 1998, ISSN: 00219517. DOI: 10.1006/jcat.1998.2203.

[163] F. Cavani, M. Koutyrev, F. Trifirò, *et al.*, "Chemical and physical characterization of alumina-supported chromia-based catalysts and their activity in dehydrogenation of isobutane," *Journal of Catalysis*, vol. 158, no. 1, pp. 236–250, Jan. 1996, ISSN: 00219517. DOI: 10.1006/jcat.1996.0023.

[164] T. Xing, H. Wan, Y. Shao, Y. Han, Z. Xu, and S. Zheng, "Catalytic combustion of benzene over γ-alumina supported chromium oxide catalysts," *Applied Catalysis A: General*, vol. 468, pp. 269–275, Nov. 2013, ISSN: 0926860X. DOI: 10.1016/j.apcata.2013.08.054.

[165] D. Shee and A. Sayari, "Light alkane dehydrogenation over mesoporous Cr_2O_3/Al_2O_3 catalysts," *Applied Catalysis A: General*, vol. 389, no. 1-2, pp. 155–164, Dec. 2010, ISSN: 0926860X. DOI: 10.1016/j.apcata.2010.09.013.

[166] S. Egorova, R. Tuktarov, A. Boretskaya, A. Laskin, R. Gizyatullov, and A. Lamberov, "Stabilizing effect of α-Cr_2O_3 on highly active phases and catalytic performance of a chromium alumina catalyst in the process of isobutane dehydrogenation," *Molecular Catalysis*, vol. 509, p. 111610, Jun. 2021, ISSN: 24688231. DOI: 10.1016/j.mcat.2021.111610.

[167] D. Nazimov, O. Klimov, I. Danilova, *et al.*, "Effect of alumina polymorph on the dehydrogenation activity of supported chromia/alumina catalysts," *Journal of Catalysis*, vol. 391, pp. 35–47, Nov. 2020, ISSN: 00219517. DOI: 10.1016/j.jcat.2020.08.006.

[168] T. HARVEY, "Hydroprocessing catalysis by supported ruthenium sulphide," *Journal of Catalysis*, vol. 101, no. 2, pp. 253–261, Oct. 1986, ISSN: 00219517. DOI: 10.1016/0021-9517(86)90251-4.

[169] H. Chang, J. Phillips, and R. Heck, "Catalytic synergism in physical mixtures," *Langmuir*, vol. 12, no. 11, pp. 2756–2761, May 1996, ISSN: 07437463. DOI: 10.1021/LA9507895.

[170] W. Fang, C. Wang, Z. Liu, *et al.*, "Physical mixing of a catalyst and a hydrophobic polymer promotes CO hydrogenation through dehydration," *Science*, vol. 377, no. 6604, pp. 406–410, Jul. 2022, ISSN: 0036-8075. DOI: 10.1126/science.abo0356.

[171] S. Echeandia, B. Pawelec, V. Barrio, *et al.*, "Enhancement of phenol hydrodeoxygenation over Pd catalysts supported on mixed HY zeolite and Al_2O_3. An approach to O-removal from bio-oils," *Fuel*, vol. 117, no. PARTB, pp. 1061–1073, Jan. 2014, ISSN: 00162361. DOI: 10.1016/j.fuel.2013.10.011.

[172] I. Shamanaev, I. Deliy, E. Gerasimov, *et al.*, "Synergetic effect of Ni_2P/SiO_2 and γ-Al2O3 physical mixture in hydrodeoxygenation of methyl palmitate," *Catalysts*, vol. 7, no. 11, p. 329, Nov. 2017, ISSN: 2073-4344. DOI: 10.3390/catal7110329.

[173] J. Y. Yan, H. H. Kung, W. M. Sachtler, and M. C. Kung, "Synergistic effect in lean NO_x reduction by CH_4 over Co/Al_2O_3 and H-zeolite catalysts," *Journal of Catalysis*, vol. 175, no. 2, pp. 294–301, Apr. 1998, ISSN: 0021-9517. DOI: 10.1006/JCAT.1998.2012.

[174] V. S. Prabhudesai and R. Vinu, "Hydrodeoxygenation of biomass-derived oxygenate mixtures over Pt/C and HZSM-5 mixed catalysts," *Topics in Catalysis*, vol. 66, no. 5-8, pp. 405–419, Mar. 2023, ISSN: 1022-5528. DOI: 10.1007/s11244-023-01782-y.

[175] I. V. Shamanaev, I. V. Deliy, E. Y. Gerasimov, V. P. Pakharukova, and G. A. Bukhtiyarova, "Enhancement of HDO activity of MoP/SiO_2 catalyst in physical mixture with alumina or zeolites," *Catalysts*, vol. 10, no. 1, p. 45, Dec. 2019, ISSN: 2073-4344. DOI: 10.3390/catal10010045.

[176] R. E. Yakovenko, A. P. Savost'yanov, G. B. Narochniy, *et al.*, "Preliminary evaluation of a commercially viable Co-based hybrid catalyst system in Fischer–Tropsch synthesis combined with hydroprocessing," *Catalysis Science & Technology*, vol. 10, no. 22, pp. 7613–7629, 2020, ISSN: 2044-4753. DOI: 10.1039/D0CY00975J.

[177] H. Shafaghat, P. Sirous Rezaei, and W. M. A. W. Daud, "Catalytic hydrogenation of phenol, cresol and guaiacol over physically mixed catalysts of Pd/C and zeolite solid acids," *RSC Advances*, vol. 5, no. 43, pp. 33 990–33 998, 2015, ISSN: 2046-2069. DOI: 10.1039/C5RA00367A.

[178] D. R. Aireddy and K. Ding, "Heterolytic dissociation of H_2 in heterogeneous catalysis," *ACS Catalysis*, vol. 12, no. 8, pp. 4707–4723, Apr. 2022, ISSN: 2155-5435. DOI: 10.1021/acscatal.2c00584.

[179] R. Prins, "Hydrogen spillover. Facts and fiction," *Chemical Reviews*, vol. 112, no. 5, pp. 2714–2738, May 2012, ISSN: 0009-2665. DOI: 10.1021/cr200346z.

[180] H. Shen, H. Li, Z. Yang, and C. Li, "Magic of hydrogen spillover: Understanding and application," *Green Energy & Environment*, vol. 7, no. 6, pp. 1161–1198, Dec. 2022, ISSN: 2468-0257. DOI: 10.1016/J.GEE.2022.01.013.

[181] X. Hu, Z. Zhang, M. Gholizadeh, *et al.*, "Coke formation during thermal treatment of bio-oil," *Energy & Fuels*, vol. 34, no. 7, pp. 7863–7914, Jul. 2020, ISSN: 0887-0624. DOI: 10.1021/acs.energyfuels.0c01323.

[182] A. Ochoa, J. Bilbao, A. G. Gayubo, and P. Castaño, "Coke formation and deactivation during catalytic reforming of biomass and waste pyrolysis products: A review," *Renewable and Sustainable Energy Reviews*, vol. 119, p. 109 600, Mar. 2020, ISSN: 13640321. DOI: 10.1016/j.rser.2019.109600.

[183] A. Ochoa, A. Arregi, M. Amutio, *et al.*, "Coking and sintering progress of a Ni supported catalyst in the steam reforming of biomass pyrolysis volatiles," *Applied Catalysis B: Environmental*, vol. 233, pp. 289–300, Oct. 2018, ISSN: 0926-3373. DOI: 10.1016/J.APCATB.2018.04.002.

[184] Y. Cheng, C. Miao, W. Hua, Y. Yue, and Z. Gao, "Cr/ZSM-5 for ethane dehydrogenation: Enhanced catalytic activity through surface silanol," *Applied Catalysis A: General*, vol. 532, pp. 111–119, Feb. 2017, ISSN: 0926-860X. DOI: 10.1016/J.APCATA.2016.12.025.

[185] T. F. Narbeshuber, A. Brait, K. Seshan, and J. A. Lercher, "Dehydrogenation of light alkanes over zeolites," *Journal of Catalysis*, vol. 172, no. 1, pp. 127–136, Nov. 1997, ISSN: 0021-9517. DOI: 10.1006/JCAT.1997.1860.

[186] S. D. Rossi, G. Ferraris, S. Fremiotti, A. Cimino, and V. Indovina, "Propane dehydrogenation on chromia/zirconia catalysts," *Applied Catalysis A: General*, vol. 81, no. 1, pp. 113–132, Jan. 1992, ISSN: 0926-860X. DOI: 10.1016/0926-860X(92)80264-D.

[187] Y. Wu, X. Xu, Y. Sun, *et al.*, "Gas-phase hydrodeoxygenation of guaiacol over Ni-based HUSY zeolite catalysts under atmospheric H2 pressure," *Renewable Energy*, vol. 152, pp. 1380–1390, Jun. 2020, ISSN: 0960-1481. DOI: 10.1016/J.RENENE.2020.01.117.

[188] L. Tai, R. Hamidi, B. de Caprariis, *et al.*, "Guaiacol hydrotreating with in-situ generated hydrogen over Ni/modified zeolite supports," *Renewable Energy*, vol. 182, pp. 647–658, Jan. 2022, ISSN: 0960-1481. DOI: 10.1016/J.RENENE.2021.10.048.

[189] Z. Cai, F. Wang, X. Zhang, R. Ahishakiye, Y. Xie, and Y. Shen, "Selective hydrodeoxygenation of guaiacol to phenolics over activated carbon supported molybdenum catalysts," *Molecular Catalysis*, vol. 441, pp. 28–34, Nov. 2017, ISSN: 24688231. DOI: 10.1016/j.mcat.2017.07.024.

[190] E. Gomez, X. Nie, J. H. Lee, Z. Xie, and J. G. Chen, "Tandem reactions of CO_2 reduction and ethane aromatization," *Journal of the American Chemical Society*, vol. 141, no. 44, pp. 17 771–17 782, Nov. 2019, ISSN: 0002-7863. DOI: 10.1021/jacs.9b08538.

[191] D. Liu, L. Cao, G. Zhang, L. Zhao, J. Gao, and C. Xu, "Catalytic conversion of light alkanes to aromatics by metal-containing HZSM-5 zeolite catalysts—A review," *Fuel Processing Technology*, vol. 216, p. 106 770, Jun. 2021, ISSN: 03783820. DOI: 10.1016/j.fuproc.2021.106770.

[192] Q. Sun, N. Wang, and J. Yu, "Advances in catalytic applications of zeolite-supported metal catalysts," *Advanced Materials*, vol. 33, no. 51, p. 2 104 442, Dec. 2021, ISSN: 0935-9648. DOI: 10.1002/adma.202104442.

[193] R. Harding, A. Peters, and J. Nee, "New developments in FCC catalyst technology," *Applied Catalysis A: General*, vol. 221, no. 1-2, pp. 389–396, Nov. 2001, ISSN: 0926860X. DOI: 10.1016/S0926-860X(01)00814-6.

[194] A. A. Avidan, "Chapter 1 Origin, Development and Scope of Fcc Catalysis," in *Studies in Surface Science and Catalysis*, C, vol. 76, Elsevier, Jan. 1993, pp. 1–39. DOI: 10.1016/S0167-2991(08)63824-0.

[195] E. M. Flanigen, "Zeolites and molecular sieves: An historical perspective," in *Studies in Surface Science and Catalysis*, vol. 137, Elsevier, Jan. 2001, ch. 2, pp. 11–35. DOI: 10.1016/S0167-2991(01)80243-3.

[196] Z. Bao, J. Wang, Z. Zhang, *et al.*, "Molecular sieving of ethane from ethylene through the molecular cross-section size differentiation in gallate-based metal–organic frameworks," *Angewandte Chemie*, vol. 130, no. 49, pp. 16 252–16 257, Dec. 2018, ISSN: 0044-8249. DOI: https://doi.org/10.1002/ange.201808716.

[197] J. J. Spivey and G. Hutchings, "Catalytic aromatization of methane," *Chem. Soc. Rev*, vol. 43, p. 792, 2014. DOI: 10.1039/c3cs60259a.

[198] X. Wang, S. Zhu, S. Wang, *et al.*, "Low temperature hydrodeoxygenation of guaiacol into cyclohexane over Ni/SiO_2 catalyst combined with Hβ zeolite," *RSC Advances*, vol. 9, no. 7, pp. 3868–3876, 2019, ISSN: 2046-2069. DOI: 10.1039/C8RA09972C.

[199] E. A. Uslamin, H. Saito, Y. Sekine, E. J. Hensen, and N. Kosinov, "Different mechanisms of ethane aromatization over Mo/ZSM-5 and Ga/ZSM-5 catalysts," *Catalysis Today*, vol. 369, pp. 184–192, Jun. 2021, ISSN: 09205861. DOI: 10.1016/j.cattod.2020.04.021.

[200] Z. R. Ismagilov, E. V. Matus, and L. T. Tsikoza, "Direct conversion of methane on Mo/ZSM-5 catalysts to produce benzene and hydrogen: achievements and perspectives," *Energy & Environmental Science*, vol. 1, no. 5, p. 526, 2008, ISSN: 1754-5692. DOI: 10.1039/b810981h.

[201] V. Balan, D. Chiaramonti, and S. Kumar, "Review of US and EU initiatives toward development, demonstration, and commercialization of lignocellulosic biofuels," *Biofuels, Bioproducts and Biorefining*, vol. 7, no. 6, pp. 732–759, Nov. 2013, ISSN: 1932-104X. DOI: 10.1002/bbb.1436.

[202] R. Saini, C. S. Osorio-Gonzalez, K. Hegde, *et al.*, "Lignocellulosic biomass-based biorefinery: An insight into commercialization and economic standout," *Current Sustainable/Renewable Energy Reports*, vol. 7, no. 4, pp. 122–136, Dec. 2020, ISSN: 2196-3010. DOI: 10.1007/s40518-020-00157-1.

[203] Y. Sorunmu, P. Billen, and S. Spatari, "A review of thermochemical upgrading of pyrolysis bio-oil: Techno-economic analysis, life cycle assessment, and technology readiness," *GCB Bioenergy*, vol. 12, no. 1, pp. 4–18, Jan. 2020, ISSN: 1757-1693. DOI: https://doi.org/10.1111/gcbb.12658.

[204] M. Masih, I. Algahtani, and L. De Mello, "Price dynamics of crude oil and the regional ethylene markets," *Energy Economics*, vol. 32, no. 6, pp. 1435–1444, Nov. 2010, ISSN: 01409883. DOI: 10.1016/j.eneco.2010.03.009.

[205] Elena Lázaro Hernández, "Techno-economic analysis of hydrodeoxygenation of guaiacol with ethane as hydrogen donor for aromatics production," Imperial College London, Tech. Rep., 2023.

[206] W. Hu, Q. Dang, M. Rover, R. C. Brown, and M. M. Wright, "Comparative techno-economic analysis of advanced biofuels, biochemicals, and hydrocarbon chemicals via the fast pyrolysis platform," *Biofuels*, vol. 7, no. 1, pp. 57–67, Jan. 2016, ISSN: 1759-7269. DOI: 10.1080/17597269.2015.1118780.

[207] H. Zimmermann and R. Walzl, "Ethylene," in *Ullmann's Encyclopedia of Industrial Chemistry*, Weinheim, Germany: Wiley-VCH Verlag GmbH & Co. KGaA, Apr. 2009, ISBN: 9783527306732. DOI: 10.1002/14356007.a10{_}045.pub3.

[208] GloablData, *Ethylene Market Installed Capacity and Capital Expenditure, Announced Projects, 2023-2027*, 2023.

[209] GlobalData, *Propylene Market Forecast by Region & Announced Projects to 2027*, 2023.

[210] CHEMANALYST, *Methanol Market Size, Growth, Analysis & Forecast To 2032*, 2023.

[211] R. Mohammadi and M. Hadizadeh Harandi, "Methanol to olefin (MTO) value chain management," *New Applied Studies in Management, Economics & Accounting*, vol. 6, no. 1, pp. 7–17, 2023. DOI: 10.22034/nasmea.2023.176134.

[212] AgileIntel Research (ChemIntel360), "Market volume of benzene worldwide from 2015 to 2022, with a forecast for 2023 to 2030 (in million metric tons) [Graph].," *Statista*, 0.

[213] AgileIntel Research (ChemIntel360), *Market volume of toluene worldwide from 2015 to 2022, with a forecast for 2023 to 2030 (in million metric tons) [Graph]*, 0.

[214] CHEMANALYST, *Mixed Xylene Market Size, Share, Growth & Forecast, 2035*, 2023.

[215] AgileIntel Research (ChemIntel360), *Market volume of phenols worldwide from 2015 to 2022, with a forecast for 2023 to 2030 (in million metric tons) [Graph].*

[216] F. Keller, R. P. Lee, and B. Meyer, "Life cycle assessment of global warming potential, resource depletion and acidification potential of fossil, renewable and secondary feedstock for olefin production in Germany," *Journal of Cleaner Production*, vol. 250, p. 119 484, Mar. 2020, ISSN: 09596526. DOI: 10.1016/j.jclepro.2019.119484.

[217] O. Mynko, I. Amghizar, D. J. Brown, *et al.*, "Reducing CO_2 emissions of existing ethylene plants: Evaluation of different revamp strategies to reduce global CO2 emission by 100 million tonnes," *Journal of Cleaner Production*, vol. 362, p. 132 127, Aug. 2022, ISSN: 09596526. DOI: 10.1016/j.jclepro.2022.132127.

[218] T. P. Vispute, H. Zhang, A. Sanna, R. Xiao, and G. W. Huber, "Renewable chemical commodity feedstocks from integrated catalytic processing of pyrolysis oils," *Science*, vol. 330, no. 6008, pp. 1222–1227, Nov. 2010, ISSN: 00368075. DOI: 10.1126/SCIENCE.1194218/SUPPL{_}FILE/VISPUTE.SOM.PDF.

[219] Y. Zhang, T. R. Brown, G. Hu, and R. C. Brown, "Techno-economic analysis of two bio-oil upgrading pathways," *Chemical Engineering Journal*, vol. 225, pp. 895–904, Jun. 2013, ISSN: 13858947. DOI: 10.1016/j.cej.2013.01.030.

[220] K. Wang, L. Ou, T. Brown, and R. C. Brown, "Beyond ethanol: a techno-economic analysis of an integrated corn biorefinery for the production of hydrocarbon fuels and chemicals," *Biofuels, Bioproducts and Biorefining*, vol. 9, no. 2, pp. 190–200, Mar. 2015, ISSN: 1932-104X. DOI: 10.1002/bbb.1529.

[221] K. S. Ng and E. Martinez-Hernandez, "Techno-economic assessment of an integrated bio-oil steam reforming and hydrodeoxygenation system for polygeneration of hydrogen, chemicals, and combined heat and power production," in *Towards Sustainable Chemical Processes*, Elsevier, Jan. 2020, pp. 69–98. DOI: 10.1016/B978-0-12-818376-2.00003-X.

[222] Z. Xiong, S. S. A. Syed-Hassan, X. Hu, *et al.*, "Pyrolysis of the aromatic-poor and aromatic-rich fractions of bio-oil: Characterization of coke structure and elucidation of coke formation mechanism," *Applied Energy*, vol. 239, pp. 981–990, Apr. 2019, ISSN: 03062619. DOI: 10.1016/j.apenergy.2019.01.253.

[223] R. Vincent, R. Lindstedt, N. Malik, I. Reid, and B. Messenger, "The chemistry of ethane dehydrogenation over a supported platinum catalyst," *Journal of Catalysis*, vol. 260, no. 1, pp. 37–64, Nov. 2008, ISSN: 00219517. DOI: 10.1016/j.jcat.2008.08.014.

[224] E. Gobina, K. Hou, and R. Hughes, "Ethane dehydrogenation in a catalytic membrane reactor coupled with a reactive sweep gas," *Chemical Engineering Science*, vol. 50, no. 14, pp. 2311–2319, Jul. 1995, ISSN: 00092509. DOI: 10.1016/0009-2509(95)00059-E.

[225] A. Avila, Z. Yu, S. Fazli, J. Sawada, and S. Kuznicki, "Hydrogen-selective natural mordenite in a membrane reactor for ethane dehydrogenation," *Microporous and Mesoporous Materials*, vol. 190, pp. 301–308, May 2014, ISSN: 13871811. DOI: 10.1016/j.micromeso.2014.02.024.

[226] E. V. Shelepova and A. A. Vedyagin, "Intensification of the dehydrogenation process of different hydrocarbons in a catalytic membrane reactor," *Chemical Engineering and Processing - Process Intensification*, vol. 155, p. 108 072, Sep. 2020, ISSN: 02552701. DOI: 10.1016/j.cep.2020.108072.

[227] E. V. Shelepova and A. A. Vedyagin, "Theoretical prediction of the efficiency of hydrogen production via alkane dehydrogenation in catalytic membrane reactor," *Hydrogen*, vol. 2, no. 3, pp. 362–376, Sep. 2021, ISSN: 2673-4141. DOI: 10.3390/hydrogen2030019.

[228] P. Ciavarella, D. Casanave, H. Moueddeb, S. Miachon, K. Fiaty, and J.-A. Dalmon, "Isobutane dehydrogenation in a membrane reactor," *Catalysis Today*, vol. 67, no. 1-3, pp. 177–184, May 2001, ISSN: 09205861. DOI: 10.1016/S0920-5861(01)00311-X.

[229] B.-H. Jeong, K.-I. Sotowa, and K. Kusakabe, "Catalytic dehydrogenation of cyclohexane in an FAU-type zeolite membrane reactor," *Journal of Membrane Science*, vol. 224, no. 1-2, pp. 151–158, Oct. 2003, ISSN: 03767388. DOI: 10.1016/j.memsci.2003.08.004.

[230] J. K. Ali, E. Newson, and D. Rippin, "Exceeding equilibrium conversion with a catalytic membrane reactor for the dehydrogenation of methylcyclohexane," *Chemical Engineering Science*, vol. 49, no. 13, pp. 2129–2134, Jul. 1994, ISSN: 00092509. DOI: 10.1016/0009-2509(94)E0035-O.

[231] W.-H. Lin and H.-F. Chang, "A study of ethanol dehydrogenation reaction in a palladium membrane reactor," *Catalysis Today*, vol. 97, no. 2-3, pp. 181–188, Oct. 2004, ISSN: 09205861. DOI: 10.1016/j.cattod.2004.03.068.

Chapter A

Experimental

This chapter includes supplementary information on the experimental activities including physical properties, instrumentation and experiment design. Section A.1 includes supplementary information regarding the experimental setup. Section A.2 highlights the physical properties of involved chemicals.

A.1 Hydrocracker

A.1.1 Hydrocracker setup

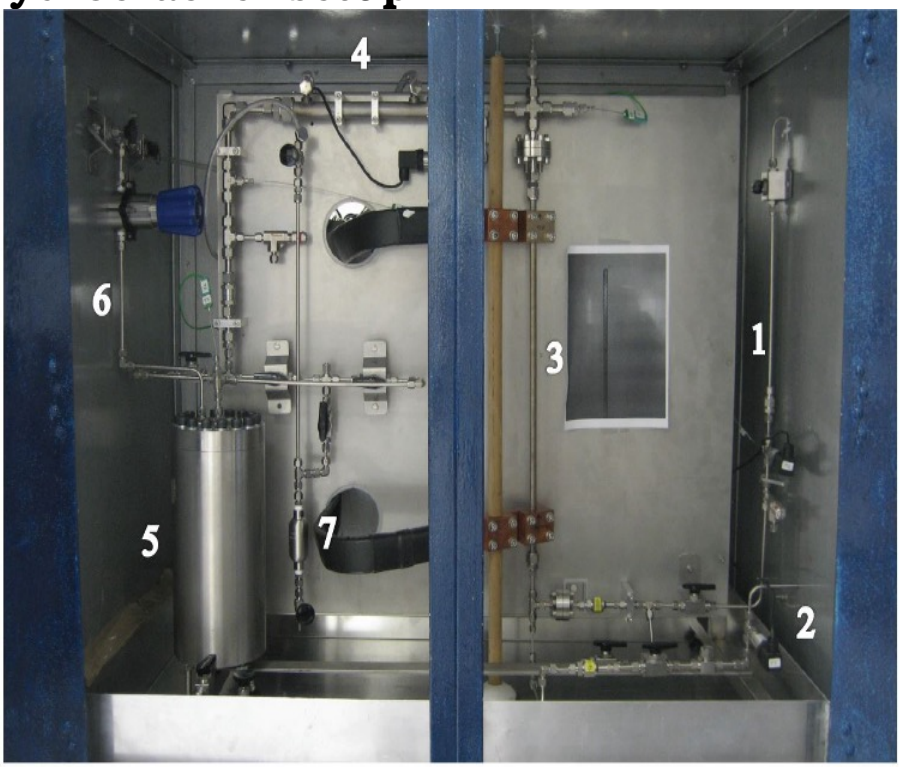


Figure A.1: Picture of hydrocracker setup for parts inside the cabinet

A.1.2 Control system

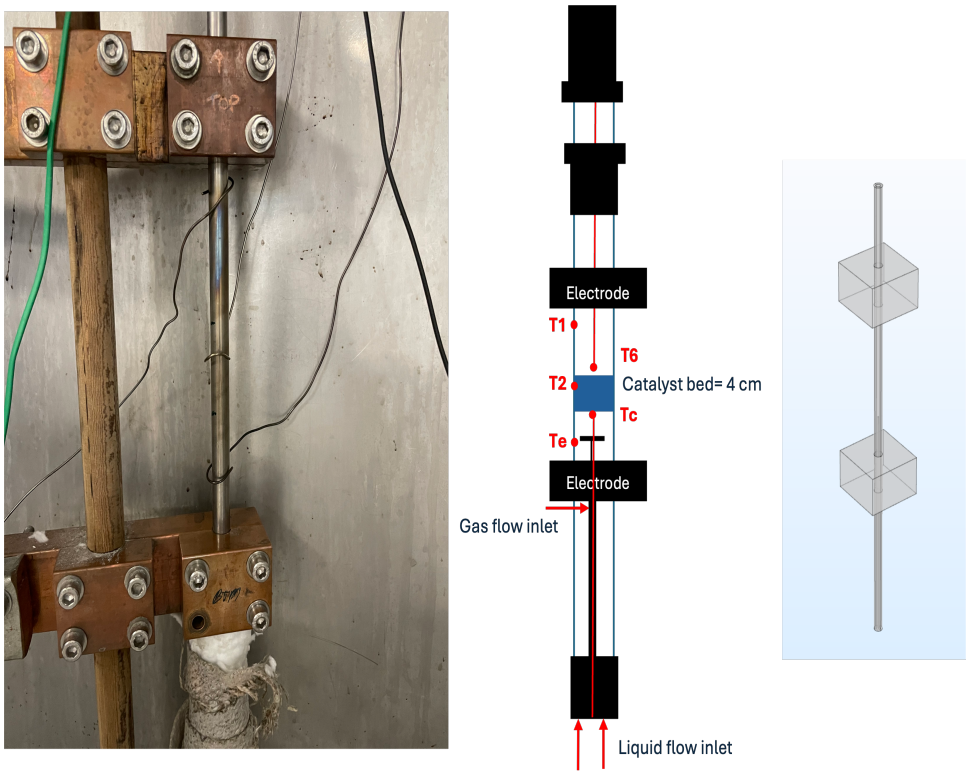


Figure A.2: [Left] Experiment Hydrocracker reactor zone [Middle] a schematic indicating thermocouples' positions and catalyst bed [Left] COMSOL built reactor model.

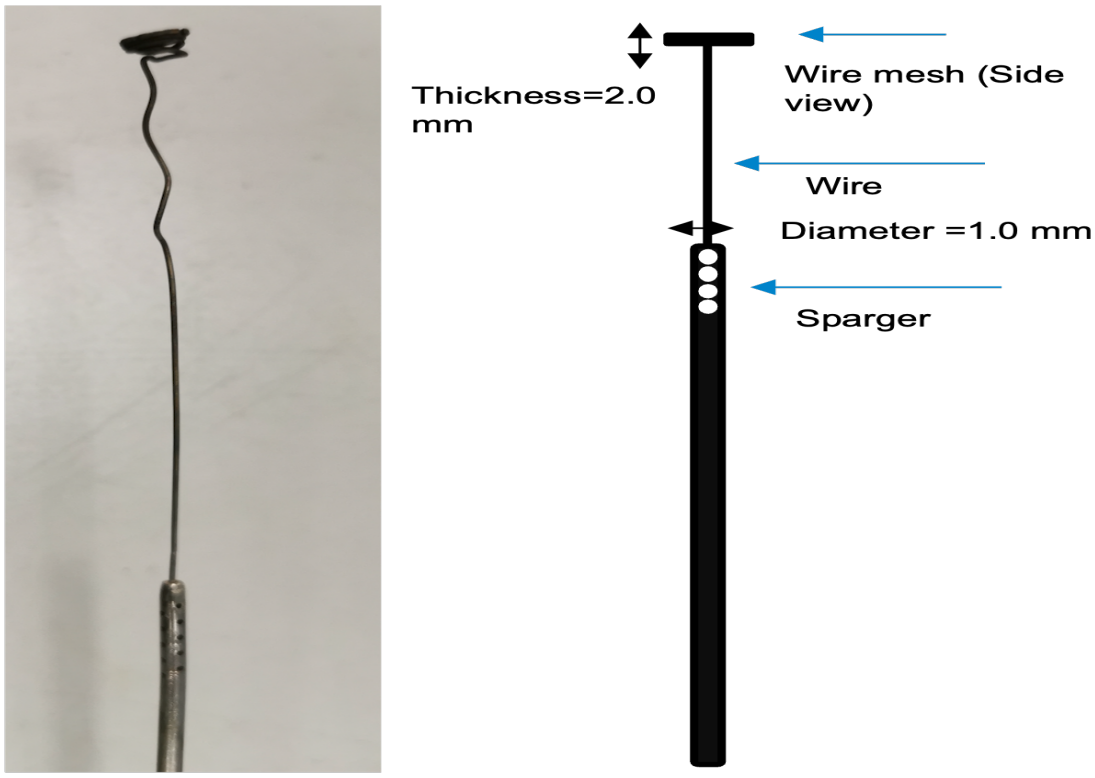


Figure A.3: Gas flow sparger positioned inside the reactor below the catalyst bed

A.2 Physical properties for involved reactants and products

Below tables summaries the physical properties for the chemicals involved in liquid product, as shown in Table A.2 for solvents and Table A.3 for aromatics and oxygenated aromatic

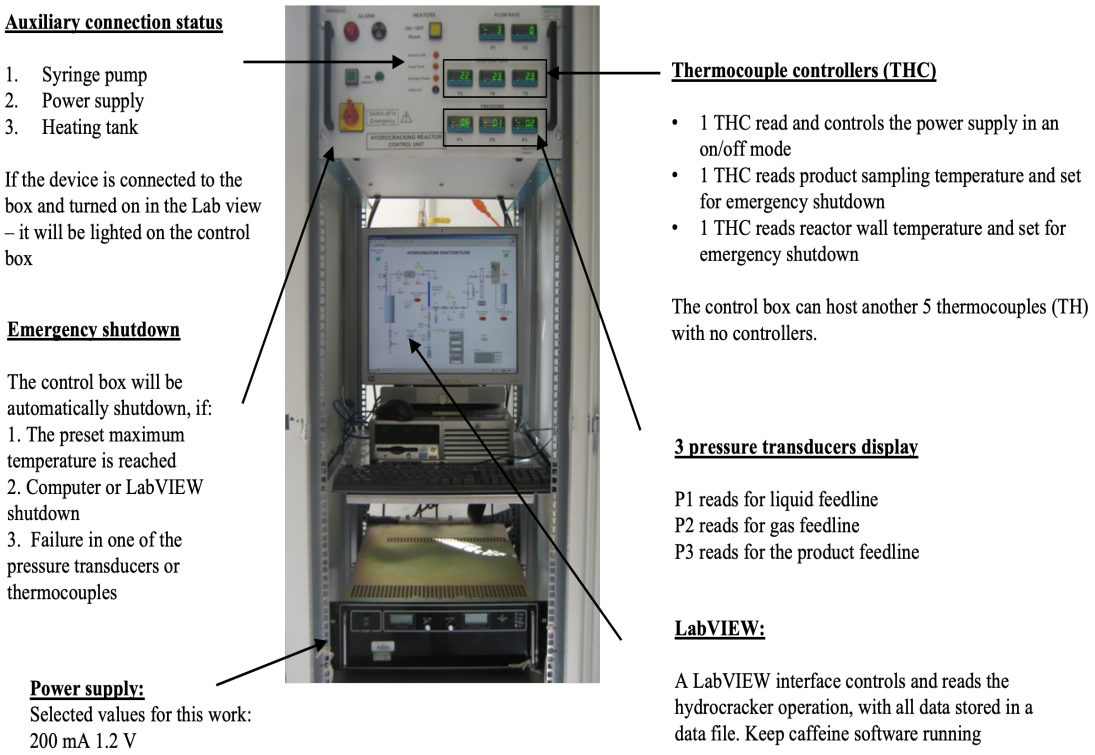


Figure A.4: Hydrocracker control box and LabVIEW interface

compounds, and gas mixture, as shown in Table A.1.

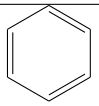
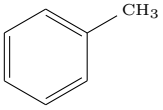
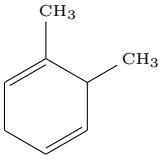
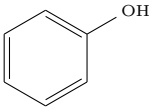
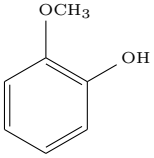
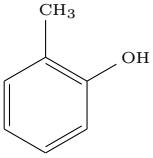
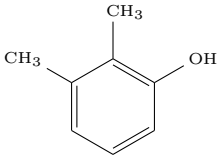
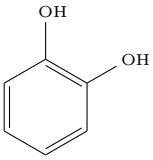
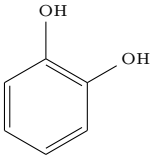
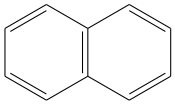
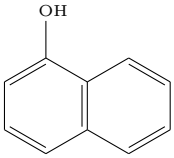
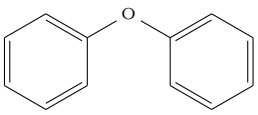
Table A.1: Properties of all chemicals observed in gas phase at standard operating condition

Chemical	Component	MW $g{\cdot}mol^{-1}$	ρ g/L	λ (W/m · K)
Nitrogen	N_2	28.02	1.251	0.0258
Hydrogen	H_2	2.02	0.0899	0.1805
Methane	CH_4	16.04	0.717	0.0312
Carbon Monoxide	CO	28.01	1.165	0.0152
Carbon Dioxide	CO_2	44.01	1.977	0.0147
Ethane	C_2H_6	30.07	1.356	0.0221
Ethylene	C_2H_4	28.05	1.250	0.0188
Propane	C_3H_8	44.10	1.882	0.0159
Propylene	C_3H_6	42.08	1.447	0.0184
Butene	C_4H_8	56.11	2.490	0.0150

Table A.2: Properties of the main non-aromatic chemicals and solvent observed in liquid phase at standard operating condition

Chemical	Structure	MW $g{\cdot}mol^{-1}$	ρ $g{\cdot}mL^{-1}$	BP °C	MP °C
Acetone	C_3H_6O	58.08	0.785	56.3	-94.7
Methanol	$CH_3 — OH$	32.04	0.791	64.7	-97.7
Ethanol	$CH_3 — CH_2 — OH$	46.07	0.789	78.4	-114.1
Chloroform	$CHCl_3$	119.38	1.489	61.2	-63.5

Table A.3: Properties of the main chemicals observed in liquid phase at standard operating condition

Chemical	Structure	MW $g{\cdot}mol^{-1}$	ρ $g{\cdot}mL^{-1}$	BP °C	MP °C
Benzene		78.11	0.879	80.1	5.5
Toluene		92.14	0.866	110.6	-93
Xylene		106.17	0.864	138.5	-47.8
Phenol		94.11	1.071	181.7	40.9
Guaiacol		124.14	1.129	205	26
Cresol		108.14	1.04	191	30
Methyl Cresol		136.18	1.02	218	18
Catechol		110.11	1.34	245	104
Methyl Catechol		122.14	1.24	239	38
Naphthalene		128.18	1.14	218	80.2
Naphthalenol		144.2	1.14	280	71.0
Diphenyl ether		170.2	1.07	258.6	26.9

A.3 Reactor model

The reactor model was constructed with a catalytic zone which is built based on $NiMo/Al_20_3$.

The thermal and electrical characteristics of the porous medium within the model were as-

sessed using parameters outlined in Table A.4, accounting for volume percentage. These properties were considered invariant across the temperature range of the investigation, spanning from 50 to 550 °C. Furthermore, a porosity value of 0.75 was assigned to the catalytic bed.

Table A.4: Parameters used for defining the catalytic bed parameters in COMSOL

	wt%	ρ (g·cm^{-3})	vol%	λ (W·m-k^{-1})	Cp (J·kg-K^{-1})
NiO	10	6.67	6.60	5.0	450
MoO_3	35	4.69	32.8	2.0	290
Al_2O_3	55	3.99	60.6	30	900

Chapter B

Analytical Instrument

This chapter includes specification, parameters and calibration information for the analytic instruments used in this work for gas, liquid and solid products.

B.1 Gas analysis (GC-TCD)

The gas samples are analysed using PerkinElmer's Clarus 500 gas chromatography (GC) equipped with a TCD detector and a capillary column. The column is Carboxen TM 1010 PLOT supplied from SUPELCO. The column dimension is 30 m long and 0.32 mm in diameter. With a flow rate of 4.0 mL·min^{-1}, Ar is selected as the carrier gas to detect all expected components, including hydrogen. The detector and injector temperatures are both set to 150 °C. To ensure components detection and excellent separation, the developed analysis method is set to an initial oven temperature of 35 °C, with a ramp-up rate of 15 °C·min^{-1} until 230 °C. The temperature is then maintained at this temperature for 10 min. Pure gases and calibration mixtures are tested to develop calibration curves for the target gases with low and high volumetric injections ranges up to 250 uL (the maximal syringe volume). Table B.1 contains the composition of the calibration mixtures used. Since ethane is the target gas feedstock, TCD response factors are factored against ethane to normalise the total area. Table B.2 contains the factors utilised in this study. Periodically, these calibration factors have been reviewed to ensure reliable results. An example of TCD chromatogram appears in Figure B.2.

B.2 GC-FID

Liquid samples are analysed on a Clarus 500 gas chromatography from PerkinElmer equipped with an FID detector and HT5 column from SGE. The column has length, diameter, and thickness of 25 m, 0.32 mm and 0.1 um, respectively. The method developed for FID analysis is based on a sample injection of 1.0 um with argon as career gas at a flow rate of 4.0 mL·min^{-1}. The FID's injector and detector temperatures are set to 150 and 280 °C, respec-

Table B.1: TCD calibration mixtures used in this work to develop TCD calibration curves for target gases.

Component	Mixture 1 (vol%)	Mixture 2 (vol%)	Mixture 3 (vol%)	Mixture 4 (vol%)
He	-	Balanced (26)	-	-
Ar	-	-	-	-
N_2	Balanced (27)	-	-	-
H_2	20	20	5	30
CO	5	20	5	15
CO_2	1	20	Balanced (55)	Balanced (54)
CH_4	1	10	-	1
C_2H_4	-		-	-
C_2H_6	-	1	-	-
C_3H_6	-	1	10	-
C_3H_8	-	1	25	-
C_4H_{10}	-	1	-	-

Table B.2: TCD calibration factors used to quantify the gas composition.

Hydrocarbons	Factor
H_2	0.45
C_2H_2	1.40
C_2H_4	1.33
C_2H_6	1.0
C_3H_6	0.9
CH_4	2.24
C_3H_8	0.69
C_4H_{10}	.54



Figure B.1: Picture of used GC with a TCD detector for gas analysis

tively. The sample's components are separated within a heated column located inside an oven. The oven is configured to initiate at a temperature of 40 °C and gradually increase

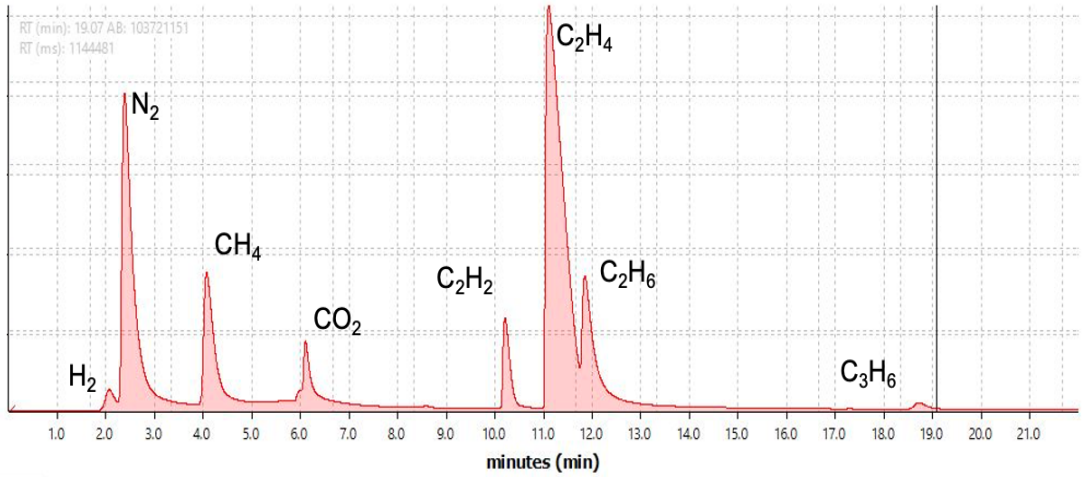


Figure B.2: An example of GC-TCD chromatogram

to 280 °C at a rate of 20 °C·min^{-1}. In order to ensure the detection of the components, the analysis is extended for an additional 20 min at a temperature of 280 °C. Calibration curves are created for the predicted components to ensure precise quantification.

The peaks observed in the FID spectrum are classified into eight groups based on their retention time as indicated in Table B.3. An example of a GC-FID spectrum evaluated using OpenChrom software is depicted in Figure B.4. All peaks appear before the predominant feed, guaiacol, are associated with component containing less than two oxygen atoms per aromatic ring. Conversely, the subsequent peaks after guaiacol's peak are mostly associated with the presence of two oxygen atoms per aromatic ring.

Table B.3: TCD calibration factors used to quantify the gas composition.

Group	Group/Component	1	2	3
1	BTX	Benzene (5.0)	Toluene (6.0)	Xylenes and ethylbenzene (6.0-7.6)
2	Anisole	8.1	-	-
3	Cresol+ methyl cresol	8.2<-9.4	9.5	-
4	Phenol	7.6	-	-
5	GUA	9.4		-
6	Catechol	9.9	-	-
7	Methyl catechol + methyl anisole	10-16	-	-
8	Heavy	16.4 and beyond	-	-

B.3 GC-MS

Figure B.5 shows the instruments used for compound identification.



Figure B.3: Picture of used GC with a FID detector for liquid analysis

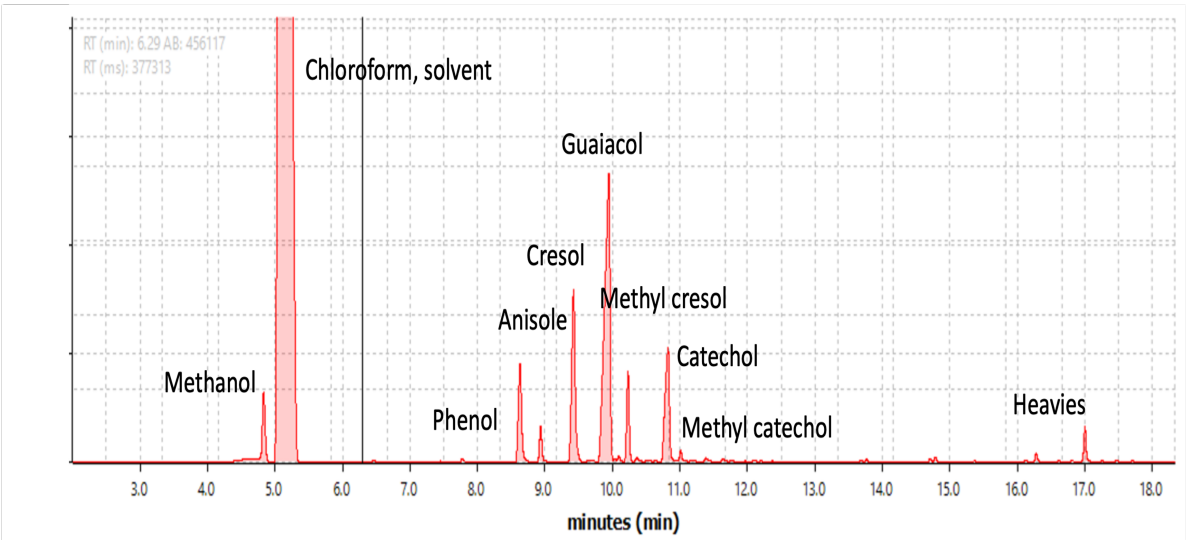


Figure B.4: An example of GC-FID chromatogram

B.4 Thermogravimetric analysis (TGA)

This work uses TGA to quantify two phenomena from a 5-10 mg spent catalyst sample : (1) condensate adsorbed at the catalyst surface and (2) the extent of coke deposition. The former is expected to desorbed from the catalyst surface at high temperatures in an inert environment, whereas the latter requires an oxidant to combust deposited coke. Therefore, the developed method for TGA runs involves gradually heating the catalyst sample to 500 °C at a heating rate of 15 °C·min^{-1}, and thereafter holding the temperature for 5 min. Further, a gradual rise in temperature to 850 °C at a heating rate of 15 °C·min^{-1} is employed under an airflow of 40 mL·min^{-1} for combusting deposited coke. Finally, the temperature is held

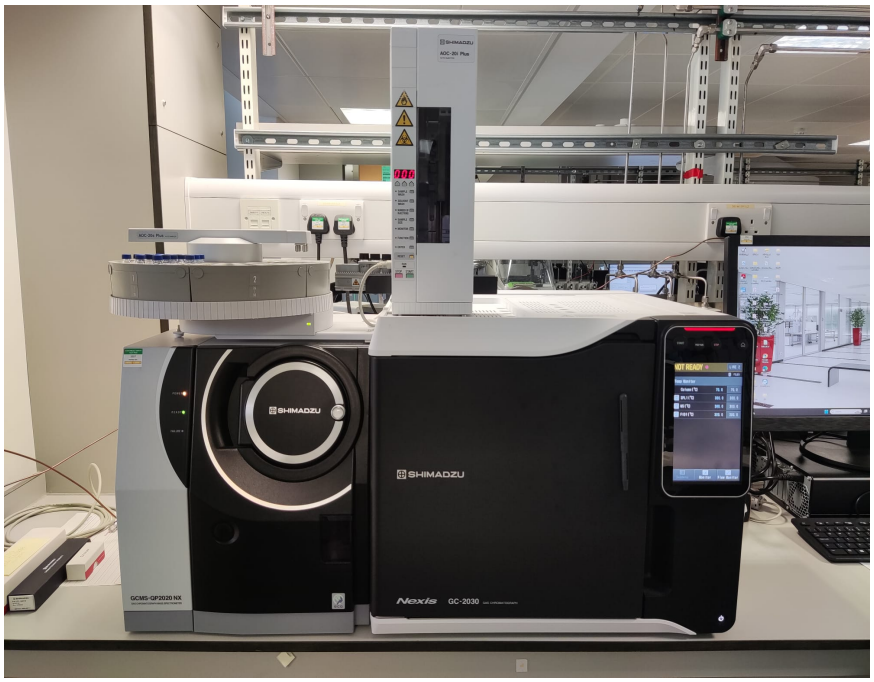


Figure B.5: Picture of used GC with MS and FID detectors for liquid compound identification

at at 850 °C for further combustion for 10 min to ensure the complete removal of carbon deposition before ending the analysis.

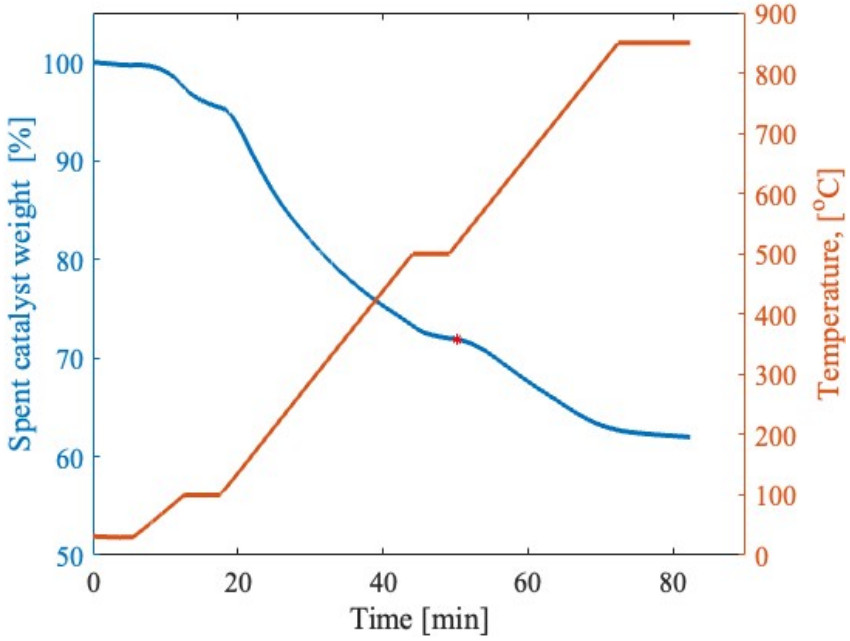


Figure B.6: An example of TGA results

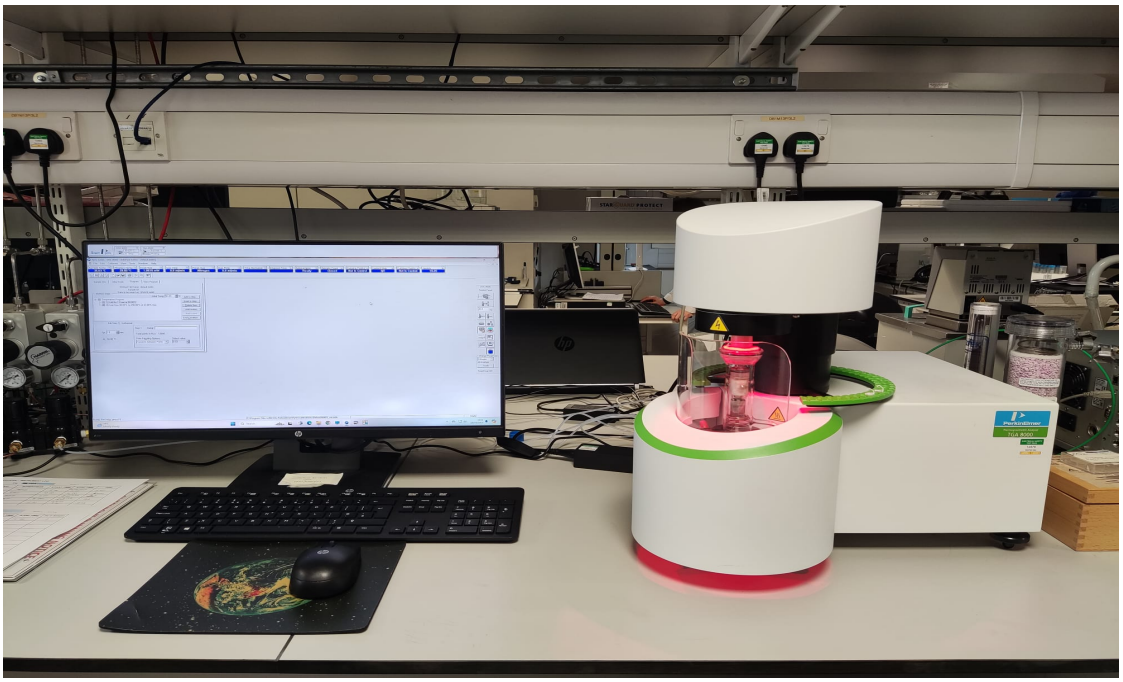


Figure B.7: Picture of used for spent catalyst analysis

B.5 BET

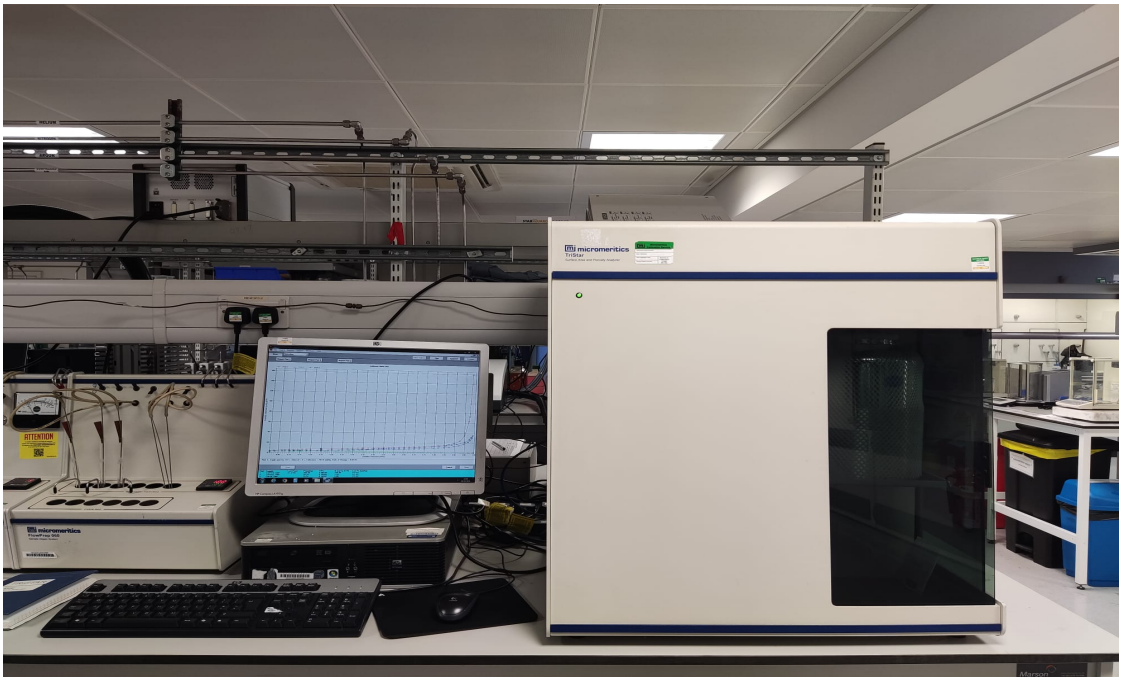


Figure B.8: Picture of used BET for catalyst surface analysis

B.6 XRF

Figure B.9 shows the XRF unit used for analysing supplied and synthesised catalysts.



Figure B.9: Picture of used XRF for catalyst composition analysis

B.7 TGA-MS

The gaseous effluent of the TGA was examined using MS to verify the complete combustion of coke deposits on the catalyst's surface as well as the subsequent oxidation of active sites. Figure B.10 illustrates a sample of analysed TGA data, with the asterisk indicating the moment when the nitrogen flow is changed to air for combustion. The steady rate of weight loss at the end suggests that all of the coke has been completely burned. This is further confirmed by evaluating the effluent using MS, as shown in reference B.10, where the absence of carbon dioxide production is observed after 18 min.

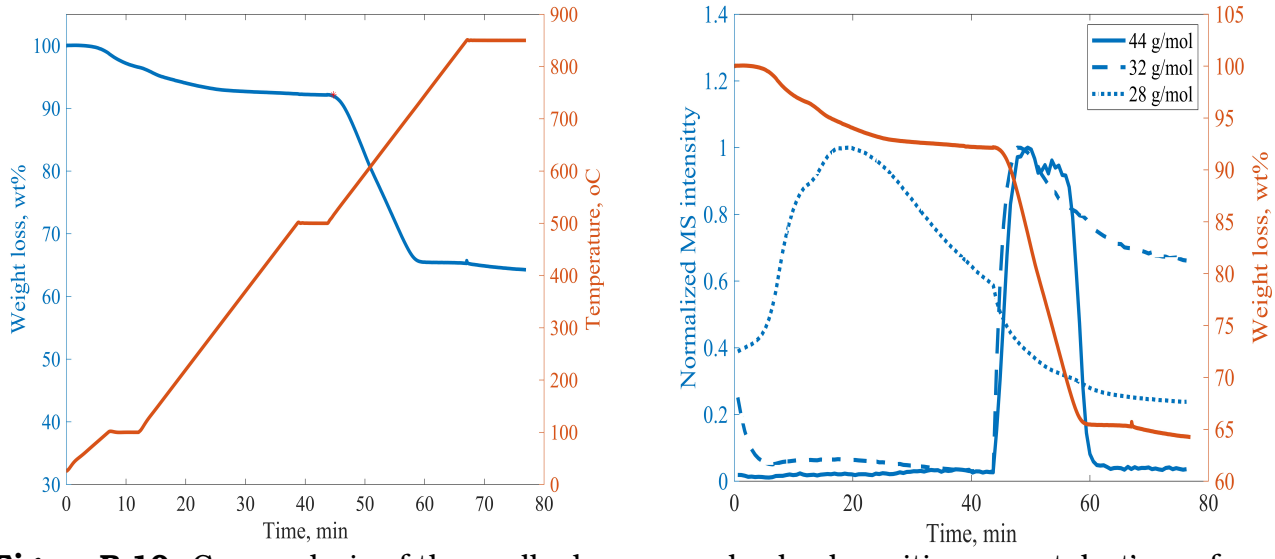


Figure B.10: Gas analysis of thermally decomposed coke deposition on catalyst's surface

B.8 Catalyst calcination

Zeolite-supported catalysts were subjected to a calcination step using thermogravimetric analysis (TGA) to identify the optimal calcination temperature for the synthesis process, as seen in Figure B.11. The weight change stabilises at around 550 °C, suggesting that the calcination temperature employed in this study at 600 °C for four is sufficient for active site and support interaction.

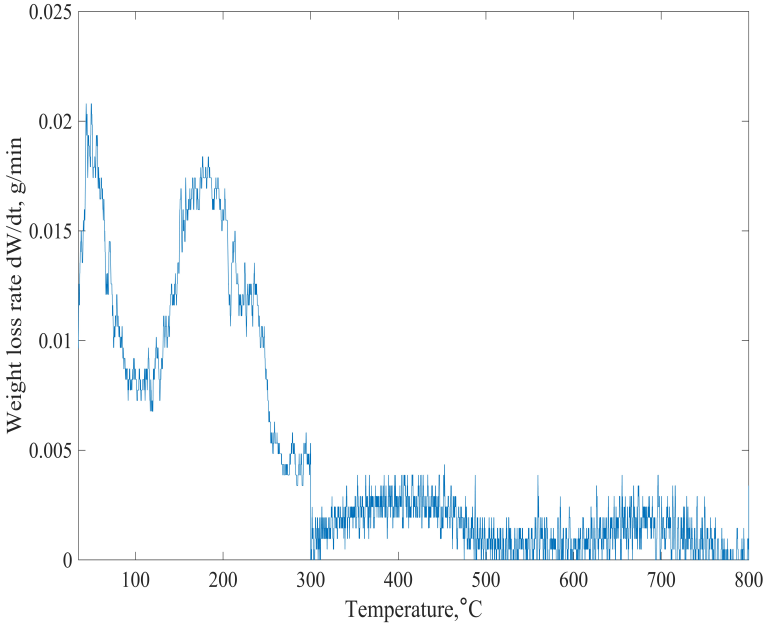


Figure B.11: Weight loss during catalyst calcination for zeolite-supported catalysts

Chapter C

Process development and techno-economic supplementary information

This section includes supplementary information of Chapter 7 including flowsheet, and used mathematical equation for assessing DeH-HDO. The assessment is designed for integrating (1) DeH-HDO with SC, and (2) DeH-HDO with FCC.

C.1 Aspen process flow sheet

C.1.1 The integration of DeH-HDO with SC process

Developed flowsheet, in Figure C.1, for \ac{DeH-HDO} based on integrating SC with DeH-HDO. The process is mainly developed into two sections: DeH-HDO conversion and separation trains. The flowsheet separation trains section is synthesised based on SC process. The additional HDO liquid separation is presented by two columns in the flowsheet to reflect the results on another dedicated flowsheet developed by [205]. Compression, liquid/gas separation, and combustion are included in the separation section. The SC is designed to process ethane with 1,100 kta, with an ethane-cut for DeH-HDO. The separation section for HDO liquid is synthesised by another work [205], and the gas product separation follows ethane SC separation trains, which consists of de-methanizer, de-ethanizer, C_2 splitter, de-propanizer, and C_3 splitter columns as well as hydrogenation reactor. Function of unit operation and main process parameters are listed in Table C.1.1.

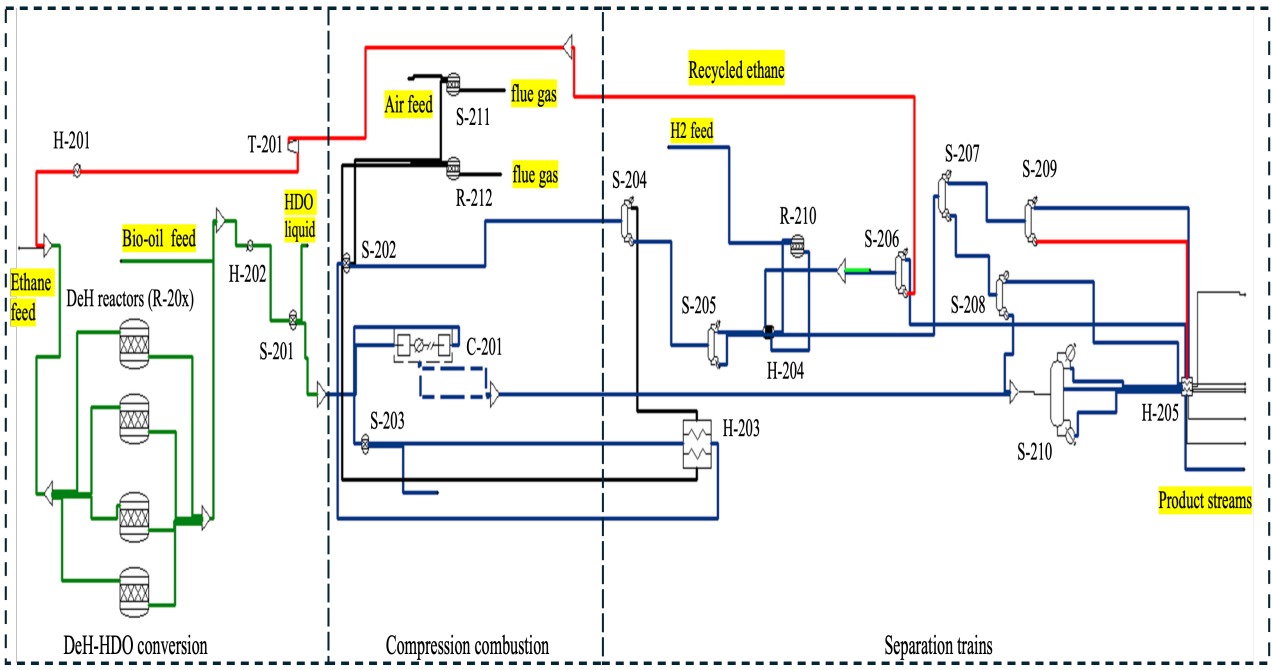


Figure C.1: Aspen developed flowsheet for DeH-HDO based on experimental findings

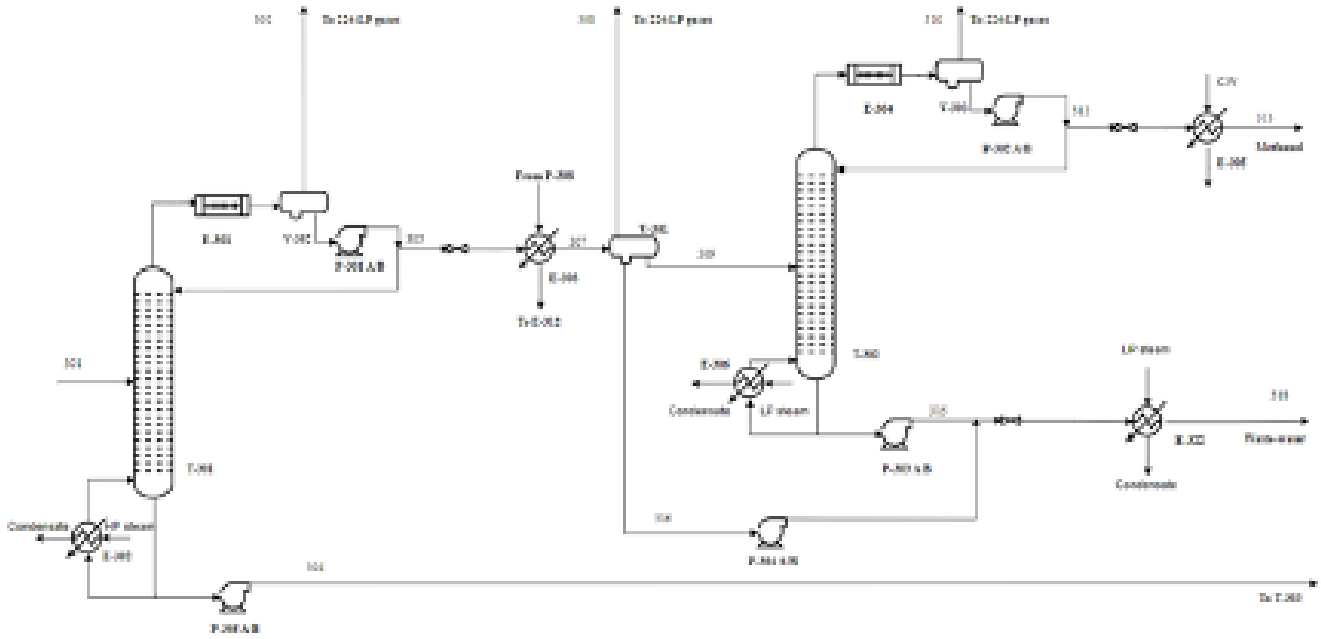


Figure C.2: PFD for HDO separation section (Adopted from [205])

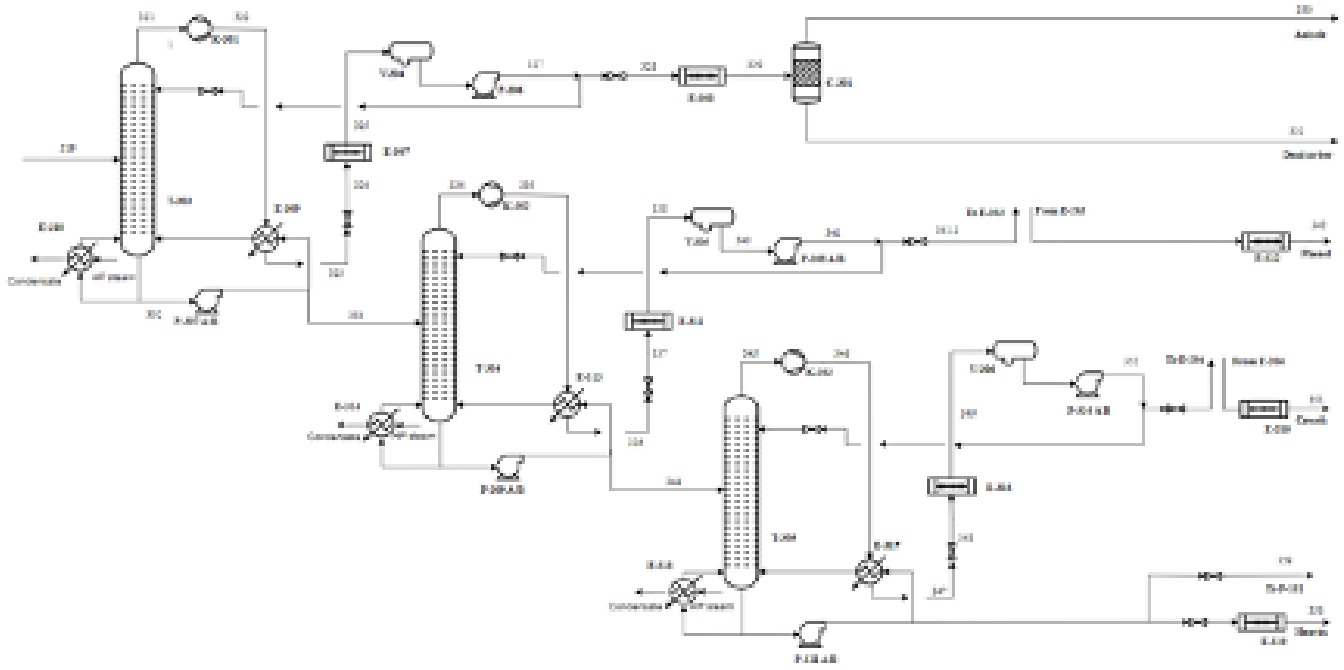


Figure C.3: Continued PFD for HDO separation section (Adopted from [205])

Table C.1: Main nit operation list of DeH-HDO integrated with SC

Label	unit	function	Parameter 1	Parameter 2	Parameter 3
C-101	3-stage compressor	Increase the pressure of conversion section product for separation	31.4 bar	Isentropic model	between stage cooling
T-101	Expander	Reduce the recycle alkane pressure	Isentropic model	1-2.2 bar	
R-101	Steam cracker	steam cracking of ethane	900 °C	2.2 barg	0.5 mol/mol steam-to-HC
R-102	DeH-HDO reactor	Ethane and guaiacol conversion	600 °C	1.0 barg	isothermal
R-110	Hydrogenator	Convert acetylene to ethylene	100 °C	Complete conversion	Selective to ethylene
R-111	Burner	H_2 combustion	800 °C	atmospheric pressure	complete conversion
R-112	Burner	CH_4 combustion	800 °C	atmospheric pressure	complete conversion
S-101	Steam separator	Remove steam from hydrocarbon stream			
S-102	HDO liquid sep.				
S-103					
S-104	Hydrogen extraction	Extract hydrogen from produced hydrocarbon mixture			
S-105	De-methanizer	Extract methane from produced hydrocarbon mixture	Condenser pressure 26 bar	RR= 50	
S-106	De-ethanizer	Extract ethane and ethylene from produced hydrocarbon mixture			
S-107	C_2 splitter	Separate ethylene with 99.9% purity from unreacted ethane	Cryogenic model	Condenser 16 bar	Controlled by ethylene purity
S-108	De-propanizer	Extract propane and propylene from produced hydrocarbon mixture			
S-109	C_3 splitter	Separate propylene with 99.9% from unreacted propane	Cryogenic model	115 stages	condenser 6.0 bar

Figure C.4: Aspen developed flowsheet for improved DeH-HDO with improved process performance based on published findings for HDO

Parameter	Unit	Fresh ethane	Recycle ethane	Ethane feed	Ethane to SC	Steam to SC	Ethane to DeH-HDO	Bio-oil to DeH-HDO	Gas product HDO	Liquid product HDO	Mix gas	Compressed	HC	Fuel gas 1	C1+	Fuel gas 2	C2	C2+	Ethylene	Recycle ethane	Propylene	Propane	C3+
		1	2	3	4	5	6	7	8	9	10	11	12	13	14	15	16	17	18	19	20	21	22
Temperature	C	45.0	-18.1	20.4	20.4	35.0	20.4	35.0	600.0	600.0	-220.8	-238.2	-228.2	-228.2	-283.6	-362.5	-285.8	-199.9	-228.2	-290.5	-278.3	-244.8	-242.9
Pressure	bar	1.0	3.0	1.0	1.0	1.0	1.0	1.0	1.0	1.0	1.0	31.4	31.4	31.4	26.0	26.0	25.0	25.0	16.0	16.0	6.0	6.0	9.0
Mass Liquid Fraction	-	0.0	0.0	0.0	0.0	1.0	0.0	1.0	0.0	0.0	0.0	0.0	0.0	0.0	1.0	0.0	1.0	1.0	0.0	1.0	1.0	1.0	0.7
Mass Enthalpy	MJ/kg	-2.8	-2.6	-2.7	-2.7	-15.9	-2.7	-2.5	-1.0	-0.5	-0.3	-0.3	-0.4	0.3	-0.6	-4.3	-0.6	-0.2	1.9	-3.0	-0.1	-0.6	-0.2
Mass Entropy	kJ/kg-K	-5.7	-5.7	-5.7	-5.7	-5.7	-5.7	-5.7	-5.7	-5.7	-5.7	-5.7	-5.7	-5.7	-5.7	-5.7	-5.7	-5.7	-5.7	-5.7	-5.7	-5.7	-5.7
Mass Density	kg/cum	1.1	4.4	1.2	1.2	984.3	1.2	1118.7	0.3	0.9	0.7	24.7	41.0	2.4	413.6	41.3	413.6	541.4	18.6	436.1	545.8	705.4	53.6
Enthalpy Flow	MW	-141.5	-85.9	-227.4	-204.7	-590.7	-22.7	-119.5	-3.7	-26.8	-20.8	-26.4	-27.0	0.9	-39.6	-16.8	-39.3	-0.3	71.3	-98.8	0.0	-0.2	-0.2
Mole Flows	kmol/hr	6152.4	3928.8	10081.2	9073.1	7410.9	1008.1	1388.0	604.6	2724.9	14933.4	14933.4	9596.8	5336.7	8760.8	836.0	8654.9	105.9	4726.1	3928.8	28.1	24.9	52.9
Mass Flows	tonne/hr	185.0	117.7	302.7	272.4	133.5	30.3	172.3	12.9	181.3	280.2	280.2	269.5	10.8	255.5	14.0	250.1	5.4	132.5	117.7	1.2	1.5	2.7
Mass Fractions	-																						
ETHANE	frac	1.00	0.95	0.98	0.98	0.00	0.98	0.00	0.48	0.00	0.40	0.40	0.41	0.00	0.44	0.00	0.45	0.02	0.00	0.95	0.05	0.00	0.02
ETHENE	frac	0.00	0.05	0.02	0.02	0.00	0.02	0.00	0.12	0.00	0.49	0.49	0.51	0.00	0.53	0.10	0.54	0.00	0.99	0.05	0.00	0.00	0.00
HYDROGEN	frac	0.00	0.00	0.00	0.00	0.00	0.00	0.00	0.01	0.00	0.04	0.04	0.00	1.00	0.00	0.00	0.00	0.00	0.00	0.00	0.00	0.00	0.00
BENZENE	frac	0.00	0.00	0.00	0.00	0.00	0.00	0.00	0.00	0.00	0.01	0.01	0.01	0.00	0.01	0.00	0.00	0.37	0.00	0.00	0.00	0.64	0.37
METHANE	frac	0.00	0.00	0.00	0.00	0.00	0.00	0.00	0.32	0.00	0.05	0.05	0.05	0.00	0.00	0.90	0.00	0.00	0.00	0.00	0.00	0.00	0.00
CARBON	frac	0.00	0.00	0.00	0.00	0.00	0.00	0.00	0.00	0.00	0.00	0.00	0.00	0.00	0.00	0.00	0.00	0.00	0.00	0.00	0.00	0.00	0.00
1-MN	frac	0.00	0.00	0.00	0.00	0.00	0.00	0.00	0.00	0.00	0.00	0.00	0.00	0.00	0.00	0.00	0.00	0.00	0.00	0.00	0.00	0.00	0.00
1-MNH2	frac	0.00	0.00	0.00	0.00	0.00	0.00	0.00	0.00	0.00	0.00	0.00	0.00	0.00	0.00	0.00	0.00	0.00	0.00	0.00	0.00	0.00	0.00
GUAIACOL	frac	0.00	0.00	0.00	0.00	0.00	0.00	1.00	0.00	0.00	0.00	0.00	0.00	0.00	0.00	0.00	0.00	0.00	0.00	0.00	0.00	0.00	0.00
PHENOL	frac	0.00	0.00	0.00	0.00	0.00	0.00	0.00	0.00	0.24	0.00	0.00	0.00	0.00	0.00	0.00	0.00	0.00	0.00	0.00	0.00	0.00	0.00
TOLUENE	frac	0.00	0.00	0.00	0.00	0.00	0.00	0.00	0.00	0.00	0.00	0.00	0.00	0.00	0.00	0.00	0.00	0.00	0.00	0.00	0.00	0.00	0.00
ANISOLE	frac	0.00	0.00	0.00	0.00	0.00	0.00	0.00	0.00	0.02	0.00	0.00	0.00	0.00	0.00	0.00	0.00	0.00	0.00	0.00	0.00	0.00	0.00
XYLENE	frac	0.00	0.00	0.00	0.00	0.00	0.00	0.00	0.00	0.00	0.00	0.00	0.00	0.00	0.00	0.00	0.00	0.00	0.00	0.00	0.00	0.00	0.00
CRESOL	frac	0.00	0.00	0.00	0.00	0.00	0.00	0.00	0.00	0.27	0.00	0.00	0.00	0.00	0.00	0.00	0.00	0.00	0.00	0.00	0.00	0.00	0.00
CATACHOL	frac	0.00	0.00	0.00	0.00	0.00	0.00	0.00	0.00	0.00	0.00	0.00	0.00	0.00	0.00	0.00	0.00	0.00	0.00	0.00	0.00	0.00	0.00
WATER	frac	0.00	0.00	0.00	0.00	1.00	0.00	0.00	0.00	0.06	0.00	0.00	0.00	0.00	0.00	0.00	0.00	0.00	0.00	0.00	0.00	0.00	0.00
METHANOL	frac	0.00	0.00	0.00	0.00	0.00	0.00	0.00	0.00	0.15	0.00	0.00	0.00	0.00	0.00	0.00	0.00	0.00	0.00	0.00	0.00	0.00	0.00
PROPANE	frac	0.00	0.00	0.00	0.00	0.00	0.00	0.00	0.07	0.00	0.00	0.00	0.00	0.00	0.00	0.00	0.00	0.20	0.00	0.00	0.00	0.36	0.20
PROPYLEN	frac	0.00	0.00	0.00	0.00	0.00	0.00	0.00	0.00	0.00	0.01	0.01	0.01	0.00	0.01	0.00	0.00	0.41	0.00	0.00	0.95	0.00	0.41
ACE	frac	0.00	0.00	0.00	0.00	0.00	0.00	0.00	0.00	0.00	0.01	0.01	0.01	0.00	0.01	0.00	0.01	0.00	0.01	0.00	0.00	0.00	0.00
C41	frac	0.00	0.00	0.00	0.00	0.00	0.00	0.00	0.00	0.00	0.00	0.00	0.00	0.00	0.00	0.00	0.00	0.00	0.00	0.00	0.00	0.00	0.00
C42	frac	0.00	0.00	0.00	0.00	0.00	0.00	0.00	0.00	0.00	0.00	0.00	0.00	0.00	0.00	0.00	0.00	0.00	0.00	0.00	0.00	0.00	0.00
X43	frac	0.00	0.00	0.00	0.00	0.00	0.00	0.00	0.00	0.00	0.00	0.00	0.00	0.00	0.00	0.00	0.00	0.00	0.00	0.00	0.00	0.00	0.00
O2	frac	0.00	0.00	0.00	0.00	0.00	0.00	0.00	0.00	0.00	0.00	0.00	0.00	0.00	0.00	0.00	0.00	0.00	0.00	0.00	0.00	0.00	0.00
CO2	frac	0.00	0.00	0.00	0.00	0.00	0.00	0.00	0.00	0.00	0.00	0.00	0.00	0.00	0.00	0.00	0.00	0.00	0.00	0.00	0.00	0.00	0.00
H2O	frac	0.00	0.00	0.00	0.00	0.00	0.00	0.00	0.00	0.00	0.00	0.00	0.00	0.00	0.00	0.00	0.00	0.00	0.00	0.00	0.00	0.00	0.00
MCATA	frac	0.00	0.00	0.00	0.00	0.00	0.00	0.00	0.00	0.00	0.00	0.00	0.00	0.00	0.00	0.00	0.00	0.00	0.00	0.00	0.00	0.00	0.00
NAPHT-01	frac	0.00	0.00	0.00	0.00	0.00	0.00	0.00	0.00	0.26	0.00	0.00	0.00	0.00	0.00	0.00	0.00	0.00	0.00	0.00	0.00	0.00	0.00
XYLENO	frac	0.00	0.00	0.00	0.00	0.00	0.00	0.00	0.00	0.00	0.00	0.00	0.00	0.00	0.00	0.00	0.00	0.00	0.00	0.00	0.00	0.00	0.00
BUTENE	frac	0.00	0.00	0.00	0.00	0.00	0.00	0.00	0.00	0.00	0.00	0.00	0.00	0.00	0.00	0.00	0.00	0.00	0.00	0.00	0.00	0.00	0.00
BUTANE	frac	0.00	0.00	0.00	0.00	0.00	0.00	0.00	0.00	0.00	0.00	0.00	0.00	0.00	0.00	0.00	0.00	0.00	0.00	0.00	0.00	0.00	0.00
Volume Flow	l/hr	161614792.0	26697754.2	24389084.6	21950175 7.6	135645.1	24389084.2	154011.7	43904810.0	197515794.0	403326798.0	11336828.1	6572250.0	4561825.3	617593.7	338672.4	604749.6	9908.4	7130017.7	269936.5	2123.7	2159.2	50049.7

C.1.2 The integration of HDO-DeH with published FCC process

Developed flowsheet, in Figure C.5, for DeH-HDO based on integrating DeH-HDO with FCC using published results for HDO by V et al. where BTX formation is optimised. The additional SC reactors are included to include extra ethane or propane capacity to meet hydrogen requirement by HDO.

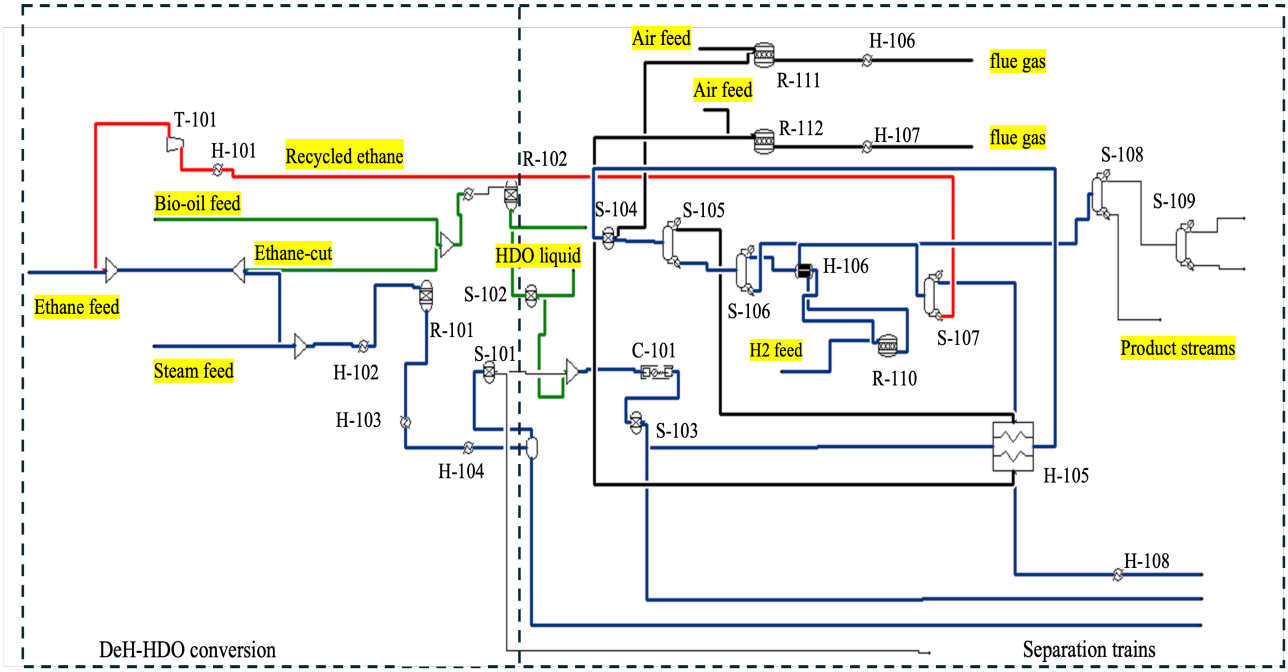


Figure C.5: Aspen developed flowsheet for improved DeH-HDO with improved process performance based on published findings for HDO

Table C.2: Main unit operation list of DeH-HDO integrated with FCC

Label	unit	Function	Parameter 1	Parameter 2	Parameter 3
C-201	3-stage compressor	Increase the pressure of conversion section product for separation	31.4 bar	Isentropic model	between stage cooling
T-201	Expander	Reduce the recycle alkane pressure	Isentropic model	1-2.2 bar	
R-20x	DeH-HDO reactors	Multiple reactors in parallel		600 °C	Max capacity 70 t/hr per reactor
R-210	Hydrogenator	Convert acetylene to ethylene			
R-211	Burner	H_2 combustion	600 °C	atmospheric pressure	air added for complete combustion
R-212	Burner	CH_4 combustion	800 °C	atmospheric pressure	air added for complete combustion
S-201	HDO liquid and gas flash				
S-202	Hydrogen removal				
S-203	Water removal				
S-204	De-methanizer	Extract methane from produced hydrocarbon mixture	Condenser pressure 26 bar	RR= 50	
S-205	De-ethanizer	Extract ethane and ethylene from produced hydrocarbon mixture			
S-206	C_2 splitter	Separate ethylene with 99.9% from unreacted ethane	Cryogenic model	Condenser 16 bar	Controlled by ethylene purity
S-207	De-propanizer	Extract propane and propylene from produced hydrocarbon mixture			
S-208	C_3 splitter	Separate propylene with 99.9% from unreacted propane	Cryogenic model	115 stages	condenser 6.0 bar
S-209	C_4 separator	Separate C_4 from BTX			
S-210	BTX fractionator	Fractionate BTX into pure products	Petro./wide-boiling	5.0 bar	partial-vapor liquid condenser

- RR refers to reflex ratio in mass basis

Figure C.6: Aspen developed flowsheet for improved DeH-HDO with improved process performance based on published findings for HDO

Parameter	Unit	Fresh ethane	Recycle ethane	Ethane feed	Ethane to SC	Steam to SC	Ethane to DeH-HDO	Bio-oil to DeH-HDO	Gas product HDO	Liquid product HDO	Mix gas	Compressed	HC	Fuel gas 1	C1+	Fuel gas 2	C2	C2+	Ethylene	Recycle ethane	Propylene	Propane	C3+
		1	2	3	4	5	6	7	8	9	10	11	12	13	14	15	16	17	18	19	20	21	22
Temperature	C	45.0	-18.1	20.4	20.4	35.0	20.4	35.0	600.0	600.0	-220.8	-238.2	-228.2	-228.2	-283.6	-362.5	-285.8	-199.9	-228.2	-290.5	-278.3	-244.8	-242.9
Pressure	bar	1.0	3.0	1.0	1.0	1.0	1.0	1.0	1.0	1.0	1.0	31.4	31.4	31.4	26.0	26.0	25.0	25.0	16.0	16.0	6.0	6.0	9.0
Mass Liquid Fraction	-	0.0	0.0	0.0	0.0	1.0	0.0	1.0	0.0	0.0	0.0	0.0	0.0	0.0	1.0	0.0	1.0	1.0	0.0	1.0	1.0	1.0	0.7
Mass Enthalpy	MJ/kg	-2.8	-2.6	-2.7	-2.7	-15.9	-2.7	-2.5	-1.0	-0.5	-0.3	-0.3	-0.4	0.3	-0.6	-4.3	-0.6	-0.2	1.9	-3.0	-0.1	-0.6	-0.2
Mass Entropy	kJ/kg-K	-5.7	-5.7	-5.7	-5.7	-5.7	-5.7	-5.7	-5.7	-5.7	-5.7	-5.7	-5.7	-5.7	-5.7	-5.7	-5.7	-5.7	-5.7	-5.7	-5.7	-5.7	-5.7
Mass Density	kg/cum	1.1	4.4	1.2	1.2	984.3	1.2	1118.7	0.3	0.9	0.7	24.7	41.0	2.4	413.6	41.3	413.6	541.4	18.6	436.1	545.8	705.4	53.6
Enthalpy Flow	MW	-141.5	-85.9	-227.4	-204.7	-590.7	-22.7	-119.5	-3.7	-26.8	-20.8	-26.4	-27.0	0.9	-39.6	-16.8	-39.3	-0.3	71.3	-98.8	0.0	-0.2	-0.2
Mole Flows	kmol/hr	6152.4	3928.8	10081.2	9073.1	7410.9	1008.1	1388.0	604.6	2724.9	14933.4	14933.4	9596.8	5336.7	8760.8	836.0	8654.9	105.9	4726.1	3928.8	28.1	24.9	52.9
Mass Flows	tonne/hr	185.0	117.7	302.7	272.4	133.5	30.3	172.3	12.9	181.3	280.2	280.2	269.5	10.8	255.5	14.0	250.1	5.4	132.5	117.7	1.2	1.5	2.7
Mass Fractions	-																						
ETHANE	frac	1.00	0.95	0.98	0.98	0.00	0.98	0.00	0.48	0.00	0.40	0.40	0.41	0.00	0.44	0.00	0.45	0.02	0.00	0.95	0.05	0.00	0.02
ETHENE	frac	0.00	0.05	0.02	0.02	0.00	0.02	0.00	0.12	0.00	0.49	0.49	0.51	0.00	0.53	0.10	0.54	0.00	0.99	0.05	0.00	0.00	0.00
HYDROGEN	frac	0.00	0.00	0.00	0.00	0.00	0.00	0.00	0.01	0.00	0.04	0.04	0.00	1.00	0.00	0.00	0.00	0.00	0.00	0.00	0.00	0.00	0.00
BENZENE	frac	0.00	0.00	0.00	0.00	0.00	0.00	0.00	0.00	0.00	0.01	0.01	0.01	0.00	0.01	0.00	0.00	0.37	0.00	0.00	0.00	0.64	0.37
METHANE	frac	0.00	0.00	0.00	0.00	0.00	0.00	0.00	0.32	0.00	0.05	0.05	0.05	0.00	0.00	0.90	0.00	0.00	0.00	0.00	0.00	0.00	0.00
CARBON	frac	0.00	0.00	0.00	0.00	0.00	0.00	0.00	0.00	0.00	0.00	0.00	0.00	0.00	0.00	0.00	0.00	0.00	0.00	0.00	0.00	0.00	0.00
1-MN	frac	0.00	0.00	0.00	0.00	0.00	0.00	0.00	0.00	0.00	0.00	0.00	0.00	0.00	0.00	0.00	0.00	0.00	0.00	0.00	0.00	0.00	0.00
1-MNH2	frac	0.00	0.00	0.00	0.00	0.00	0.00	0.00	0.00	0.00	0.00	0.00	0.00	0.00	0.00	0.00	0.00	0.00	0.00	0.00	0.00	0.00	0.00
GUAIACOL	frac	0.00	0.00	0.00	0.00	0.00	0.00	1.00	0.00	0.00	0.00	0.00	0.00	0.00	0.00	0.00	0.00	0.00	0.00	0.00	0.00	0.00	0.00
PHENOL	frac	0.00	0.00	0.00	0.00	0.00	0.00	0.00	0.00	0.24	0.00	0.00	0.00	0.00	0.00	0.00	0.00	0.00	0.00	0.00	0.00	0.00	0.00
TOLUENE	frac	0.00	0.00	0.00	0.00	0.00	0.00	0.00	0.00	0.00	0.00	0.00	0.00	0.00	0.00	0.00	0.00	0.00	0.00	0.00	0.00	0.00	0.00
ANISOLE	frac	0.00	0.00	0.00	0.00	0.00	0.00	0.00	0.00	0.02	0.00	0.00	0.00	0.00	0.00	0.00	0.00	0.00	0.00	0.00	0.00	0.00	0.00
XYLENE	frac	0.00	0.00	0.00	0.00	0.00	0.00	0.00	0.00	0.00	0.00	0.00	0.00	0.00	0.00	0.00	0.00	0.00	0.00	0.00	0.00	0.00	0.00
CRESOL	frac	0.00	0.00	0.00	0.00	0.00	0.00	0.00	0.00	0.27	0.00	0.00	0.00	0.00	0.00	0.00	0.00	0.00	0.00	0.00	0.00	0.00	0.00
CATACHOL	frac	0.00	0.00	0.00	0.00	0.00	0.00	0.00	0.00	0.00	0.00	0.00	0.00	0.00	0.00	0.00	0.00	0.00	0.00	0.00	0.00	0.00	0.00
WATER	frac	0.00	0.00	0.00	0.00	1.00	0.00	0.00	0.00	0.06	0.00	0.00	0.00	0.00	0.00	0.00	0.00	0.00	0.00	0.00	0.00	0.00	0.00
METHANOL	frac	0.00	0.00	0.00	0.00	0.00	0.00	0.00	0.00	0.15	0.00	0.00	0.00	0.00	0.00	0.00	0.00	0.00	0.00	0.00	0.00	0.00	0.00
PROPANE	frac	0.00	0.00	0.00	0.00	0.00	0.00	0.00	0.07	0.00	0.00	0.00	0.00	0.00	0.00	0.00	0.00	0.20	0.00	0.00	0.00	0.36	0.20
PROPYLEN	frac	0.00	0.00	0.00	0.00	0.00	0.00	0.00	0.00	0.00	0.01	0.01	0.01	0.00	0.01	0.00	0.00	0.41	0.00	0.00	0.95	0.00	0.41
ACE	frac	0.00	0.00	0.00	0.00	0.00	0.00	0.00	0.00	0.00	0.01	0.01	0.01	0.00	0.01	0.00	0.01	0.00	0.01	0.00	0.00	0.00	0.00
C41	frac	0.00	0.00	0.00	0.00	0.00	0.00	0.00	0.00	0.00	0.00	0.00	0.00	0.00	0.00	0.00	0.00	0.00	0.00	0.00	0.00	0.00	0.00
C42	frac	0.00	0.00	0.00	0.00	0.00	0.00	0.00	0.00	0.00	0.00	0.00	0.00	0.00	0.00	0.00	0.00	0.00	0.00	0.00	0.00	0.00	0.00
X43	frac	0.00	0.00	0.00	0.00	0.00	0.00	0.00	0.00	0.00	0.00	0.00	0.00	0.00	0.00	0.00	0.00	0.00	0.00	0.00	0.00	0.00	0.00
O2	frac	0.00	0.00	0.00	0.00	0.00	0.00	0.00	0.00	0.00	0.00	0.00	0.00	0.00	0.00	0.00	0.00	0.00	0.00	0.00	0.00	0.00	0.00
CO2	frac	0.00	0.00	0.00	0.00	0.00	0.00	0.00	0.00	0.00	0.00	0.00	0.00	0.00	0.00	0.00	0.00	0.00	0.00	0.00	0.00	0.00	0.00
H2O	frac	0.00	0.00	0.00	0.00	0.00	0.00	0.00	0.00	0.00	0.00	0.00	0.00	0.00	0.00	0.00	0.00	0.00	0.00	0.00	0.00	0.00	0.00
MCATA	frac	0.00	0.00	0.00	0.00	0.00	0.00	0.00	0.00	0.00	0.00	0.00	0.00	0.00	0.00	0.00	0.00	0.00	0.00	0.00	0.00	0.00	0.00
NAPHT-01	frac	0.00	0.00	0.00	0.00	0.00	0.00	0.00	0.00	0.26	0.00	0.00	0.00	0.00	0.00	0.00	0.00	0.00	0.00	0.00	0.00	0.00	0.00
XYLENO	frac	0.00	0.00	0.00	0.00	0.00	0.00	0.00	0.00	0.00	0.00	0.00	0.00	0.00	0.00	0.00	0.00	0.00	0.00	0.00	0.00	0.00	0.00
BUTENE	frac	0.00	0.00	0.00	0.00	0.00	0.00	0.00	0.00	0.00	0.00	0.00	0.00	0.00	0.00	0.00	0.00	0.00	0.00	0.00	0.00	0.00	0.00
BUTANE	frac	0.00	0.00	0.00	0.00	0.00	0.00	0.00	0.00	0.00	0.00	0.00	0.00	0.00	0.00	0.00	0.00	0.00	0.00	0.00	0.00	0.00	0.00
Volume Flow	l/hr	161614792.0	26697754.2	243890841.6	219501757.6	135645.1	24389084.2	154011.7	43904810.0	197515794.0	403326798.0	11336828.1	6572250.0	4561825.3	617593.7	338672.4	604749.6	9908.4	7130017.7	269936.5	2123.7	2159.2	50049.7

C.1.3 Economic equations

$$\text{NPV} = \sum_{t=0}^{n} \frac{CF_t}{(1+r)^t} \qquad \text{(Equation 1)}$$

Where:

- NPV represents the Net Present Value.
- t is the time period, ranging from 0 to n.
- CF_t represents the cash flow at time period t.
- r is the discount rate.

$$\text{AVG. Monte Carlo} = \frac{1}{N} \sum_{i=1}^{N} f(x_i) \qquad \text{(Equation 2)}$$